Performance of the TFU network of the First Level Trigger of HERA–B and determination of efficiencies for $J/\psi \to \mu^+\mu^-$

Dissertation
zur Erlangung des Doktorgrades
des Fachbereichs Physik
der Universität Hamburg

vorgelegt von
Holger Fleckenstein
aus Karlsruhe

Hamburg
2002

Gutachter der Dissertation:	Dr. A. Schwarz Prof. Dr. W. Schmidt-Parzefall
Gutachter der Disputation:	Dr. A. Schwarz Prof. Dr. B. Naroska
Datum der Disputation:	13.03.2002
Dekan des Fachbereichs Physik und Vorsitzender des Promotionsausschusses:	Prof. Dr. F.-W. Büßer

To my wife Ulrike and in memory
of my mother who passed away far too early

Leistungsverhalten des TFU Netzwerks des First Level Trigger von HERA–B und Bestimmung der Effizienzen für $J/\psi \to \mu^+\mu^-$

Kurzfassung

Das Experiment HERA–B am Deutschen Elektronen Synchrotron (DESY) ist entwickelt worden, um die Verletzung der CP Symmetrie im System neutraler B Mesonen zu messen. Aufgrund des kleinen Produktionsquerschnittes für $b\overline{b}$ in Protonkollisionen bei 920 GeV und kleiner Verzweigungsverhältnisse ist ein schnelles und leistungsfähiges Trigger (Auslöse) System erforderlich. Das Trigger System umfasst vier Stufen und ist optimiert, den Zerfall $J/\psi \to l^+l^-$ zu selektieren.

Die erste Triggerstufe (FLT) führt eine schnelle Spursuche in Echtzeit aus, die in einem speziell entwickelten Elektronikmodul, der Track Finding Unit (TFU), realisiert ist. Der FLT muss eine Eingangsrate von 10.4 MHz verarbeiten und eine Reduktion um einen Faktor 200 erreichen. Das gesamte Netzwerk besteht aus 55 TFUs.

In der vorliegenden Arbeit wird das Leistungsverhalten des TFU Netzwerks bzgl. der Totzeit und der zu erwartenden Ausgangsrate bei verschiedenen Wechselwirkungsraten untersucht. Die maximale Totzeit beträgt 4.4 % bei einer Wechselwirkungsrate von 5 MHz und 10.1 % bei 10 MHz. Wird nur eine Spur vom FLT als Triggerbedingung verlangt, beträgt die Rate 20.7 kHz bei einer Proton Wechselwirkungsrate von 5 MHz und 52.9 kHz für 10 MHz. Die maximale Eingangsrate der zweiten Triggerstufe beträgt 30 kHz. Dies ist nur mit einer Vetoschaltung für Ereignisse mit hoher Spurmultiplizität bei einem Verlust von 5 % der J/ψ Ereignissen erreichbar. Die Ausgangsrate bei einer höheren Wechselwirkungsrate kann nur entsprechend reduziert werden, wenn statt einer Spur zwei Spuren ungleicher Ladung und einer invarianten Masse von mindestens 2.0 GeV/c^2 verlangt werden.

Die FLT Effizienz, ein Myon eines $J/\psi \to \mu^+\mu^-$ Ereignisses nachzuweisen, wird aus den Daten, die im Jahre 2000 aufgezeichnet wurden, und mithilfe von "perfekten" Monte-Carlo (MC) Ereignissen als auch von realistischen MC Ereignissen, die das Leistungsverhalten des Detektors des Jahres 2000 beschreiben, bestimmt. Die Einzelspur-Effizienz beträgt für perfekte MC Ereignisse 59 %, für realistische 16 % und für die Daten 18 %. Die Effizienz ein J/ψ Ereignis nachzuweisen ist 36 % im Falle der perfekten MC Ereignisse und 4 % im Falle der Daten und der realistischen MC Ereignisse. Die Effizienzen werden auch als Funktion der kinematischen Parameter sowohl des Transversalimpulses p_T^{track} der Spuren als auch des $p_T^{J/\psi}$ des J/ψ und der Feynman Variablen x_F bestimmt.

Die Analyse der Daten zeigt einen Effizienzverlust in der Grössenordnung von 36 % im ersten Detektor MU 1 im Myon System. Der grösste Anteil, (25-28) % (abs.), geht aufgrund der schlechten Effizienz der Spurkammer verloren. Der Ineffizienz, die durch den Algorithmus verursacht wird, wird mittels perfekter MC Ereignisse zu 9.2 % ermittelt.

Abstract

The experiment HERA–B at the Deutsches Elektronen Synchrotron (DESY) is designed to measure the violation of CP symmetry in the neutral B meson system. The relatively small cross section for $b\overline{b}$ production for proton collisions at 920 GeV together with the small branching fractions require a fast and efficient trigger system. The trigger system comprises four levels and is optimized to select decays of $J/\psi \to l^+l^-$.

The First Level Trigger (FLT) performs a fast online tracking which is implemented in a custom-designed electronics board, the Track Finding Unit (TFU). The FLT has to cope with an input rate of 10.4 MHz and has to reach a suppression factor of 200. In total, the network consists of 55 boards.

The performance of the TFU network is studied with respect to deadtime and trigger rate as a function of the interaction rate. The upper limit of the deadtime is 4.4 % for an interaction rate of 5 MHz and 10.1 % for a rate of 10 MHz. Under the trigger condition to require a single track the trigger rate is 20.7 kHz for 5 MHz and 52.9 kHz for 10 MHz proton interaction rate. The limit for the input rate of the Second Level Trigger is 30 kHz which can be achieved by operating a multiplicity veto at a loss of 5 % of J/ψ events. The trigger rate at a higher interaction rate can only be reduced sufficiently by requiring instead of one track two tracks with opposite sign and an invariant mass of at least 2.0 GeV/c^2.

The FLT efficiency to find a muon track originating from a $J/\psi \to \mu^+\mu^-$ event is determined from data taken during the year 2000 and from a perfect Monte Carlo (MC) sample and a realistic MC sample that describes the detector performance of the year 2000. The single-track efficiency is 59 % for perfect MC, 16 % for realistic MC and 18 % for the data. The efficiency to trigger a J/ψ event is 36 % for perfect MC and 4 % for realistic MC as well as for the data. These efficiencies are also determined with respect to the transverse momentum p_T^{track} of the track as well as the $p_T^{J/\psi}$ of the J/ψ and with respect to the Feynman variable x_F.

The analysis of the data shows a decrease of efficiency of the order of 36 % in the first muon layer MU 1. A major fraction, (25-28) % (abs.), are due to a bad efficiency of the tracking layer. The inefficiency due to the algorithm is determined by perfect MC and results in 9.2 %.

Contents

Introduction **1**

1 Theory **3**
1.1 Symmetry and Conservation Laws . . . 3
1.1.1 Combined Transformation CP . . . 5
1.2 CP Violation in the Standard Model . . . 5
1.2.1 Appearance of CP Violation in the Standard Model . . . 5
1.2.2 The Cabbibo-Kobayashi-Maskawa-Matrix . . . 7
1.3 CP Violation in B meson Decays . . . 10
1.3.1 Mixture of neutral B mesons . . . 10
1.3.2 CP Violation in Decays of neutral B mesons . . . 11
1.3.3 The Golden Decay $B^0 \to J/\psi K_S^0$ . . . 14
1.4 Heavy Flavour Physics . . . 15
1.4.1 Heavy Quarkonium Production . . . 15

2 The HERA–B Detector **21**
2.1 Requirements for the HERA–B Detector . . . 21
2.2 The HERA Ring and the Target . . . 22
2.2.1 The Beam . . . 22
2.2.2 The Target . . . 22
2.3 The Detector Components of HERA–B . . . 23
2.3.1 The Vertex–Detector . . . 24
2.3.2 The Inner Tracker . . . 25
2.3.3 The Ring Imaging Čerenkov Counter . . . 25
2.3.4 The Transition Radiation Detector . . . 26
2.3.5 The Electromagnetic Calorimeter . . . 27
2.4 Detector Components relevant for this thesis . . . 28
2.4.1 The Outer Tracker . . . 28
2.4.2 The Muon system . . . 29

3 The Trigger System of HERA–B **31**
3.1 The Trigger Concept of HERA–B . . . 31
3.2 The Pretriggers . . . 34
3.2.1 The Electron Pretrigger . . . 34
3.2.2 The Muon Pretrigger . . . 35
3.3 The First Level Trigger . . . 35

3.3.1 The Implementation of the FLT Network . . . 37
3.3.2 The Data Link and Data Format . . . 38
3.3.3 The Track Finding Unit . . . 39
3.3.4 The Track Parameter Unit . . . 40
3.3.5 The Trigger Decision Unit . . . 41
3.4 The Higher Level Trigger . . . 42
3.4.1 The Second Level Trigger . . . 43
3.4.2 The Third Level Trigger . . . 44
3.4.3 The Fourth Level Trigger . . . 44

4 The Track Finding Unit 47
4.1 Introduction . . . 47
4.1.1 The Concept of the First Level Trigger . . . 47
4.1.2 Conventions and Mathematical Remarks . . . 48
4.1.3 The Implementation of the Tracking Algorithm . . . 51
4.1.4 The Principle of the Tracking Algorithm . . . 53
4.2 Tracking Algorithm in Detail . . . 55
4.2.1 Calculating the current Region Of Interest . . . 55
4.2.2 The Wire Memory . . . 61
4.2.3 The Coincidence Matrix . . . 61
4.2.4 Prediction of the next ROI and Message Update . . . 63
4.3 The Implementation in Hardware . . . 67
4.4 Simulation Framework . . . 70

5 Latency and Rate Measurements 73
5.1 Analysis of the Network at 5 and 10 MHz Target Rate . . . 73
5.1.1 Effect of Channel Masking . . . 77
5.1.2 Correlation with Multiplicity Veto Components . . . 78
5.1.3 Network Load . . . 83
5.1.4 Estimated Single-Track Trigger Rate . . . 85
5.1.5 Rate Estimation for the Pair Trigger . . . 89
5.2 Analysis of the Network at 20 MHz Target Rate . . . 91
5.2.1 Estimated Single-Track Trigger Rate . . . 97
5.2.2 Rate Estimation for the Pair Trigger . . . 98
5.3 Estimation of the Systematic Error . . . 99
5.4 Summary and Conclusion . . . 101

6 Acceptance and Efficiency Studies 103
6.1 Data and Monte Carlo Samples . . . 103
6.1.1 "Hard Selected" J/ψ . . . 103
6.1.2 Monte Carlo Samples . . . 104
6.2 Method . . . 104
6.2.1 Selection of Reference Tracks . . . 104
6.2.2 Matching Procedure . . . 105
6.3 Results for Single-Track Acceptance and Efficiency . . . 108
6.3.1 Track Acceptance . . . 108

6.3.2 Hit Efficiency . . . 109
6.3.3 Bias due to SLT Trigger Decision . . . 111
6.3.4 Single-Track Efficiency . . . 112
6.3.5 Single-Track Efficiency as a Function of p_T^{track} . . . 115
6.4 Results on J/ψ Event Basis . . . 117
6.4.1 General Decay Kinematics . . . 117
6.4.2 Event Acceptance . . . 118
6.4.3 A Cross Check: 'Single-Track' versus 'Event' Acceptance . . . 120
6.4.4 Event Efficiency . . . 121
6.4.5 Total Acceptance times Efficiency . . . 122
6.5 Acceptance and Efficiency as a Function of Transverse Momentum of J/ψ . 122
6.6 Acceptance and Efficiency with respect to x_F . . . 124
6.6.1 Single-Track and Event Acceptance vs x_F . . . 126
6.6.2 Single-Track and Event Efficiency vs x_F . . . 128
6.7 Measurement of the J/ψ Efficiency from Event-Counting in Data . . . 130
6.7.1 Method . . . 130
6.7.2 Results . . . 131
6.8 Estimation of the Systematic Error . . . 132
6.9 Summary and Conclusion . . . 134

7 Efficiency Loss in Muon Layer MU 1 **137**
7.1 Method . . . 138
7.2 Track Categories . . . 139
7.3 Algorithmic Inefficiency . . . 139
7.4 Tracks *inside* the ROI resulting in invalid messages . . . 139
7.4.1 Effect of the "shift flag" . . . 140
7.4.2 Effect of Multiple Scattering . . . 141
7.4.3 Mapping Problems . . . 142
7.4.4 Calculation of the First Wire of the ROI . . . 143
7.4.5 Inefficiencies related to Geometrical Effects . . . 146
7.4.6 Estimation of the Detector Inefficiency . . . 147
7.5 Tracks *outside* the ROI resulting in invalid messages . . . 149
7.6 Summary and Conclusion . . . 150

Summary and Conclusion **153**

A Glossary **157**

B Parameter definitions **159**

C Overview of TFU Look Up Tables **163**

Bibliography **169**

Acknowledgement **177**

List of Figures

1.1 A unitarity triangle of the CKM matrix 9
1.2 Feynman graphs of $B^0\overline{B^0}$ oscillations 11
1.3 Feynman graph of golden decay 14
1.4 A dependance as a function of x_F and p_T 19
1.5 b production cross section versus beam energy 19

2.1 Structure of the proton beam 22
2.2 Target setup 23
2.3 Schematic overview of the experiment HERA–B 24
2.4 Schematic overview of the vertex detector system 25
2.5 The GEM chamber 26
2.6 The functionality of the RICH 27
2.7 Calorimeter module 28
2.8 Drift cell of the outer tracker 29
2.9 Muon detection system 30
2.10 Schematic drawing of a muon tube and a muon pad cell 30

3.1 Trigger architecture of HERA–B 33
3.2 Pretrigger coincidences for the muon pretrigger 35
3.3 FLT network 36
3.4 FLT sector arrangement and TFU assignment 38
3.5 Schematic drawing of TPU calculation 41
3.6 Trigger system overview 45

4.1 The coordinate systems used by the FLT 49
4.2 Extrapolation in y-direction of the FLT 50
4.3 Extrapolation in x-direction of the FLT 51
4.4 Transformation of a coordinate to a bit value 52
4.5 The principle of a Look Up Table 53
4.6 The principle of the tracking algorithm of the FLT 54
4.7 Overview of LUT processing of a TFU 56
4.8 Calculation of n1 57
4.9 Calculation of dn1+ 58
4.10 Calculation of l2 59
4.11 Calculation of h 60
4.12 Realisation of the Coincidence Matrix 62
4.13 Geometrical boundary for new track slope $d\xi$ 63

4.14 Calculation of new ROI 64
4.15 Calculation of $\eta 1$ 66
4.16 Calculation of ξ_{next} 67
4.17 Data flow from detector to the TFU 68
4.18 Picture of TFU and Message board 69
4.19 Architecture of FLT simulation 70

5.1 Distribution of physical BX 74
5.2 Occupancy of the OTR at 5 MHz 75
5.3 Deadtime of the TFU network at 5 MHz 76
5.4 Occurrence of the TFU with maximal message at 5 MHz 76
5.5 Correlation of detector hits and energy deposition 79
5.6 Number of messages as a function of detector hits at 5 MHz 80
5.7 Deadtime at 5 MHz target rate 82
5.8 Deadtime at 10 MHz target rate 83
5.9 Interconnection of TFU network 84
5.10 Average message load per superlayer at 5 MHz 84
5.11 Message distribution at TDU at 5 MHz 86
5.12 Trigger rate at 5 MHz 88
5.13 Trigger rate at 10 MHz 89
5.14 Occupancy of the OTR at 20 MHz 92
5.15 Deadtime of the TFU network at 20 MHz 92
5.16 Deadtime at 20 MHz target rate 93
5.17 Beam structure of the analysed runs of 20 MHz 94
5.18 Deadtime at 20 MHz as a function of occupancy 95
5.19 Deadtime of TFU network at 20 MHz versus occupancy 95
5.20 Correlation of hits and number of messages at 20 MHz 96
5.21 Trigger rate at 20 MHz 98

6.1 Residuals of hard selected and simulated tracks 106
6.2 s^2 distribution of hard selected J/ψ 107
6.3 Geometrical acceptance of tracks from $J/\psi \to \mu^+\mu^-$ 109
6.4 p_T spectrum of MC reference track 110
6.5 Single-track efficiency 113
6.6 FLT single-track efficiency versus p_T 115
6.7 Effect of multiple scattering on the single-track efficiency 116
6.8 Spectrum of p_T of J/ψ 117
6.9 Correlation of transverse momenta of $J/\psi \to \mu^+\mu^-$ leptons 118
6.10 Event acceptance versus p_T 119
6.11 J/ψ efficiency versus p_T 121
6.12 FLT acceptance as a function of $p_T^{J/\psi}$ 123
6.13 FLT efficiency as a function of p_T of J/ψ 124
6.14 Total FLT efficiency as a function of $p_T^{J/\psi}$ 125
6.15 x_F distribution of $J/\psi \to \mu^+\mu^-$ events 126
6.16 Geometrical acceptance for the inner part versus x_F 127
6.17 FLT efficiency as a function of x_F 128

6.18 Total J/ψ efficiency as a function of x_F 129
6.19 Invariant mass of $J/\psi \to \mu^+\mu^-$ events 131
6.20 Efficiency of $J/\psi \to \mu^+\mu^-$ events per superlayer 132
6.21 Relative efficiency versus probability cut 133

7.1 Single-track efficiency for data and MC 137
7.2 Wire spacing for 20° layer 140
7.3 Effect of multiple scattering from MC $J/\psi \to \mu^+\mu^-$ events 141
7.4 Difference between the hit wire and the first wire of ROI 144
7.5 Wire difference as function of n 145
7.6 Correlation plot of wire differences 146
7.7 Difference of reference wire and wire of wire memory 147
7.8 Occupancies of muon tube chambers 148
7.9 Occupancy of TFU wire memory for data 148
7.10 Extrapolation from MU 3 to MU 1 149

List of Tables

1.1 The standard model 6

3.1 Definition of a pretrigger or TFU message 40

4.1 Assignment of reference layers 49
4.2 Result of h calculation 60

5.1 Assignment of TFU number in trigger layer 77
5.2 Veto cuts and J/ψ loss 79
5.3 Deadtime and trigger rate at 5 MHz 87
5.4 Deadtime and trigger rate at 10 MHz 90
5.5 Pair trigger rate at 10 MHz 91
5.6 Deadtime and trigger rate at 20 MHz 97
5.7 Pair trigger rate at 20 MHz 99
5.8 Summary of the latency and rate measurement 101

6.1 Hit efficiency per superlayer 111
6.2 Ratio for the efficiencies per superlayer due to SLT bias 112
6.3 Effect of detector inefficiencies on track efficiency 114

7.1 Results of FED and channel comparison 143
7.2 Sources of inefficiency in MU 1 151
8.1 Summary of the track and J/ψefficiency 154
8.2 Summary of the track and J/ψefficiency for p_T^{track}, $p_T^{J/\psi}$ and x_F 155

Introduction

Since the origin of mankind, man has tried to understand its environment and the manyfold processes that are related with it. Man has tried to find rules or regularities underlying the observations. As time evolves the techniques to investigate and describe observation evolved, too. The goal was all the time to find one coherent description for all processes.

Today, mankind observes very small as well as very large scale objects and tries to find one coherent description for both. The very small objects are subject of the field of particle physics. The observations are described by the standard model [Gla61, Wei67] which consists of 12 fundamental constituents, the leptons and the quarks, and three kinds of interaction, the electromagnetic, the strong and the weak interaction. The first and the last interaction could be unified to one whereas the strong interaction is treated separately.

The very large scale objects are described by the theory of gravitation which cannot be described within the standard model. Many parameters of the standard model need to be chosen arbitrarily. New theories are needed to overcome the problem of unknown parameters and to arrive at a better understanding of the processes. The behaviour of a physics process with respect to an underlying symmetry is of special interest since conservation laws such as momentum or energy conservation are derived from a symmetry.

The experiment HERA–B at the Hadron Electron Ring Accelerator (HERA)[1] at the Deutsches Elektronen Synchrotron (DESY) was planned to contribute to the understanding of the violation of CP symmetry. CP violation means that a physics process for a particle and its antiparticle do not give the same result. This is an important phenomenon which can clarify why the universe as we know it favours matter over antimatter. The main goal of HERA–B was the investigation of the gold plated decay $B^0 \to J/\psi K^0_S$. The detector and the trigger as described in this thesis were optimised to select and to detect the J/ψ meson out of a large background.
Due to the challenging techniques needed for the experiment it was delayed. The physics program was adapted to fields being also accessible and manageable with the detector and the trigger system. The new goals of the experiment cover QCD[2] physics, the production of heavy quarks and bound states of heavy quarks such as charmonium.

The first chapter of this thesis provides an overview of the theoretical models to de-

[1] Abbreviations and specific expressions are listed in the glossary
[2] Quantum Chromo Dynamics, theory to describe the strong interaction

scribe CP violation in the standard model. In addition, various models of quarkonium production are discussed briefly. The beam facilities and the detector are subject of the second chapter. The trigger and data acquisition system are presented in the third chapter. Special emphasis is put on the trigger components of the First Level Trigger (FLT). The fourth chapter is dedicated to the description of the tracking algorithm and its realisation in a custom designed hardware board, the Track Finding Unit (TFU). The measurement of the latency for the TFU processor network and the expected output rates for different interaction rates are subject of chapter 5. Chapter 6 describes the geometrical acceptance and the efficiency of the FLT for the decay $J/\psi \to \mu^+\mu^-$ based on data taken during the year 2000 and Monte Carlo samples. The analysis of the track efficiency shows a drastic decrease in the first muon layer. The investigation of this loss and possible improvements are discussed in chapter 7. Finally, we summarise the results of this thesis and provide the conclusions of the studies.

Chapter 1

Theory

1.1 Symmetry and Conservation Laws

In physics, symmetry is of fundamental importance. Symmetry means that a transformation of a physical system keeps the system itself unchanged. Many processes in physics can be described easily by the help of a symmetry on which the process is based on. The other way round is also possible: Detecting a symmetrical structure of laws of nature can lead to the prediction of new laws and theories.

Of large importance in physics is the correlation of symmetry and conservation law which is described by the Noether-Theorem [Noe16]. According to this theorem, the existence of a conserved physical quantity is derived by the invariance of a physical system undergoing a transformation. The conservation of energy is a result of the invariance of a system with respect to transformation in time or the conservation of angular momentum as the invariance with respect to spatial rotation.
The presence of conserved quantities leads to specific selection rules in physics manifesting that some processes do not occur in nature. If they occur in nature a conservation law and consequently the symmetry are broken.

In nature, many symmetries are realised completely and exactly. However, there are symmetries that are only valid for certain physical systems and interactions. There are symmetries that are satisfied only approximately, too. Usually, a symmetry introduces a physical quantity that cannot be measured. If the symmetry is broken, this physical quantity becomes visible and can be detected experimentally.

In elementary particle physics, discrete symmetries such as time reversal T (**T**ime), spatial inversion P (**P**arity) and particle-antiparticle conjugation C (**C**harge-conjugation) are of special interest.

Spatial Inversion P

Spatial inversion P, also called parity transformation, changes the sign of polar vectors such as momentum or location while axial vectors such as angular momentum keep unchanged. It is indeed an inversion of the coordinate system at the origin.

$$\vec{x} \xrightarrow{\mathbf{P}} -\vec{x}\,, \qquad \vec{p} \xrightarrow{\mathbf{P}} -\vec{p}\,, \qquad \text{but} \qquad \vec{L} \xrightarrow{\mathbf{P}} \vec{L}\,. \tag{1.1}$$

Parity P changes a quantum mechanical wave function like:

$$\mathbf{P}\psi\left(\vec{x},t\right)=\psi\left(-\vec{x},t\right). \tag{1.2}$$

Repeating the parity operation ascribes the wave function to its original state which yields the eigenvalues of the parity operator that are +1 and -1:

$$\mathbf{PP}\psi(\vec{x},t)=\psi(\vec{x},t).$$

P symmetry is conserved in the strong and electromagnetic interaction but not in the weak interaction where it is maximally violated. Lee and Yang predicted it in 1956 [Lee56]. Only one year later, it was proven in the β-decay of nuclei [CWu57]. The maximal violation of parity P in the weak interaction has as a consequence that no righthanded neutrinos exist. A righthanded particle is a particle whose projection of spin is in the same direction as its momentum. For lefthanded particle consequently the spin is directed opposite to its momentum. Parity operation P changes the direction of motion but not the angular momentum. In case of neutrinos, a lefthanded one transforms to righthanded and vice versa. The weak interaction produces only lefthanded neutrinos. Applying the parity operation to such a process changes a lefthanded neutrino to a righthanded which does not exist in nature. The weak interaction allows to distinguish left from right.

Charge Conjugation C

Charge conjugation operation C replaces a particle by its antiparticle and changes the sign of all additive, chargelike quantum numbers such as electrical charge, lepton and baryon number. Strong and electromagnetic interactions are invariant under this transformation which means that they treat particles and anitparticles in the same way.
Like parity operation, charge conjugation is violated in the weak interaction.

$$q \xrightarrow{\mathbf{C}} -q\,, \qquad \vec{x} \xrightarrow{\mathbf{C}} \vec{x}\,, \qquad t \xrightarrow{\mathbf{C}} t\,. \tag{1.3}$$

The violation of the C symmetry was proven in the decay $\pi^+ \to \mu^+\nu_\mu$ in 1957 [Fri57, Gar57]. If the C parity was not violated the muons from the decay would have no polarisation along their direction of flight. The measurement of the polarisation of the decay products $e\nu_e\nu_\mu$ from the muon showed a strong polarisation of the muon. Consequently, the violation of C symmetry was proven.

Time Reversal T

Time reversal T changes the direction of chronology of processes. A transformation looks like:

$$t \xrightarrow{\mathbf{T}} -t\,, \qquad \vec{x} \xrightarrow{\mathbf{T}} \vec{x}\,, \qquad \text{consequently} \qquad \vec{v} \xrightarrow{\mathbf{T}} -\vec{v}\,. \tag{1.4}$$

Time reversal is also referred to as inversion of motion because of the sign flip of the momentum vector. The Newtonian as well as the relativistic equations of motion, the strong and weak interaction are invariant under time reversal operation. Physical processes in reversed time direction that are described by these laws are identical with the original

process. The presence of a time direction for every day's life is only due to the increase in entropy, i.e. the transition to a more probable state. The underlying elementary processes of this transition are invariant under T transformation.
Like P and C symmetry, T symmetry is also violated in weak interaction. Recently, T violation in weak interaction was proven by two experiments [Ang98, Aff99]. T violation was expected since the detection of CP violation. This is an important discovery as it guarantees the validity of the CPT-theorem.

CPT-Theorem

The weak interaction is not invariant under the standalone operations of C, P and T. The combination CPT of all three transformations however manifests a symmetry even for weak processes. The invariance of all interactions under CPT transformation is a fundamental result of quantum field theory [Schw51, Lue54, Pau55]. CPT invariance is a result of common demands like validity of quantum mechanics, Lorentzian invariance of the theory and the assumption that forces are mediated by the means of fields [Gri87] which form the basis of nowadays theories.
A consequence of CPT invariance, is that particles and their antiparticles have the same lifetime and mass and same but opposite signed magnetic momenta. Up to now, there are no experimental results that indicate a violation of CPT invariance [Car90, Kaw02].

1.1.1 Combined Transformation CP

For a long period, the combined transformation of charge conjugation and parity operation CP was considered to be a symmetry valid for all interactions.

A process to be invariant under CP transformation means that the probability from initial state to final state is exactly the same as for the CP conjugated states, respectively. If processes exist for which this statement is violated the CP invariance is broken:

$$\Gamma(|i\rangle \to |f\rangle) \quad \neq \quad \Gamma(CP|i\rangle \to CP|f\rangle)$$
$$\Longrightarrow \qquad CP \text{ symmetry is broken.}$$

CP violation in weak interaction was detected in 1964 in the decay of neutral K mesons [Chr64]. The nowadays accepted theory that describes elementary particle physics (i.e. the standard model) features also the phenomenon of CP violation. However, it is the least checked aspect of the standard model.

1.2 CP Violation in the Standard Model

1.2.1 Appearance of CP Violation in the Standard Model

The standard model describes attributes and interactions of elementary modules of matter. The particles are listed in Table 1.1. They are divided into two parts: the leptons and the quarks and the field bosons. The leptons and quarks have spin 1/2. The field bosons have spin 1. The leptons however are not subjected to strong interactions. The lepton families consist of electron, muon and tau as well as three different electrically neutral neutrinos.

Leptons and Quarks				Field Bosons	
Generation	1	2	3	Interaction	Force carrier
leptons	e	μ	τ	strong	8 gluons (g)
	ν_e	ν_μ	ν_τ		
quarks	u	c	t	electromagnetic	photon (γ)
	d	s	b	weak	$W^\pm$, Z^0

Table 1.1: *The standard model*

The six types of quarks that are distinguished by their "quark flavour" quantum number. For a certain kind of quark the value of this number is 1 whereas the other numbers are 0. For each type of quark and lepton shown above an antiparticle with same mass but opposite charge exists. In case of a quark, the flavour quantum number is inverted, too.

Interactions in the standard model are described by the mediation of particles with spin 1 (bosons). In the case of the weak interactions, its force is exchanged by charged bosons such as W^+, W^- and by the neutral Z^0 boson. The electromagnetic interaction is mediated by the photon. Both interactions are described in the standard model by one unified quantum field theory. The strong interaction is carried by the gluons among quarks.

Masses in the standard model are generated by the Higgs mechanism [Wei67]. A Higgs field ϕ is introduced which couples to fermions, gauge bosons and with itself.

A Lagrange density describes the dynamics of particles. In the standard model, it can be divided up into three parts:

$$\mathcal{L}_{SM} = \mathcal{L}_{kin} + \mathcal{L}_{Higgs} + \mathcal{L}_{Yukawa} \tag{1.5}$$

The first term in equation 1.5 describes the coupling of fermions to gauge bosons and that of the gauge bosons with each other. The second term reflects the self-coupling of the Higgs field and $\mathcal{L}_{Yukawa}$ describes the interaction of fermions with the Higgs field.

$\mathcal{L}_{kin}$ as well as the Higgs self-coupling in its simplest parameterisation do not violate CP symmetry [Nir99]. Nevertheless, it is shown in [Jar85] that CP violation in the standard model appears if the Yukawa coupling consists of complex parts. The Yukawa part of the Lagrange density can be formulated such:

$$\mathcal{L}_{Yukawa} = Y^d_{ij}\overline{Q^I_{Li}}\phi d^I_{Rj} + Y^u_{ij}\overline{Q^I_{Li}}\phi u^I_{Rj} + Y^l_{ij}\overline{L^I_{Li}}\phi l^I_{Rj} + hermitian\ conjugate\ (h.c). \tag{1.6}$$

Q^I_{Li} and L^I_{Li} are wave functions of lefthanded quarks and leptons, respectively, u^I_{Rj}, d^I_{Rj} and l^I_{Rj} are those of righthanded u-type ($= u$, c, t) quarks, d-type ($= d$, s, b) quarks and those of righthanded leptons. The index I shows that the particles are represented in interactions basis. Those particles couple to the charged gauge bosons of weak interaction. The operators $Y^{(d,u,l)}_{ij}$ describe the Yukawa coupling.

The expectation value for the ground state (vacuum) of the Higgs field is nonzero. Evolving the Lagrange density with respect to the value of the Higgs field in ground state, the terms of the Yukawa interaction separate into one part for the interaction itself and the other one for fermion masses[1]. The mass terms look like:

$$\overline{d^I_{Li}}(\mathcal{M}^d)_{ij}d^I_{Rj} + \overline{u^I_{Li}}(\mathcal{M}^u)_{ij}u^I_{Rj} + \overline{l^I_{Li}}(\mathcal{M}^l)_{ij}l^I_{Rj} \tag{1.7}$$

[1] A detailed description of the Higgs mechanism can be found in [Hal84]

for u-type and d-type quarks and for negative charged leptons. The Higgs mechanism does not predict the range of fermion masses. They enter the standard model as free parameters that have to be determined experimentally. The Yukawa operators $\mathcal{M}^{(u,d,l)} = \frac{v}{\sqrt{2}} Y^{(u,d,l)}$ determine the mass operators M^u, M^d and M^l exactly within a scalar factor which is the vacuum expectation value of the Higgs field. The mass operators are not mandatory diagonal. In order to have them diagonalised, transformation matrices V_L^d, V_R^d, V_L^u and V_R^u need to be introduced:

$$V_L^{(u,d)} \mathcal{M}^{(u,d)} V_R^{(u,d)\dagger} = M_{diag}^{(u,d)} \ . \tag{1.8}$$

The matrices transform fermion states from the interaction basis to the mass eigen basis:

$$u_{(L,R)}^M = V_{(L,R)}^u u_{(L,R)}^I \ , \tag{1.9}$$

$$d_{(L,R)}^M = V_{(L,R)}^d d_{(L,R)}^I \ . \tag{1.10}$$

A weak charged current describes the coupling of charged gauge bosons W^+ and W^- of weak interaction to the fermions. For quarks, this current looks like:

$$J_\mu^{charged} \propto \overline{u}_{Li}^I \gamma^\mu d_{Lj}^I + h.c. \ . \tag{1.11}$$

Replacing the states of interaction basis by mass eigen states, the equation for quarks looks like equation 1.10:

$$J_\mu^{charged} \propto \overline{u}_{Li}^M \gamma^\mu (V_L^u V_L^{d\dagger})_{ij} d_{Lj}^M + h.c. \ , \tag{1.12}$$

with

$$V_{CKM} = V_L^u V_L^{d\dagger} \tag{1.13}$$

referred to as Cabbibo-Kobayashi-Maskawa-Matrix or CKM-matrix [Cab63, Kob73]. CP violation can only appear if the Yukawa coupling consists of complex parts which can only happen if the CKM matrix possesses a complex phase which is unlike zero. The existence of a complex phase of the CKM matrix may lead to CP violation in the standard model.

1.2.2 The Cabbibo-Kobayashi-Maskawa-Matrix

The CKM matrix describes the mixture of mass eigen states $\left(d^M \, s^M \, b^M\right)$ with quark eigen states of the charged weak current $\left(d^I \, s^I \, b^I\right)$. It does not matter if the d-, s- and b-quarks or the u-, c- and t-quarks are rotated. The states are chosen in such a way that the mass and interaction eigenstates of the u-type quarks are alike:

$$\begin{pmatrix} d^I \\ s^I \\ b^I \end{pmatrix} = \begin{pmatrix} V_{ud} & V_{us} & V_{ub} \\ V_{cd} & V_{cs} & V_{cb} \\ V_{td} & V_{ts} & V_{tb} \end{pmatrix} \begin{pmatrix} d^M \\ s^M \\ b^M \end{pmatrix} \ . \tag{1.14}$$

The $W^\pm$-bosons couple to the dubletts

$$\begin{pmatrix} u^I \\ d^I \end{pmatrix} , \begin{pmatrix} c^I \\ s^I \end{pmatrix} , \begin{pmatrix} t^I \\ b^I \end{pmatrix} \ . \tag{1.15}$$

As there are three families of particles the CKM matrix is a complex 3×3 matrix which incorporates 18 parameters – nine real and nine imaginary parts. The matrix has to be unitary because it represents a transformation between equivalent bases:

$$V_{CKM} V_{CKM}{}^\dagger = Id_3 \tag{1.16}$$

with Id_3 being the identity matrix in three dimensions. The requirement of unitarity leads to nine equations. With their help, nine parameters can be eliminated. The parameters can be chosen such that there are three real angles and six complex phases. Five of those six phases are relative quark phases that can be set to zero by an appropriate rotation of the CKM matrix. In total, three real parameters and one complex phase remain as physical quantities whose values are not predicted by the standard model but have to be determined experimentally. CP violation occurs if the complex phase is nonzero.

The situation would be different if there were only two generations of quarks. In this case, the CKM matrix would be a real 2×2 matrix whose parameters except one real one could be set to zero. The CKM matrix would be entirely real with the result that there would be no CP violation in the standard model. Only the existence of a third generation of quarks allows for CP violation which prompted Kobayashi and Maskawa to introduce well before the experimental evidence a third generation of quarks into the Cabbibo matrix. For the appearance of mixtures and complex phases it is mandatory that the fermions have a mass. As neutrinos are thought to be massless the matrix $V_{MNS} = V_{\nu L} {V_{lL}}^{\dagger}$ that describes the mixture can be transformed to the unit matrix because of the possibility to choose $V_{\nu L}$ arbitrary [Mak62]. A mixture of generations and of the complex phase cannot appear. If there will be experimental evidence of neutrino oscillations which implies a mass of neutrinos which is unlike zero, a mechanism similar to that of the quark sector needs to be introduced to the lepton sector. CP violation in the lepton sector is possible, too. Experimental indication of flavour mixing for neutrinos dates to 1998 by the Super-Kamiokande experiment [Fuk98].

The CKM phase is the only source of CP violation inside the standard model whereas numerous extensions of the standard model take additional sources for CP violation into account. The main goal of experiments that look for CP violation is to check whether the measured phase of the CKM matrix explains CP violation in a quantitative way. Deviations from the predictions indicate that there are other contributions from outside the standard model to CP violation.

Wolfenstein-Parameterisation of the CKM Matrix

The Wolfenstein-Parameterisation evaluates all matrix elements of CKM matrix with respect to the parameter $\lambda = |V_{us}| = \sin\theta_{Cabbibo} \approx 0.21$

$$\mathbf{V_{CKM}} = \begin{pmatrix} 1 - \frac{\lambda^2}{2} & \lambda & \lambda^3 A(\rho - i\eta) \\ -\lambda & 1 - \frac{\lambda^2}{2} & \lambda^2 A \\ \lambda^3 A(1 - \rho - i\eta) & -\lambda^2 A & 1 \end{pmatrix} + \mathcal{O}(\lambda^4) \tag{1.17}$$

with three real parameters λ, ρ, A and one imaginary part $i\eta$. The Wolfenstein-Parameterisation reflects clearly the sizes of the different matrix elements. The diagonal elements are approximately one whereas the values decrease with increasing distance from the main diagonal. The mixture of the third quark generation is weaker than those of the first or of the second one. Measurements of the various matrix elements at 90 % confidence level are summarised below ([Cas98]):

$$|V| = \begin{pmatrix} 0.9745 - 0.9760 & 0.217 - 0.224 & 0.0018 - 0.0045 \\ 0.217 - 0.224 & 0.9737 - 0.9753 & 0.036 - 0.042 \\ 0.004 - 0.013 & 0.035 - 0.042 & 0.9991 - 0.9994 \end{pmatrix} . \tag{1.18}$$

Unitarity Relations

Nine equations result from the requirement of the unitarity (see equation 1.16) of the CKM matrix:

$$\begin{aligned} \sum_{i=d,s,b} V_{\alpha i} {V_{\alpha i}}^* &= 1 \qquad \alpha \in \{u,c,t\} \ , \\ \sum_{\alpha=u,c,t} V_{\alpha i} {V_{\alpha j}}^* &= 0 \qquad i \neq j \qquad \text{and} \quad i,j \in \{d,s,b\} \ , \\ \sum_{i=d,s,b} V_{\alpha i} {V_{\beta i}}^* &= 0 \qquad \alpha \neq \beta \qquad \text{and} \quad \alpha,\beta \in \{u,c,t\} \ . \end{aligned} \tag{1.19}$$

The equations above represent the sum of three complex numbers. The lower two rows represent six equations which are all zero and can be interpreted as triangles (i.e. unitarity triangles) in the complex plane.

$$V_{ud} {V_{ub}}^* + V_{cd} {V_{cb}}^* + V_{td} {V_{tb}}^* = 0 \tag{1.20}$$

Equation 1.20 reflects the triangle shown in Figure 1.1a. The side $V_{cd} {V_{cb}}^*$ of the triangle is approximately real (the imaginary part is of the order of $\mathcal{O}(\lambda^7)$ which is negligible) if the phase convention of the Wolfenstein-Parameterisation is chosen. It can be put on the real axis. The triangle of Figure 1.1b is the result of scaling all sides with the length of $V_{cd} {V_{cb}}^*$. The top of the triangle has the coordinates (ρ, η) because of $V_{ud} \approx 1$. The height of this unitarity triangle is the imaginary parameter $i\eta$ of the CKM matrix. The angles of the triangle are related to the CKM matrix elements by

$$\alpha = \arg\left(-\frac{V_{td} {V_{tb}}^*}{V_{ud} {V_{ub}}^*}\right) \ , \quad \beta = \arg\left(-\frac{V_{cd} {V_{cb}}^*}{V_{td} {V_{tb}}^*}\right) \quad \text{and} \quad \gamma = \arg\left(\frac{V_{ud} {V_{ub}}^*}{V_{cd} {V_{cb}}^*}\right) . \tag{1.21}$$

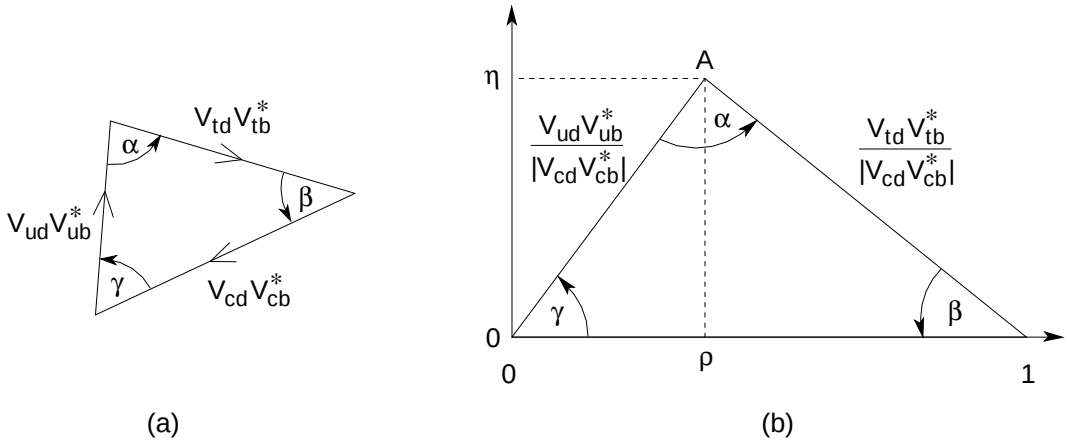

Figure 1.1: *The unitarity triangle as described by equation 1.20. Right: Same triangle rescaled in $\rho - \eta$ plane. [Bab98]*

Direct measurements of the angles of the unitarity triangle are a consistency check of the description of CP violation in the standard model. The collaborations BABAR

and BELLE provide to date the most accurate measurements of the angle β and give the following results:

$$\begin{aligned} \sin 2\beta = \ & 0.59 \pm 0.14(stat.) \pm 0.05(syst.) \quad \text{(BABAR)} \quad [\text{Aub01}] \,, \\ \sin 2\beta = \ & 0.99 \pm 0.14(stat.) \pm 0.06(syst.) \quad \text{(BELLE)} \quad [\text{Abe01}] \,. \end{aligned}$$

The results manifest CP violation in the B system.

1.3 CP Violation in B meson Decays

The standard model predicts for B meson decays especially for neutral B mesons large CP violating effects which are very suitable for measuring the CKM phase independently. The mixture of states (often referred to as oscillation) is of large interest with respect to CP violation in decays of neutral B mesons. The following assumptions for the mixture of states in the $B_d^0\overline{B_d^0}$ system can be extended also for the $B_s^0\overline{B_s^0}$, $K^0\overline{K^0}$ or $D^0\overline{D^0}$ systems.

1.3.1 Mixture of neutral B mesons

B_d^0 mesons, abbreviated by B^0, consist of a $\overline{b}$ and of a d quark. Consequently, the $\overline{B^0}$ consists of a b and a $\overline{d}$ quark. The states $|B^0\rangle$ and $|\overline{B^0}\rangle$ define the valence quark content of the mesons and are called flavour eigenstates. At generation by the strong interaction, the mesons exist as pure flavour eigenstates $|B^0\rangle$ and $|\overline{B^0}\rangle$. Transitions from one eigenstate to the other are realised by processes of the weak interaction (Figure 1.2). After a time t has passed, the mesons are in a mixed state:

$$|B(t)\rangle = a(t)|B^0\rangle + b(t)|\overline{B^0}\rangle. \tag{1.22}$$

The Schrödinger equation describes the evolution in time [Nir99]

$$i\frac{d}{dt}\begin{pmatrix} a(t) \\ b(t) \end{pmatrix} = \mathbf{H}\begin{pmatrix} a(t) \\ b(t) \end{pmatrix} = \left(\mathbf{M} - \frac{i}{2}\mathbf{\Gamma}\right)\begin{pmatrix} a(t) \\ b(t) \end{pmatrix}. \tag{1.23}$$

In case that the Hamiltonian is parametrised by

$$\mathbf{H} = \begin{pmatrix} A & p^2 \\ q^2 & A \end{pmatrix} \qquad A, p, q \in \mathbf{C} \,, \tag{1.24}$$

the eigenstates of the Hamiltonian look like:

$$\begin{aligned} |B_L\rangle &= p|B^0\rangle + q|\overline{B^0}\rangle \qquad \text{eigenvalue:} \quad \mu_L = A + pq \,, \\ |B_H\rangle &= p|B^0\rangle - q|\overline{B^0}\rangle \qquad \text{eigenvalue:} \quad \mu_H = A - pq \,. \end{aligned} \tag{1.25}$$

The eigenvalues can be separated by real and imaginary part: $\mu_L = m_L - i\frac{\Gamma_L}{2}$ and $\mu_H = m_H - i\frac{\Gamma_H}{2}$, with m_L and m_H being the masses of the eigenstates and Γ_L and Γ_H being their decay widths. Both eigenstates are different in mass and lifetime. The difference in lifetime is rather small: $\Delta\Gamma/\Gamma \leq \mathcal{O}(10^{-2})$ and can be neglected [Nir99]. Hence, the decay rate for the B^0 system looks like $\Gamma \approx \Gamma_L \approx \Gamma_H$. The states are distinguished

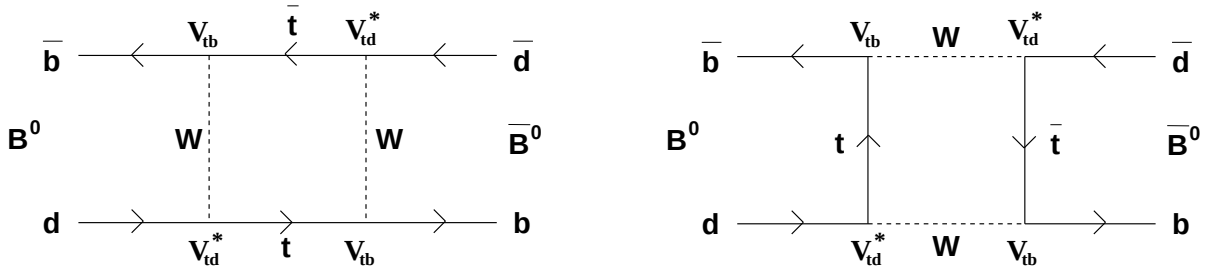

Figure 1.2: *Feynman graphs of $B^0\overline{B^0}$ oscillations. In addition to the exchange of t quarks, diagrams with c and u quark exchange contribute to the oscillation, too. Processes with t quark exchange dominate the oscillation because of the high mass of the t quark.*

by their masses, $|B_L\rangle$ represents a light and $|B_H\rangle$ a heavy state, and referred to as mass eigenstates. An arbitrary state of a B meson that satisfies the Schrödinger equation 1.23 at time t is the result of a linear combination of the eigenstates $|B_L\rangle$ and $|B_H\rangle$:

$$|B^0_{phys}(t)\rangle = k_L e^{-i\mu_L t}|B_L\rangle + k_H e^{-i\mu_H t}|B_H\rangle. \tag{1.26}$$

We get the evolution in time of the physical B states by substituting the mass eigenstates by the flavour eigenstates according to equation 1.25 and the initial condition that we have pure states of $|B^0\rangle$ and $|\overline{B^0}\rangle$ at t = 0. We are able to resolve the constants k_L and k_H and finally come to the evolution in time:

$$\begin{aligned}
|B^0_{phys}(t)\rangle &= e^{-\Gamma t/2}e^{-imt}\left[\cos\left(\frac{\Delta m}{2}t\right)|B^0\rangle + i\left(\frac{q}{p}\right)\sin\left(\frac{\Delta m}{2}t\right)|\overline{B^0}\rangle\right] , \\
|\overline{B^0}_{phys}(t)\rangle &= e^{-\Gamma t/2}e^{-imt}\left[i\left(\frac{p}{q}\right)\sin\left(\frac{\Delta m}{2}t\right)|B^0\rangle + \cos\left(\frac{\Delta m}{2}t\right)|\overline{B^0}\rangle\right] .
\end{aligned} \tag{1.27}$$

$\mu_L = (2m - \Delta m - i\Gamma)/2$ and $\mu_H = (2m + \Delta m - i\Gamma)/2$ are the eigenvalues of the mass eigenstates where m is the average mass of the B states and Δm their mass difference.

1.3.2 CP Violation in Decays of neutral B mesons

CP violation appears in particle decays if the phase of the CKM phase is involved in the calculation of decay probabilities. The decay amplitude from an initial state $|i\rangle$ to a final state $|f\rangle$ can be written as [Nir99]:

$$\mathcal{M}_f = |\mathcal{M}_f|e^{i\delta}e^{i\phi} . \tag{1.28}$$

The phase δ which is called a weak phase changes sign under CP transformation and originates from the involved CKM matrix elements. The sign flip occurs because of the complex conjugated matrix elements that are a part of the calculation. A second phase, the strong phase ϕ occurs because of the strong interaction in the final states. The strong phase does not change sign because the strong interaction is invariant under the CP transformation [Nir99].

The sign of the weak phase does not influence the decay probability which is proportional to $|\mathcal{M}_f|^2$ if there is only one amplitude contributing to the particle decay. In case

that the decay involves several amplitudes, the decay probability is the sum of all single contributions:

$$\Gamma \propto \left| \sum_i \mathcal{M}_i \right|^2 = \left| \sum_i |\mathcal{M}_i| e^{i\delta_i} e^{i\phi_i} \right|^2 , \tag{1.29}$$

especially with two decay amplitudes:

$$\Gamma \propto |\mathcal{M}_1 + \mathcal{M}_2|^2 = |\mathcal{M}_1|^2 + |\mathcal{M}_2|^2 + 2|\mathcal{M}_1||\mathcal{M}_2| \cos(\delta_2 - \delta_1 + \phi_2 - \phi_1) . \tag{1.30}$$

In the CP conjugated process $CP|i\rangle \to CP|f\rangle$, the decay probability is given by:

$$\overline{\Gamma} \propto |\overline{\mathcal{M}_1} + \overline{\mathcal{M}_2}| = |\mathcal{M}_1|^2 + |\mathcal{M}_2|^2 + 2|\mathcal{M}_1||\mathcal{M}_2| \cos(-\delta_2 + \delta_1 + \phi_2 - \phi_1), \tag{1.31}$$

because the weak phase changes sign under CP operation. The interference term of the two amplitudes as a consequence of the sign flip of the weak phase may lead to different decay probabilities between the original and the CP conjugated process. CP violation appears only if there are two interfering terms with different weak phases. There are three different cases for meson decays:

1. CP violation in decay: The total decay amplitudes of a given process and its CP conjugated process are different. This type of CP violation can happen in case of neutral and charged mesons.

2. CP violation by mixture: The mass eigenstates of neutral mesons are not the eigenstates of the CP operator.

3. CP violation by interference of decays of neutral mesons with and without mixture: This kind of CP violation appears when B^0 und $\overline{B^0}$ decay into one common final state.

All three kinds of CP violation occur in the Kaon system. Several amplitudes with different weak and strong phases contribute to the decay and cause CP violation in decay. Different weak phases of amplitudes that contribute to the mixture are the source of CP violation by mixture because the mass eigenstates are not at the same time CP eigenstates. This results in $|q/p| \neq 1$ in equation 1.25. The probability of one flavour eigenstate oscillating to another one is larger than the other way round. The mixed physical mass eigenstates contain different amounts of flavour eigenstates. In contrary to the Kaon system, CP violation by mixture in the B^0 system is negligible because of $|q/p| \approx 1$ [Nir99].

CP Violation by Interference of Decays with and without Oscillation

In the B^0 system, a large CP violation by interference of decays with and without interference is expected. This manner of CP violation happens in decay channels of B^0 mesons when B^0 and $\overline{B^0}$ decay to a common final state. They decay directly or an oscillation takes place before. The interference of the two adjoint amplitudes cause the required weak phase difference. The decay amplitudes of such decays are derived by using the mixed physical states instead of the pure initial states $|B^0\rangle$ and $|\overline{B^0}\rangle$ (equation 1.27):

$$\langle f|\mathcal{H}|B^0_{phys}(t)\rangle = e^{-\Gamma t/2t} e^{-imt} \left[\cos\left(\frac{\Delta m}{2} t\right) \langle f|\mathcal{H}|B^0\rangle + i \left(\frac{q}{p}\right) \sin\left(\frac{\Delta m}{2} t\right) \langle f|\mathcal{H}|\overline{B^0}\rangle \right]$$

$$\langle f|\mathcal{H}|\overline{B^0}_{phys}(t)\rangle = e^{-\Gamma t/2}e^{-imt}\left[i\left(\frac{p}{q}\right)\sin\left(\frac{\Delta m}{2}t\right)\langle f|\mathcal{H}|B^0\rangle + \cos\left(\frac{\Delta m}{2}t\right)\langle f|\mathcal{H}|\overline{B^0}\rangle\right] \tag{1.32}$$

$\mathcal{H}$ represents the Hamiltonian that describes the decay of mesons. The matrix elements can be described according to equation 1.28 by the absolute value of the amplitude and by the strong and the weak phase:

$$\langle f|\mathcal{H}|B^0\rangle = |\mathcal{M}_1|e^{i\delta_1}e^{i\phi_1} \quad \text{and} \quad \langle f|\mathcal{H}|\overline{B^0}\rangle = |\mathcal{M}_2|e^{-i\delta_2}e^{i\phi_2}\ . \tag{1.33}$$

The amplitudes of the CP conjugated transitions result in

$$\langle \overline{f}|\mathcal{H}|\overline{B^0}\rangle = |\mathcal{M}_1|e^{-i\delta_1}e^{i\phi_1} \quad \text{and} \quad \langle \overline{f}|\mathcal{H}|B^0\rangle = |\mathcal{M}_2|e^{i\delta_2}e^{i\phi_2}\ . \tag{1.34}$$

We consider the special case that the final state $|f\rangle$ is a CP eigenstate:

$$CP|f\rangle = |\overline{f}\rangle = \eta_f|f\rangle \qquad \text{with } \eta_f \in \{-1;1\}. \tag{1.35}$$

In this case, we get

$$\langle f|\mathcal{H}|\overline{B^0}\rangle = \eta_f\langle \overline{f}|\mathcal{H}|\overline{B^0}\rangle = \eta_f|\mathcal{M}|e^{-i\delta_1}e^{i\phi_1}\ . \tag{1.36}$$

We need only one weak and one strong phase for the matrix elements $\langle f|\mathcal{H}|B^0\rangle$ and $\langle f|\mathcal{H}|\overline{B^0}\rangle$. The decay rates of the physical B states result in

$$\Gamma_f(t) = \left|\langle f|\mathcal{H}|B^0_{phys}(t)\rangle\right|^2 \qquad \text{and} \qquad \overline{\Gamma}_f(t) = \left|\langle f|\mathcal{H}|\overline{B^0_{phys}(t)}\rangle\right|^2. \tag{1.37}$$

According to equation 1.32 with the corresponding matrix elements of 1.33 and 1.36 we get:

$$\begin{aligned}\Gamma_f(t) &= e^{-\Gamma t}\,|\mathcal{M}|^2\,[1+\eta_f\sin(\Delta m t)\sin(\varphi_w)]\ ,\\ \overline{\Gamma}_f(t) &= e^{-\Gamma t}\,|\mathcal{M}|^2\,[1-\eta_f\sin(\Delta m t)\sin(\varphi_w)]\ .\end{aligned} \tag{1.38}$$

We use for the B^0 the valid approximation $|q/p| \approx 1$. The weak phase φ_w consists of the weak phase δ of the decay diagram and the phase of the $B^0\overline{B^0}$ mixture $\chi_M = -1/2\arg(q/p)$: $\varphi_w = 2(\delta + \chi_M)$. The decay rates no longer depend on the strong phase. Decays into CP eigenstates are very suitable to determine the weak phase φ_w and consequently to verify the CKM theory of CP violation. The weak phase is determined experimentally by means of the time dependant asymmetry

$$\mathcal{A}_{CP}(t) = \frac{\Gamma_f(t) - \overline{\Gamma}_f(t)}{\Gamma_f(t) + \overline{\Gamma}_f(t)}. \tag{1.39}$$

In case of decays into CP eigenstates the result according to equations 1.38 is

$$\mathcal{A}_{CP}(t) = \eta_f\sin(\Delta m t)\sin(\varphi_w). \tag{1.40}$$

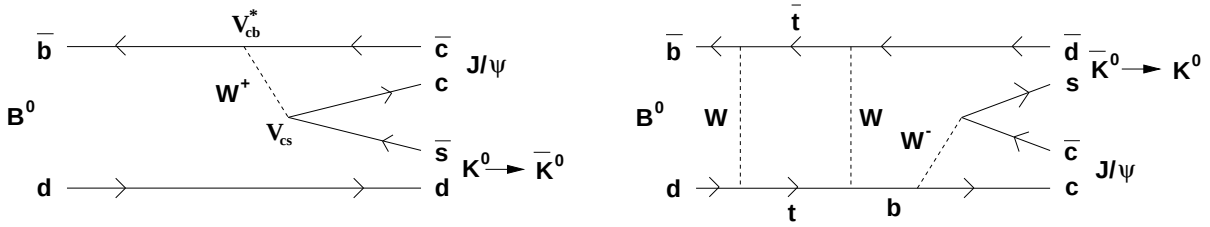

Figure 1.3: *Left: Feynman graph in first order for the golden decay* $B^0 \to J/\psi K_S^0$. *Right: Another decay possibility of the* B^0 *which oscillates before into a* $\overline{B^0}$ *and decays afterwards.*

1.3.3 The Golden Decay $B^0 \to J/\psi K_S^0$

The assumptions presented in the previous section are based on an essential simplification: We assume for the matrix elements for both equations 1.33 and 1.36 that only one amplitude (with and without mixture) contributes to the decay or higher order contributions are neglected, respectively. In this case, we do not consider CP violation in the decay. This is valid for the so called golden decay $B^0 \to J/\psi K_S^0$. The Feynman diagrams of the golden decay are shown in Figure 1.3. This decay allows for investigation of CP violation because the K_S^0 decays into two pions which has a relatively simple signature to be detected experimentally. The J/ψ is a CP eigenstate with eigenvalue $\eta_{J/\psi} = 1$. Only the CP even component of the K_S^0 is selected out of the decays because only the two pions of the short lived kaon are taken into account. The final state $J/\psi K_S^0 (\to \pi^+\pi^-)$ is a CP eigenstate with CP eigenvalue $\eta_{\psi K}$ = -1. The negative sign originates from the angular momentum of the J/ψ with respect to the K_S^0 whose value is one all the time[2].

B^0 and $\overline{B^0}$ of the golden channel decay into different states: $B^0 \to K^0$ and $\overline{B^0} \to \overline{K^0}$. The mixture of Kaons in the final state is responsible for the decay into a common final state and consequently for the interference of decays with and without B mixture. It is necessary to consider the weak phase of kaon mixture $\chi_{M,K}$ for the calculation of the total phase φ_w:

$$\varphi_w = 2(\chi_{M,B} + \delta + \chi_{M,K}) \; . \tag{1.41}$$

The single contributions are [Bab98]

$$\begin{aligned}
\chi_{M,B} = & \quad -\tfrac{1}{2} \arg\left(\tfrac{q}{p}\right)_{B\overline{B}} & = -\frac{1}{2} \arg\left(\frac{{V_{tb}}^* V_{td}}{V_{tb} {V_{td}}^*}\right) \; , \\
\delta = & \quad -\tfrac{1}{2} \arg\left(\tfrac{1}{\eta_{\psi K}} \frac{\langle J/\psi K_S^0 | \mathcal{H} | \overline{B^0} \rangle}{\langle J/\psi K_S^0 | \mathcal{H} | B^0 \rangle}\right) & = -\frac{1}{2} \arg\left(-\frac{{V_{cs}}^* V_{cb}}{V_{cs} {V_{cb}}^*}\right) \; , \\
\chi_{M,K} = & \quad -\tfrac{1}{2} \arg\left(\tfrac{q}{p}\right)_{K\overline{K}} & = -\frac{1}{2} \arg\left(\frac{{V_{cd}}^* V_{cs}}{V_{cd} {V_{cs}}^*}\right) \; .
\end{aligned} \tag{1.42}$$

For the phases of the mixtures, we only consider the dominating one[3]. We get for the weak phase for the golden decay

$$\varphi_w = -\arg\left(-\frac{{V_{tb}}^* V_{td}}{V_{tb} {V_{td}}^*} \frac{{V_{cs}}^* V_{cb}}{V_{cs} {V_{cb}}^*} \frac{{V_{cd}}^* V_{cs}}{V_{cd} {V_{cs}}^*}\right) = 2 \cdot \arg\left(-\frac{V_{cd} {V_{cb}}^*}{V_{td} {V_{tb}}^*}\right) = 2\beta \; . \tag{1.43}$$

[2] B^0 and K_S^0 are both spin 0 particles. As the J/ψ has spin 1 the angular momentum between J/ψ and K_S^0 has to be 1. The CP eigenvalue results in $\eta_{\psi K} = \eta_\psi \cdot \eta_K \cdot (-1)^l = -1$.

[3] The largest contribution to $K^0\overline{K^0}$ mixture arises from the Feynman diagram with c quark exchange whereas all other contributions are Cabbibo suppressed.

The time dependant asymmetry of the golden decay $\mathcal{A}_{CP}(t)$ results in

$$\mathcal{A}_{CP}(t) = -\sin(\Delta m t)\sin(2\beta)\ . \tag{1.44}$$

Time Integrated Asymmetry

It is also possible to perform a time independent measurement which counts directly the observed B^0 and $\overline{B^0}$ decays instead of determining the time dependant asymmetry $\mathcal{A}_{CP}$. We get the time integrated asymmetry by integrating the decay rates:

$$\mathcal{A}_{CP}^{int} = \frac{\int_{t_0}^{\infty}\Gamma(t)dt - \int_{t_0}^{\infty}\overline{\Gamma}(t)dt}{\int_{t_0}^{\infty}\Gamma(t)dt + \int_{t_0}^{\infty}\overline{\Gamma}(t)dt}\ . \tag{1.45}$$

We get by partial integration and with equations 1.38 and 1.43

$$\mathcal{A}_{CP}^{int} = M(\tilde{t}_0)\sin(2\beta) \tag{1.46}$$

with

$$M(\tilde{t}_0) = \frac{\sin(x\tilde{t}_0) + x\cos(x\tilde{t}_0)}{1+x^2}. \tag{1.47}$$

Lifetime Γ and mass difference Δm of the $B^0\overline{B^0}$ system are united in to the parameter $x = \Delta m/\Gamma$ which is determined to be $x = 0.73 \pm 0.05$ [Arg87]. The time $\tilde{t}_0$ is presented in units of B^0 lifetime: $\tilde{t}_0 = t_0/\tau_B$. Time integration does not start at production of B mesons $\tilde{t}_0 = 0$ but at a later point in time because a minimal life time $\tilde{t}_0$ of the decaying particle is required. Only B mesons with a lifetime of at least $\tilde{t}_0$ are taken into account to contribute to the decay asymmetry.

1.4 Heavy Flavour Physics

HERA–B is not in the position to contribute competitive measurements in the area of CP violation in the B meson system. The large acceptance of the HERA–B detector and the good particle identification devices however allow to measure and improve knowledge in the wide field of heavy flavour physics and QCD.
The measurement of the $b\overline{b}$ cross section is of interest for HERA–B since it would give an indication of the feasibility of possible future contributions to the physics of b quarks. It would also help to improve the theoretical models.

1.4.1 Heavy Quarkonium Production

The charm, bottom and top quark are considered to be heavy quarks because their masses ($m_c \simeq 1.5$ GeV/c^2, $m_b \simeq 5$ GeV/c^2 and $m_t \simeq 175$ GeV/c^2) are well above the QCD constant $\Lambda_{QCD} \simeq 200\ MeV$. If the involved quark masses are larger than the QCD constant Λ_{QCD} perturbation theory can be used to describe physics processes.
The investigation of heavy quarkonia production in hadron–hadron–interactions can lead to an improvement of understanding the production mechanisms and the properties of the

final states. Fixed target experiments[4] like HERA–B cover the kinematical region of low transverse momenta which are subject to non-perturbative effects as well as the regime of negative x_F. The results obtained can contribute to an improved understanding of non-perturbative regions.
We provide an overview of the models elaborated to describe heavy quarkonia production:

Colour Singlet Model (CSM)

The Color Singlet Model assumes that the production of a charmonium state proceeds through parton (quarks and gluons are summarised as partons) processes that produce a $c\overline{c}$ pair in a colour singlet state.
The CSM assumes that the production of charmonium is a two step process. The first step is the production of a $c\overline{c}$ pair. The second is step is the binding of $c\overline{c}$ pair into a charmonium state. In order to have a significant probability of binding, the $c\overline{c}$ pair needs to be produced with a relative momentum which is small in the rest frame of the $c\overline{c}$ compared to the mass of m_c of the charm quark. Otherwise, the c and the $\overline{c}$ fly apart and form for example D and $\overline{D}$ mesons.
The cross section estimation factorises into two parts: a short-ranged, with perturbative QCD (pQCD) calculable part which describes the production of $c\overline{c}$ and a long-ranged not pQCD calculable part that describes the transition to charmonium. According to the CSM, $c\overline{c}$ pairs generated by open hadroproduction form charmonium only if they build up within a time scale of $\simeq 1/m_c$ a colour neutral state (colour singlet) with the same quantum numbers as charmonium. This follows from the fact that the short-range part is sensitive to changes in the relative 3-momentum of the c and the $\overline{c}$. These changes are less than $1/m_c$. The cross section looks like:

$$\sigma(ch) = \hat{\sigma}(c\overline{c_1}(ch))\frac{R_{ch}(0)^2}{4\pi} \tag{1.48}$$

In equation 1.48, $c\overline{c_1}(ch)$ represents the colour neutral state with the quantum numbers of the specified charmonium and $R_{ch}(0)$ the value of the charmonium's wave function at the origin. The factor $\hat{\sigma}(c\overline{c_1}(ch))$ is the short-ranged term and proportional to the production rate of a $c\overline{c}$ pair. The last factor represents the long-ranged part and is a measure for the probability that a $c\overline{c}$ pair with the quantum numbers of a J/ψ merges to a J/ψ.
The cross section derived by leading order calculations does not agree with experimental data since higher order terms contribute significantly. A correction term K of the order of 2 is introduced to reach an agreement between theory and experimental data. The CSM predicts precisely the relations of cross sections of different charmonia and their polarisation. The model however contains some theoretical and experimental inconsistencies.
The calculations do not take into account $c\overline{c}$ pairs that are generated as colour octet state and afterwards transform to colour singlet by emission of soft (i.e. low energetic) gluons. The validity of the assumed factorisation in a short-range and long-range part for the calculation is not proven for higher order. Relativistic corrections for the relative velocity v between quark and antiquark are not taken into account by the CSM. These corrections are probably not negligible since the average value of v^2 is of the order of 1/3.
The CSM is described in further detail in [Bra96, Gas87, Hum87].

[4] high energetic particles fired at unmovable target material.

Colour Evaporation Model (CEM)

An alternative model for quarkonia production is the Color Evaporation Model. In this model, it is assumed that the different quarkonia states originate from $c\overline{c}$ pairs created below the threshold for open charm production. The CEM describes the formation of charmonium from a $c\overline{c}$ pair which neutralises its colour by interaction (i.e. the emission of soft gluons) with the collision-induced colour field ("colour evaporation"). During this process, the c and the $\overline{c}$ either combine with light quarks to produce charmed mesons or they bind with each other to form a charmonium state. Consequently, the colour state and the quantum numbers of the $c\overline{c}$ pair and the charmonium are independent. The cross section is evaluated by:

$$\sigma(ch) = \rho_{ch}\frac{1}{9}\int_{2m_c}^{2m_D} dm \frac{d\sigma_{c\overline{c}}}{dm} \tag{1.49}$$

m_c is the mass of the c quark and m_D is the mass of the D meson. The factor ρ_{ch} is assumed to be constant and process independent. This parameter is not well defined in QCD but is merely a phenomenological parameter that has to be fixed by using experimental data. The factor $\frac{1}{9}$ originates from the statistical treatment of colour. The c as well as the $\overline{c}$ can be found in three different colours leading to $3 \times \overline{3}$ possibilities. One out of these nine possibilities is a colour singlet state whereas the remaining states are assigned to colour octet. The value of the integral can be calculated within pQCD.
The model lacks an exact description of production process since it only reflects the process in a phenomenological way. The parameters ρ_{ch} are introduced arbitrarily and cannot be calculated within the model framework itself.
A detailed description of the CEM can be found in [Fri97, Gav95, Schu94].

Colour Octet Model (COM)

Contrary to the basic assumption of the colour singlet model, a $c\overline{c}$ pair that is produced in a colour octet state can bind to form charmonium. The $c\overline{c}$ pair that forms charmonium has to be in a colour singlet state. However, the short-range part of the process can involve the production of a colour octet $c\overline{c}$ pair.
The COM takes the processes of the CSM and additional generation processes into account. There are no restrictions concerning the colour state of the $c\overline{c}$ pair that results in charmonium in the final state. Besides the colour singlet states colour octet states that transform into a colour neutral state by the emission of one or more gluons are allowed, too.
The large mass m_c and the small relative velocity of the c quarks inside the charmonium make a perturbative solution feasible. The differential cross section for a charmonium H looks like:

$$d\sigma(H+X) = d\hat{\sigma}(c\overline{c}(1)+X)|R_H(0)|^2 + d\hat{\sigma}(c\overline{c}(8)) < \mathcal{O}_8^H > \tag{1.50}$$

The first term is the conventional term of the colour singlet model. In this term, the short-range factor is the cross section for producing a $c\overline{c}$ pair with small relative momentum in a colour singlet state. The second term represents a contribution to the cross section from a colour octet mechanism. The short-range factor in this term is the cross section for producing a $c\overline{c}$ pair with small relative momentum in a colour octet state.

The long-range non-perturbative term $< \mathcal{O}_8^H >$ is proportional to the probability for a $c\overline{c}$ pair in a colour octet state to bind and form a charmonium H.
This model removed a lot of discrepancies that existed between CSM and data. All three models show yet inconsistencies with data indicating that a search for a common model that describes heavy quarkonia production is not finalised. Investigations of production mechanisms for quarkonia in different interaction processes and in as huge as possible kinematic range is necessary for a better understanding of involved mechanisms. Recent analysis show evidence for the COM for prompt J/ψ production in $\gamma\gamma$ collisions [Kla01]. Further discussion of the COM can be found in [Bod95, Bra96].

Nuclear dependence of charmonium production

For nuclear suppression we have to take into account the environment of the process. The behaviour of a process is different for nucleon–nucleon– and proton–nucleon–interactions. The latter process usually appears in fixed target experiments. The nuclear medium influences the interaction. A comparison of cross section of proton–proton–interactions with proton–nucleon–interactions shows that the production of J/ψ is suppressed compared to proton–proton–interactions. This suppression is usually represented by equation:

$$\sigma(ch) = \sigma_0 A^\alpha \tag{1.51}$$

$\sigma(ch)$ being the cross section for the charmonium of interest, σ_0 being a constant, A being the atomic mass and α is a parameter that describes the suppression and is seen take on values between 0.7 (suppressed production) and 1 (no suppression) when averaged of p_T. Figure 1.4 shows the parameter α as a function of x_F and as a function of the transverse momentum p_T. The transverse momentum is defined as:

$$p_T = \sqrt{p_x^2 \ + \ p_y^2}. \tag{1.52}$$

x_F is the Feynman variable and is defined as:

$$x_F = \frac{p_z}{p_{z,max}}. \tag{1.53}$$

We present briefly some possible effects that are utilised to explain nuclear suppression due to kinematics. The models are described in detail in [Vog99].

- Nuclear absorption
  The unbound $c\overline{c}$ pair can interact with the surrounding nuclear material before hadronization and consequently be absorbed or dissociated into charm. The absorption probability increases with path length after which a formation of quarkonium takes place. The suppression of ψ' (an excited resonance state of $c\overline{c}$) is larger than that of a J/ψ because the size and the formation time are larger.

- Comover absorption
  It is also possible that a bound quarkonium state interacts with secondary co-moving hadrons that are produced in the collision. In this way, the state can be dissociated before the decay. The kinematic dependences are similar to nuclear absorption.

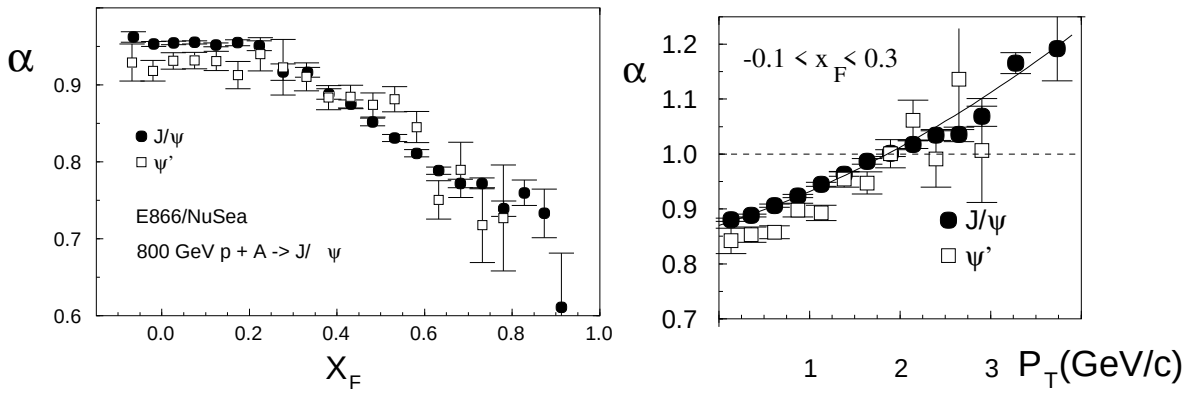

Figure 1.4: *Measured A dependence as a function of Feynman variable x_F (left) and p_T (right) for J/ψ and ψ'. The measurement was done by the E 866 collaboration. [Lei00]*

- Multiple scattering and energy loss
  In any stage of quarkonium production interaction with the surrounding hadronic matter can cause a suppression. A parton that is involved in the creation of the quark-antiquark pair can loose energy due to soft multiple scattering before the interaction.

Generation of B–Mesons

The generation of B–mesons in fixed target experiments was measured by two experiments (E771 and E789) at Fermilab. Both experiments measured the cross section for the decay $b \to J/\psi \to \mu^+\mu^-$ in proton gold interactions (E771) and in proton silicon interactions (E789). The results obtained were contradictory and dominated by large errors due to the limited statistics and the different kinematical regime.

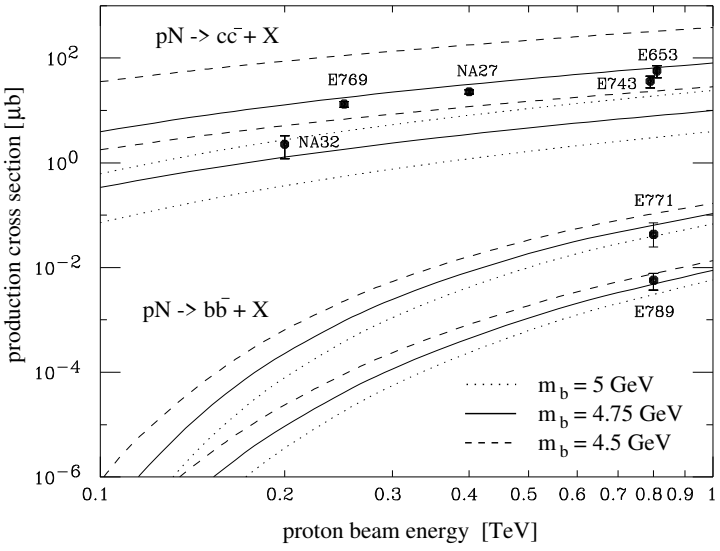

Figure 1.5: *The b production cross section as a function of the beam energy taken from [Fri97].*

In the case of HERA–B, the 920 GeV protons interact inelastically with the target wires and produce the B–Mesons. The center–of–mass energy in this fixed target setup is 41.6 GeV. Heavy quarks are generated either by quark annihilation $q\overline{q} \rightarrow b\overline{b}$ or by gluon fusion $gg \rightarrow b\overline{b}$ which is the dominating process at HERA energies. The production rate of heavy quarks is calculated by the product of a parton structure function with a hadronic cross section consisting of a Born cross section of the order of α_s^2 of the QCD coupling constant α_s (Leading Order) and a cross section of the order of α_s^3 (Next to Leading Order). The different partons are summed up and the invariant mass of the parton system is integrated. The theoretical calculations are done on the basis of QCD up to the order of α_s^3 which means that gluon Bremsstrahlung and gluon separation is taken into account [Alt88, Bee91, Lae92, Men90, Nas88]. At the given energy the interaction is dominated by gluon fusion processes and not by quark annihilation [Spr00]. Figure 1.5 shows the cross section as a function of the beam energy for proton nucleus interaction to $b\overline{b}$ (lower curves) and $c\overline{c}$ (upper curves). The different curves represent three assumptions for the b mass. The cross section $\sigma_{b\overline{b}}$ at a beam energy of 920 GeV is estimated to be 14 nb.

Chapter 2

The HERA–B Detector

The experiment HERA–B situated at HERA uses an internal wire target to generate heavy quark-antiquark pairs by proton-nucleus interactions with the proton beam. It was designed to measure CP violation in the B meson system.
We present in this section the requirements for the detector and provide an overview of the individual detector components. The detector components relevant for this thesis are presented in the final section.

2.1 Requirements for the HERA–B Detector

The measurement of CP violation uses the gold plated decay $B^0 \to J/\psi K_S^0$ identified by the clear signature of the subsequent decay $J/\psi \to l^+l^-$. The reconstruction and the measurement of the decay of the J/ψ demand the following requirements for the detector:

- Suppression of background events
  The hadronic background dominates by six orders of magnitude the events that are looked for. A highly efficient and fast trigger and data acquisition system is needed to identify and select the candidates and to suppress the huge background.

- Coping with high track multiplicities
  To reach the desired number of about 1000 B decays, between four and five interactions per event are needed in average which results in high track multiplicities. An event happens every 96 ns. The design of the detector must cope with the harsh radiation environment as well as the high occupancy caused by the multiple interactions. In addition, the detector should reconstruct particle trajectories and identify particles with a high efficiency.

- Reconstruction of the gold plated decay at high efficiency
  To allow for a highly efficient reconstruction of the golden decay the detector must have a large angular coverage as well as an excellent resolution with respect to position and momentum. A clear spatial separation between primary and secondary vertices is mandatory for the background rejection.

2.2 The HERA Ring and the Target

2.2.1 The Beam

The HERA ring has a circumference of 6.3 km. The protons are accelerated in various steps to an energy of 920 GeV. At the beginning, negative hydrogen ions are accelerated to an energy of 50 MeV by LINAC III (LINear ACcelerator). The ions pass a foil that strips off the electrons. The resulting protons are afterwards injected into the DESY III synchrotron. The protons are collected to a so called bunch of approximately 10^{11} protons. Ten bunches are accumulated in DESY III and are accelerated to an energy of 7.5 GeV. The frequency of DESY III is 10.417 MHz which results in a distance in time of 96 ns between the bunches. Afterwards they are transfered into PETRA (Positron Electron

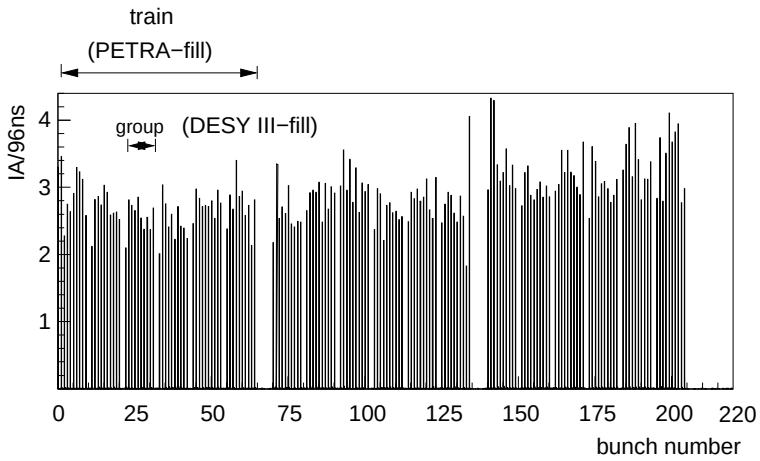

Figure 2.1: *The proton beam consists of three PETRA fills called a train. Each train contains six groups (DESY III fills). On the y-axis the mean interaction per bunch crossing is shown. [Scha98]*

Tandem Ring Accelerator). This procedure is repeated 6 times. The resulting set of 60 bunches, called a PETRA train, is then accelerated to an energy of 40 GeV. In this way, three PETRA trains are consecutively injected into the HERA ring and are accelerated to the final energy. After all injection steps one bunch consists of around $7 \cdot 10^{10}$ protons which is equivalent to a beam current of typically 0.5 mA per bunch.
The time a particle needs to travel around the HERA ring is 21.12 μs. Theoretically the ring could be filled with 220 bunches. Indeed it is filled with 180 bunches because of the filling procedure. The structure of a typical beam is shown in Figure 2.1. As a consequence interactions of a proton with the target cannot take place at any time but only if a bunch hits a wire. A number is assigned to each bunch that passes the HERA–B detector, the so called bunch crossing number (BX).

2.2.2 The Target

The target of HERA–B is realised as wires that are moved to the outer area of the proton beam. There are two main reasons to use the outer area of the beam: First, it avoids any

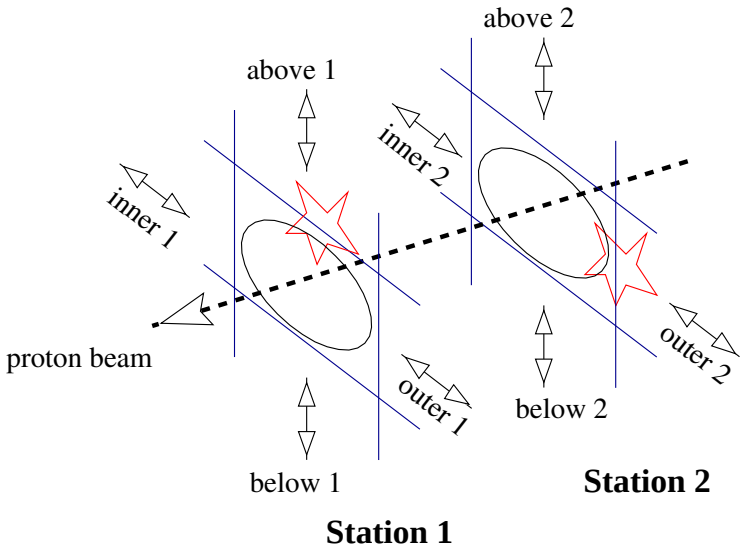

Figure 2.2: *Overview of the target stations and the different wires. [Sym00]*

damage of the beam structure that is necessary for the other experiments and second, the wires can be used to shape the beam, i.e. scrape protons and function as a collimator.
In total, there are two stations separated by 5 cm in the beam direction with four wires each to distribute the 4–5 interactions per bunch crossing (see Figure 2.2). The distance between the stations is chosen to assure a proper separation of the vertices. The wire materials are Carbon, Aluminum, Titanium and Tungsten. The first three materials have a small atomic number compared to Tungsten. The mass number plays also a roll as the cross section for $b\bar{b}$ production increases with it. The dimensions of the wires are 50 μm perpendicular to the beam and 500 μm for Aluminum, Titanium and Tungsten and 1000 μm for Carbon along the beam.
Due to the fact that only 180 of 220 bunches are filled the effective rate for one interaction of a proton with the target (i.e. one BX) is 8.5 MHz. To reach the desired amount of gold plated decays, between 4 and 5 interactions per bunch in mean are necessary which is equivalent to a target rate of 40 MHz.

2.3 The Detector Components of HERA–B

In this section, we present the detector components with increasing distance from the target. The vertex detector is used to detect displaced vertices of B mesons. The magnet with a field of 0.8 T is necessary to determine the momentum of the particles. Inside the magnet, some tracking layers are installed. Outside the magnet, chambers of the outer and inner tracking system are installed. The Čerenkov counter is installed in front of two final tracking chambers. A transition radiation detector and the calorimeter follow. At the end, the muon detection system is installed. A schematic overview of the experiment HERA–B is shown in Figure 2.3.

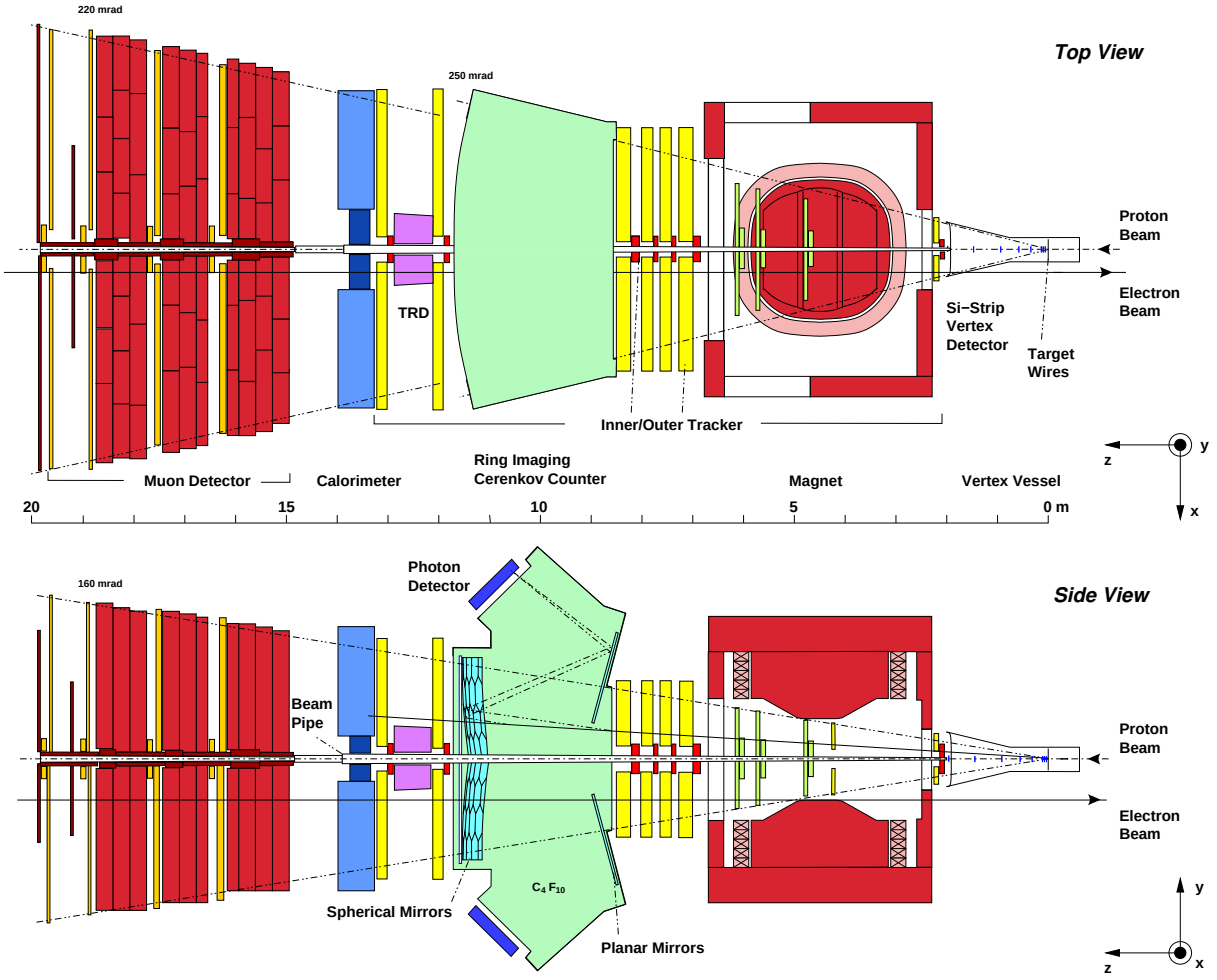

Figure 2.3: *Schematic overview of the HERA–B experiment. The proton beam impings a wire target. The vertex detector and the system of tracking chambers follow directly behind the target. Some of the tracking chambers are installed inside a magnet. A ring imaging Čerenkov detector, a transition radiation detector, a electromagnetic calorimeter and muon system are used for particle identification. [Her95]*

2.3.1 The Vertex–Detector

The vertex detector system (VDS) is shown in Figure 2.4. The separation of primary vertices of multiple interactions and the evaluation of secondary vertices of J/ψ mesons that are produced by p–N interactions out of the huge background are among these tasks. The vertex detector is situated in a 2.6 m long stainless steel vessel that is evacuated to a pressure of 10^{-8} mbar to preserve the vacuum of HERA's proton beam. This vessel houses the target as well. The vertex detector contains 64 double sided silicon microstrip detectors that are arranged in 8 superlayers. A superlayer is built up by four quadrants surrounding the beam. Seven superlayers are inside the vessel realised as a Roman pot system, the eighth is located behind the window of the vacuum tank. The strip orientations of the double sided detectors are tilted by $\pm 2.5°$ relative to the x- and to the y-axis (axis perpendicular to the beam forming a right handed coordinate system). In total, a

superlayer consists of four sensitive detector planes with stereo angles of $-2.5°$, $+2.5°$, $87.5°$ and $92.5°$ relative to the y-axis. The active size is $50 \cdot 70\ mm^2$ and the pitch of the strips is 50 μm. The angular coverage ranges from 10 to 250 mrad.
The pitch is a compromise between the number of channels and the expected occupancy.

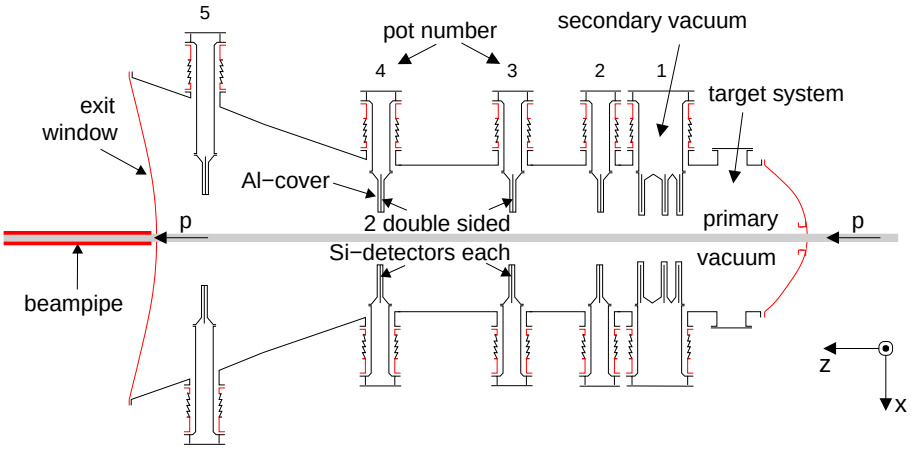

Figure 2.4: *Schematic overview of the vertex detector system. [Wag 99]*

2.3.2 The Inner Tracker

The inner tracker (ITR) covers the angular range larger than 10 mrad up to a radial distance of 25 cm from the beam pipe. To handle the high particle fluxes and the desired resolution the inner tracker uses Micro Strip Gas Chambers (MSGC) with GEM technique (Gas Electron Multiplier). The pitch of the MSGC strips is 300 μm that yields a spatial resolution of smaller than 80 μm (see Figure 2.5). As in the vertex detector the modules are arranged in superlayers. The layers are tilted by $+5°$, $0°$ and $-5°$ with respect to the vertical axis (y–axis) around the beam axis.
The GEM technique is realised as a perforated, 50 μm thick Kapton foil that is metallised on both sides. The foil splits charge amplification in GEM and MSGC which results in a lower voltage at the MSGC anode strips at the same level of gas gain but with lower probability of sparks.
The task of the inner tracker is to provide a good track separation as 40 % of the tracks that originate from B decays are inside this angular coverage. It is foreseen that the inner tracker provides input to the First Level Trigger (FLT).

2.3.3 The Ring Imaging Čerenkov Counter

The Ring Imaging Čerenkov Counter (RICH) is used for particle identification on one hand and on the other to evaluate precise information on the direction and velocity of charged particles.
The Čerenkov effect arises when a particle enters a medium with a velocity larger than that of light in the medium. The medium itself is polarised asymmetrically by a charged particle. The polarisation induces electric dipoles that emit photons in a cone with the

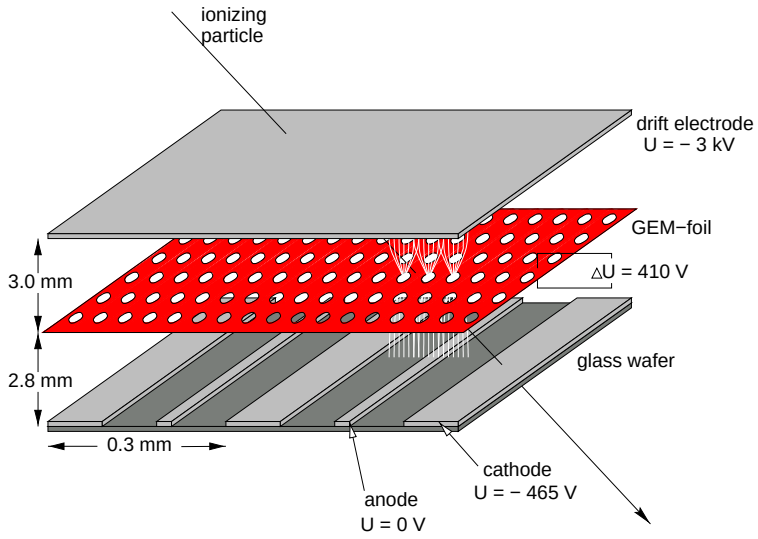

Figure 2.5: *The separation of the gas volume by the GEM foil is evident. The avalanche produced by the foil is sketched. The gas amplification takes place in the foil. [Dre98]*

Čerenkov angle θ_c while they relax to their groundstate. The Čerenkov angle θ_c is given by:

$$cos\theta_c = \frac{1}{\beta \cdot n} \tag{2.1}$$

The parameter β = v/c is the fraction of the particle's velocity v and the speed of light c. n is the refraction index of the medium.
Out of the Čerenkov angle in combination with the measurement of the momentum from the tracking chambers the mass of the particle can be calculated. The principle of the RICH and some reconstructed rings are shown in Figure 2.6. The RICH of HERA–B is built as a tank that is filled with C_4F_{10} as radiator gas. The Čerenkov light is focussed by spherical mirrors and is directed by planar mirrors to an array of multi channel photomultipliers that is located outside the detector acceptance. The threshold for emitting Čerenkov light with respect to the momenta of the particle is 2.6 GeV/c for pions, 9.0 GeV/c for kaons and 17.2 GeV/c for protons. The RICH is able to separate pions from kaons in a momentum range between 4 and 80 GeV/c.

2.3.4 The Transition Radiation Detector

The transition radiation detector (TRD) is used for hadron–electron–separation with high electron efficiency in the region of the electromagnetic calorimeter that is subject to the highest occupancy. The TRD is positioned between the outer tracker layers TC 1 and TC 2 (see section 2.4.1).
Transition radiation arises when a particle transverses media with a different dielectricity constant. The particle that moves towards the border of the two media builds an electric dipole with its mirror charge. The strength of the dipole field changes as the particle moves and leads to the emission of electromagnetic radiation.
The detector is built of 18 layers of proportional straw tubes interleaved with transition

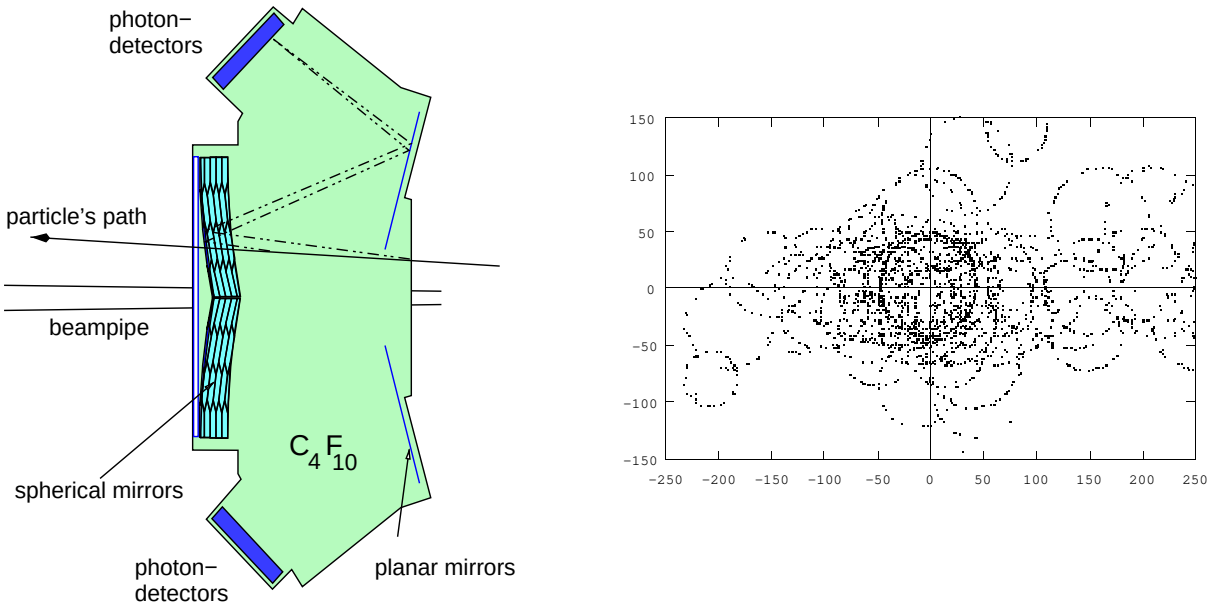

Figure 2.6: *Left: Cut view of the RICH. Right: The analysis of the information of the photomultiplier tubes which yield rings with different diameters. From the diameter of the ring the particles mass and hence the particle itself can be identified. [Duj01]*

radiator material. The radiator material consists of polypropylene fibres. The straw tubes are made out of four different layer of Kapton foil, polyurethane, aluminum and poly-imide. The gas mixture consists of Xe:CO_2:CF_4 in the ratio 70:20:10.

2.3.5 The Electromagnetic Calorimeter

The electromagnetic calorimeter (ECAL) is located behind the last superlayer of the Outer Tracker (TC 2). The ECAL is necessary to perform a clear identification of electrons and positrons that originate from the decay $J/\psi \rightarrow e^+e^-$. The ECAL should provide a pretrigger signal to the FLT (see 3.2.1) in an energy range of 5–200 GeV.
To insure an overall occupancy of less than 10 % the ECAL is partitioned into three domains of different granularity. The module size of $[11.15 \times 11.15]\ cm^2$ remains the same throughout the whole calorimeter but the number of cells of one module increases from 1 for the outer region to 4 for the middle and 25 for the inner region. Each module is manufactured out of alternating layers of absorbers and plastic scintillators. Wavelength shifter fibres cross the module perpendicular and guide the light to photomultipliers. The structure of a module is drawn in Figure 2.7. In the inner part tungsten, in the middle and outer part lead is used as absorber material. In the middle and outer part, the cell depth measures 20 X_0 and in the inner part 22 X_0. The Molière radius is a measure of the transversal size of the shower. The absorber materials are chosen because the Molière radius is much smaller than the ECAL module size which leads to a small leakage to adjacent cells.

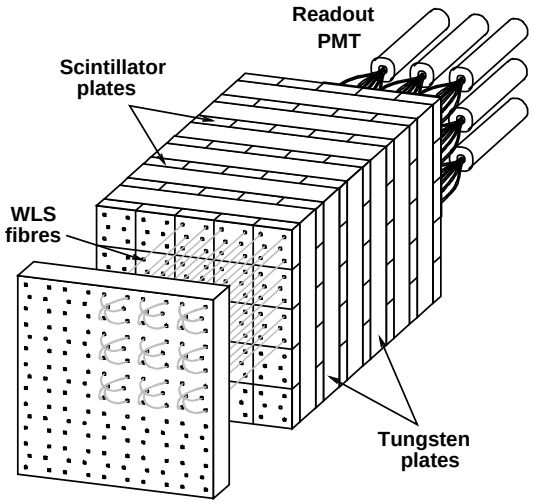

Figure 2.7: *ECAL module: Absorber and scintillator layers are arranged in alternating order. Thin wavelength shifter fibres cross the module perpendicular to the layers and transport the produced light to the photomultipliers. [Her95]*

2.4 Detector Components relevant for this thesis

2.4.1 The Outer Tracker

The outer tracker (OTR) takes over the coverage of regions with a radial distance larger than 20 cm from the beam pipe up to an angular coverage of 250 mrad (220 mrad behind the RICH) in the bending xz-plane and up to 160 mrad in the non-bending yz-plane. The outer tracker layers are situated at different z-positions along the beam axis. There are nine layers in the magnet to follow the particle tracks back to the vertex detector and to evaluate the momenta and to reconstruct the decays of the K_s^0. Between the magnet and the RICH detector the outer tracker has four layers for pattern recognition and track reconstruction (PC 1-PC 4). Between the RICH and the ECAL are the last two layers of the outer tracker (TC 1, TC 2). Their purpose is to provide information that is needed for extrapolation to the ECAL and the muon system.
The outer tracker uses drift cells with a honeycomb structure. The structure of a single and a double layer is shown in Figure 2.8. The cells measure 5 mm in the inner part and 10 mm in diameter for the outer part. The outer tracker is subdivided into sectors to reach a detector occupancy less than 20 %.
The anode of a cell is made of a 25 μm Gold-plated Tungsten wire. The cathode is the wall of the cell which is made out of 50 μm Pokalon–C. On the inside it is coated with a few nanometres of gold.
The drift time is determined by the drift velocity of charged particles in the gas. The spatial resolution is a function of the gas mixture. The parameters need to be chosen such that all charge is collected within one BX resulting in a clear separation of events.
Each layer consists of tilted modules like in the inner tracker in order to reconstruct three dimensional tracks. The superlayers PC 1, PC 4, TC 1 and TC 2 are made of double layers to give redundancy for the triggers. Cells that are on top of each other are ORed to reach

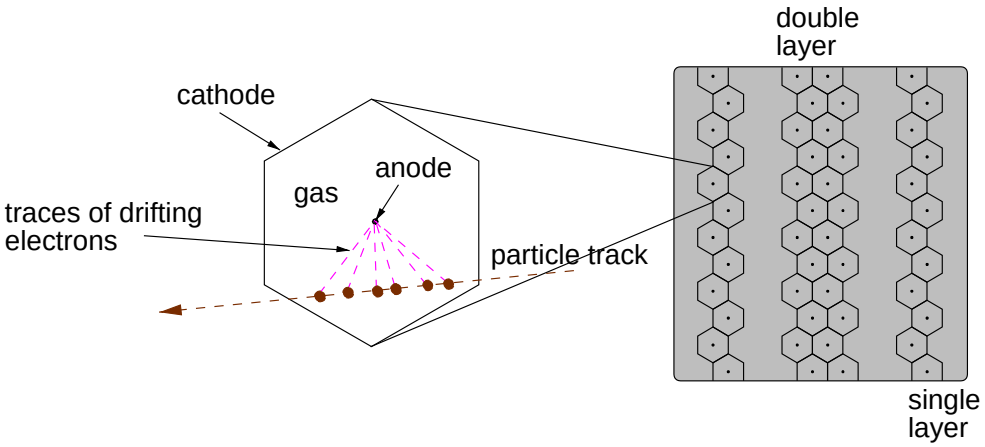

Figure 2.8: *Left: The principle of a drift cell. Right: The structure of a single and double layer.*

a good performance of the FLT track finding. Single layers are sufficient for the pattern recognition in the other layers of the OTR.

2.4.2 The Muon system

The main purpose of the muon system is to provide a pretrigger signal to the FLT and to separate muons from hadrons. The muon system should be able to detect muons from the decay $J/\psi \rightarrow \mu^+\mu^-$ within an energy range of 5–200 GeV.
The muon system consists of the muon filter and four superlayers of muon chambers. There are concrete and steel absorbers in front of all the layers up to layer 3 (MU 3). An iron absorber is installed behind each of the last two muon layers MU 3 and MU 4 to suppress back scattering (see Figure 2.9). There is no thick absorber between MU 3 and MU 4 to provide clean information about the position and direction of particles. The absorbers cut off muons whose momenta are below 4.5 GeV/c [Her95].
The superlayers MU 1 and MU 2 consist of three layers of muon tube chambers with a stereo angle of 0° and ±20°. Only the layer MU 1 is used for trigger purposes. The layers MU 3 and MU 4 are used for the muon pretrigger and for the FLT. Each of the layers consists of one 0° layer with pad and wire readout. The region with the highest occupancy in each superlayer is equipped with gas pixel chambers. The demand on granularity of the detector is much weaker than for the main tracking because the occupancy is lower. The size of one detector cell is limited by the fact that the signal has to be formed within one bunch crossing.
A gas pixel chamber is realised as square cells that are formed by one sense wire and four potential wires which are oriented along the beam axis. The basic sensitive element of the tube chamber is a drift cell. Its dimension are chosen such that the electron drift time throughout the entire cell is below 90 ns. The chambers are made of two layers comprising 16 cells. The layers are shifted by half a cell with respect to each other. A drawing of a tube chamber is shown in Figure 2.10 (left). The pad chambers are made of two sided Aluminum profiles as shown in Figure 2.10 (right). Two rows are shifted by half a cell with

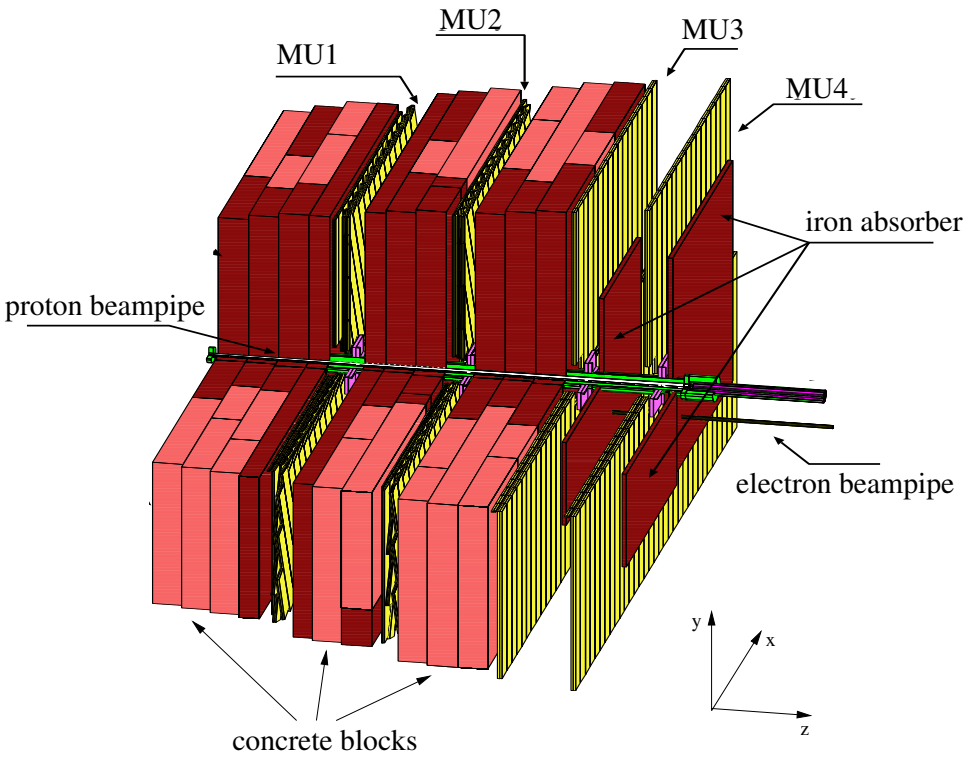

Figure 2.9: *View of the muon system consisting of four layers of tracking chambers (MU 1-4). Between the layers are absorbers made of concrete and iron. [Fom97]*

respect to each other. Cathode readout provides information with respect to y-direction which is used together with the x-information by the pretrigger.

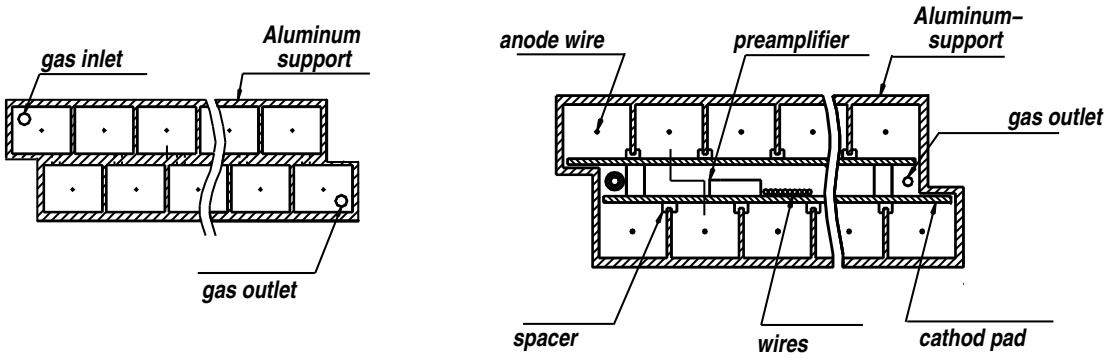

Figure 2.10: *Left: A schematic view of a muon tube layer. The cells are shifted by half a cell with respect to each other. Right: A muon pad cell. The pads are used by the muon pretrigger to form coincidences and generate a pertrigger. [Her95]*

Chapter 3

The Trigger System of HERA–B

In this chapter, we provide a brief introduction to the trigger system and its requirements. We present the trigger concept of HERA–B and provide an overview of the multilevel trigger components.

For most of the measurements that can be performed by HERA–B it is not desirable that every bunch crossing is recorded, i.e. the HERA–B detector is read out. The total amount of data per event that is delivered by the detector is more than 450 kB which results in 5 TByte/s at a bunch crossing rate of 10.4 MHz. Such a huge amount of data can neither be recorded and analysed nor be stored on tape. The rate at which interesting events occur is rather low which means that a sophisticated selection system –the trigger system– needs to be implemented.
The tasks of the trigger system are to reduce the event rate by six orders of magnitude and at the same time to provide a high probability to select the interesting events (high trigger efficiency).
The selection is difficult because of the topology of hadronic events. The tracks originating from heavy quark decays are accompanied by many other particles. To be able to resolve such events a detector with high granularity (i.e. many read out channels) is required. As the ratio of the $b\overline{b}$ and the inelastic cross section turns out to be of the order of 10^{-6} at a center-of-mass (CMS) energy of 42 GeV triggering becomes a real challenge.

3.1 The Trigger Concept of HERA–B

In an ideal case, we would use the complete available data to select events. The large amount of data channels like in HERA–B makes such a strategy technically impossible. The HERA–B trigger system is divided into four logical trigger levels that are to a large extend implemented separately and perform successively the event selection. The trigger concept is based on two inputs (constraints):

- The necessary target interaction rate of 40 MHz and
- the limit to write events to mass storage media that is presently around some 10 Hz.

With these two inputs the trigger system has to be designed to reduce the input rate by a factor 10^6. The system is primarily built to exploit the decay channel B $\rightarrow J/\psi$. It makes use of the following physical properties of B hadrons and their decay products:

- The b quark is much heavier than the quarks of the first and second generation. The momentum distribution and the large mass of the B hadrons result in the fact that the decay products feature a larger transverse momentum than products from interactions with light quarks,

- the lifetime of the B mesons is ≈ 1.5 ps. As a consequence, the B mesons travel in average a distance of about 10 mm because of the boost along the beam axis ($\gamma \approx 21$). The decay products of B mesons originate from a secondary vertex,

- charged, high energetic electrons can be easily identified as they cause electromagnetic showers in the calorimeter. Muons can be detected due to their property to penetrate thick absorbers,

- the invariant mass of the decay products provide kinematical constraints. Pairs of opposite charge leptons or hadrons that yield an invariant mass of 3.1 GeV/c^2 or 5.3 GeV/c^2 indicate that they may result from a J/ψ or B meson, respectively.

Additionally, the trigger concept and the hardware should be realised to allow more general trigger settings to be able to accept events of any combination of charge, momentum, transverse momentum and mass.

The decay of the J/ψ to a lepton pair makes a clear signature available that should be exploited for the electron and muon channel. Electron candidates are identified by ECAL showers and muon candidates by track seeds in the muon system. These tasks are realised on custom designed electronics boards that built the pretrigger and the First Level Trigger (FLT). The higher level triggers make use of ordinary, commonly used personal computers.

Since the First Level Trigger (FLT) has to look for interesting signatures at every bunch crossing it has to cope with the full bunch crossing rate of 10.4 MHz. Only a fraction of the information provided by the detector can be used by the FLT which means that the event data of the entire event has to be stored until the processing of the FLT is finalised. The data are stored by the detector components in a pipeline storage[1] within the readout electronics. The limited size of the pipeline storage determines the available time slot since the data taking is not stopped if the stored data is close to become overwritten. For HERA–B the pipeline length is 128 bunch crossings. The computing time (latency) of the FLT is therefore limited to 12.3 μs (128·96 ns). Trigger algorithms that need to be executed in such a time frame can only be implemented in custom designed electronics. The reduction of the FLT should reach a factor of 200 which results in an input rate of 50 kHz to the Second Level Trigger (SLT).
The input rate to the SLT reaches a level to allow for the use of off-the-shelf hardware but is still too high to permit access to the entire available detector data. Trigger algorithms are restricted to search regions (Regions Of Interest, ROI) that contain interesting candidates. During the execution time of the SLT it is necessary to store the detector data in the Second Level Buffer (SLB).
The event selection of the SLT should reduce the rate to 500 Hz which is low enough to

[1] Pipeline storage is a ring buffer with sequential access. For each clock cycle (here: bunch crossing) two separate pointers, one for read and and one for write access, are incremented.

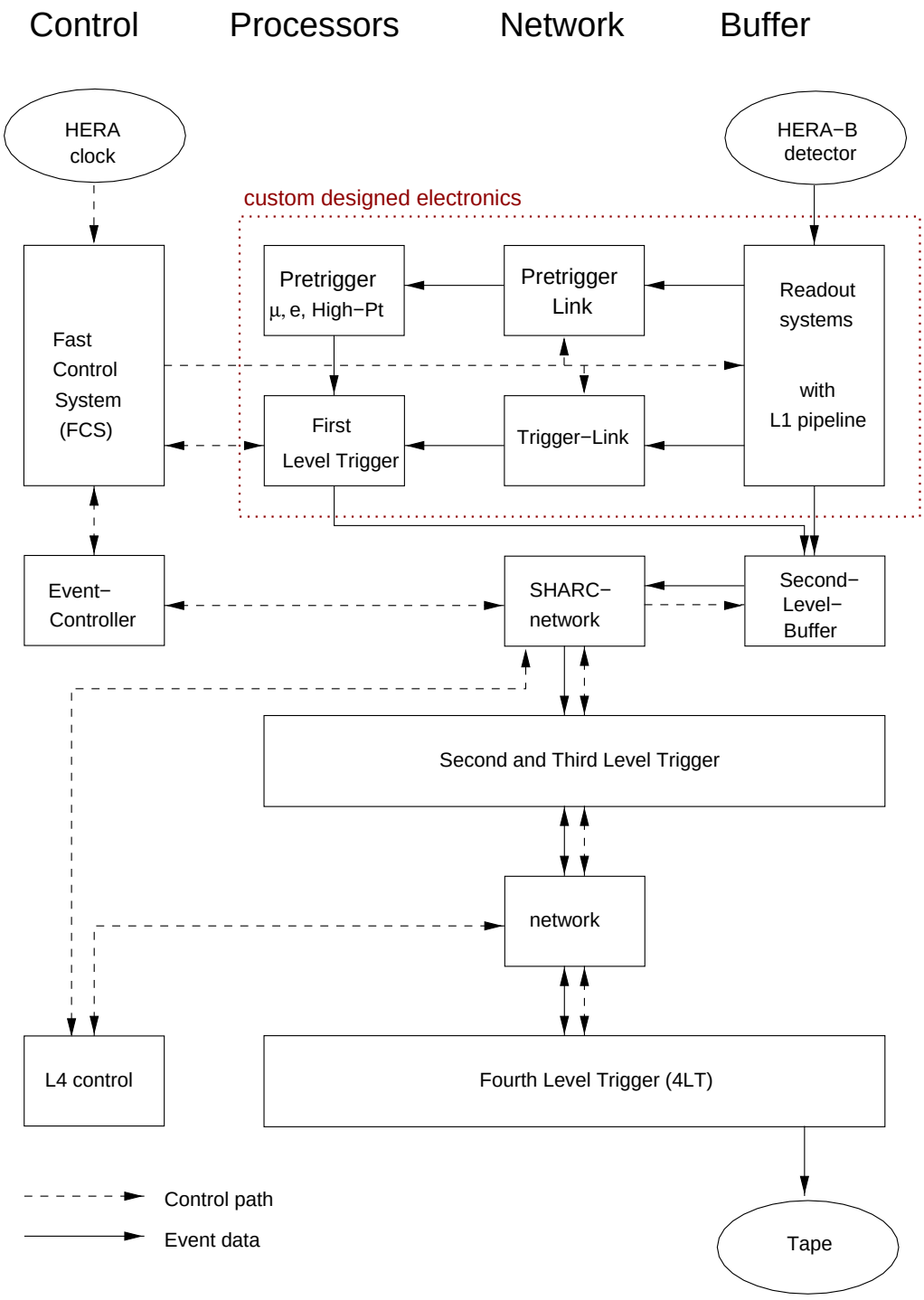

Figure 3.1: *Trigger architecture of HERA–B. The detector data are transfered to the pre-trigger and the FLT by optical data lines. If the FLT accepts an event the data are stored in the Second Level Buffer while the SLT executes the trigger algorithm. From SLT/TLT farm the data are sent to the 4LT via Ethernet network. Events that pass the 4LT are stored on tape. [Wag00]*

use the entire available detector information for event selection at the Third Level Trigger (TLT). A storage of detector data is not necessary since the entire event data is made available for the TLT and the Fourth Level Trigger (4LT). For the first time, the trigger decision is not based on an ROI but on the entire information of all detector components. We assume a further reduction of data that are sent to the 4LT at a rate of 25 to 50 Hz. Figure 3.1 shows the four level trigger system of HERA–B.

3.2 The Pretriggers

The pretriggers start the processing of an event. They generate information of possible candidates that is transformed into a certain format (see section 3.3.2) and is passed to the FLT. The information points to a certain area in the detector, the so called Region Of Interest (ROI). The reduction at the pretrigger level decreases with increasing number of interactions per bunch crossing because each interaction causes in general at least one ROI. The number of ROIs is dominated by random coincidences, hadronic and electromagnetic showers.
The next two sections describe the electron and the muon pretrigger of HERA–B.

3.2.1 The Electron Pretrigger

The electron pretrigger signal is generated if in a 3×3 matrix the energy exceeds a threshold E_{th} and more than 50 % of the total energy are released in the central cell. E_{th} is defined as:

$$E_{th} = K_{trig} \cdot \left(\frac{1}{R} + \frac{1}{\sqrt{x^2 + |y^3|/cm}} \right) \tag{3.1}$$

where

- R = $\sqrt{x^2 + y^2}$ is the radial distance of the cluster with respect to the beam pipe,
- x and y is the position of the cluster,
- K_{trig} is a parameter between 500 GeV·cm and 1000 GeV·cm.

K_{trig} is an adjustable parameter that is defined by the minimal transverse momentum p_T which is required for the cluster (typically 0.5 GeV/c) and the distance between target and ECAL (≈ 1400 cm). It can be used to control the event rate that is delivered to the FLT [Res96]. The asymmetric treatment of x and y for the threshold energy regards the bending of tracks in the x-z-plane.
Besides the evaluation of coincidences the pretrigger electronics determines the center of gravity of the charge to provide the FLT a better position estimate and hence ROIs smaller in size than one ECAL cell. The electronics features the recovery of energy losses due to Bremsstrahlung, too. The position of electrons or positrons that emitted Bremsstrahlung in front of the magnet can be calculated from the position of the corresponding cluster, its energy, the known p_T kick of the electron and positron in the magnet (≈ 650 MeV/c) and the assumption of the target position. In total, there are two possible positions reflecting the fact that it can be either an electron or a positron. The energy measured in one of the positions is added to the cluster energy.

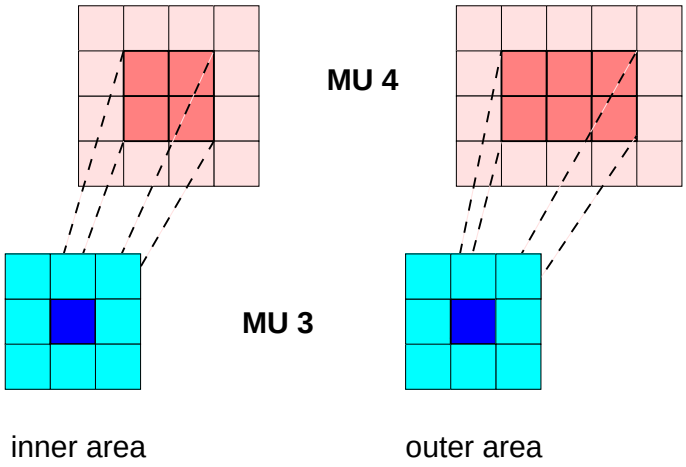

Figure 3.2: *Conditions that have to be fulfilled to initiate a pretrigger signal by the muon pretrigger.*

3.2.2 The Muon Pretrigger

The muon pretrigger determines three dimensional space points as the basis for muon track seeds consisting of position and direction. The pretrigger accepts only those points whose projection towards the target agrees with the target position. It analyses coincidences between pads in the layer MU 3 and MU 4. A coincidence is accepted if one pad of MU 3 and at least one out of the six possible pads of MU 4 is hit. In the case of the pixel chambers, four adjacent cells are combined to one read out channel and six of those form a so called pseudo pad. A coincidence in the pixel system is accepted if one pseudo pad in MU 3 and one associated in MU 4 is hit. The absence of massive absorbers between MU 3 and MU 4 improves the track parameters of the candidate because there is almost no multiple scattering. The evaluated position and direction is coded in a bit pattern and sent to the FLT. As the hadron background is almost completely filtered out by the absorbers the $J/\psi \rightarrow \mu^+\mu^-$ signal can be isolated cleanly and has a higher efficiency than in the electron case. Figure 3.2 shows the combinations that result in a pretrigger generated by the muon pretrigger.

3.3 The First Level Trigger

The FLT performs a track search in detector layers behind the magnet. The pretriggers provide a region of interest (ROI) for particle tracks. The FLT tries to reconstruct the track in the direction to the target up to the magnet.
The electron pretrigger provides a two dimensional search region at the last superlayer of the outer tracker (TC 2). The muon pretrigger provides a search region at the last layer of the muon system (MU 4).
The information is updated according to a found hit. A hit for the layer MU 3 and MU 4 is defined by a wire since those two layers have only vertical wires. In all other trigger layers a hit requires a coincidence of three stereo views. To increase the detector efficiency of the inner and outer tracker as well as the muon system the trigger layers are built as double

layers. Two subsequent channels of the double layer of the outer tracker with respect to the path of flight are combined by a logical OR. In order to minimise the calculation effort the drift time information of the outer tracker is not used. If a hit is found, the information is updated and evaluated for the next superlayer. This process is repeated until it is unsuccessful in one superlayer or it has arrived at the last trigger chamber. It has to be emphasised that the FLT tracking requires a hit in every tracking layer, i.e. an electron has to be detected in 12 layers of four outer tracker superlayers.
The algorithm is implemented in custom designed electronics boards, the Track Finding Unit (TFU). Each TFU covers a particular region in a superlayer. The last processor

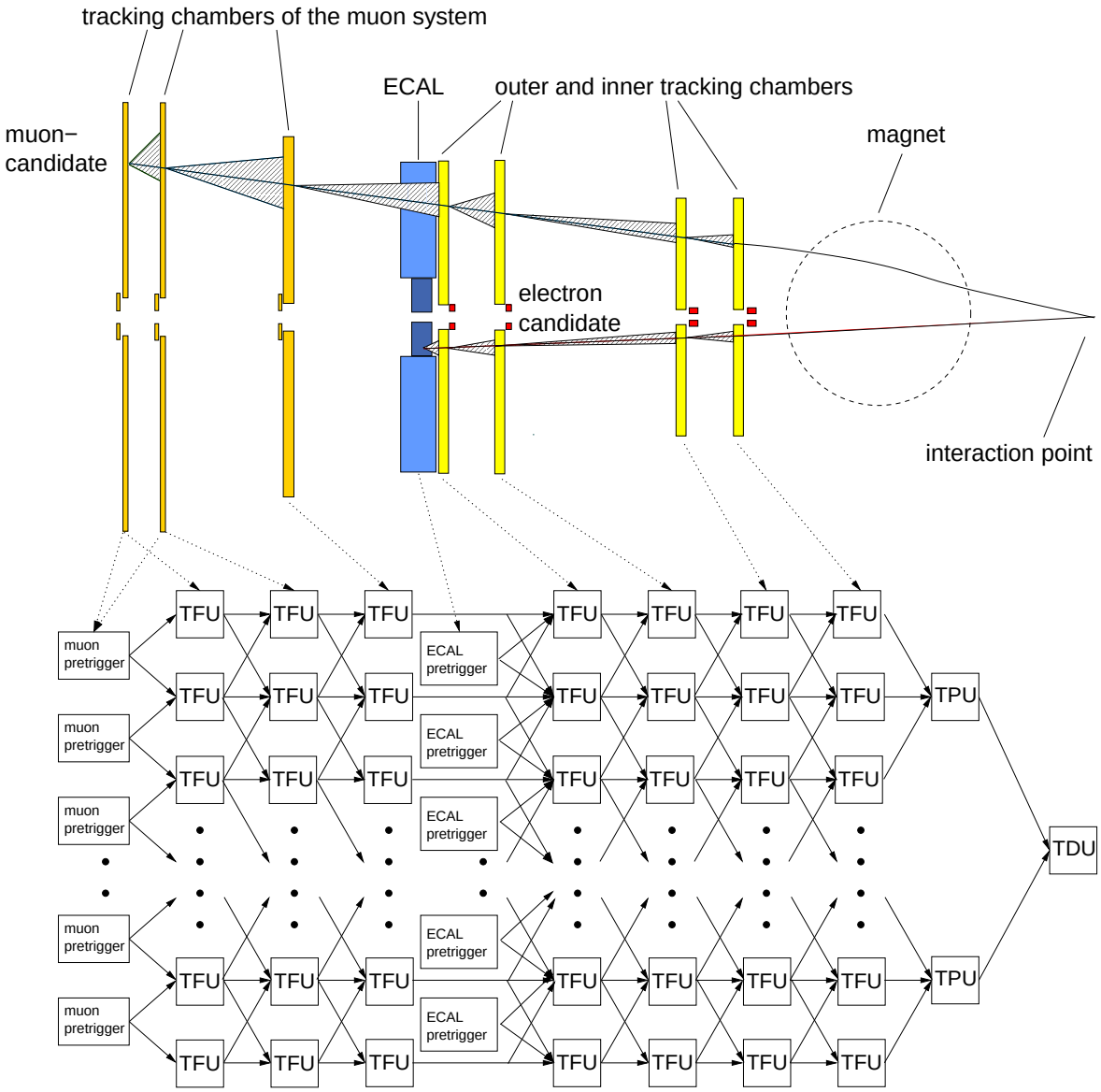

Figure 3.3: *Setup of the First Level Trigger. A network of TFUs looks for track candidates in the inner and outer tracker chambers and in the muon system. The track candidate search is launched by pretriggers. The track parameters are calculated by the TPU. The TDU decides whether the event is accepted or not. [Noe99]*

board in the filter process communicates position and direction of a found lepton track to a dedicated board, the Track Parameter Unit (TPU). It uses the information of the TFU and the constraint that the track originated from the target to calculate the momentum. At this level cuts can be applied to suppress and remove clones[2].
Finally, invariant masses of pairs of accepted lepton tracks are computed by a processor board called Trigger Decision Unit (TDU). The trigger decision is taken by a comparison of the parameters of each combination with the entries in a table that contains the trigger variables. Special triggers are activated by loading of the table accordingly. The trigger decision activates the readout into the Second Level Buffer.
Events with many primary interactions produce many random coincidences and consequently have a higher chance to be accepted by the FLT. Such events are rare but if they occur they inflict a high load with respect to the computing effort of the trigger processors. The FLT should be able to ignore events with high multiplicities.

In the following sections, we present the implementation of the FLT network and the sector arrangement of the TFUs for the outer tracker layers and the muon system. We provide an overview of the message format and introduce the processor modules of the FLT.

3.3.1 The Implementation of the FLT Network

The concept of above is shown in Figure 3.3 in a network of roughly 80 custom designed, massively parallel and pipelined processors operating at a clock of 50 MHz. At each processor detector data arrives at full initial event rate of 10.4 MHz to avoid dead time. The chamber hit information are transfered from the front end electronics (Front End Driver, FED) to the processors via high speed serial links or by optical transmission via fibres. The TFUs operate on the full data of all views of the dedicated trigger layers. The received pattern of fired detector channels are stored on-board in the Wire Memory (see section 4.2.2) of the TFU for 128 bunch crossings.
The pretriggers initiate the tracking of the FLT. They define for each found track candidate a search region that is coded as an 80 bit word, the so called message (see section 3.3.2), and broadcast to the TFU of the subsequent superlayer. In the muon system the pretrigger sends the message to one of the TFUs of MU 4. The electron sends its messages to one or more of the TFUs of TC 2. Afterwards the FLT performs as described above.
In the case that the search region overlaps with several TFUs the message is sent to all TFUs concerned. Up to 12 TFUs are used to cover a superlayer. The arrangement of sectors is shown in Figure 3.4. The sector setup used by the FLT is slightly different to that of the outer tracker concerning the gap between two adjacent wires. The OTR setup makes a clear separation of sectors with different wire spacing whereas the FLT deals with an overlap of 5 and 10 mm cells. This has to be taken into account when the connection of the wires to FLT modules (called mapping) is established. A detailed description of the mapping can be found in [Neg00].

[2]The same physical track is described by several ROIs which increases the processing load of the TDU.

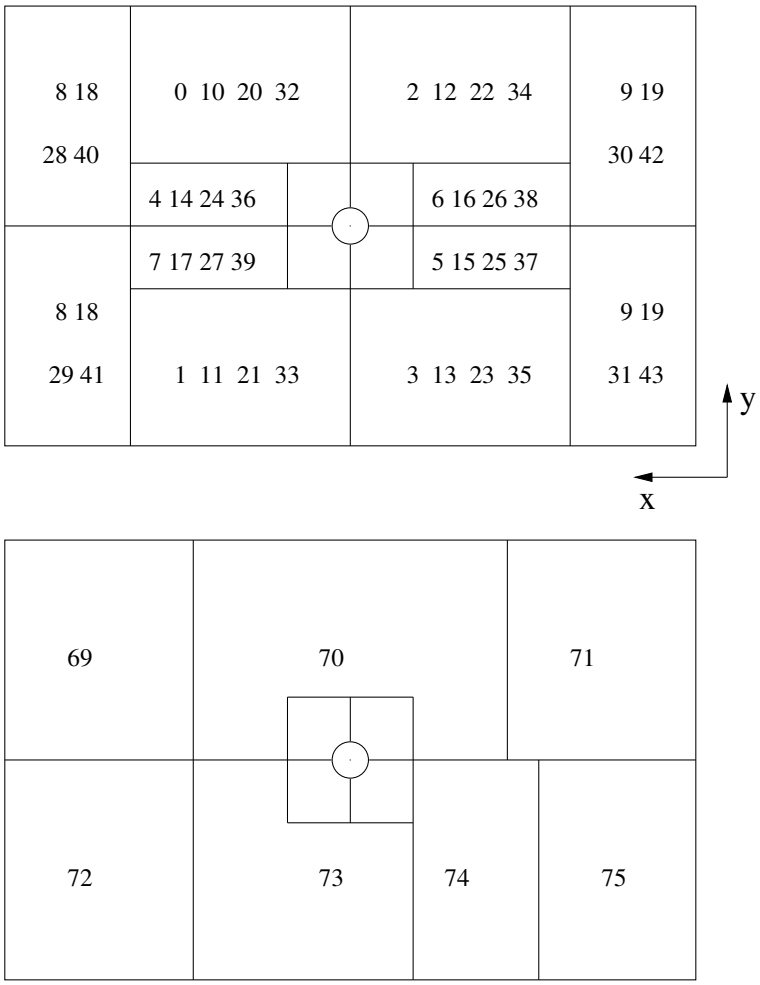

Figure 3.4: *The arrangement of FLT sectors in the outer tracker (above) and MU1 (below). MU3 and MU4 are not shown because these layers are divided into two halves in y-direction. One TFU serves the upper and one the lower half, respectively. The numbers in the sectors correspond to the TFU numbers according to Table 5.1. In the PC layers the outermost sectors are not divided in y-direction.*

3.3.2 The Data Link and Data Format

This section describes the path of data from the detector to the FLT and the format in which the information is coded. In addition, the information transfer between the pretriggers and the TFUs are presented. The communication within the FLT network uses the same format.

The signals in the detector are amplified and digitised. Afterwards they are serialised in custom designed electronics board, the Linkboard. The Linkboard combines several detector channels to a bit pattern that is transmitted via a 50 m optical fibre to the electronics hut outside the detector. As transmission with connections like coaxial or twisted pair cables cannot manage the amount of data with a desirable frequency the optical transmission was chosen.

The hit data need to be multiplexed to reduce the number of connections. For this pur-

pose, the AUTOBAHN chip from Motorola is used. It offers a transfer rate of 900 Mbit/s which yields a data transmission frequency of 450 MHz. The chip provides a 32 bit wide interface for data transfer. The clock frequency of the chip is 25 MHz. Each transmitted 32 bit pattern consists of eight bits for the bunch crossing number and 24 bits of hit information. The bunch crossing number is used to assign an address in the wire memory (see section 4.2.2) and can be used to find errors in the transmission.
The data link between the pretriggers and the TFUs and within the FLT network itself is realised by a LVDS (Low Voltage Differential Signal) based messaging system. The pretrigger output itself is a PECL (Positive Emitter Coupled Logic) signal that is tranformed to a LVDS signal.
The information (called message) between TFUs that is interchanged contains 80 bits and has the following structure:

- 7 bits for bunch crossing identifier (BX),
- 2 bits for the pretrigger type (electron, muon or High–p_T),
- the transverse coordinates x and y/z of the hit. They are coded with respect to the FLT frame and called ξ and η. ξ is a 10 bit value and η a 9 bit one. η reflects the track direction in the non bending plane. The receiving TFU centers its ROI around these coordinates,
- the information of the track direction in the x–z–plane is called $d\xi$ and reflects the deviation of the track from one with infinite momentum (i.e. a straight line). The information is coded in 8 bits,
- the size of the ROI uses two variables: a 2 bit value w and an 8 bit value $dd\xi$. w is the width of the hit cluster. A maximum of four successive wires that are hit are combined to one cluster,
- energy or momentum $-E^{\pm}-$ depending on pretrigger are coded in 7 bits,
- two additional flags with one bit each,
- a numerator $n\xi$ if the ROI is larger than the maximal allowed range of 32 wires. In that case, a second message to describe the remainder of the ROI is generated and the numerator which uses 1 bit is set to one and finally,
- the destination identifier TDI to decide to which TFU the message should be sent.

Table 3.1 summarises the message parameters. The only parameters in the message that are normally modified by each TFU are $d\xi, dd\xi, n\xi$, All and $DEST$. All other parameters are forwarded unchanged. Exception is the updating of ξ and w at superlayer TC2 and at the Muon detection layers and η at the MU1 layer. Parameters indicated by "delay" are passed along the processing. They are needed by some calculations but are not altered. The following sections give a short overview of the FLT electronics components.

3.3.3 The Track Finding Unit

As the TFU is theme of this thesis the board is described in more detail in chapter 4.

parameter		length in bits	starts at bit	to TFU	from TFU	delay
TDI	destination identifier	8	0		X	
$n\xi$	two messages	1	8	X	X	
ξ	x coordinate at reference plane	10	9	X	X	
$d\xi$	minimal track slope	8	19	X	X	
$dd\xi$	size of track window	8	27	X	X	
η	y/z at reference plane	9	35	X	X	
w	number of adjacent cells	2	44	X	X	
all	hit in every TFU	1	46	X	X	
BX	bunch-crossing number	8	47	X		X
ID	pretrigger identifier	2	55	X		X
P	estimated nominal momentum	7	57	X		X
$flag$	pass to next TFU	1	64	X		X
E^+	ECAL energy	7	65			X
E^-	ECAL energy	7	72			X
nc	not used yet	1	79			X

Table 3.1: Message definition for TFU and pretrigger boards.

3.3.4 The Track Parameter Unit

The Track Parameter Unit receives the information of the TFUs of the outer tracker superlayer PC 1. In total, there are four TPU modules that receive the messages of ten TFUs of PC 1. The track coordinates described by the message are extrapolated to the center of the magnet. This information together with the assumption that the generation of the lepton took place at the target is needed for the determination of the track parameters. The momentum in the x-z-plane is calculated out of the impact parameter x_0 and the x-position x_M of the track at the center of the magnet. A deviation of the track in y-direction is neglected. The momentum in the y-z-plane is evaluated out of the track direction in y. Figure 3.5 shows a schematic overview of the momentum determination of the TPU. Cuts on the momentum and the transverse momentum can be applied in order to reduce the event rate. The threshold of the cuts can be programmed via registers. The charge is calculated out of the deflection in the magnetic field.
The calculations of the TPU are based on Look Up Tables (LUTs). Details of the LUTs can be found in [Fla00a]. In addition to the calculations done for leptons the TPU applies calculations for High–p_T and photon candidates.
The TPU may perform a Bremsstrahlung correction of the momentum for electron candidates. The ECAL provides in addition to the cluster reconstruction the reconstruction of a cluster of Bremsstrahlung that is emitted in front of the magnet. Since the charge of a particle is known at the TPU an explicit association of particle and Bremsstrahlung cluster is possible.
A track multiplication can appear if many hits are close to each other. To prevent a high load of the TDU with identical tracks the TPU is able to discard identical tracks by comparing the reconstructed momenta and charge of a track candidate with already

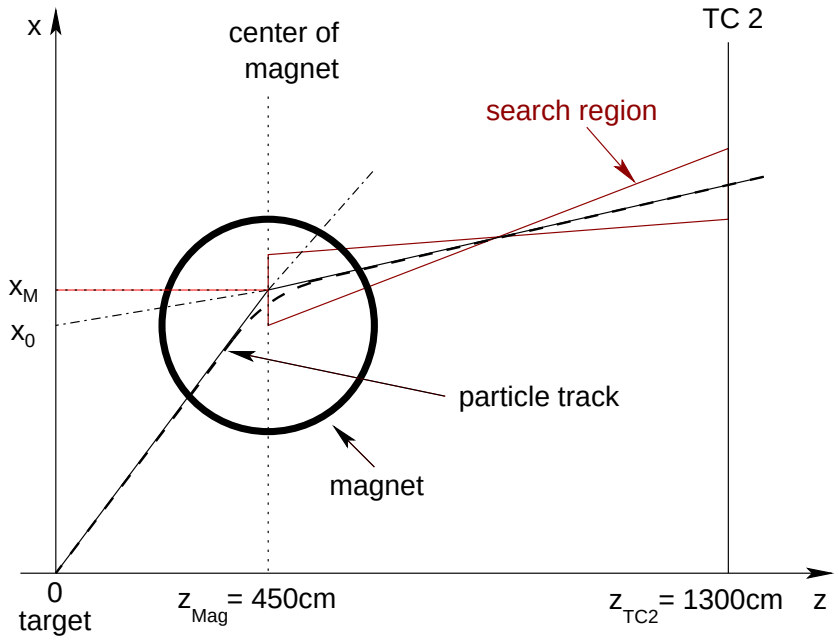

Figure 3.5: *Determination of track parameters by the TPU. The track that is reconstructed by the TFUs is extrapolated through the magnet under the assumption that the track originated from the target.*

reconstructed tracks of the same event.
A cut on the number of reconstructed tracks for the same event can be applied in addition to the clone removal in order to reduce the load of the TDU for events with a high track multiplicity.
Further details of the TPU can be found in [Fla00a]. After all the calculations of the TPU are finished the information is passed to Trigger Decision Unit.

3.3.5 The Trigger Decision Unit

The Trigger Decision Unit receives the kinematical parameters of reconstructed tracks from the TPU and takes the trigger decision on the basis of this information. The track and message information that arrives at the TDU are counted and stored in two different memories, track– and message memory. The redundancy of information is unavoidable because both memories must be addressable independently of each other. The information that is needed to derive a trigger decision is stored in the track memory while in the message memory the complete information is held available.
The invariant mass calculation is done by four LUT processors. As there are four processors the track memory is subdivided in four parts, too. The message sequencer delivers to the LUT processors the tracks out of the four parts that they can be compared with another track of the same event for which the bunch crossing number is used as an identifier. This means that four tracks can be compared without any additional cycle which is very important with respect to latency and the maximal processing time of the FLT.
The trigger decision can be derived via two different mechanisms:

- The Count Trigger counts for each event the number of found tracks. The tracks are distinguished by eight different categories (four different particles and set or unset high flag indicating particles with high transverse momentum). For each category the threshold for a trigger decision can be adjusted individually,

- the Pair Trigger grants a trigger decision based on the pairwise calculated invariant mass of track candidates of the same event. For a J/ψ trigger a pair of leptons is required whose invariant mass is exceeding 2.0 or 2.5 GeV/c^2. The lower value takes into account possible losses due to Bremsstrahlung.

Prescalers for both triggers are available to reduce the output rate. A positive trigger decision is distributed via the Fast Control System (FCS) [Ful99]. Further details of the TDU can be found in [Noe99].
In case of a positive trigger decision, the FCS requests the complete information from all detectors which is stored in the Second Level Buffer (SLB). As the bandwidth of the detector data at that level is huge the transfer cannot be realised by commonly available network components. The Second Level Buffer is realised as a network of Digital Signal Processors (DSPs) [Wag00].

3.4 The Higher Level Trigger

This chapter provides an overview of the higher level triggers. They are all realised as programs on off-the-shelf personal computers.
The computers are grouped in so called farms. The computer farms of HERA–B consist of more than 200 PCs each. The second and the third level trigger are combined in a farm which is referred to as SLT/TLT farm. The fourth level trigger (4LT) is simply referred to as 4LT-farm. We briefly describe the architecture of the higher level trigger.
The data that is needed by the SLT is stored in a network of DSPs in a way that each PC of the SLT farm can access all available data. The interconnection between the second level buffer and the PC farm is also realised by DSPs since it guarantees fast data access. The event controller which controls the load of the SLT network runs on a DSP. The event controller is responsible for the assignment of memory for detector data to be stored and prevents that data gets overwritten. In case that an event is rejected the event controller frees the memory and frees the processor for new data. If an event is accepted the data is read by a PC and the event controller frees the used memory in the SLB. The data can be processed immediately by a TLT process. Further details of the SLT network can be found in [Wag00].
The level two framework (SLT/TLT) farm is organised as single processes that run on a PC each. In total, there are 240 harddiskless computers with Pentium II and Pentium III processors. A harddisk provides no advantage as access time is too slow during triggering. The maximal input rate is 50 kHz and the allowed processing time is limited to 5 ms. Within this time the aim is an overall reduction of events of a factor of 100.
The Third Level Trigger uses the same hardware as the SLT. The SLT/TLT farm is realised to minimise the latency of context switches and data exchange with the SLB. Only one executable that contains the SLT algorithms, event builder software and the TLT algorithm is run on each CPU. This is called the Second Level Process. The only custom designed

part of the SLT/TLT farm is a card that enables the link between the PC and the SLB. The implementation as a farm is an efficient and flexible solution for triggering. It is possible to run arbitrary trigger algorithms on the farm as long as the timing constraint is respected. The SLT/TLT farm is linked with the 4LT-farm by an ethernet switch. The 4LT-farm should not be mixed with the SLT/TLT farm as they are completely different. To be able to process the data coming from the TLT and with respect to the processing time the 4LT-farm consists of 200 CPUs.
We present in the following sections the algorithms applied by the higher level triggers.

3.4.1 The Second Level Trigger

The tracking of the FLT is very coarse and susceptible to wrong tracks. A large amount of tracks delivered by the FLT are ghost tracks which means that most of them were not generated at the target but are fakes due to photon conversion in front of or in the magnet. Other sources for misidentified tracks are hadrons or muons from particles that decay in flight.
The SLT repeats the tracking of the FLT and uses additional detector information, like drift time and hit information of the whole outer tracker. The tracks can be propagated through the magnetic field towards the vertex detector. To avoid a processing intensive tracking through the field a table is used that relates coordinates behind the magnet with coordinates in the vertex detector. Track candidates can be rejected after each step in the algorithm of the SLT. A brief overview of the various modules and the reduction rate are given.

SLICER

SLICER is the first step of the SLT algorithm and has to cope with the input rate of 50 kHz coming from the FLT. The principle of the algorithm is rather simple:
The 0° layers of the tracking chambers between magnet and calorimeter are read out. The ROIs of each layer are subdivided with respect to the x-direction. The hits for each combination of segments that are part of a straight line are counted. If the sum of hits does not exceed a certain threshold the track is rejected. A major fraction of ghost tracks provided by the FLT are removed.

X-Refit

The next two steps of the SLT algorithm reconstruct the FLT track by means of a Kalman filter technique [Boc90]. First, the track is reconstructed in the xz-plane by using the same information as SLICER. The information of the drift time is used to improve the resolution. Events with at least two tracks are passed to the next step.

Y-Refit

In this step, the stereo views are used to derive a space point reconstruction of tracks. Events with at least two tracks are passed to the next step.

Track reconstruction through the magnet

The tracks are extrapolated through the magnetic field to the vertex detector with the help of the information of the MC 1 layer of the magnet chambers and the SI 8 layer of the vertex detector. This results in clearly defined ROIs in the vertex detector.

Track reconstruction in the vertex detector

In this step, tracks are reconstructed through the vertex detector to the target. The rate can be reduced further by requiring at least two tracks in the vertex detector. For displaced vertices cuts on the impact parameter can be applied.

Vertex search

A further reduction of the trigger rate is possible by requiring that the reconstructed tracks form a common vertex.

3.4.2 The Third Level Trigger

In contrary to the FLT and SLT, the TLT algorithm is not based on ROIs. For the first time in the trigger chain, the entire data of one event is at disposal to the TLT which increases the performance as the collection of the data from several processors calculating ROIs of the same track is obsolete. At an estimated input rate of 500 Hz from the SLT about 50 out of 240 PC of the SLT/TLT farm execute the TLT step at a time. The desired suppression of a factor 10 should be achieved within 100 ms per event. In the current trigger setup, the TLT is used for the event building.
The TLT focuses on events with less kinematical constraints i.e. without a vertex formed like above. Within the allowed processing time of the TLT it is possible to perform pattern recognition in tracking and particle identification devices. For this purpose mainly the VDS is used because RICH and ECAL information alone is not adequate to assign a particle to an interaction that has been selected by FLT and SLT. Further details of the TLT algorithm with respect to pattern recognition in the VDS can be found in [Schw00].

3.4.3 The Fourth Level Trigger

The 4LT-farm has to fulfill several tasks among data handling:

- Provide fully reconstructed events online,
- perform final event selection called level 4 trigger to cope with rate feasible to write events to tape,
- carry out a detailed data quality monitoring,
- prepare data logging and archiving,
- reprocess event data when no data taking takes place.

Like in the SLT/TLT farm none of the processors of the 4LT-farm has to communicate with another CPU. Each CPU is running a copy of the reconstruction program and is applying it to data that are assigned to it by an external steering mechanism. A proper running is insured by control processes that run in parallel on the farm. Detailed descriptions of the software environment can be found in [Gel98, Gel00].
Figure 3.6 summarises the four trigger level with their allowed processing time and the aimed reduction.

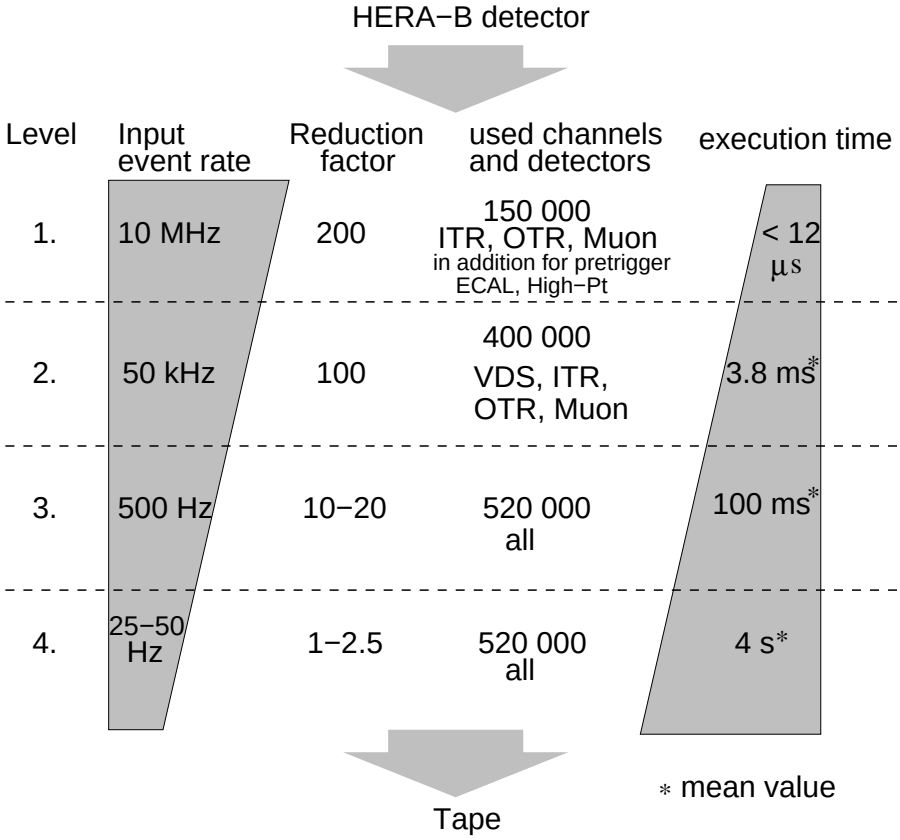

Figure 3.6: *Four successive trigger levels perform in parallel to data taking the event selection. Each level reduces the event rate for the successive level which allows for a larger execution time.*

Chapter 4

The Track Finding Unit

4.1 Introduction

In this section we present an overview of the tracking performed by the FLT. We present the concept of the FLT and provide the mathematical background which is needed to understand the tracking algorithm. The next section treats the tracking algorithm in detail and explains the behaviour of one central part of the TFU– the Coincidence Matrix (CM).
We devote a section to the implementation of the algorithm in hardware and present in the final section the simulation framework.

4.1.1 The Concept of the First Level Trigger

The implementation of the First Level Trigger (FLT) is based on the following concepts:

- Track search and track reconstruction based on messages
  The track search, the track reconstruction and the final trigger decision is based on a message that is associated to each track. A message comprises 80 bit on information of the track direction, the particle type, the search region and the number of the bunch crossing (BX) when the track was generated. The components of the momentum of the track are added to the message after the step of track reconstruction. The message is generated by the pretriggers and transmitted to the successive processor unit. The message is updated and passed to the next processor unit. The treatment of the messages of an event by the processor unit happens asynchronously.

- Calculations performed by Look Up Tables (LUTs)
  The processing time of the FLT is limited which makes a fast calculation of the necessary parameters mandatory. The calculations are based on operation with Look Up Tables. A LUT is realised as a piece of memory that is filled with the resulting values that are addressed by input parameters and returned as output values. The readout of data is much faster than a calculation.

- Pipeline architecture
  A pipeline architecture determines results of different messages in a parallel mode:

The pipeline step $n+1$ determines the result k of the message. In parallel, the pipeline step n calculates the result $k-1$ of the following message.

- tracking algorithm according to a Kalman filter
  The tracking performed by the FLT uses a Kalman filter like algorithm. The extrapolation to the successive superlayer uses kinematical constraints as well as the available hit information to improve the result (see section 4.1.4).

4.1.2 Conventions and Mathematical Remarks

The superlayers used by the FLT are connected with several TFUs. Each TFU covers a specified area of the superlayer. A TFU can cover a range of up to 384 wires and store hits in three wire memories –one for each view. The last muon layers MU 3 and MU 4 do not have any stereo view. The entire wire range is subdivided into three regions that are related each with one wire memory (see section 4.2.2).
The region that is connected with a TFU defines the TFU coordinate system and uses the following variables:

- $x0^+$, $x0^0$, $x0^-$ are the x-coordinates of the start of the TFU region for a specific stereo view,
- sx^+, sx^0, sx^- are the length of the TFU region for each view in x-direction,
- nx^+, nx^0, nx^- represent the number of wires inside the region for each view,
- $y0^+$, $y0^0$, $y0^-$ are the horizontal limit of the TFU region of each view in y-direction,
- sy^+, sy^0, sy^- are the height of each region in y-direction,
- ny^+, ny^0, ny^- are the number of cells in y-direction (only applicable for the TFUs that are connected with the muon pixel detectors). All ny are 1 for wire detectors,
- the direction α of the wires,
- $cellSx^+$, $cellSx^0$, $cellSx^-$ are the equidistant pitch of a region (i.e. $\frac{sx^i}{nx^i}$).

The direction α must not be confused with the stereo angle of the detector. The relation between stereo angle and direction is:

$$\alpha_{stereo} = -arctan(\alpha). \tag{4.1}$$

The x-coordinate of the first wire of a TFU region for a stereo view v is given by:

$$x_{first\ wire} = x0^v + 0.5 \cdot cellSx^v \tag{4.2}$$

The origin of the global coordinate system is defined by the nominal average target position. Coordinates essentially used by the FLT tracking algorithm are partially denoted by greek letters. They are introduced and defined in the following sections. A third coordinate system is defined by the calculated ROI (referred to matrix coordinates). Figure 4.1 summarises the different coordinate systems involved in the tracking of the FLT. The size

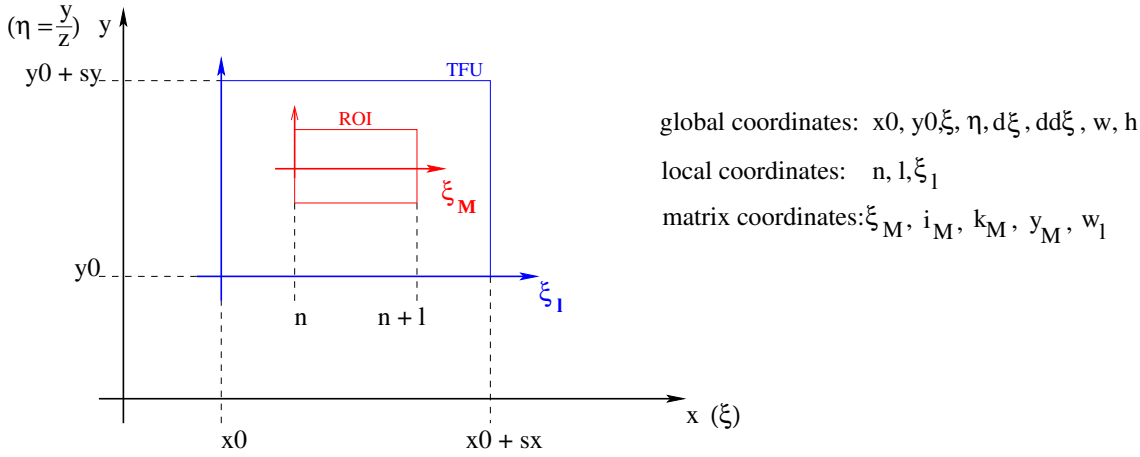

Figure 4.1: *The different coordinate systems involved in the tracking of the FLT. The TFU coordinate system is defined by the coordinates x0 and y0 and the sizes sx in x-direction and sy in y-direction. A third coordinate system is defined by the calculated ROI.*

of the ROI comprises up to 32 wires in x-direction. A found hit or coincidence needs to be transformed from the matrix coordinate system to the global coordinate system. Details of the matrix coordinates and the Coincidence Matrix are discussed in section 4.2.3.
The entire tracking algorithm of the FLT uses coordinates of a so called reference layer (denoted by the index "Ref") as well as coordinates of the current layer. The coding of variables inside the FLT frame as described in section 4.1.3 depends on current or reference superlayer. Table 4.1 summarises the current layer and its corresponding reference layer.

current layer	reference layer
PC 1	TC 2
PC 4	TC 2
TC 1	TC 2
TC 2	MU 1
MU 1	MU 3
MU 3	MU 4
MU 4	MU3PRE

Table 4.1: *Assignment of the reference layer for the superlayers used by the FLT.*

Determination of the y–Position

In y-direction, the particles are to the first order not influenced by the magnetic field. The extrapolation in y-direction is simply a projection of the current y-position in a specific layer on a straight line towards the target:

$$y = y_{Ref} \cdot \frac{z}{z_{Ref}} = \eta \cdot z. \tag{4.3}$$

From equation 4.3 we directly see the definition of the message parameter η.
The size of the ROI in y-direction is limited only by the design of the Coincidence Matrix that is discussed in more detail in section 4.2.3. Figure 4.2 shows the extrapolation in y-

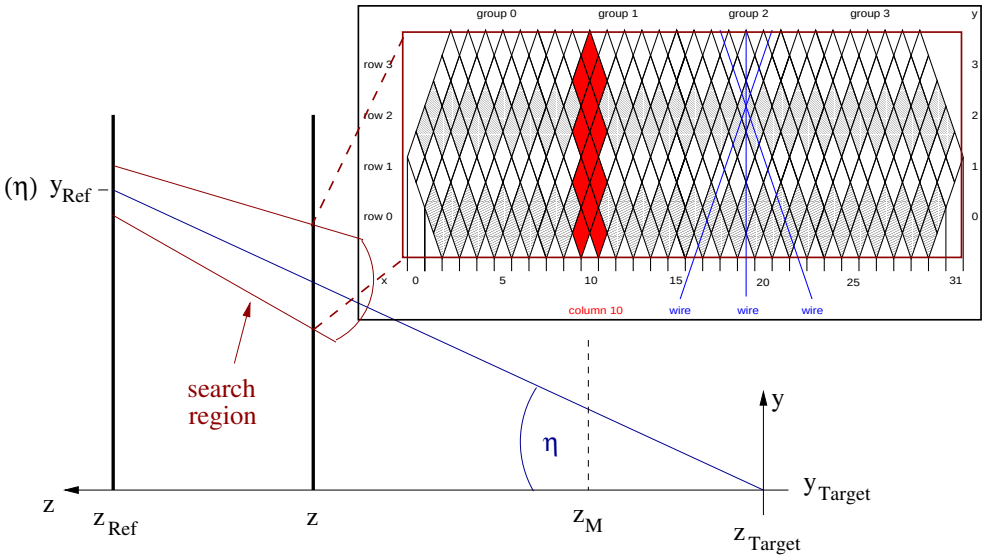

Figure 4.2: *Extrapolation in y-direction performed by the FLT. The y-position is projected on a straight line towards the target since the tracks are approximately not bent by the magnet field. The picture of the Coincidence Matrix shows the allowed size of the ROI in y-direction.*

direction and a schematic picture of the Coincidence Matrix. The rhombs in the schematic picture of the Coincidence Matrix represent the sensitive area ($\pm$ half of the pitch) around a wire. The actual wires are represented by three lines for sake of clarity. The height (cellSx/$tan(\alpha_{stereo})$) of such a rhomb is determined by the stereo angle of the wires. We define the maximal size in y-direction as:

$$\Delta y_{ROI} \;=\; 4 \cdot \frac{cellSx}{tan(\alpha_{stereo})}. \tag{4.4}$$

In total, the Coincidence Matrix covers four rhombs of height cellSx/$tan(\alpha_{stereo})$ which has its origin in the design of the Coincidence Matrix.

Determination of the x–Position

The extrapolation in x-direction assumes that the tracks originate from the target. The bending in the magnet is a priori not known but has to be taken into account to determine the x-position in the following superlayer. Moreover it is essential for the calculation of the size of the ROI to include all possible candidates that are at the borders of the ROI. The deviation of a particle with charge q in a magnetic field is calculated by the integral of the path ds that it passes in the magnetic field according to [Eck96]

$$p_0 \;=\; \int B ds \;\approx\; 0.672\ GeV/c. \tag{4.5}$$

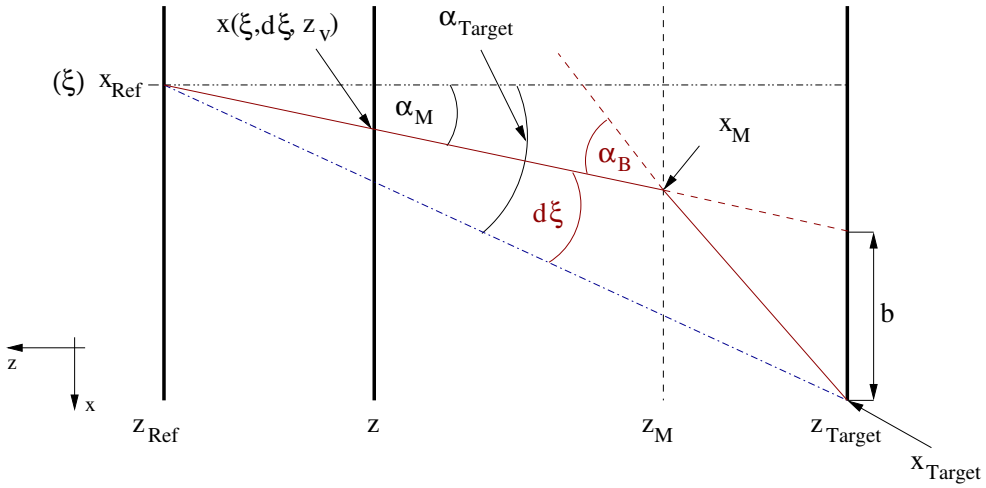

Figure 4.3: *Extrapolation in x-direction performed by the FLT. The deviation $d\xi$ from the infinite momentum track (straight line to the target) is defined as the angular difference between the angle α_M to the magnet plane and the angle α_{Target} pointing to the target.*

The bending angle α_B and the impact parameter b are obtained as

$$\alpha_B = \frac{p_0}{p} \tag{4.6}$$

and

$$b = \frac{p_0 \cdot z_{Magnet}}{p} = \frac{302.4\ GeV \cdot cm}{p} \tag{4.7}$$

with $z_{Magnet} = 450$ cm and the momentum p of the particle. The charge of the particle is determined from the sign of $d\xi$. Figure 4.3 shows a schematic view of the extrapolation performed in x-direction. We define $d\xi$ as

$$d\xi = \alpha_{Target} - \alpha_M \tag{4.8}$$

with

$$\alpha_{Target} = \frac{x_{Ref} - x_{Target}}{z_{Ref} - z_{Target}} \quad and \quad \alpha_M = \frac{x_{Ref} - x}{z_{Ref} - z} \tag{4.9}$$

The variable x in equation 4.9 is a function of ξ, $d\xi$ and the z-position (z_v) of the corresponding stereo view. Assuming $x_{Target} = z_{Target} = 0$ we finally get the formula for the extrapolation:

$$x(\xi, d\xi, z_v) = \xi \frac{z_v}{z_{Ref}} + d\xi\,(z_{Ref} - z_v)\,. \tag{4.10}$$

4.1.3 The Implementation of the Tracking Algorithm

The implementation of the tracking algorithm in hardware requires a bitwise description of the values needed for the extrapolation and the associated calculations. All the needed parameters must be transformed to bit values. Figure 4.4 shows such a transformation of the x–coordinate to a bit value. The four different slopes in the transformation take

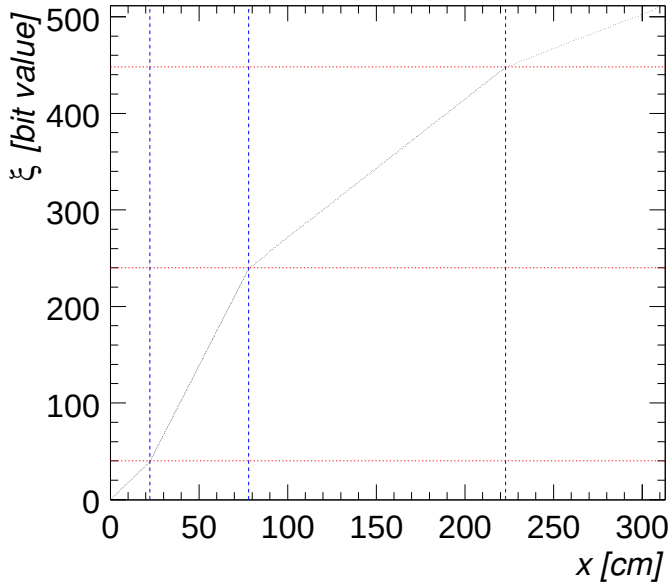

Figure 4.4: *Transformation of the x–coordinate to a bit value which is needed for the processing of the tracking algorithm. The four different slopes represent different detector granularities. [Fla01]*

the different detector granularity into account. Such a transformation depending on the variable is done for each superlayer individually. The knowledge of the reference layer is mandatory in order to decode the variable according to the instruction it was encoded. Decoding or encoding of a variable according to a wrong reference leads for example to the wrong x–position. The result of such a transformation is a reduced precision of the values that are involved in the calculation. Details of the transformation from float values to binned values for the message parameters are presented in appendix B. The limited available storage size or the limited size of the address lines are additional constraints for the representation of the parameters as bit values.

The parameters required by the calculations for the tracking are calculated beforehand to speed up the processing of the hardware. The results are stored in Look Up Tables (LUTs). The LUTs are realised as a piece of hardware memory. The parameters that are passed from the pretrigger or from a TFU serve as an address key to access the stored value. The representation of the individual parameters as bit values determines the size of the required storage. In addition, there are limits on the maximal size to guarantee a fast access to the stored values.

The calculation of the values to fill the LUTs is based on floating point calculations of the binned input variables, i.e. binned input values are transformed to floating point values. All calculations use the float values. The results are transformed to bit values. The bit values are stored in the LUT. Figure 4.5 shows the principle of generating a LUT and its usage in the hardware. A bit value ξ is the input to the calculation. The calculations are performed and the result is encoded as a bit value. This procedure is repeated in a loop over all allowed bit values. The results are stored in a table. Each input value serves as an address key. The LUT is transferred to the hardware. Each TFU has its own set of

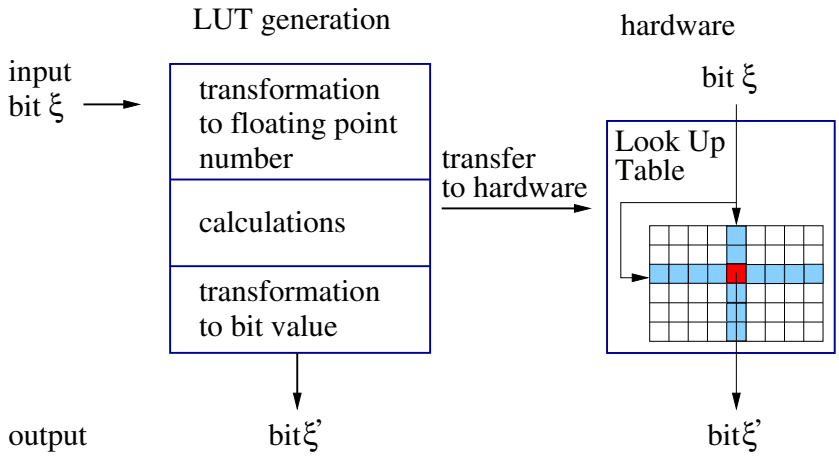

Figure 4.5: *The generation of a Look Up Table and its use in the hardware. The parameter ξ' represents the result calculated from the input variable ξ. In case of the hardware, the variable ξ serves as an address key to access the previously calculated and stored value.*

LUTs. Figure 4.5 (right) shows the usage in the hardware. An input parameter addresses a specific place in the LUT. The value which is stored there manifests the result and is read out. The usage of the LUTs in the processing of the hardware is described in section 4.3. The most important parameters that are used for the extrapolation are the following:

- ξ is the x-position of the track transformed to a bit value,
- η represents the direction to the target in the y-z-plane (i.e. the non-bending plane),
- $d\xi$ is the deviation in x-direction (i.e. the bending plane) from a track with infinite momentum which is a straight line pointing from the target to the x-position of the track,
- $dd\xi$ is the size of the ROI in x-direction.

4.1.4 The Principle of the Tracking Algorithm

The track finding algorithm is based on a Kalman filter technique [Boc90]. At each point of the tacking the available information is updated and refined by a measurement. We gain in precision at each measurement with respect to the position of the track.
The FLT tracking starts with the reception of a pretrigger signal coming either from the electromagnetic calorimeter (ECAL) or from the muon system. We concentrate on the muon system. The muon pretrigger looks for a coincidence pattern and based on this information provides a search region (ROI) to the TFUs that are connected to the last layer of the muon system. The TFU starts a hit search in the given search region. In case of a found hit, the information given by the pretrigger can be refined and forms the basis for the next measurement.
The extrapolation to the successive superlayer uses the deviation from a straight line (a track with infinite momentum which is not bent in the magnet) pointing to the target.

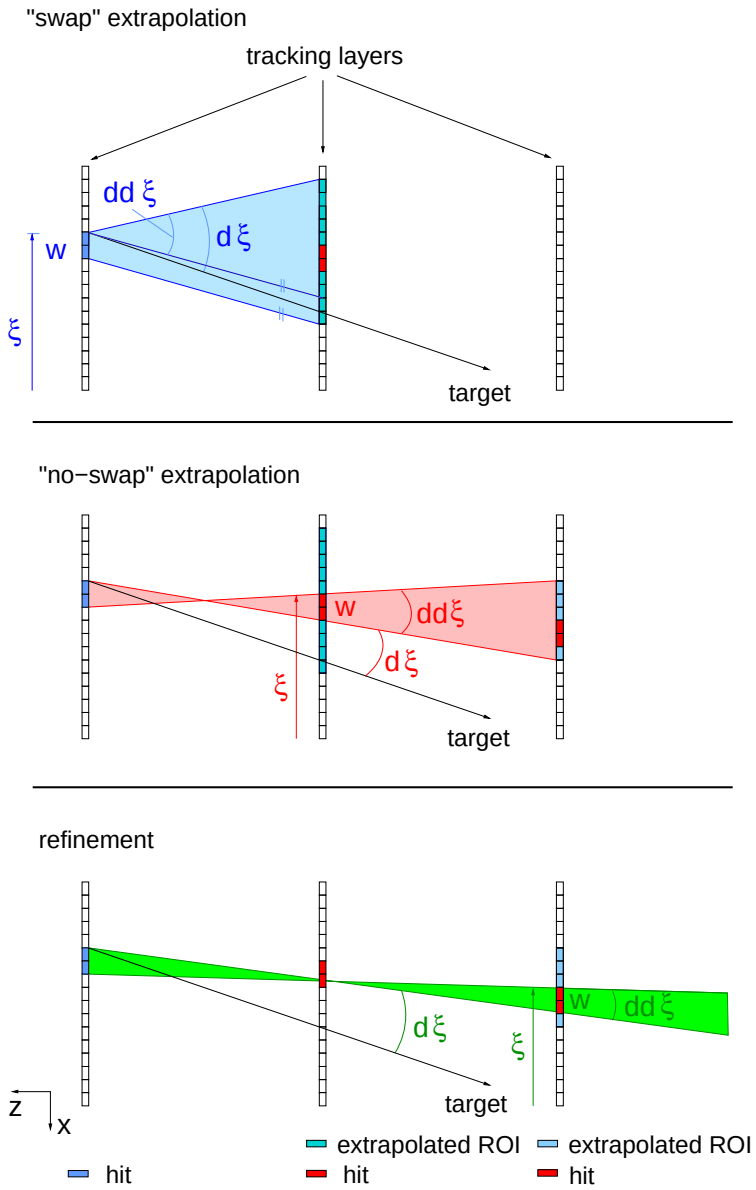

Figure 4.6: *The tracking algorithm applied by the FLT. Top: The upper edge of the current ROI points to the upper end of the next ROI ("swap" case). Middle: The upper point of the current ROI points to the lower edge of the next ROI ("no-swap" case). Bottom: Refinement of the ROI as used in PC 1 and PC 4.*

Throughout the muon system this deviation always points to the upper end of the search region on the successive layer and later on referred to as "swap" case (Figure 4.6 top).
The first muon layer (MU 1) consists of three views (0°, ±20°). The tracking algorithm recommends for all subsequent layers a triple hit coincidence to refine the measurement. If the TFU does not find at least one hit or a triple hit coincidence the track search stops immediately since no refinement of the previous measurement is possible.
The extrapolation changes in the outer tracker layer TC 1. The deviation from the straight line points to the lower edge ("no-swap" case) of the ROI on the successive superlayer. The

"no-swap" extrapolation is used in the outer tracker layers TC 1, PC 4 and PC 1 because the parameter ξ is not updated but referred to the layer TC 2. The position of the found coincidence of TC 2 is kept for all subsequent updates. This procedure narrows the ROI size in the layers up to PC 1 (Figure 4.6 middle and bottom).
The next section treats the tracking algorithm in detail.

4.2 Tracking Algorithm in Detail

In this section, we describe the track finding algorithm which we subdivide into three parts:

- The calculation of the current ROI,
- the action of the Wire Memory and the Coincidence Matrix and finally,
- the extrapolation to the following layer.

Figure 4.7 shows the flowchart of the TFU processing. The upper part shows the LUT operations to calculate the current ROI. The ROI is used to extract up to 32 wires from the wire memory which is used as input to the Coincidence Matrix. The numbers at the lines indicate the number of bits that are passed between the LUTs or other components involved in the processing. The layout of the tracking algorithm is largely influenced by boundary conditions such as number of message bits and the maximal allowed processing time. The latter condition requires that the algorithm performs as many as possible calculations by LUTs.
The number of input bits determines the size s of a LUT according to:

$$s \;=\; 2^N \cdot M. \tag{4.11}$$

N is the number of input bits and M is the number of output bits[1]. The following section describes the calculations that are needed to determine the current ROI. The performance of the Wire Memory and the Coincidence Matrix are discussed afterwards. Finally, the calculations for the extrapolation of the found hit to the succeeding layer are presented. An overview of all calculations involved in the processing of a TFU are listed in appendix C.

4.2.1 Calculating the current Region Of Interest

When the TFU receives a message it first has to determine the position and size of its Region Of Interests (ROI) in terms of wire numbers in its wire memories. These are obtained from the message parameters $\eta, \xi, w, d\xi$ and $dd\xi$ and the number of ROIs $n\xi$.

The first step is the serialisation of the ROIs: if the parameter $n\xi$ is set to 1 which means that the size of the ROI in x-direction is larger than 32 wires a copy of the message is generated for further processing (refer to page 59 for details on $n\xi$). Otherwise, the processing of the message starts immediately. For the "no-swap" case, the lower x-limit of the actual ROIs is determined from the intersection of a straight line starting at ξ ($z \geq z_{TC2}$) with the slope $d\xi$. That is the way the previous TFU (pretrigger) has coded its prediction of the ROI. Analogously the upper x-limit is obtained from a line starting at

[1] A size s = 2^{10} corresponds to 1 kB

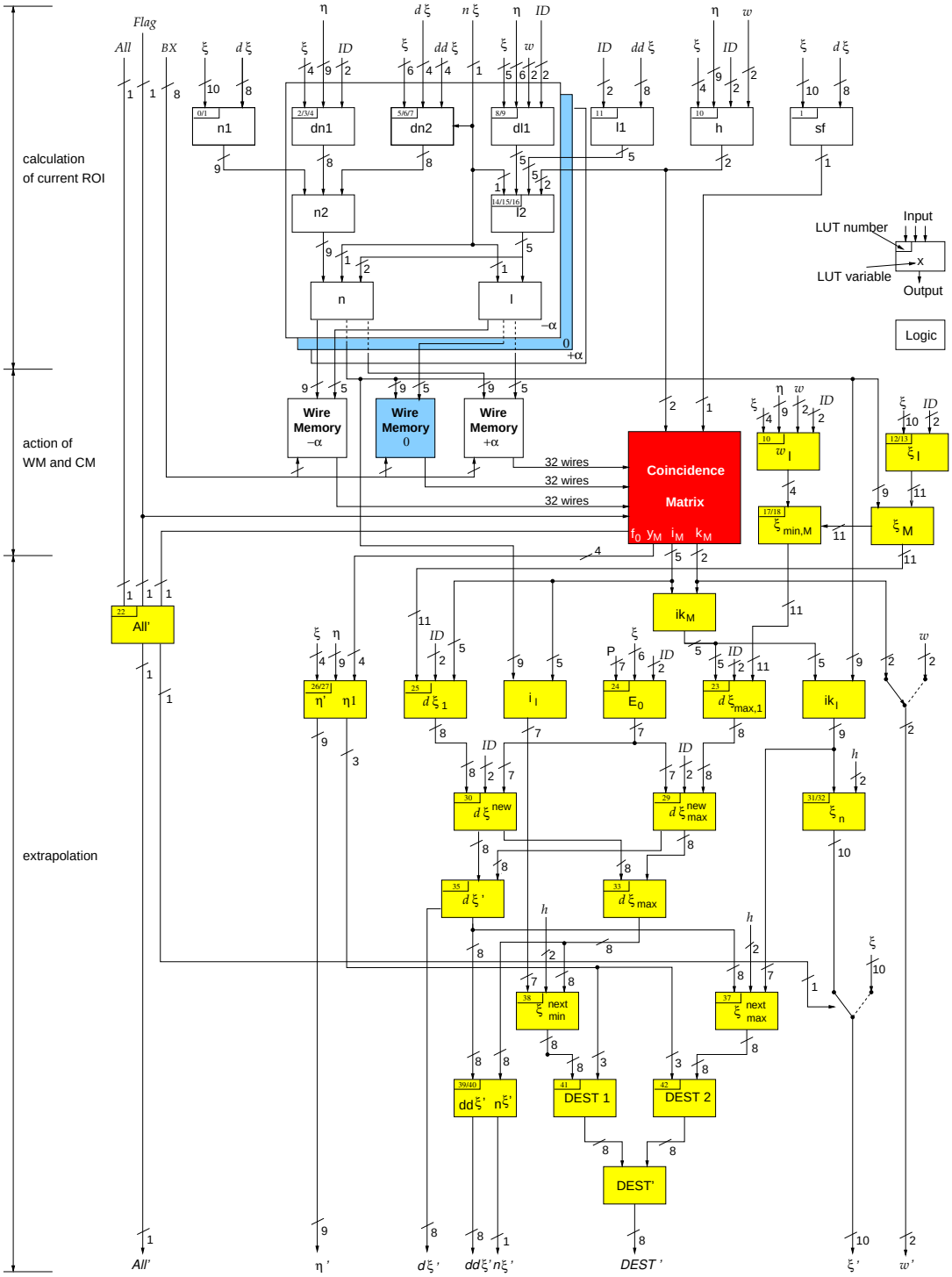

Figure 4.7: *Flowchart of LUT processing performed by the TFU. The upper part determines the current ROI. Up to 32 wires are extracted from the Wire Memory and used as input to the Coincidence Matrix. The boxes in the lower half represent LUTs that are used for the extrapolation to the next layer. Boxes without numbers represent adder or logical "or" chips.*

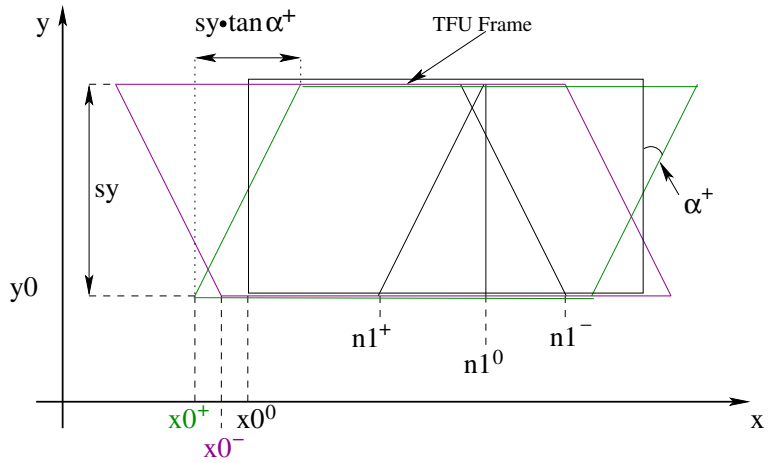

Figure 4.8: *Calculation of n1. The minimal value for n1 of all stereo views marks the start of the ROI. The starts of the ROIs for the remaining views are corrected by offsets dn1 and dn2.*

$(\xi - w)$ with the slope $(d\xi + dd\xi)$. For the "swap" case, the slope points to the upper edge. The lower edge is calculated like in the "no-swap" case (see Figure 4.6 for details). The wire numbers, n and l, are calculated from the x- and y-limits of the ROI and are needed to address the wire memory.

Determination of the y-window is straightforward from the transmitted y-coordinate (the z position is obtained via the TFU Id), the granularity there, obtained from ξ and η, and the requirement of projectivity towards the target. The height h of the ROI at the matrix and the shift flag sf are generated as input for the matrix. h has to be determined first, since it is needed in the ROI calculation. The LUTs involved or delivering the results are denoted by LUT n with n being the number of the LUT as shown in Figure 4.7. The TFU of the following superlayer receives this extrapolated x-position coded as parameter ξ of the message. The TFU determines out of this information the first wire of the ROI (LUT 0).
Out of the extrapolated x-position (ξ) from the previous layer the corresponding wire of each view of the actual TFU is determined. The result is the leftmost wire $n1$ and marks the start of the ROI in local coordinates correct to first order.

$$n1 = MIN \left\{ \begin{array}{rl} (x(\xi, d\xi, z_-) - x0^-) & \cdot \frac{nx^-}{sx^-} \\ (x(\xi, d\xi, z_0) - x0^0) & \cdot \frac{nx^0}{sx^0} \\ (x(\xi, d\xi, z_+) - (x0^+ + sy \tan\alpha^+)) & \cdot \frac{nx^+}{sx^+} \end{array} \right\}$$

The value x(ξ,$d\xi$,z_v) is calculated according to equation 4.10. The result is common for all stereo views. The wires of the stereo views are corrected by a shift with respect to the y-position ($dn1$) and by a shift due to the different z-positions of the views ($dn2$). The shifts are performed in steps of a half a cell size cellSx/2.

$$\begin{aligned} dn1- &= (y0 - y_{mid}) \tan(\alpha^-) \cdot \frac{2}{cellSx^-} \\ dn1 &= 0 \\ dn1+ &= (y0 + sy - y_{mid}) \tan(\alpha^+) \cdot \frac{2}{cellSx^+} \end{aligned} \tag{4.12}$$

with

$$\eta_{max} = \eta + d\eta/2, \quad \eta_{min} = \eta - d\eta/2, \quad y_{mid} = 1/2 \cdot (\eta_{max} + \eta_{min}) \tag{4.13}$$

Figure 4.9 shows a schematic drawing of the calculation for $dn1+$. The vertical wires need not to be shifted. The shifts $dn1$ are performed by the LUTs 2, 3 and 4. The shift due to

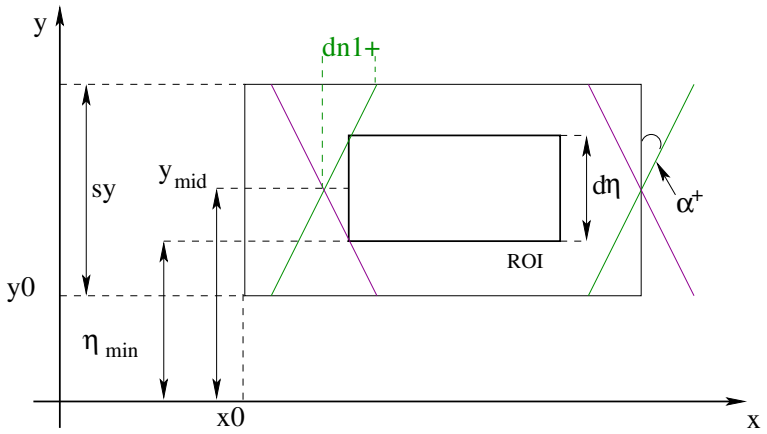

Figure 4.9: *Calculation of dn1+ due to a shift of the wires depending on the y–position.*

the different z–position of the stereo views is done in LUTs 4, 5 and 6. We briefly present the calculations:

$$\begin{aligned} dn2+ &= \Big(x(\xi, d\xi, z_+) - \Big(x0^+ - sy \cdot \tan(\alpha^+) + cellSx \cdot n1(\xi, d\xi, z)\Big)\Big) \cdot \frac{2}{cellSx^+} \\ dn2 &= \Big(x(\xi, d\xi, z_0) - \Big(x0^0 + cellSx \cdot n1(\xi, d\xi, z)\Big)\Big) \cdot \frac{2}{cellSx^0} \\ dn2- &= \Big(x(\xi, d\xi, z_-) - \Big(x0^- + cellSx \cdot n1(\xi, d\xi, z)\Big)\Big) \cdot \frac{2}{cellSx^-} \end{aligned} \tag{4.14}$$

The result is the shift relative to the leftmost wire as calculated above for all stereo views. The minimal value of $dn2$ is set to zero. The remaining combinations are shifted such that their ratio with respect to each other stays constant. Since $n1$ is the left most wire of all stereo views, the z-position of this stereo view is used in all the calculations. The extrapolated x-position of each view uses the z-position of the associated view (denoted by $x(\xi,d\xi,z_v)$).
The size of the ROI in x-direction is calculated using the opening angle $dd\xi$ and the width w of the hit cluster in the previous layer. The width w comprises up to four adjacent wires that are hit. The width $l1$ is the maximal size of the ROI of the different stereo views. The width $l1$ is calculated for the minimal z-position (measured from the target) of one of

the views. The result of $l1$ is counted in double cells. The size dl due to the range of the hit cluster in the previous layer is calculated individually for each view.
The size $l2$ is calculated depending on the extrapolation scheme, i.e. "swap" or "no-swap" case. Figure 4.10 presents the difference for the two cases:

$$l2 = 2 \cdot l1 \pm dl + h/2. \tag{4.15}$$

The final size l of the ROI is $l2$ or 31 for $n\xi = 1$. For sake of security, the width dl is added to include possible coincidences outside the lower border. The calculation takes twice the value of l1 since it is coded in double cells. The half of the height counted in number of rhombs is added for the stereo views since they contribute to size in x-direction. The half of the height h (result of LUT 10) is only added for the zero degree in the "swap" case in order to have a larger ROI and to take into account eventually hit wires at the boundary. For the "swap" case, the start of the ROI is calculated from the upper boundary (i.e. the end). The "swap" case implies another complication at the beginning of a TFU region. If the size of the ROI is larger than the distance from the start of the ROI to the predicted upper boundary of the ROI the calculation of the first wire fails. The result is a wire number exceeding 384 which leads to an invalid address of Wire Memory (the so called "negative n–problem").

If a predicted ROI exceeds a range in x-direction of 32 wires an additional message

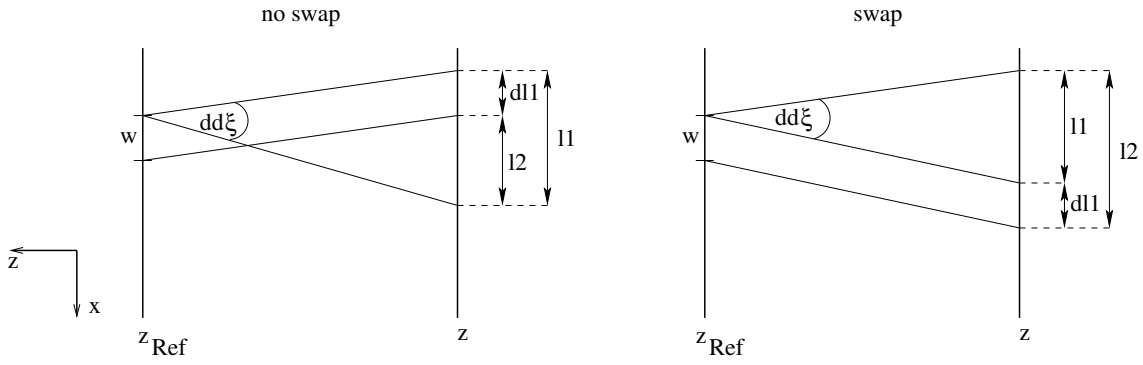

Figure 4.10: *Calculation of l2 for "swap" and "no-swap" case. In the "swap" case the projected width dl of the hit cluster is added for sake of security.*

is generated and sent to the following layer. The parameter $n\xi = 1$ indicates a second message. The size of the ROI is set to 32 wires in the case of $n\xi = 1$. The calculated size which is the result $l2$ of the LUT is added to the 32 wires. Hence, the maximal size of an ROI is 64 wires.
The determination of the size of the ROI in x-direction needs also the information of its size in y-direction. The message parameter η represents the middle of the ROI in y-direction. The height h is determined by the number of rhombs above and below of η. The limits on top and bottom are the TFU borders, respectively since it can happen that the ROI on the specific superlayer covers more than one TFU. The height h is calculated by the following parameters:

$$\begin{aligned} h_{cross} &= cellSx/\tan(\alpha_{stereo}) \\ n_{bottom} &= (\eta - 1/2 \cdot d\eta - y_{cross})/h_{cross} \\ n_{top} &= (\eta + 1/2 \cdot d\eta - y_{cross})/h_{cross} \end{aligned} \tag{4.16}$$

The size of the ROI in y-direction depends on the pitch and the stereo angle of the detector. The ROIs calculated for the muon system are smaller in y due to the larger stereo angle compared to the outer tracker. Figure 4.11 shows the principle of the calculation. The

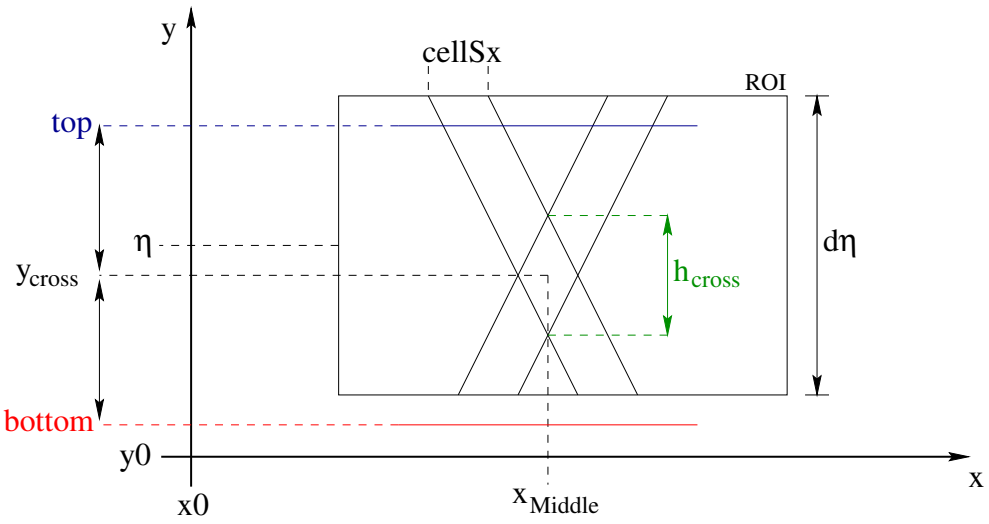

Figure 4.11: *Calculation of h. h_{cross} represents the height of a rhomb. The expected position of the track is denoted by x_{Middle}. The number of rhombs to top and bottom determine the result of h.*

values n_{bottom} and n_{top} are the number of rhombs to lower and upper boundary, respectively. The height of a rhomb is denoted by h_{cross}. Table 4.2 summarises the result h with respect to the number of rhombs: The result of h is used as an input to calculate $l2$ and in addition

n_{bottom}	n_{top}	h
< 1	< 1	0
< 2	< 1	1
< 1	< 2	2
> 2	> 2	3

Table 4.2: *The result of the h calculation performed by LUT 10 as a function of the number of rhombs to the upper and lower boundary, respectively.*

serves as input for the Coincidence Matrix which uses this information for the search for coincidences (see section 4.2.3).
The "shift flag" sf is only needed for the first muon layer MU 1. It is used to correct the shift of the crossing point of the stereo wires with respect to the vertical wire. It is not yet

implemented in the tracking algorithm.
The first wire of each ROI of the associated stereo view is determined by:

$$n2 = n1 + \frac{dn1 + dn2}{2}. \tag{4.17}$$

The final ROI is determined by n and $l2$ which are calculated differently for "no-swap"

$$\begin{aligned} n &= n2 \\ n &= n2 + l2,\ n\xi = 1 \end{aligned} \tag{4.18}$$

and "swap" case:

$$\begin{aligned} n &= n2 - l2 \\ n &= n2 - l2 - 32,\ n\xi = 1 \end{aligned} \tag{4.19}$$

The case of $n\xi = 1$ is treated in an additional step which returns n for the first message and the correctly shifted first wire for the second message according to the "swap" and "no-swap" case as shown in equations 4.18, 4.19. For the $\alpha = 0$ wire memory (WM 0) this value is forwarded to the update step in order to get the actual ξ position of the Matrix.

4.2.2 The Wire Memory

The Wire Memory (WM) is connected to each of the stereo views and stores the hit information of up to 384 wires. The bunch-crossing number is used as an address key to access the information of an event.
The calculated first wire n defines a local address in the WM of the corresponding view. The size of the ROI l is added and defines the end address. The maximal allowed range is 32 wires. If the ROI is larger than 32 wires a second message is generated that covers the range larger than the 32 wires. An additional start and end inside the WM is defined by the second message. The wire range that is extracted from the WM is a projection of the hits onto the x-axis: the hits are represented by a 32-bit pattern. The input to the Coincidence Matrix are one or –in the case of $n\xi = 1$ both– wire ranges.
The last muon layers (also referred to as pad layers), MU 3 and MU 4, have only vertical wires. All the wires of one pad layer are subdivided in three ranges comprising less than 384 wires and are assigned to a wire memory. To avoid inefficiency, a small overlap is created between the different ranges which means that wires are mapped to two wire memories. The TFU is then operated in a different mode (see section 4.3).

4.2.3 The Coincidence Matrix

The Coincidence Matrix (CM) looks for triple hit coincidences in the bit pattern (i.e. the calculated ROI) that are the output of the Wire Memory. In case of the muon layers MU 3 and MU 4, the CM forms only a logical "or" of all hits inside the ROI. Each hit leads to the generation of a message. Figure 4.12 presents the realisation of the Coincidence Matrix.

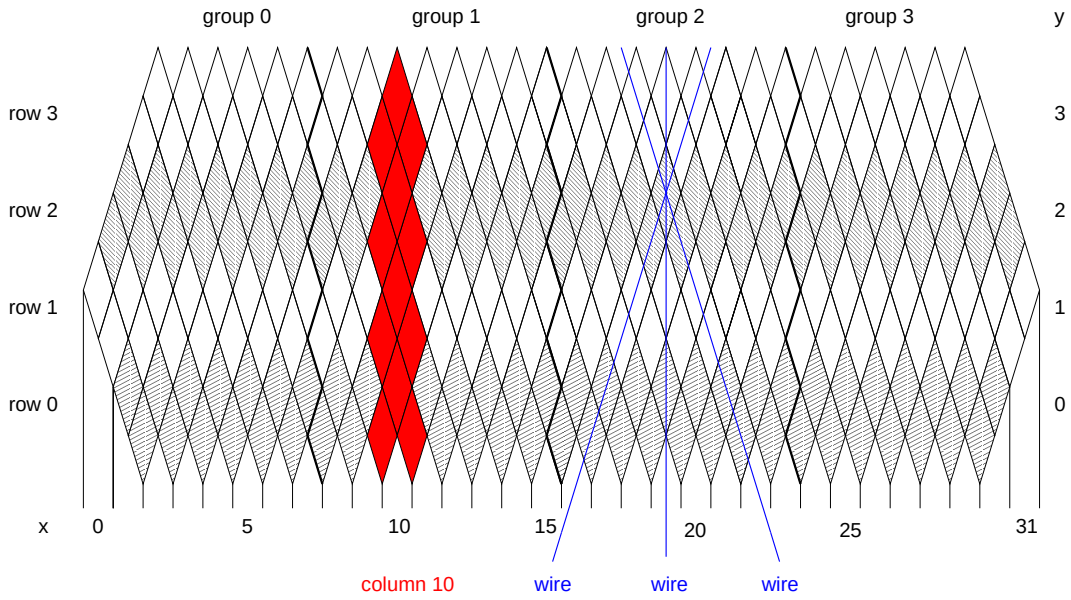

Figure 4.12: *Realisation of the Coincidence Matrix. The lines indicated by "wire" show the wire position. The rhombs indicate the sensitive area (± half of the pitch) around the wire. The Coincidence Matrix is subdivided into groups, rows and columns. Column 10 shows the combinations of wires that form a coincidence.*

The assumption for the drawing of Figure 4.12 is that a particle that passes a wire in a difference of half a pitch causes a hit for that wire. The rhombs represent this sensitive area. The horizontal width of a rhomb represents the sensitive area for the vertical wires. The Coincidence Matrix looks for triple hit coincidences in the hit information of the detector which is stored in the Wire Memory. The hits in the detector are projected onto the x-axis in such a way that it is sufficient to generate and check a bit pattern for triple coincidences. A triple coincidence found in the outer tracker layers or the first muon layer forms the basis for the tracking of the FLT since it is a precise measurement of the track position. The found coincidence marks the start of the extrapolation of the ROI onto the successive superlayer.
The Coincidence Matrix is subdivided into four groups in x-direction and divided into four rows in y-direction. Each group consists of eight columns. A column represents four times three possible coincidences with different y-position but same x-position that can be detected. If a track has hits in three stereo views and the hits form a coincidence like shown in Figure 4.12 (column 10) the track is found and updated. The conditions that lead to a coincidence can also be seen from Figure 4.12. The maximal allowed difference between two wires of different stereo views is four which is shown by the top most rhomb of column 10 in Figure 4.12. For the same rhomb the maximal distance between the associated vertical wire and one of the stereo wires is two. Four successive wires that are hit are combined to one cluster.
One of the input parameters to the matrix is the height h which was presented in section 4.2.1. The CM looks for coincidences in y-direction (i.e. the rows) depending on h: For $h = 0$ the matrix only checks the rows 1 and 2, for $h = 1$ the rows 0, 1 and 2 are checked, for $h = 2$ the rows 1, 2 and 3 are revised and for $h = 3$ all rows are revised.

The search for coincidences in groups of the x-direction does not depend on any additional input parameter.
The output of the matrix is the position i_M of the first wire of a found coincidence, the cluster width k_M and a bit pattern y_M which gives the y-position of the found coincidences. A flag $f0$ indicates if a coincidence was found. The values i_M, k_M and y_M are needed for the extrapolation in x- and y-direction [TFU99].

4.2.4 Prediction of the next ROI and Message Update

The next general step is the extrapolation of the track region to the next superlayer, to predict the ROI there. The knowledge of the next ROI determines the target TFU(s) and where to transmit the output message and update the message parameters. The output parameters are marked by a prime like ξ', coordinates in the system of the matrix like ξ_M and coordinates in the local TFU frame ξ_l. To determine the x-limits of the next ROI one has to consider two constraints:

- The geometrical boundary as given by the magnet. Figure 4.13 shows the maximal allowed slope. For muons in TC 2 and the muon system a correction due to multiple scattering needs to be added. The endpoints of the hit cluster ξ and $(\xi - w)$ at the reference superlayer and the actually found hit cluster (i_l and i_{kl}) are an additional geometrical constraint (see Figure 4.14). i_l is the number of the wire of the cluster calculated from the Matrix output i_M and the wire number n of the start of the ROI taken for the vertical wires (content of WM 0). i_{kl} is the number of the last wire of the cluster calculated with respect to n of WM 0.

- The kinematical constraint is given by the minimal and maximal slopes of tracks compatible with the momentum P of the message which is available from the pre-trigger.

Whichever of the two slope boundaries is more restrictive has to be used to obtain the x-limits of the next ROI. First the geometrical limits in terms of the slopes from ξ and $\xi - w$ are determined: $d\xi_1$ and $d\xi_{max,1}$. The calculation of the kinematical slope limits and the decision which of the two cases holds is done in one LUT step. This step needs w

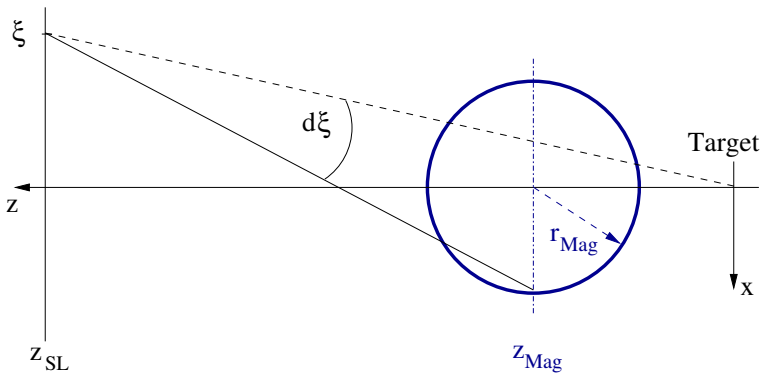

Figure 4.13: *Geometrical boundary for the predicted track slope $d\xi$.*

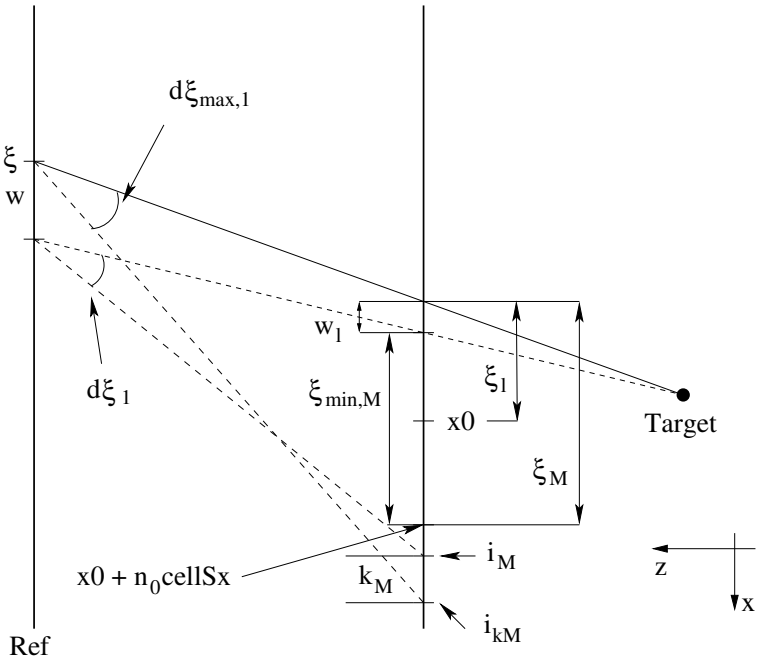

Figure 4.14: *The calculation of the new minimal and maximal track slopes. The restriction for the slopes to match with the hit cluster is shown. The offsets ξ_M, ξ_l, and $\xi_{min,M}$ used to transform the hit from matrix coordinates to global ones.*

(matrix output k_M), the size of the hit cluster in the previous layer since the geometrical and kinematical slope limits have to be taken at the opposite side of the hit cluster. The size of the hit cluster w is updated in TC 2 for the last time. The TFUs of all successive outer tracker layers only forward w.
The prediction of the next ROI and the message update can be subdivided into several groups. First, a transformation to local coordinates is done. Next, the track slopes are calculated. The parameter η is updated depending on the superlayer. The final groups are the addressing of the destination TFUs and another coordinate transformation.

Transformation to Local Coordinates

The calculations are performed only on data contained in the message to prepare the update step. They run in parallel to the matrix operation. ξ_l is calculated by LUT12/13. ξ_l is the coordinate of the first stored point in the coordinate system of the TFU. It is the projection of ξ onto the following layer along the straight line to the target. It represents the start of a TFU region (x0) in local coordinates. For the calculation of the start of the ROI in local coordinates ξ_l needs to be inverted (ξ_l is negative in Figure 4.14). In fact, a subtraction is necessary to obtain ξ_M but in the hardware it is realised as an adder. The start ξ_M of the ROI in local coordinates is determined by

$$\xi_M \ = n_0 + \xi_l \tag{4.20}$$

and marks the origin of the matrix coordinate system. The width w of the hit cluster is projected onto the current layer and is called w_l. The lower boundary $\xi_{min,M}$ of the

reference point (ξ - w) in local coordinates is calculated by LUT 17/18 and is expressed by:

$$\xi_{min,M} = \xi - w_l. \tag{4.21}$$

Calculation of Track Slope

The calculation of the new track slope is performed within the geometrical or kinematical limit which are determined by (LUT 24):

$$\begin{aligned} d\xi_{kin} &= \frac{A}{p \cdot z_{curr}}, \quad A = 302.4\ GeV \cdot cm \\ d\xi_{geo} &= \frac{|\xi| + r_{Mag}}{z_{curr} - z_{Mag}}. \end{aligned} \tag{4.22}$$

The calculations of the upper point of the cluster i_{kM} as well as the calculation of the start i_l and the end i_{kl} of the cluster with respect to the start of the TFU region are performed by adder operation.
The new slopes $d\xi_1$ and $d\xi_{max,1}$ are determined by geometrical boundaries only (refer to Figure 4.14 for details). The lower bound of the ROI is given by $d\xi_1$ and the upper bound is given by $d\xi_{max,1}$ (for the "no-swap" case). Both slopes are determined from matrix coordinates. Two LUTs (29/30) perform a comparison of these track slopes to the track slopes determined by kinematical restrictions. For the outer tracker layers PC 1, PC 4 and TC 1 the geometrical boundary is chosen. The decision whether the new slope points to the upper or lower boundary ("swap" or "no-swap" case) is taken by another LUT step (LUT 35). The calculation of $d\xi_{max}$ is only needed for the destination calculation.

Update of η

The message parameter η is only updated in MU 1. The update of η is done in LUTs (26/27) based on the parameter y_M from the Coincidence Matrix. The layers MU 3 and MU 4 only forward the η information of the pretrigger. The outer tracker layers code the η information with respect to the reference layer for the following layer.

Addressing of destination TFUs

Since a TFU is connected to several TFUs of the target superlayer it is useful to determine destination TFUs which have an overlap with the predicted ROI. This reduces the message load in the network and avoids the negative n problem. In a first step, the possible destination TFUs are determined from the available y-information (coded as η). There are four defined reference points to be able to distinguish the six possibilities of overlap with TFUs for a track (see Figure 4.15). The TFU borders in y-direction overlap slightly which is necessary for tracks that eventually belong to two TFUs. The lower border belongs to the upper TFU and vice versa (see Figure 4.15 right). The overlap of TFUs is calculated from the actual geometric configuration. A crossing from the +y half to the -y half is not foreseen in the network.
In x-direction, the lower and the upper edge are calculated which determine the TFUs that need to be addressed. The lower (ξ_{min}^{next}) and upper (ξ_{max}^{next}) border are determined by the

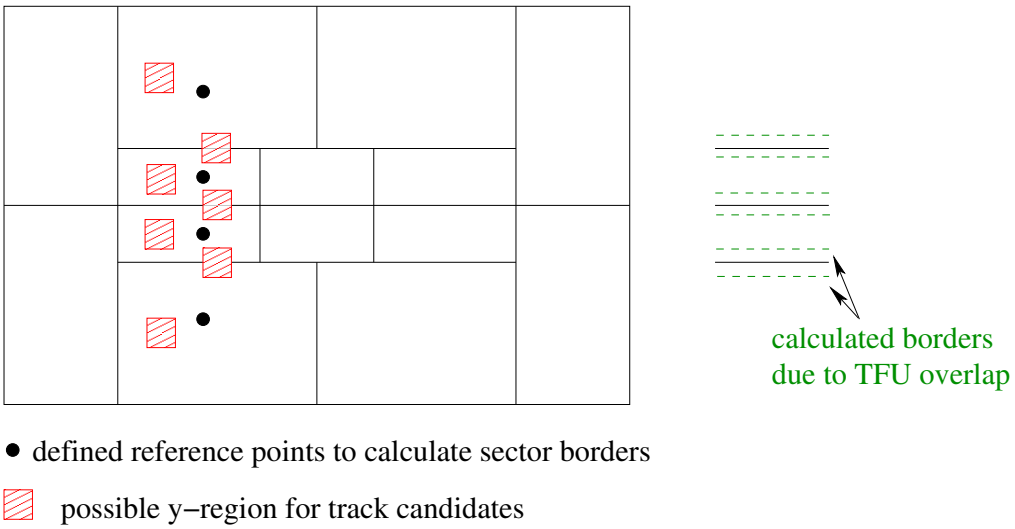

Figure 4.15: *The defined reference points (circles) and the possible overlaps of TFUs (squares) for a track. Right: Overlap of TFU regions. The lower border belongs to the upper TFU and vice versa. The solid line represents the sector of a TFU.*

final track slope $d\xi'$ and the maximal track slope $d\xi_{max}$ taken at the x-position of the start (i_l) of the hit cluster and at the x-position of the end (i_{kl}) of the cluster (LUT37/38).

$$\begin{aligned} \xi_{max}^{next} &= ((i_{kl}+1)\cdot cellSx)\cdot\frac{z_{next}}{z_{curr}} + d\xi'\cdot(z_{curr}-z_{next}) \\ \xi_{min}^{next} &= (i_l\cdot cellSx)\cdot\frac{z_{next}}{z_{curr}} + d\xi_{max}\cdot(z_{curr}-z_{next}) \end{aligned} \tag{4.23}$$

The index "next" refers the position on the following layer and index "current" refers to the actual layer.
A destination identifier TDI (a number between 0 and 7) is assigned to each TFU. The x-information together with the information which TFUs need to be addressed in y is combined into two bit patterns (one for the lower and one for the upper border). Both patterns are combined to the final destination $DEST' = DEST1$ OR $DEST2$. If a message arrives with a $DEST$ pattern that does not have the bit at position TDI according to the identifier set to one the TFU ignores (i.e. does not start to process) this message.

Transformation to Global Coordinates

Finally some steps to code the parameters in global coordinates are still needed. The value of ξ for the following layer is calculated from i_{kl} according to (LUT 31/32):

$$\xi' = (x0 + cellSx\cdot(i_{kl}+1))\cdot\frac{z_{ref,next}}{z_0}. \tag{4.24}$$

z_0 is the z-position of the of the 0° layer. The result of ξ' as well as the width w are only determined for the layers of the muon system and TC 2. The remaining layers of the outer tracker simply forward the values.

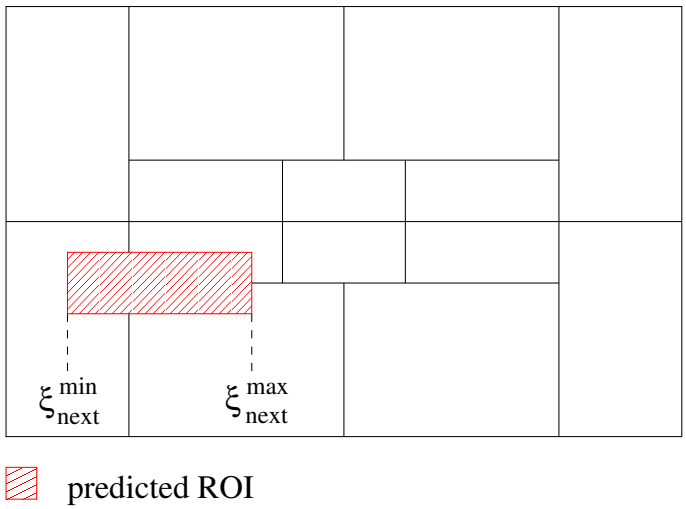

Figure 4.16: *Determination of the destination TFUs in x-direction. The lower and upper border of the ROI are calculated by the maximal ($d\xi_{max}$) and the updated ($d\xi'$) track slope.*

Finally, the opening angle $dd\xi$ in x-direction is calculated from the track slopes $d\xi'$ and $d\xi_{max}$(LUT39/40).

$$dd\xi' = (d\xi_{max} - d\xi') \cdot (z_{Ref} - z_{Next}) \tag{4.25}$$

If the range of $dd\xi$ is exhausted the counter $n\xi$ is used to code that more then one ROI has to be searched the next time and the size of the last ROI is stored in $dd\xi$ (all others are maximal sized). $n\xi$ is set to one if $dd\xi$ divided by an average cell size of the destination superlayer exceeds 32. The modified parameters as well as those bypassed to the tracking algorithm are put in the message and sent to the destination.
All calculations involved in the processing of a TFU are listed in appendix C.

4.3 The Implementation in Hardware

The TFU is realised as multilayer board with 14 layers and has a size of $36 \times 40\ cm^2$. The board is controlled by an on-board CPU MC 68020 from Motorola with 4 MB storage. The TFU is clocked with 50 MHz. The communication with the CPU happens by VME bus. Parameters of the TFU can be readout or set by accessing registers on the CPU. Sensors that record voltages and temperatures can be accessed in this way, too. Each TFU needs to be set to a specific run mode since they are connected with different types of detectors. The run mode is assigned to a register on the CPU. The run-mode determines the action of the Coincidence Matrix which is different for superlayers with stereo views and for the last two muon superlayers MU 3 and MU 4.
The tracking algorithm as described above is realised in a synchronous pipeline. A pipeline consists of several pipeline steps. The output of a pipeline step forms the input of the following pipeline step. One pipeline step takes one clock cycle (20 ns). The variables of the calculations are modified in each pipeline step. Each modification is done by LUT or logic operation as shown in Figure 4.7). In total, the processing of the TFU takes 19 pipeline steps ($\approx$ 400 ns). The first three pipeline steps are used to calculate the current

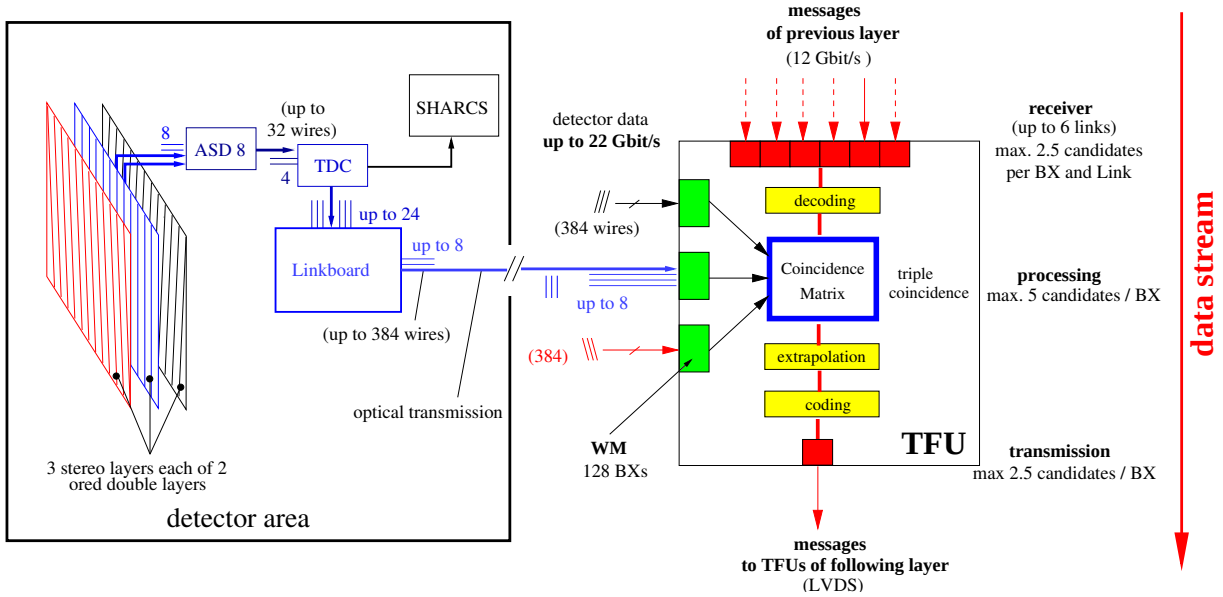

Figure 4.17: *The signal of a hit wire is shaped by the ASD 8 amplifier. The drift time in formation is digitised by the TDC board. The Linkboard converts the input from the TDC for optical transmission. The hit information is stored in the Wire Memory of the TFU. The messages from the previous layer contain the information of the ROI. If a coincidence is found the message is updated and sent to next layer. [Fla01]*

ROI. The detector data are read out from the Wire Memory during the pipeline steps 4 to 6. The logic of the Coincidence Matrix is very complex and needs several pipeline steps (7 to 15). The final pipeline steps are needed to calculate the update and to predict the ROI for the following layer.

The values needed by the pipeline processor are stored in LUTs. The advantages of using LUTs for the calculations are the flexibility to adapt the system to a changed setup and the short time for a calculation (it only takes the time of one pipeline step). The time consuming calculations are done beforehand and only stored in the LUTs. The total size of the LUTs is limited to 2 MB.

The detector data arrive at the TFU via optical links. In total, a TFU can handle up to 24 optical links which sums up to a data rate of approximately 22 Gbit/s. The data are stored in the Wire Memory and addressed by the BX number. The Wire Memory is realised by six identical ASIC (Application Specific Integrated Circuit) chips. Besides the memory, the logic to read and write simultaneously is also housed in the ASIC (it is a dual-port-memory). The pipeline processor reads out the data for the corresponding ROI. The Coincidence Matrix (CM) is subdivided into groups, rows and columns for the purpose of processing. The CM looks for coincidences. The found coincidence is serialised and transformed into a message. If more than one coincidence is found, the previous pipeline steps are stalled until the serialisation is completed. More on the CM can be found in [TFU99].

The communication with TFUs of the following layers happens by the Message Board which is plugged to the backside of the VME backplane. The clock of the Message board

is only half of the TFU clock: 25 MHz. In total, there are four input receivers for TPU and TDU and six receivers for the TFU. Each board has only one transmitter. The input and output is FIFO buffered (First In First Out, a piece of memory that decouples input and output which are processed asynchronously). The FIFO is needed since it can happen

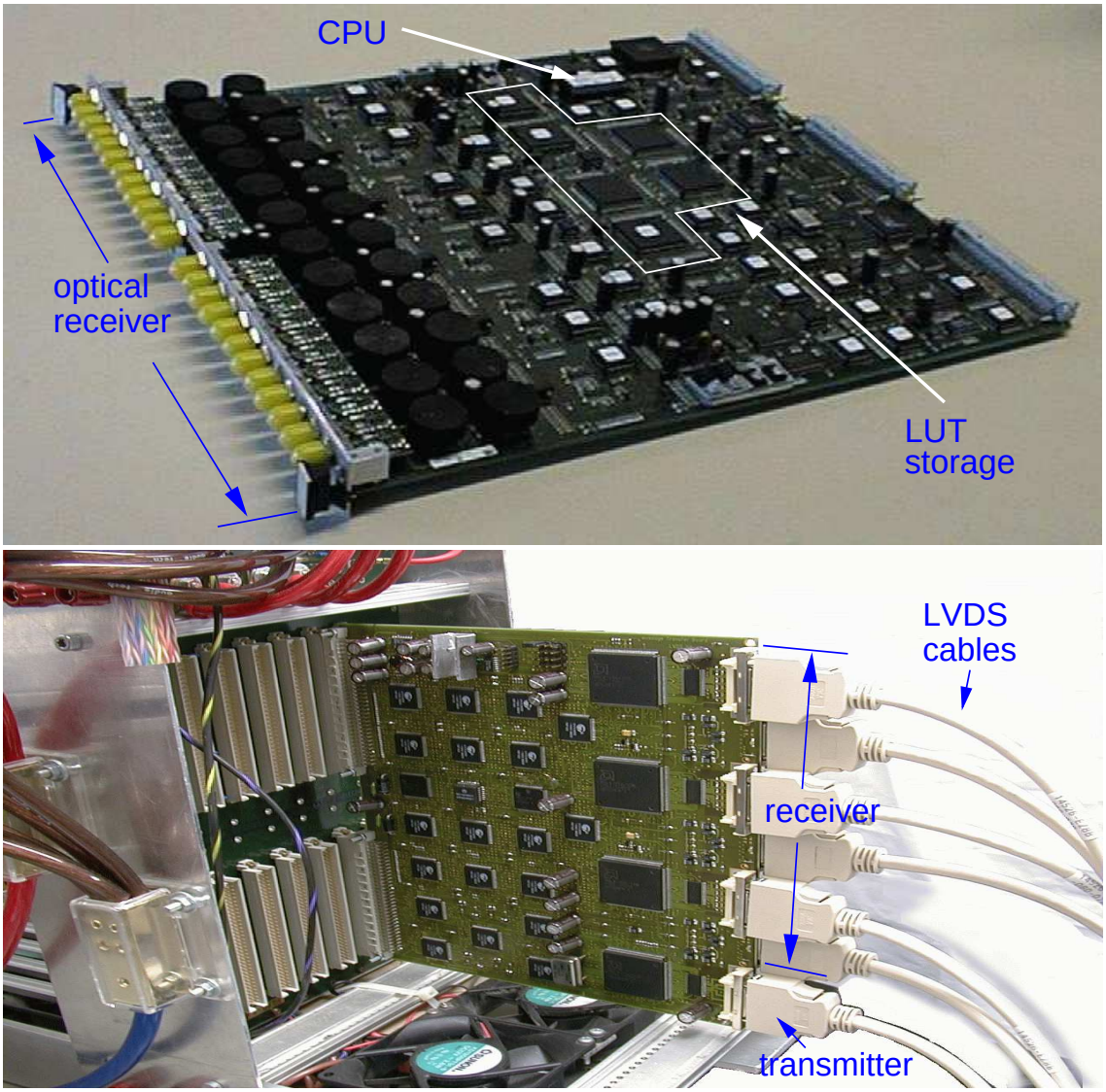

Figure 4.18: *Top: TFU processor board. The optical receivers can be seen on the left. Bottom: Message Board plugged to the backside of a VME crate. The transmitter is located at the bottom of the board. Above, the six receivers are installed.*

that more messages arrive at one TFU (or at the Message Board) than the TFU is able to process in the time of one BX. The same argumentation holds for the transmission of messages to another TFU due to the different clock cycles. Details of the Message Board can be found in [TFU00].
Figure 4.17 summarises the purpose of the TFU. The detector data arrive via the optical link and are stored in the Wire Memory. Messages arrive from the pretrigger or from the previous TFU and contain the information of an ROI. The TFU first calculates the ROI

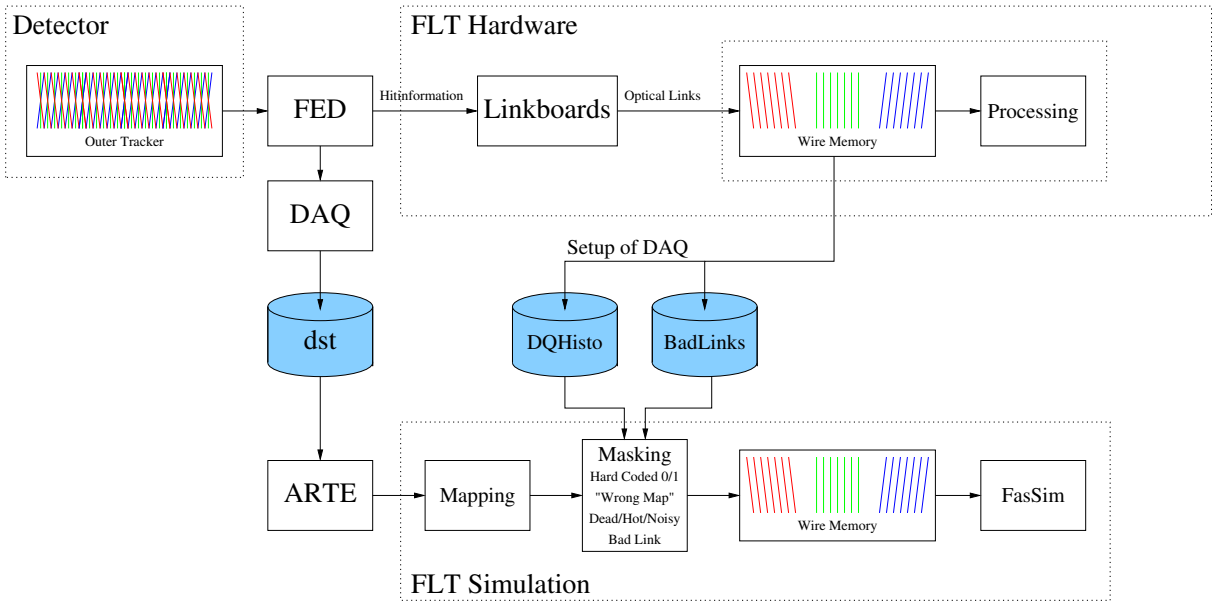

Figure 4.19: *The architecture of the FLT simulation and how it reflects the hardware. [Noe01]*

and extracts the detector data from the Wire Memory. Second, the Coincidence Matrix looks for coincidences. If a coincidence is found the message is updated and transmitted by the Message Board to the destination TFU(s). Figure 4.18 shows the TFU and the Message Board hardware

4.4 Simulation Framework

In this section, we discuss the simulation of the FLT. A sketch of the architecture is shown in Figure 4.19. The trigger simulation –from now on called FasSim (Fast Simulation)– can be used in various setups and with different kind of inputs. It is built in such a way that it can run in stand-alone mode and inside the analysis and reconstruction program ARTE of HERA–B [Art96].
The input can be read from Data Summary Tape (DST) files. It is possible to process either data taken by the HERA–B data acquisition system or Monte Carlo events. In addition, there is the possibility to read DAQif (Monte Carlo events in DAQ format) files and process them. The simulation reflects all the aspects as needed in the real hardware.
At start up, all the connections between the boards are initialised. The connections from the detector to the input of the TFUs (mapping) are created. The connection from FED to TFU as realised in hardware is read from the mapping file. The hit data are taken from the DST file. Before the hits are set as a bit pattern for the TFU of interest, different “maskings” can be applied that reflect problems with trigger or detector hardware encountered during the run:
The channels that were or have to be masked are read from data quality histograms. After all maskings have been applied, the hit pattern (i.e. the wire memory of the TFU) is made available to FasSim. FasSim offers the possibility to call the Muon or ECAL Pretrigger

simulation [Ada01a, Fla01]. This provides the input to start the simulation of the TFU network. The TFU is simulated bitwise and uses either already existing Look Up Tables (LUTs) or the functions that are used to generate them. To calculate one specific value all the needed LUT functions are called recursively. All calculations and results of each pipeline step are accessible in the FasSim framework.
FasSim assigns to each message at generation a time stamp which is a useful information if this message arrives in the allowed time frame (i.e. 103 bunch crossings after the interaction took place) at the TDU. Messages that arrive later at the TDU are discarded. The time limit is chosen according to the one applied during running [Her00]. The difference between 103 BX and the allowed latency of 128 BX stated earlier is needed for the communication with the FCS and for the readout of the detector.
The TDU has a buffer for 24 messages per event that can be read out by the DAQ. This implies that not more than 24 messages per event can be sent to the SLB. It can happen in the simulation that more than 24 messages arrive. Message multiplicities larger than 24 per event are discarded by the TDU hardware.
It can also happen that one TFU of the network is still processing messages of a previous event while new messages from the succeeding event arrive. Those messages are delayed by the time when they arrive at the TFU until the old messages are processed. In the case that more and more messages arrive from succeeding events the TFU blocks one part of the network. Such a situation is referred to as message pile-up which cannot be simulated.

Chapter 5

Latency and Rate Measurements

The analysis of the year 2000 run estimated that in the muon channel 12 % of the events were lost because they arrived too late at the TDU [Her00]. We process minimum bias data from DST files with the FLT simulation to investigate the behaviour of the network and to check its latency at different interaction rates.
The load of the network in each superlayer, as well as the amount of messages via single interconnections of TFUs is analysed.
We also study the performance of the network with respect to pretrigger input. We check for differences with muon pretrigger only and in combination with the electron pretrigger. The correlation of network load with the number of hits in the RICH, in PC 2, in MU 2 and with the energy deposition in the inner calorimeter is investigated, too.
The general strategy for the analysis is to check that the data samples are completely randomly triggered to avoid any bias. We investigate the occupancy for each data set as seen by the wire memory of the TFU. We determine the deadtime of the TFU network and estimate the single-track as well as the pair trigger rate.

5.1 Analysis of the Network at 5 and 10 MHz Target Rate

For the analysis of the network load at 5 MHz target rate we chose run 14577. In total, 300000 events are analysed. In order to get sufficient statistics for the different rate estimates for 10 MHz target rate we have to use several successive runs for the analysis. The data were taken with different target wires. We check the bunch spectra of each analysed run to avoid hot bunches in any of the analysed data set which can dominate the final trigger rate. In total, we analyse 141260 events of runs 14545, 14547, 14568, 14570, 14593 and 14595 at an interaction rate of 10 MHz.
A number, the physical BX, is assigned to each proton bunch that passes the HERA–B detector. We expect for minimum bias data that all physical BXs are triggered equally, i.e. no peak at a specific value of the physical BX exists. The fluctuations in the distribution of the physical bunch crossing number (BX) as shown in Figure 5.1 are within the statistical error. The distribution of physical bunch crossing number is flat which indicates a completely randomly triggered data sample. If the data sample is not randomly triggered the results can be dominated by the contribution of such pronounced bunches.

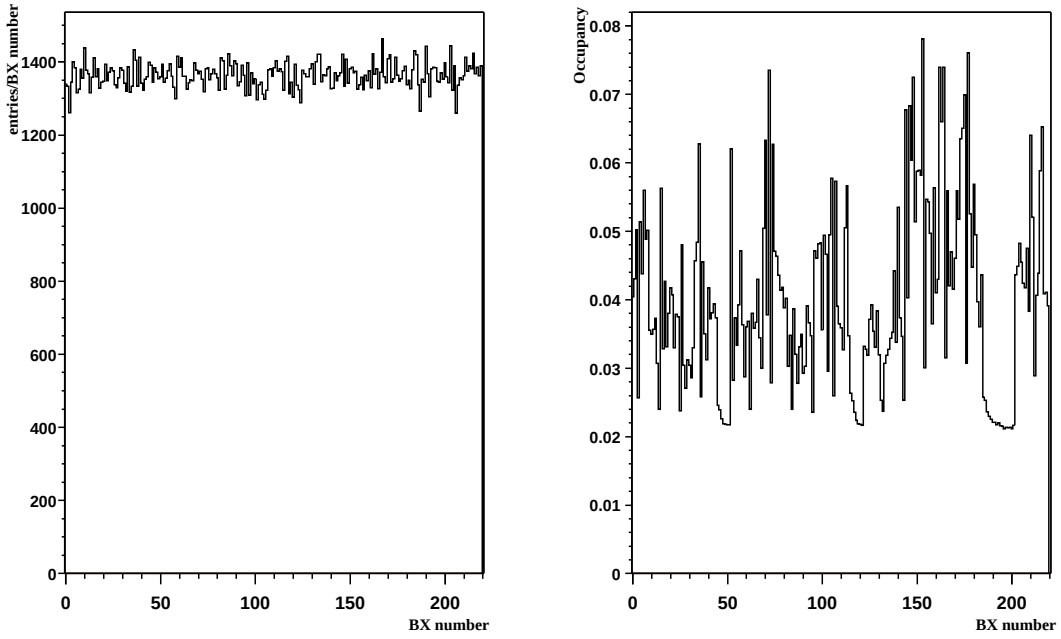

Figure 5.1: *Left: The distribution of the physical bunch-crossing number (BX) for the 5 MHz data sample. Random triggering selects all physical BXs equally. Right: The outer tracker occupancy per physical BX as seen by the FLT. The fact that the holes in the beam structure do not reach zero is due to switched on channels.*

Figure 5.1 (right) shows the bunch crossing number weighted by the occupancy of the outer tracker as seen in the wire memory of the TFUs. The expected beam structure is not as clearly evident as shown in Figure 2.1 because the link and channel masking produces a pedestal. A difference in the beam structure between the two figures is due to a different normalisation with respect to the BX number: The so called kicking gap of 20 bunches is in Figure 5.1 between BX number 180 and 200 whereas in Figure 2.1 it is at the end (BX numbers 200-220).
Figure 5.2 shows the distribution of the occupancy of the trigger layers in the outer tracker. For each event the number of hit wires with respect to the total number of wires used by the trigger is filled in a histogram. "Applied masking" refers to link and channel masking (see section 5.1.1). In total, approximately 2 % of the trigger wires in the outer tracker are switched on permanently which Figure 5.2 (left) confirms. These switched on wires are mandatory to ensure for example an equidistant spacing of the wires in the wire memory. The link and channel masking switches on additional 2 % of the wires. This explains why the histograms start at 2 % and 4 %, respectively. The average occupancy for the 5 MHz run is $(3.97 \pm 0.01\ (stat.))$ % without any masking and $(5.99 \pm 0.01\ (stat.))$ % with masking (Figure 5.2). The average occupancy for all analysed runs of 10 MHz target rate is $(5.71 \pm 0.01\ (stat.))$ % without any masking and $(6.40 \pm 0.05\ (stat.))$ % with masking. The occupancy varies between 5.5 % and 5.9 % from run to run. Compared to the 5 MHz run the averaged occupancy is 45 % higher without any masking and 28 % higher with masking.
The distribution of the physical BX looks similar to the one presented in Figure 5.1. Again,

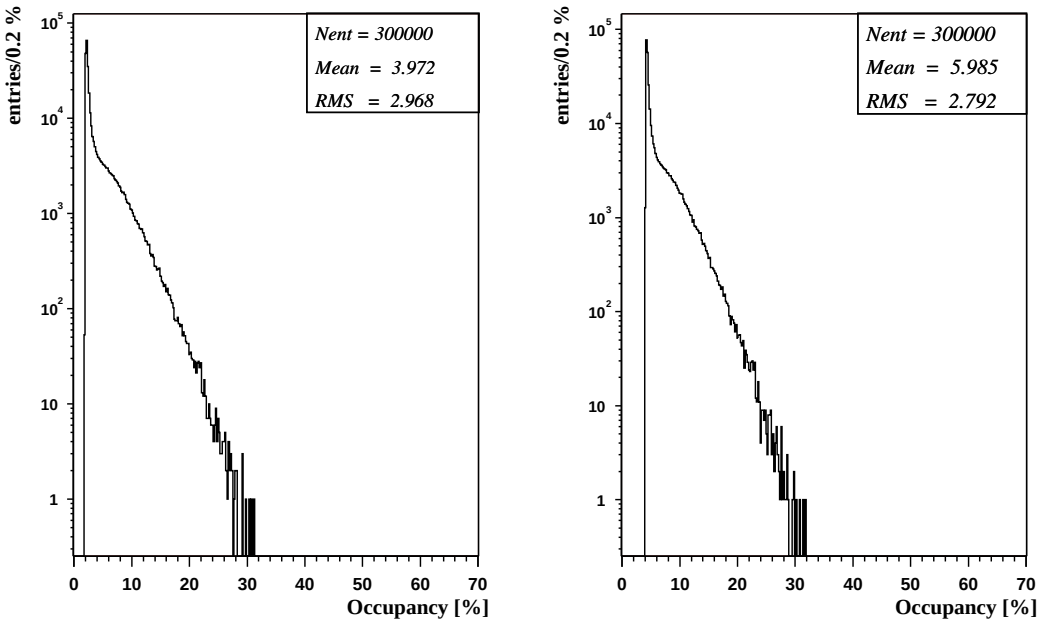

Figure 5.2: *The occupancy of all trigger layers of the outer tracker as seen by the wire memories of the TFUs. Left: No masking. Right: The masking is applied.*

the data of the 10 MHz run are taken completely random with respect to BX. The beam structure becomes more visible than in the 5 MHz run because the mean value being well above the 4 % pedestal.

For each event the number of messages per TFU and per superlayer is recorded. We use this information to figure out which TFU has to process the maximal number of messages which results in an average number for the fraction of events at which a specific TFU has to process more than 5 messages per event. This information is used to determine the latency of the system. Here it is assumed that this TFU will block the entire system if the number of messages exceeds 5. The deadtime of the system is calculated from Figure 5.3 according to the following formula:

$$deadtime \approx \left(\sum_{i>5}^{\infty} \frac{n_{entr}(i) \cdot i \cdot 20\ ns}{100\ ns} \right) / \ total\ number\ of\ entries \tag{5.1}$$

If in equation 5.1 the index i which runs over all bins of the histogram exceeds 255 the value of i is fixed to 255. $n_{entr}(i)$ is the occurrence of events with i messages at the TFU with the maximal number of messages. Formula 5.1 takes also into account the time which is needed to process all messages of that TFU. The limit of 255 for entries larger than that value arises from the fact that the FIFO depth of the Message Board is limited to 255 which means that messages exceeding the limit are not considered. The 20 ns are equivalent to the duration of one pipeline step. The 100 ns in the denominator represents a rounded value of the HERA clock (nominal value: 96 ns). The deadtime according to formula 5.1 is easy to calculate. If the result is small we conclude that there is no problem with respect to deadtime. The deadtime which is determined in this analysis covers only the deadtime caused inside the TFU network. The TDU operated in pair trigger mode can

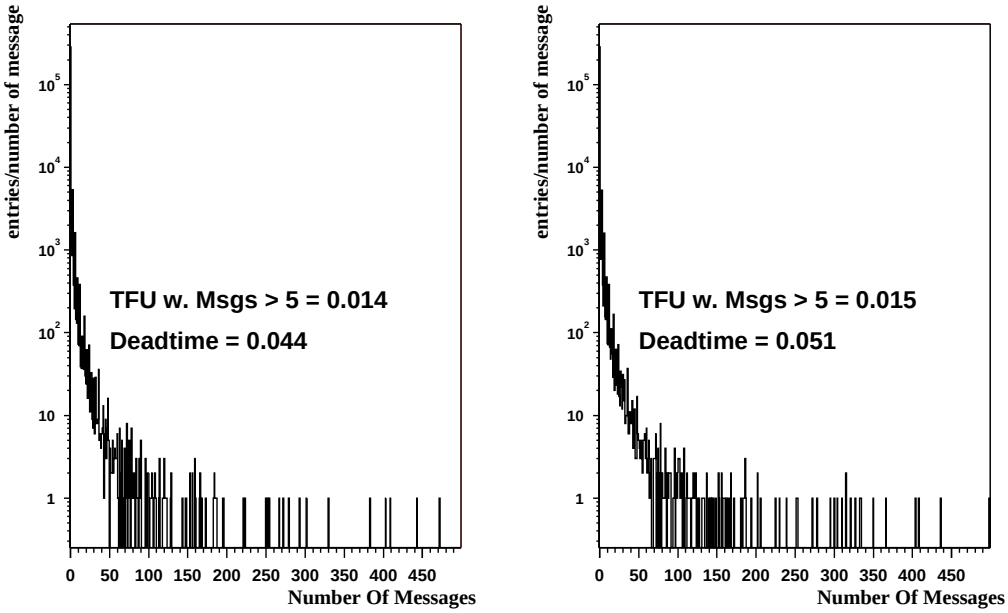

Figure 5.3: *The maximal number of messages arriving at a TFU per event and the calculated deadtime for the 5 MHz interaction. Left: Without masking the deadtime is 4.4 %. In 1.4 % of events a TFU has to process more than 5 messages. Right: With applied masking the deadtime is 5.1 %. In 1.5 % of the events a TFU has to process more than 5 messages.*

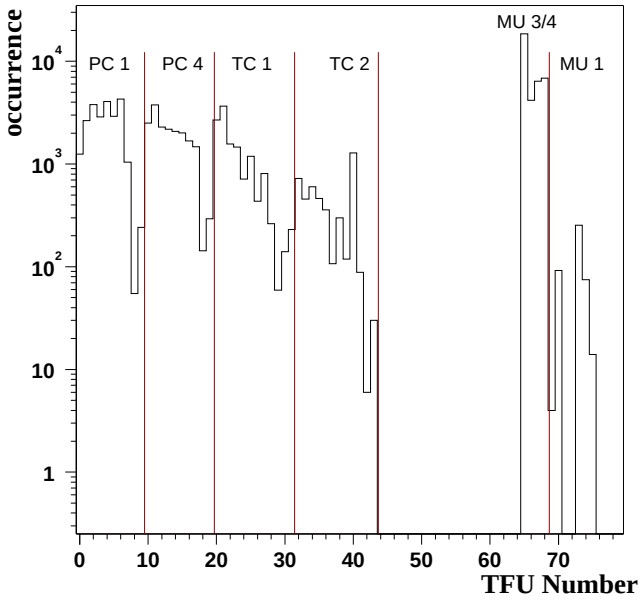

Figure 5.4: *Occurrence of the TFU of the entire network that has to process the maximal number of messages. The TFUs of MU 3/4 dominate since each hit generates a message. The TFUs 44 to 64 are foreseen for the inner tracker.*

Layer	TFU number
PC 1	0-9
PC 4	10-19
TC 1	20-31
TC 2	32-43
MU 1	69-75
MU 3	67-68
MU 4	65-66

Table 5.1: *Assignment of TFU numbers for the different trigger layers.*

also contribute to the FLT deadtime depending on how many tracks arrive at the TDU. The calculation of the invariant mass out of the combinations of up to five tracks induce no stall cycle. Any additional track that arrives at the TDU and is involved in the mass calculation increases the deadtime of the FLT [Ger00, Noe99].
Figure 5.3 shows the maximal number of messages of one TFU of the entire network per event which is used to evaluate the deadtime according to formula 5.1. The bins on the x–axis represent the maximal number of messages at a specific TFU of the network. It should be emphasised that the evaluated deadtime represents an upper limit because it is very unlikely that one TFU with more than 5 messages per event will block the entire network. Only a small part of the system will be blocked while the rest can process its data asynchronously.
In addition, the TFU with the largest number of messages is evaluated. Figure 5.4 shows the occurrence of the TFU that has to process the maximal number of messages per event. The TFUs in the muon layers MU 3 and MU 4 dominate this distribution since each hit of the wire memory that is inside the determined ROI leads to the generation of a message. The TFUs with significantly lower occurrence like TFU 9 for example are connected with the outermost areas of the detector. These areas have a lower message multiplicity since most of the tracks are found in the inner area. TFUs with numbers between 44 and 64 are foreseen to serve the inner tracker which is not yet implemented either in the hardware nor in the simulation. The underlying numbering scheme is shown in Table 5.1.

5.1.1 Effect of Channel Masking

In FasSim imperfections of the hardware are applied as masks. To arrive at different categories of maskings a large amount of data was analysed [Riu01]. Each single channel of a TFU was investigated and finally marked as dead, hot, noisy, hard coded and wrongly mapped. We briefly explain the categories:
A channel is considered “dead” if its integrated (full data sample) occupancy is less than 10 % of the mean TFU occupancy of the full sample. A “hot” channel is flagged if its mean occupancy is larger than 99 % in more than half of the analysed runs. A channel is marked “noisy” if its average occupancy is larger than 2.5 times the average TFU occupancy.
The so called “hard-coded channels” represent dead channels of the outer tracker that are switched on on the Linkboard.
Wrongly plugged cables are represented by the “wrongly mapped” channels. They could

be identified by a comparison of wire memory occupancy with outer tracker occupancy [Fla00b]. This analysis is based on a statistical comparison of both data.
The deadtime for the combined input of muon and electron pretrigger to the FLT with and without masking are

$$(5.1 \pm 0.02\ (stat.))\ \%\ \text{ and }\ (4.4 \pm 0.02\ (stat.))\ \%,$$

respectively. The increase is due to additional channels that are switched on. The amount of events for which one TFU of the network has to process more than five messages turns out to be 1.4 % without masking and 1.5 % with masking. The results stated above are the upper limit of the deadtime. Both numbers are small and consequently there is no deadtime problem at an interaction rate of 5 MHz.
The deadtime of the network for 10 MHz target rate according to formula 5.1 is averaged over the analysed runs and found to be without masking

$$(10.3 \pm 0.02\ (stat.))\ \%\ \text{ and }\ (11.1 \pm 0.03\ (stat.))\ \%$$

in the case of applied masking, respectively. The observed deadtime and the average message load per superlayer are twice the ones for 5 MHz target rate. The reasons for that difference are equivalent to one stated above. The range of the deadtime for all runs lies between 7.6 % and 12.3 % without any masking and with applied masking between 8.8 % and 13.7 %. The difference in deadtime is due to a run to run variation of the bunch spectrum. The bunch spectra of runs that cause a higher deadtime ($\geq$ 10 %) show some higher occupied bunches than runs with lower deadtime. The fraction of events for which one TFU in the network has to process more than five messages varies without masking from 2.5 % up to 3.2 % and with masking from 2.8 % to 3.4 %.
The muon messages cause a major fraction of the deadtime because of the triple pretrigger messages. Most of them are removed in MU 1 because they are clones but the ROIs get too large when they are projected onto TC 2. In those cases, the messages are split into two messages. The input from the electron pretrigger that enters the network in TC 2 increase the message load, too.
The masking which is used in our simulation is determined from runs towards the end of the year 2000 run. The detector performance became worse during the run of the year 2000. The minimum bias data were taken at the beginning of the run. A proper reproduction of the situation of this run period is not possible. The results determined with the masking are higher because of additionally switched on channels. They reflect a different behaviour of the FLT than it is without masking.

5.1.2 Correlation with Multiplicity Veto Components

In this section, we investigate if the deadtime can be reduced by a multiplicity veto at different levels of J/ψ loss.
We are interested if a correlation of the number of messages with respect to the number of hits in the RICH, in PC 2, in MU 2 and with respect to the energy deposition in the inner calorimeter exists. This information is suitable for a veto to reject high multiplicity events. If there is a correlation between those events and high load in the network it will be helpful to discard them.

Detector	1 % J/ψ loss		5 % J/ψ loss		10 % J/ψ loss	
	N_{cut}	Reject.	N_{cut}	Reject.	N_{cut}	Reject.
RICH	3795	10 %	2540	29 %	1750	51 %
PC 2	1220	10 %	790	30 %	640	44 %
ECAL [GeV]	585	10 %	425	26 %	340	44 %

Table 5.2: *Veto cuts as function of J/ψ loss and background rejection (indicated by "Reject.") determined from SLT triggered events. [Ada01]*

For each event, the number of hits in the RICH, in PC 2 and in MU 2 are counted because they are not involved in trigger actions which guarantees unbiased information. In parallel, the energy deposition in the inner calorimeter is summed up. Table 5.2 summarises the cuts in the various components for a loss of 1 %, 5 % and 10 % J/ψ candidate events (from now on abbreviated by J/ψ loss). The numbers are determined from SLT triggered data. A selection of J/ψ candidate events out of the entire event sample is done. The cuts for the veto components are derived from the distributions of hits in the RICH and PC 2 and from the energy deposition in the inner calorimeter from the J/ψ candidate events. The rejection of the background events of the SLT triggered data is determined at the different levels of J/ψ loss [Ada01]. Since we use minimum bias data for this analysis which have a different track multiplicity and occupancy than SLT triggered events we expect a different rejection of background events than stated in Table 5.2.

Figure 5.5 shows the correlation of hits in PC 2 and in the RICH with the energy deposition

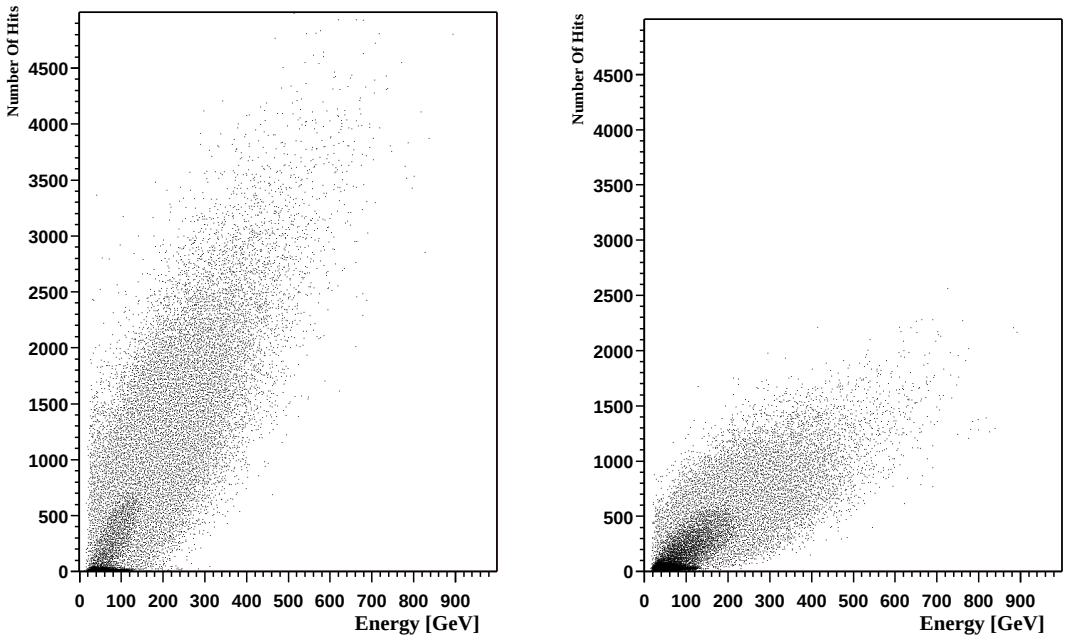

Figure 5.5: *Correlation of hits in the RICH (left) and in PC 2 (right) with respect to energy deposition in the calorimeter for 5 MHz interaction rate.*

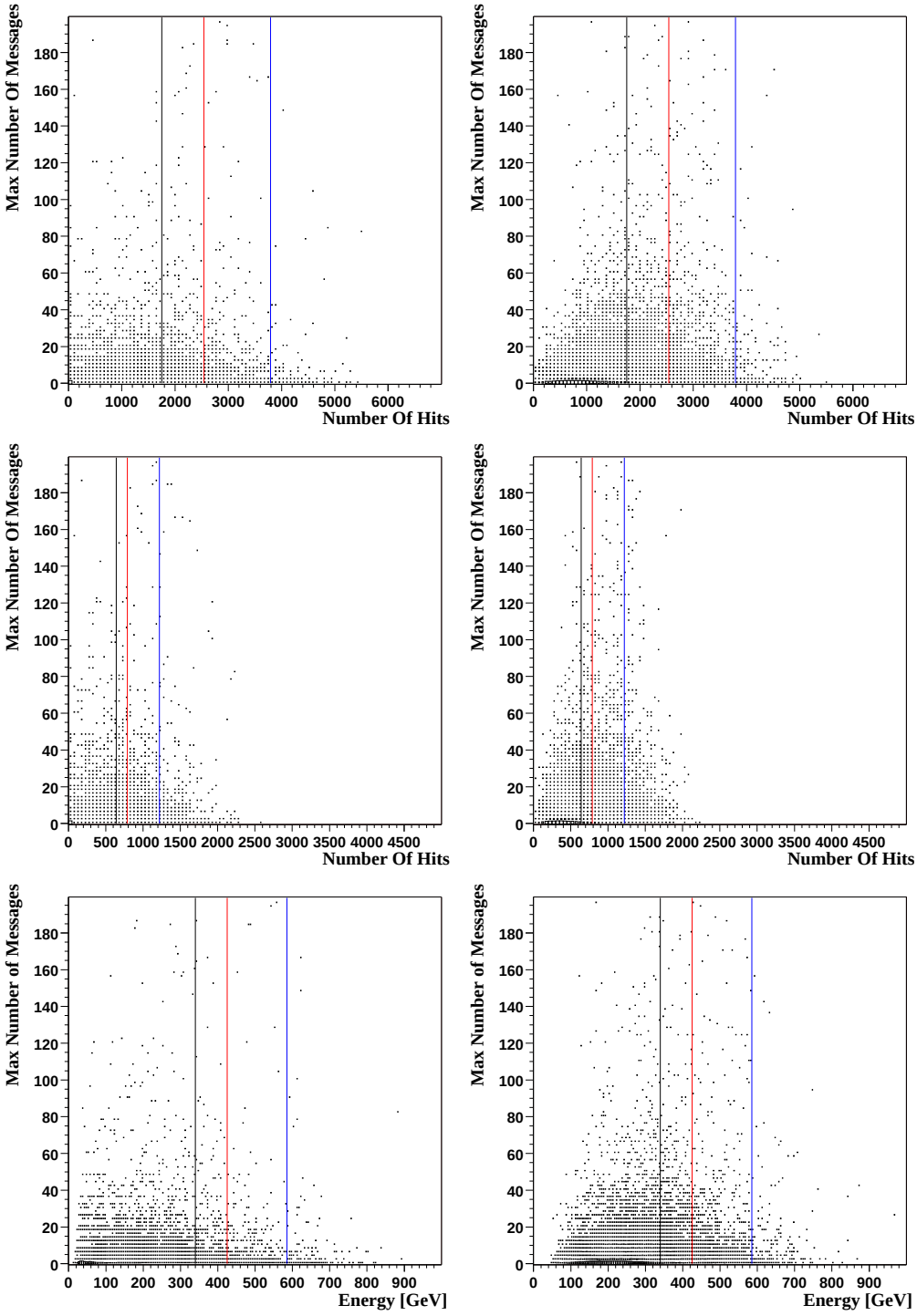

Figure 5.6: *The maximal number of messages of one TFU of the network as a function of the hits in the RICH (top) or of the hits in PC 2 (middle) or of the energy deposition in the inner calorimeter (bottom). The vertical lines indicate the veto cut at different levels of J/ψ loss. Left: The plots for a combined usage of muon and electron pretrigger. Right: The same plots for a triggered run with the ECAL pretrigger only.*

in the ECAL, respectively. We naively expect a similar correlation between the messages in the network and the hits or energy deposition. We investigated if a correlation between hits in MU 2 and the other components is evident, too. The correlation is not as clear as presented above, because of the huge amount of concrete that filters most of the particles and thus reduces the amount of hits enormously. We look at the behaviour of the FLT network. The number of messages of the TFU that has to process the maximal number of messages is plotted in Figure 5.6 (left) with respect to the veto cuts for the RICH, PC 2 and the energy deposition in the inner calorimeter. There is no clear correlation between hits and network load for a combined usage of electron and muon pretrigger.
We investigate the fact that in particular events there are only a few hits in PC 2 but more than 80 messages in the network. The reason for this are localised showers in the muon pad system. The shower originates either from the back, i.e. from the electron beam pipe or by a shower out of the concrete in front of MU 3. Each hit in the pad layers generates a message. Those messages end in MU 1 because there are no coincidences at all. We exclude that a malfunctioning electronics board causes the large amount of messages because the hits are randomly distributed throughout the wire memory of the TFU in the MU 3 or MU 4 layer. The clear correlation as presented in Figure 5.5 is not visible because most of the time one of the TFUs of the muon system has to process the maximal number of messages. These messages localised in the muon system destroy a clear correlation. The veto reduces the deadtime drastically but not all of the events with high multiplicity are rejected.
It is noted that Figure 5.6 –derived from a setup with muon pretrigger only– shows a band structure at multiples of three for the number of messages. This structure can be explained as follows: The pads are approximately 10 cm high in y-direction. The ROIs projected onto the Muon layers are too large to get handled by the TFU. In fact it is a limitation of the coincidence matrix that only covers a height of maximal 19 cm in the muon system. To avoid inefficiencies because of this limitation the muon pretrigger sends three messages with different y positions, one central, one above the central, one below the central.
We investigated the behaviour of the FLT network without the muon pretrigger to prove that the muon pretrigger weakens out the correlation. We use 38119 events of run 17163 to look for correlations. It is a triggered run taken at 5 MHz target rate. It cannot be used for rate estimates because a triggered sample is already biased and does not reflect the behaviour of the FLT as it will be in reality (i.e. without any trigger decision). The advantage of using a triggered run for the correlation plots is a reduced processing time compared to the minimum bias data. Figure 5.6 (right) shows the result. A correlation is more evident than in the case that the muon pretrigger is used. Events with very few hits or energy deposition in the detectors and high number of messages disappeared. Figure 5.7 separates the deadtime of the FLT with respect to the used pretrigger. The applied cuts on hits in the RICH and in PC 2 and on the energy deposition in the inner calorimeter are taken from the analysis [Ada01] that determines the loss in J/ψ yield. The main contribution to the deadtime of the system originates from the muon pretrigger which was expected [Ger00]. A cut at 5 % J/ψ loss in the RICH or in the calorimeter reduces the total deadtime by roughly 23 %. The reduction with respect to veto cuts in PC 2 is slightly higher and suppresses the deadtime by more than 25 %. A multiplicity veto is desirable with respect to the deadtime of the TFU network. The veto does not discard all of the high multiplicity events but it reduces the deadtime of the order of 20 %. Investigations of

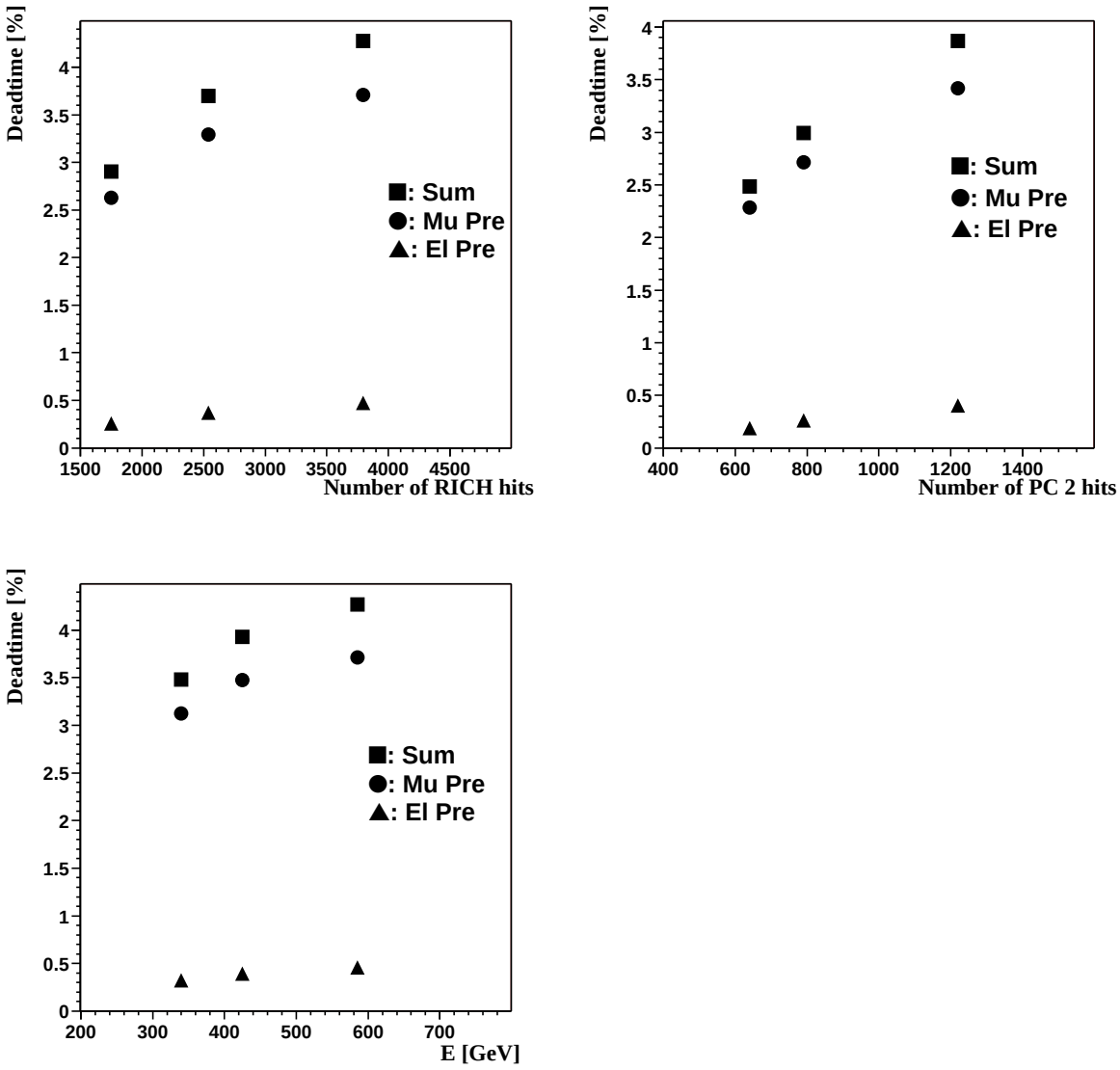

Figure 5.7: *Deadtime at 5 MHz target rate with respect to a multiplicity veto at different levels of J/ψ loss separated by the pretrigger source. Top left: The deadtime as a function of the cut on hits in the RICH. Top right: The deadtime as a function of the cut on hits in PC 2. Bottom: The deadtime as a function of the cut on the energy deposition in the inner calorimeter.*

the effect of a multiplicity veto on the trigger rate follow in the sections about the trigger rate estimate.

The reduction in deadtime for 10 MHz target rate with respect to veto cuts as shown in Figure 5.8 is of the order of more than 20 % for 5 % J/ψ loss. The reduction factor in deadtime for a calorimeter veto is less pronounced than for the RICH veto. The difference in rejection power presented here and in [Ada01] has its origin in the different data samples: in this analysis we use minimum bias data whereas in [Ada01] triggered data are analysed. The large number of messages in the system as function of hits in the RICH and PC 2 and

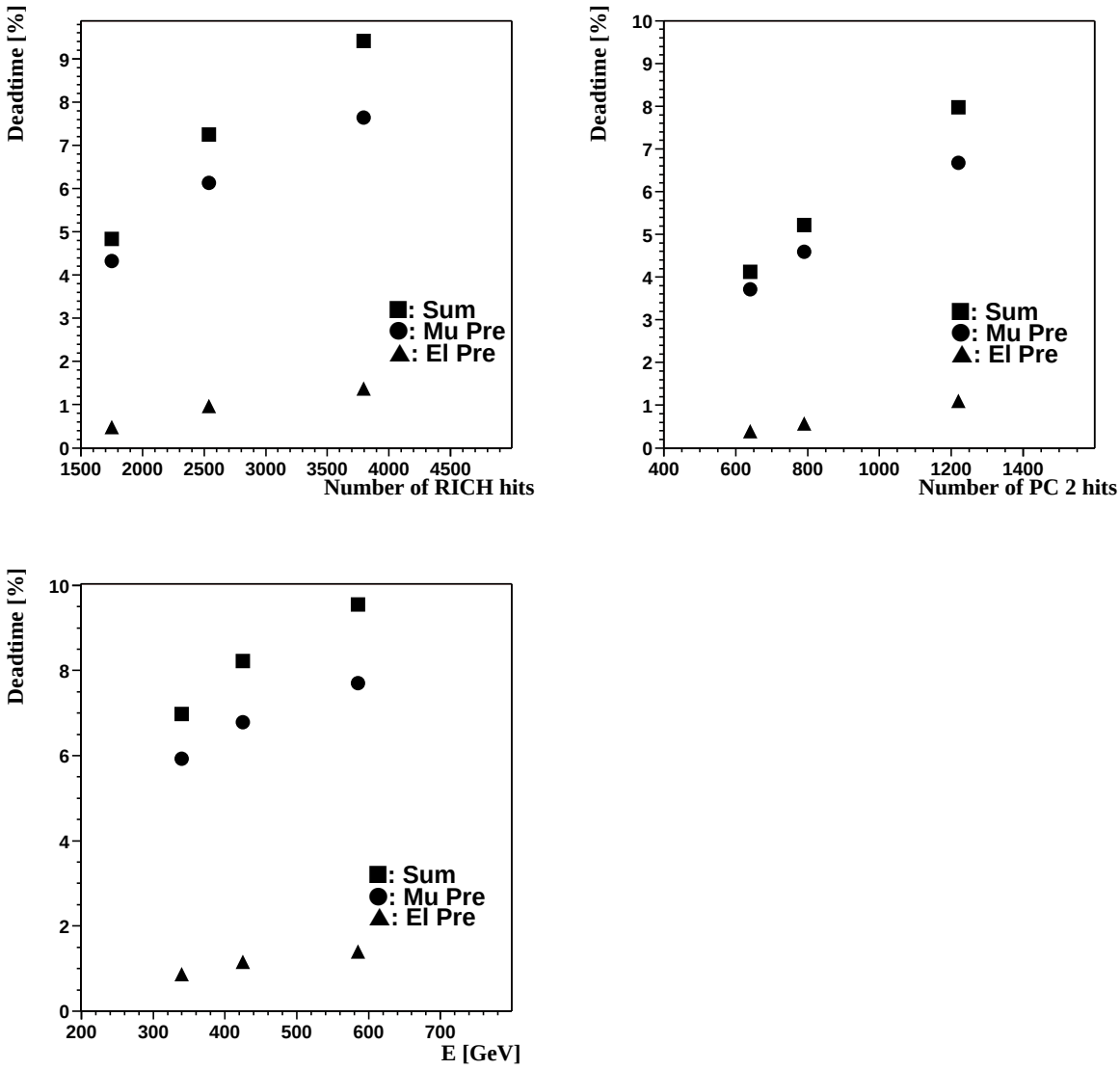

Figure 5.8: *Deadtime at 10 MHz target rate with respect to a multiplicity veto separated by the pretrigger source. Top left: The deadtime as a function of the cut on hits in the RICH. Top right: The deadtime as a function of the cut on hits in PC 2. Bottom: The deadtime as a function of the cut on the energy deposition in the inner calorimeter.*

with the energy deposition in the calorimeter is a factor 2 higher as presented in Figure 5.6. This gives a first indication that it is beneficial to reject busy events with a veto at higher interaction rates. A clear correlation as shown in Figure 5.5, however, is not visible.

5.1.3 Network Load

We also monitor the various interconnections between the TFUs in the network. This gives us the information where most of the messages travel inside the network.
In Figure 5.9 the connections between the TFUs and their load are presented. On the

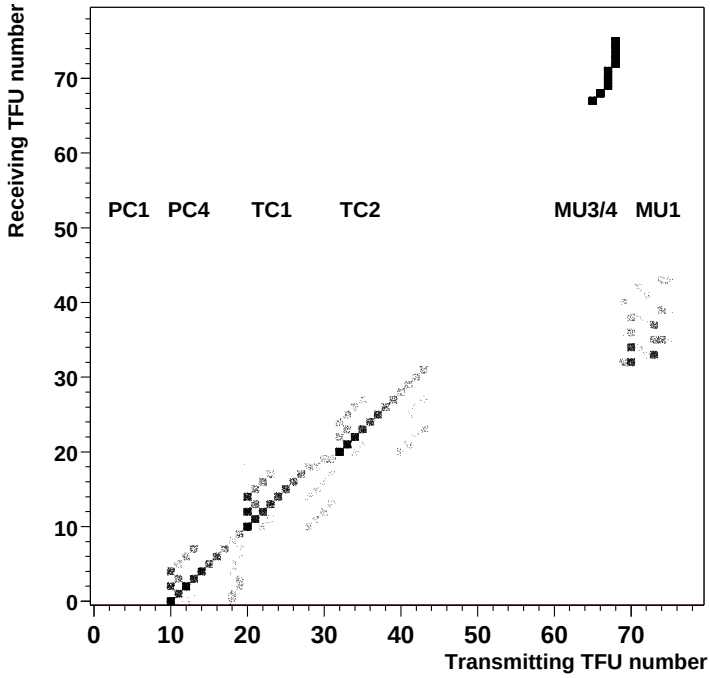

Figure 5.9: *The interconnections of the TFU network and the load of single connections.*

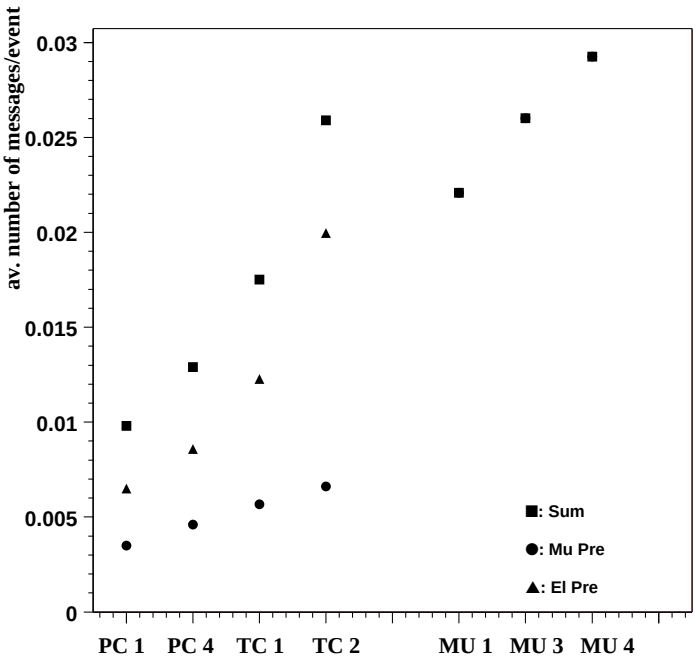

Figure 5.10: *Average input message load per trigger layer and per event for 5 MHz interaction rate separated by the pretrigger source.*

x-axis the transmitting TFUs and on the y-axis the corresponding receiving ones are plotted. Table 5.1 and Figure 3.4 present the underlying numbering scheme. The TFUs of the outer tracker are numbered from 0 through 43. The TFUs of the muon system count from 65 to 75. Several receiving TFUs connect to the same transmitting one because one TFU can send messages to more than one TFU of the next superlayer. This connection scheme is necessary because predicted ROIs for the next superlayer cover more than one TFU geometrically. Most of the messages originate from the pad layers (TFUs 65-68) and enter MU 1. In MU 1, most of the messages are discarded due to missing coincidences which removes a major fraction of triple messages sent by the muon pretrigger. In the outer tracker, the connections between TFUs of the inner sectors are more occupied than the others because of the $1/r^2$ dependance.
Figure 5.10 shows the average amount of all messages per superlayer and event. All messages means the number of messages that are received by the TFU. It also takes into account if a message is duplicated because of several found hits or coincidences. It confirms the above statement with respect to message removal in MU 1. The ECAL pretrigger provides also input that enters the FLT at TC 2 which is also responsible for the increase of message load per event. In addition, an LVDS message multiplexer is installed to collect the messages from the TFUs of MU 1 and to transmit them to the TFUs of TC 2. This multiplexer causes an increase in message load in TC 2. As small effect which is not visible in Figure 5.10 increases the message load in TC 2 because the updated messages of MU 1 are split into two messages. This is necessary because the projected ROIs on TC 2 are too large in x–direction to be handled by a single message.

5.1.4 Estimated Single-Track Trigger Rate

A message is "valid" if there is a hit in the muon pad layers or a triple coincidence in the MU 1 layer or in the outer tracker layers. For each event, the "valid" messages that get propagated all the way to the TDU and arrive in time at the TDU –i.e. the difference in time from the proton interaction to the trigger decision is less than 103 bunch crossings [Her00]– are filled in the histogram in Figure 5.11. The allowed time frame of 103 bunch crossing is less than 12.3 μs as stated earlier because the communication to the control system (FCS) and readout of the detector data needs some time. The FLT trigger rate is evaluated according to the following formula:

$$rate \approx \left(\frac{\sum_{n>0}^{\infty} n_{valid}^{TDU}}{total\ events} \right) \cdot 10\ MHz \tag{5.2}$$

n_{valid}^{TDU} reflects the number of events that have at least one valid message at the TDU. For the rate estimate it does not matter how many messages the TDU has received because they all belong to one BX and a positive trigger decision can be made only once per BX. The rate of 10 MHz represents the HERA bunch crossing rate.
Without any cut on TPU level, the full track rate is the output of the TDU which is of the order of several hundred kHz. To get a realistic trigger output rate in the simulation, the nominal p_T-cut in the TPU is set to 1.4 GeV/c for electrons and 1.0 GeV/c for muons as in the hardware. The minimal p_T-cut is set to 0.5 GeV/c for muons and electrons, respectively. The estimated trigger rates at minimal and nominal p_T-cut are

$$47.6 \pm 1.3\ (stat.)\ kHz \ \text{ and } \ 20.7 \pm 0.8\ (stat.)\ kHz,$$

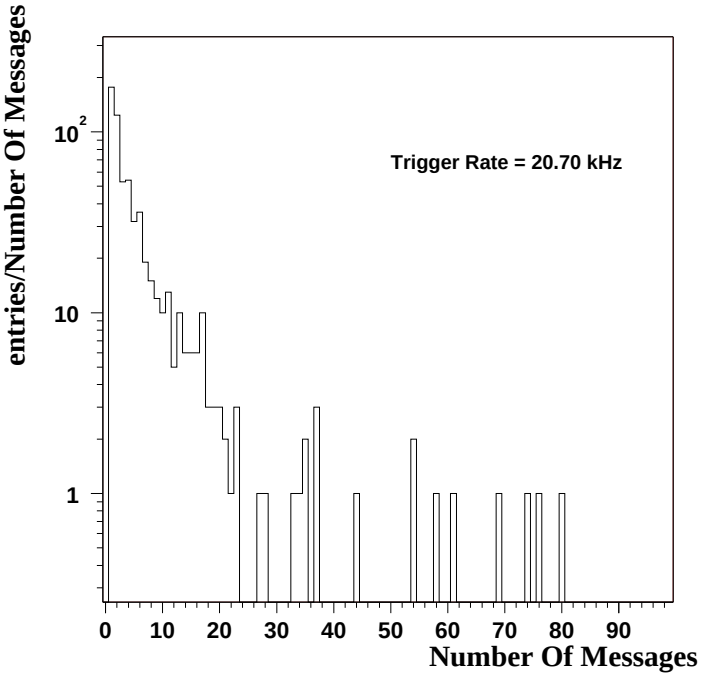

Figure 5.11: *Distribution of the number of valid messages that arrive within 103 bunch crossings after the interaction at the TDU. The single-track trigger rate is calculated according to formula 5.2 and is 20.7 kHz without masking. The summation over all number of messages results in 621 events.*

respectively. With masking applied, we estimate the rates to be

$$52.1 \pm 1.3\ (stat.)\ kHz \text{ and } 25.5 \pm 0.9\ (stat.)\ kHz$$

with minimal and nominal p_T-cut, respectively. The masking increases the trigger rate by 23 %. The rates stated in Table 5.3 for muon and electron pretrigger only do not exactly result in the number for a combined usage of pretriggers because there are events accepted by both pretriggers which means that they contribute to the muon as well as to the electron rate. We also calculate trigger rates when cuts on RICH, PC 2 and ECAL are applied. The results are summarised in Table 5.3. Figure 5.12 summarises the number given in Table 5.3 for the nominal setting which is a p_T-cut of 1.0 GeV/c for muons and 1.4 GeV/c for electrons, respectively. This cut is fixed for the plots with varying cuts on hits and energy deposition. For the variation of the p_T-cut, the cuts in the RICH is fixed to 2540 hits. The obtained results consider a J/ψ loss of 5 %. The expected trigger rate for a combined usage of muon and electron pretrigger for 5 MHz interaction at that level of loss is acceptable with respect to the input capacity of the SLT [Schu95].
The reduction in trigger rate as determined in this study with respect to the various J/ψ losses is lower than the values obtained in [Ada01]. The relative reduction using veto cuts at 1 %, 5 % and 10 % J/ψ loss are 0.02, 0.13 and 0.24, respectively, i.e. a veto at 5 % J/ψ loss reduces the estimated trigger rate by 13 %. The reduction in trigger rate with applied p_T-cut as a function of the veto cuts is higher than at nominal p_T-cut. The reduction for the PC 2 veto is slightly higher. A comparison of the number of hits in PC 2 for minimum

5 MHz Target Rate	No Veto	Maximal Hits in RICH			Maximal Hits in PC 2			Max. Energy In. ECAL [GeV]		
		1750	2540	3795	640	790	1220	340	425	585
Deadtime [%]	4.4	3.3	3.7	4.3	2.6	3.0	3.9	3.6	3.9	4.3
Deadtime (mask)[%]	5.1	3.7	4.1	4.9	2.8	3.3	4.4	4.0	4.4	4.9
μ Rate (nom) [kHz]	6.6	2.9	4.7	6.0	2.1	3.1	4.8	4.3	5.3	6.4
e Rate (nom) [kHz]	14.3	8.6	11.7	13.8	5.9	9.0	12.4	10.6	12.2	14.0
μ Rate [kHz]	13.2	7.0	10.2	12.7	5.3	7.0	10.6	9.6	11.4	13.1
e Rate [kHz]	32.6	21.8	28.4	32.0	18.0	22.4	29.6	25.7	29.1	32.1

Table 5.3: *Overview of deadtime and single-track trigger rate without masking at 5 MHz target rate at various cuts with respect to hits in RICH, PC 2 and energy deposition in inner calorimeter, respectively. The single rates (nom) are evaluated without masking at nominal p_T-cut of 1.0 GeV/c for muons and 1.4 GeV/c for electrons. The lower two rows show the single rate with a minimal p_T-cut of 0.5 GeV/c for electrons and muons.*

bias data and for the SLT triggered data showed a discrepancy. The distribution of hits in PC 2 for the J/ψ candidates ends at a lower number of hits than for the minimum bias events. The differences between this analysis and [Ada01] arises from the examined data samples. The muon rates with the minimal p_T-cuts are twice the rates at nominal cut. For the electron rate this factor is slightly above 2. The sum of the individual rates for muons and electrons is higher than in a combined setup with both pretriggers. The reason for this difference is that it can happen that events are triggered by both pretriggers. They contribute as one entry to the trigger rate. For the individual muon or electron rates they are counted separately as one entry and lead to a higher individual rate. The estimated trigger rates for 10 MHz target rate without any masking at the minimal as well as nominal p_T-cut are

$$118.9 \pm 2.9\ (stat.)\ kHz \ \text{ and } \ 52.9 \pm 2.0\ (stat.)\ kHz.$$

With applied masking we estimate the rates to

$$131.3 \pm 3.0\ (stat.)\ kHz \ \text{ and } \ 62.7 \pm 2.1\ (stat.)\ kHz$$

at minimal and nominal p_T-cut, respectively. The trigger rate for 10 MHz target rate is 2.5 times the one for the 5 MHz interaction rate. The rate is too high to be handled by the SLT whose limit is 50 kHz. Running at the design interaction rate of 40 MHz in the single track trigger mode is impossible. A veto in one of the detector components reduces the rate to an acceptable value, but only at the cost of 10 % J/ψ loss. The use of only one of the pretriggers is not problematic at all. Table 5.4 summarises the rates for each pretrigger type at the nominal p_T-cut with respect to the different veto cuts and J/ψ losses. At the level of 1 % J/ψ loss, using only the electron pretrigger can be problematic because of possible rate fluctuations that exceed the acceptable input rate to the SLT. The reduction of the trigger rates at 5 % and 10 % J/ψ loss with respect to the rate without is lower for the RICH and ECAL veto cut than stated in Table 5.2. The reduction of the rates for a veto in PC 2 at each level of J/ψ loss is drastically higher. The different data samples compared to [Ada01] and the applied p_T-cut are the reason for this drastic reduction. In

general, the reduction for the rates and the deadtime at 1 % J/ψ loss is lower than for the SLT triggered data. For 5 % and 10 % the reduction is higher than in the case of the SLT triggered data.
The sum of the individual rates for muons and electrons are higher than in a usage of both pretriggers at the same time due to the reasons stated above. The rates are graphically shown in Figure 5.13.

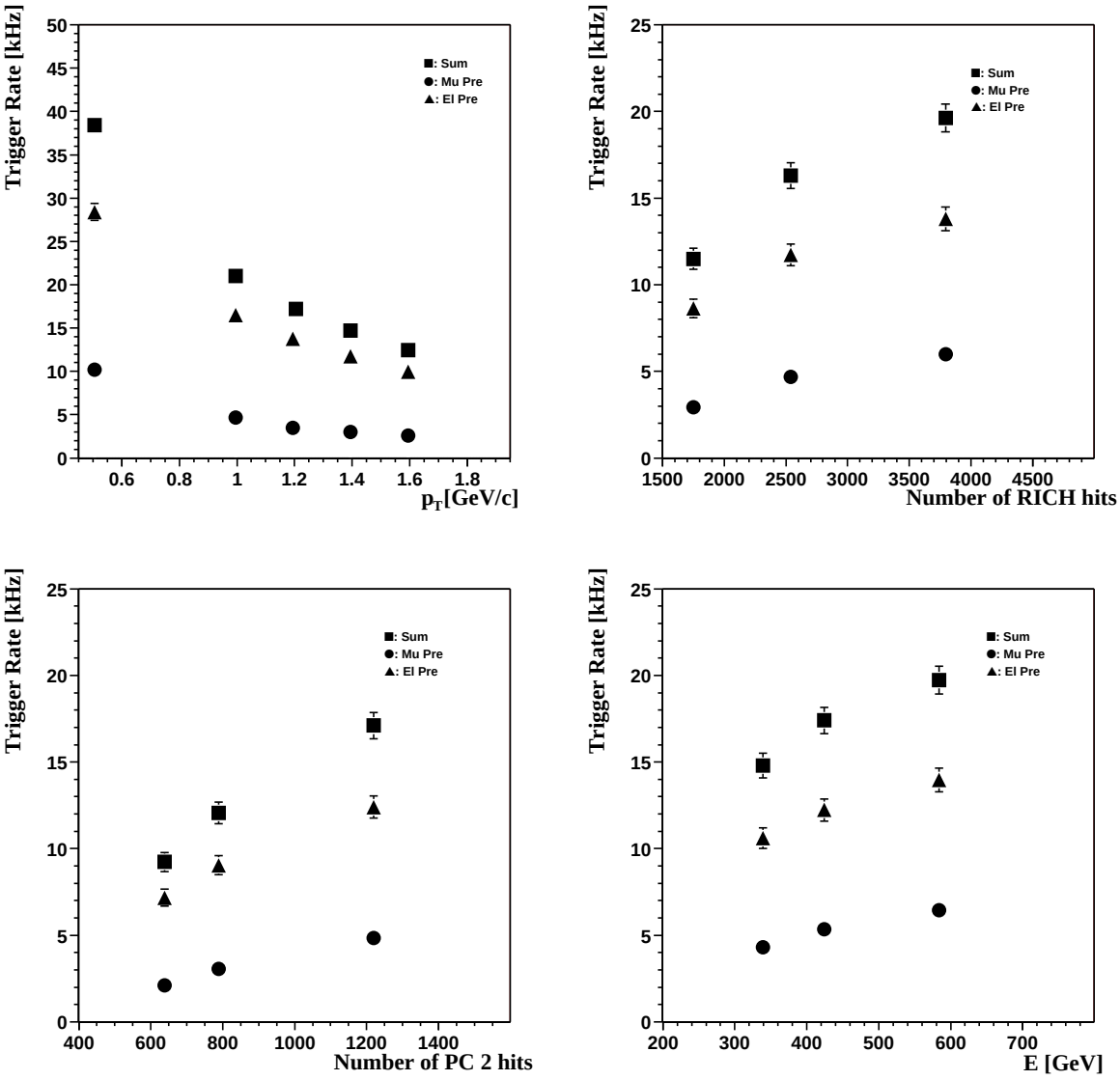

Figure 5.12: *The trigger rate for 5 MHz target rate for the various cuts. The trigger rate with respect to p_T-cut is determined at a veto cut for the RICH corresponding to a 5% J/ψ loss. The rates with respect to a veto on RICH or PC 2 or ECAL are evaluated at nominal p_T-cut of 1.0 GeV/c for muons and 1.4 GeV/c for electrons, respectively.*

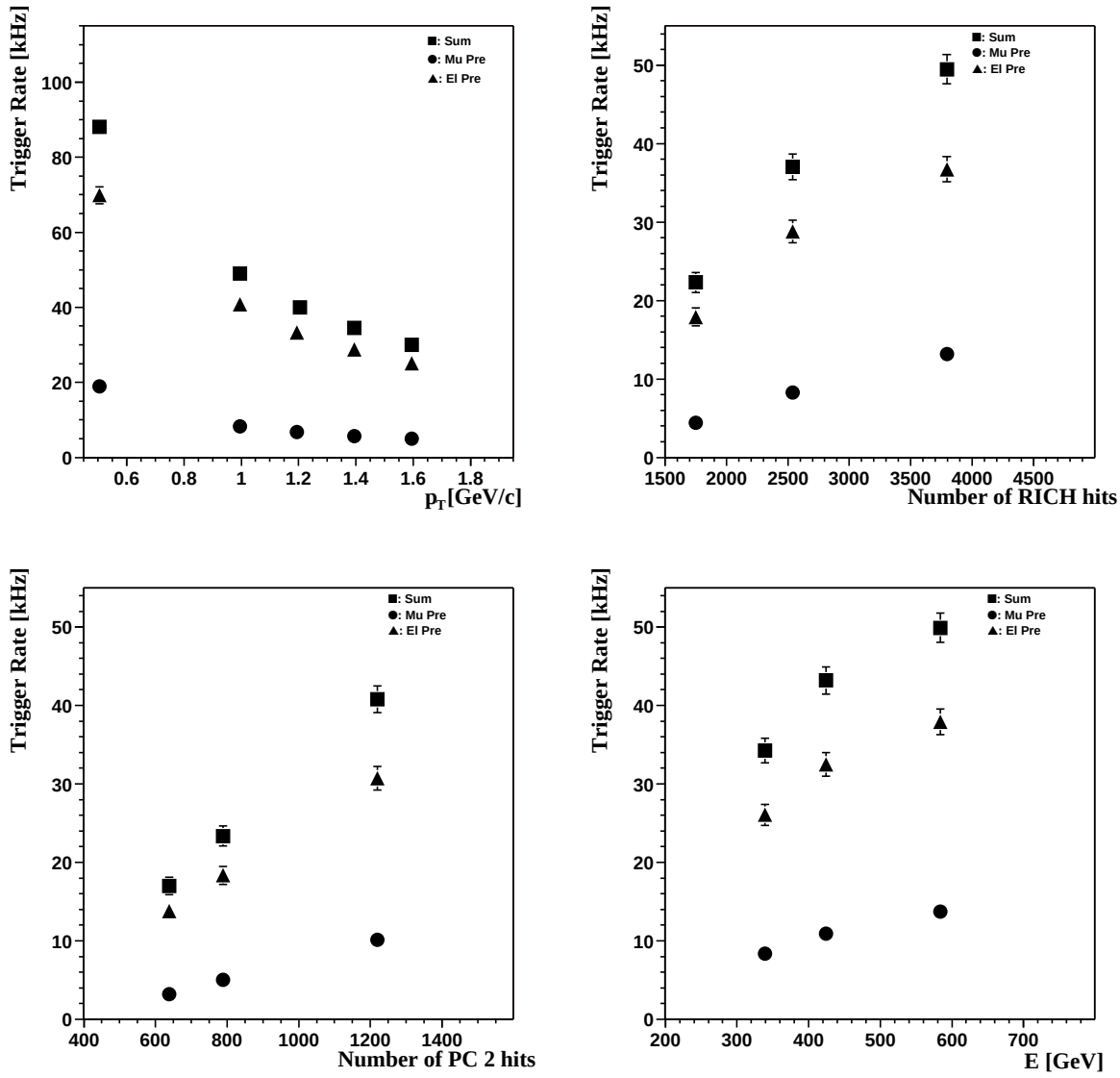

Figure 5.13: *The trigger rate for 10 MHz target rate for the various cuts. The trigger rate with respect to p_T-cut is determined at a veto for the RICH at 5% J/ψ loss. The rates with respect to a veto on RICH or PC 2 or ECAL are evaluated at nominal p_T-cut of 1.0 GeV/c for muons and 1.4 GeV/c for electrons, respectively.*

5.1.5 Rate Estimation for the Pair Trigger

Up to now, we only considered the single-track trigger ("count trigger") rate. The TDU is able to combine up to 24 tracks per event to a two-track-invariant mass ("pair trigger"). The mass threshold is programmable above which a positive trigger decision is taken. During the running of the year 2000 it was set to 2.0 GeV/c^2. A pair is accepted only if the two tracks have opposite charge and have the same particle ID.
The p_T-cuts in the TPU are set to 0.5 GeV/c for muons and 0.5 GeV/c for electrons, respectively.
The estimated pair trigger rates for a combined usage of muon and electron pretrigger at

10 MHz Target Rate	No Veto	Maximal Hits in RICH			Maximal Hits in PC 2			Max. Energy In. ECAL [GeV]		
		1750	2540	3795	640	790	1220	340	425	585
Deadtime [%]	10.1	4.9	7.4	9.7	4.2	5.3	8.2	7.0	8.4	9.8
Deadtime (mask)[%]	11.3	5.5	8.3	10.8	4.6	6.0	9.2	7.9	9.5	11.0
μ Rate (nom) [kHz]	14.1	4.4	8.4	13.5	3.2	5.1	10.3	8.5	11.1	14.0
e Rate (nom) [kHz]	39.2	18.0	28.9	37.2	13.8	18.4	30.7	16.1	32.9	37.9
μ Rate [kHz]	27.2	10.6	19.0	25.9	7.9	12.1	21.8	18.5	22.9	26.6
e Rate [kHz]	94.0	45.2	69.9	89.4	35.7	48.9	76.9	64.4	78.6	91.5

Table 5.4: *Overview of deadtime and single-track trigger rate without masking at 10 MHz target rate at various cuts with respect to hits in RICH and PC 2 and energy deposition in inner calorimeter, respectively. The single rates (nom) are evaluated at nominal p_T-cut of 1.0 GeV/c for muons and 1.4 GeV/c for electrons, respectively. The lower two rows show the single rate with a minimal p_T-cut of 0.5 GeV/c for electrons and muons, respectively.*

5 MHz target rate are

$$0.27 \pm 0.09\ (stat.)\ kHz \text{ and } 0.63 \pm 0.14\ (stat.)\ kHz$$

without applied masking and with applied masking, respectively. On the TPU, a removal of clone tracks can be switched on. Clone tracks origin from the tracking when there are hits close to each other which result in additional messages describing the same physical track. The momentum components of clone tracks are similar to each other and motivate a clone removal by comparing the momenta. In this analysis, we use a simplified algorithm for clone removal. The clone removal is based on the comparison of momentum components $\hat{p_x}$ and $\hat{p_y}$ (i.e. p_x/p_z and p_y/p_z, respectively) of the last 32 tracks. The least significant bit of both values is ignored. If the remaining values are identical one track is rejected. The rates for a combined usage of muon and electron pretrigger with clone removal enabled are

$$0.45 \pm 0.15\ (stat.)\ kHz \text{ and } 0.77 \pm 0.16\ (stat.)\ kHz$$

without applied masking and with applied masking, respectively. The rates with clone removal enabled are higher than those without because of more possible combinatorics. To make this more clear we assume that we have 24 identical tracks and one track which is different in an event. In the case without clone removal the 24 identical tracks are in the buffer of the TDU and the last one is discarded. All possible combinations of the 24 tracks do not lead to an invariant mass like stated above. With clone removal, 23 of these tracks are removed by the TPU and do not enter the buffer of the TDU. The track in the buffer and the last track which was not in the buffer without clone removal are now combined and can form an invariant mass.

The pair rate for 10 MHz target rate and a combined usage of both pretriggers yields without clone removal and with clone removal

$$1.7 \pm 0.3\ (stat.)\ kHz \text{ and } 2.0 \pm 0.4\ (stat.)\ kHz,$$

respectively. With masking the pair rate estimate is

$$2.4 \pm 0.4\ (stat.)\ kHz.$$

10 MHz Target Rate	Maximal Hits in RICH			Maximal Hits in PC 2			Max. Energy Inner ECAL [GeV]		
	1750	2540	3795	640	790	1220	340	425	585
Rate (cr) [kHz]	0.28	0.85	1.63	0.21	0.28	0.85	0.64	1.42	1.77
Rate [kHz]	0.29	0.66	1.47	0.22	0.29	0.73	0.59	1.25	1.54

Table 5.5: *Overview of pair trigger rate without masking at 10 MHz and at various cuts with respect to hits in RICH and PC 2 and energy deposition in inner calorimeter, respectively. The rates (cr) are evaluated with clone removal. In both cases, the p_T-cut is set to 0.5 GeV/c for electrons and muons, respectively.*

Due to the limited available statistics a separate estimate of the pair rate for muon or electron pretrigger only is not reliable. Table 5.5 shows the total pair trigger rate with respect to applied veto cuts. Due to the limited statistics the rate without clone removal is in some cases higher than in the setup with clone removal.
Operating the FLT in pair trigger mode is more safe than in the single-track trigger mode with respect to the maximal allowed input rate of the SLT which is 50 kHz.

In the following section, we repeat the analysis for 20 MHz interaction rate.

5.2 Analysis of the Network at 20 MHz Target Rate

We analyse runs 14546, 14569 and 14594 to get sufficient statistics for the estimates on rate and deadtime for an interaction rate of 20 MHz. In total, we use a data set of 116141 events.
The averaged occupancy for this run as shown in Figure 5.14 has larger tails towards higher values. Without any masking the averaged occupancy is $(9.22 \pm 0.03\ (stat.))$ % and with applied masking the value is $(10.91 \pm 0.03\ (stat.))$ %. The averaged occupancy for each of the analysed runs ranges without masking from 8.8 % to 9.5 % and with masking from 10.5 % to 11.2 %. The bunch spectrum for run 14546 is more uniform than those of the other two runs. The spectra of the runs 14569 and 14594 show a few more highly occupied bunches which results in less uniform bunch structure. Those more highly occupied bunches influence the trigger rate and the deadtime of the system. The deadtime of the TFU network averaged over all runs turns out to be without masking

$$(42.1 \pm 0.1\ (stat.))\ \%\ \text{ and }\ (47.5 \pm 0.1\ (stat.))\ \%$$

with masking applied. The number of events for which one TFU of the network has to process more than five messages lies in a range from 6.1 % up to 8.9 % without masking and from 6.6 % to 9.4 % with masking (Figure 5.15). The deadtime is by more than a factor three higher than for the 10 MHz run and by almost a factor 10 than for the 5 MHz target rate. The deadtime of the network does not grow linearly with the target rate. The deadtime varies from 25.5 % up to 51.5 % without masking and from 30.4 % to 57.9 % with masking for the analysed runs. It is noted that the assumption and the method to determine the deadtime do not give reliable results for an interaction rate of 20 MHz. The deadtime of the TFU network with respect to the veto cuts is shown in

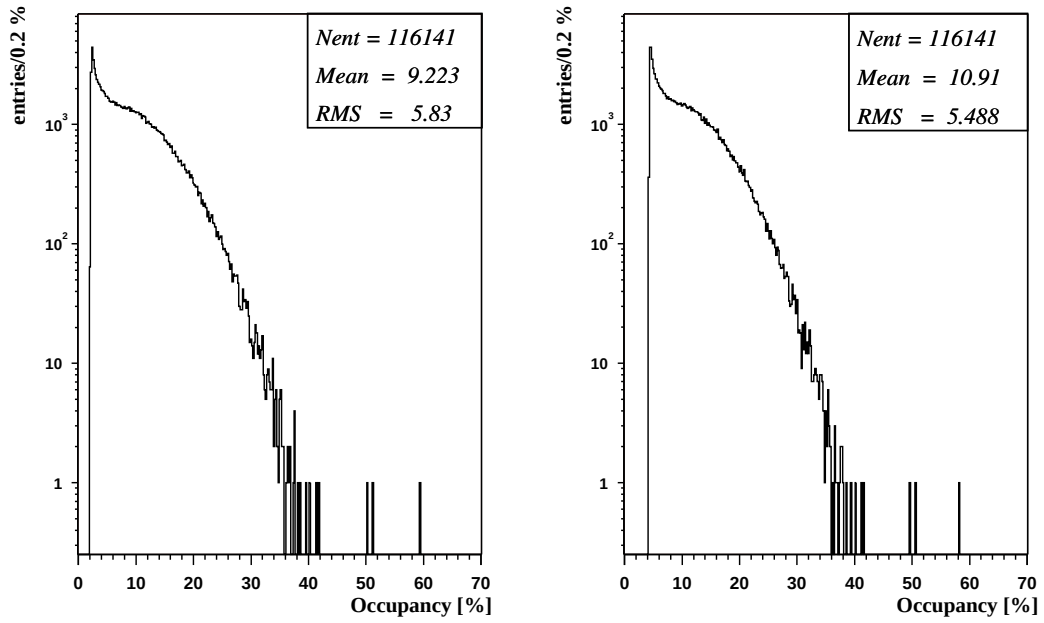

Figure 5.14: *Left: the occupancy of all trigger layers of the outer tracker as seen by the FLT. Only the link masking is switched on. Right: The channel masking is applied, too.*

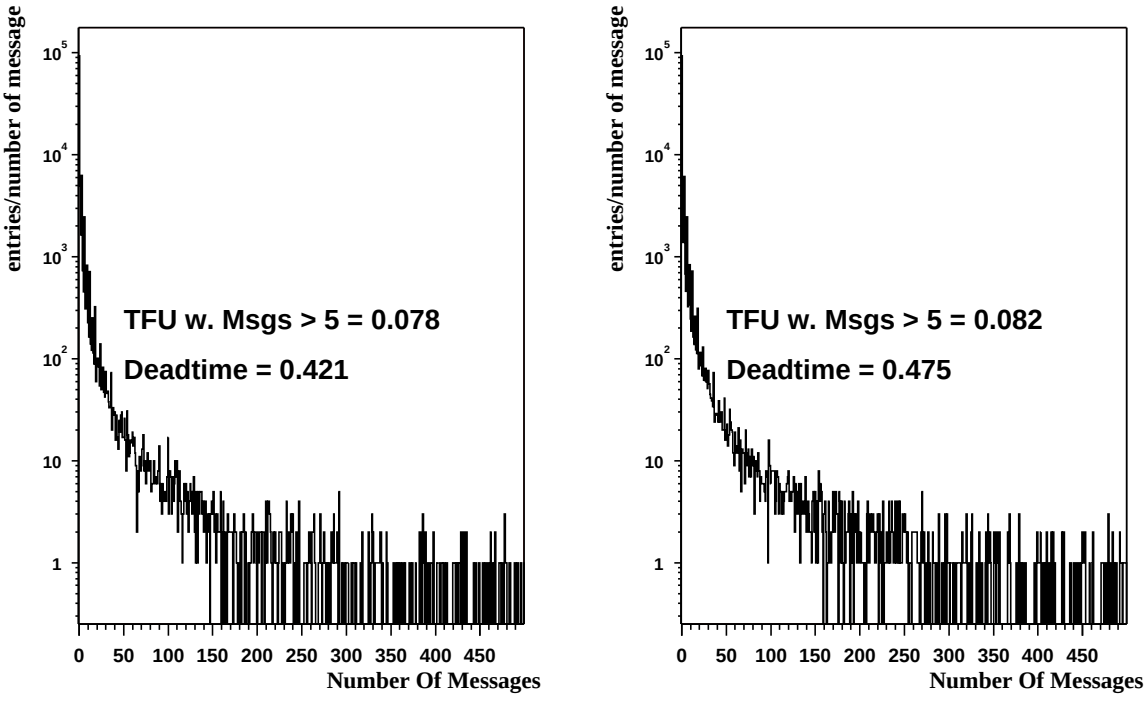

Figure 5.15: *The maximal number of messages per event and the evaluated deadtime for the 20 MHz interaction rate is shown. In 7.8 % of events a TFU has to process more than 5 messages. With masking it happens in 8.2 % of the events.*

Figure 5.16. A cut on the hits in the RICH as well as a cut on the energy deposition in the inner calorimeter at 10 % J/ψ loss lead to an almost acceptable deadtime like for the 10 MHz target rate. The reduction for the PC 2 veto is significantly higher due to the already discussed reasons. The more highly occupied bunches are the reason for this large

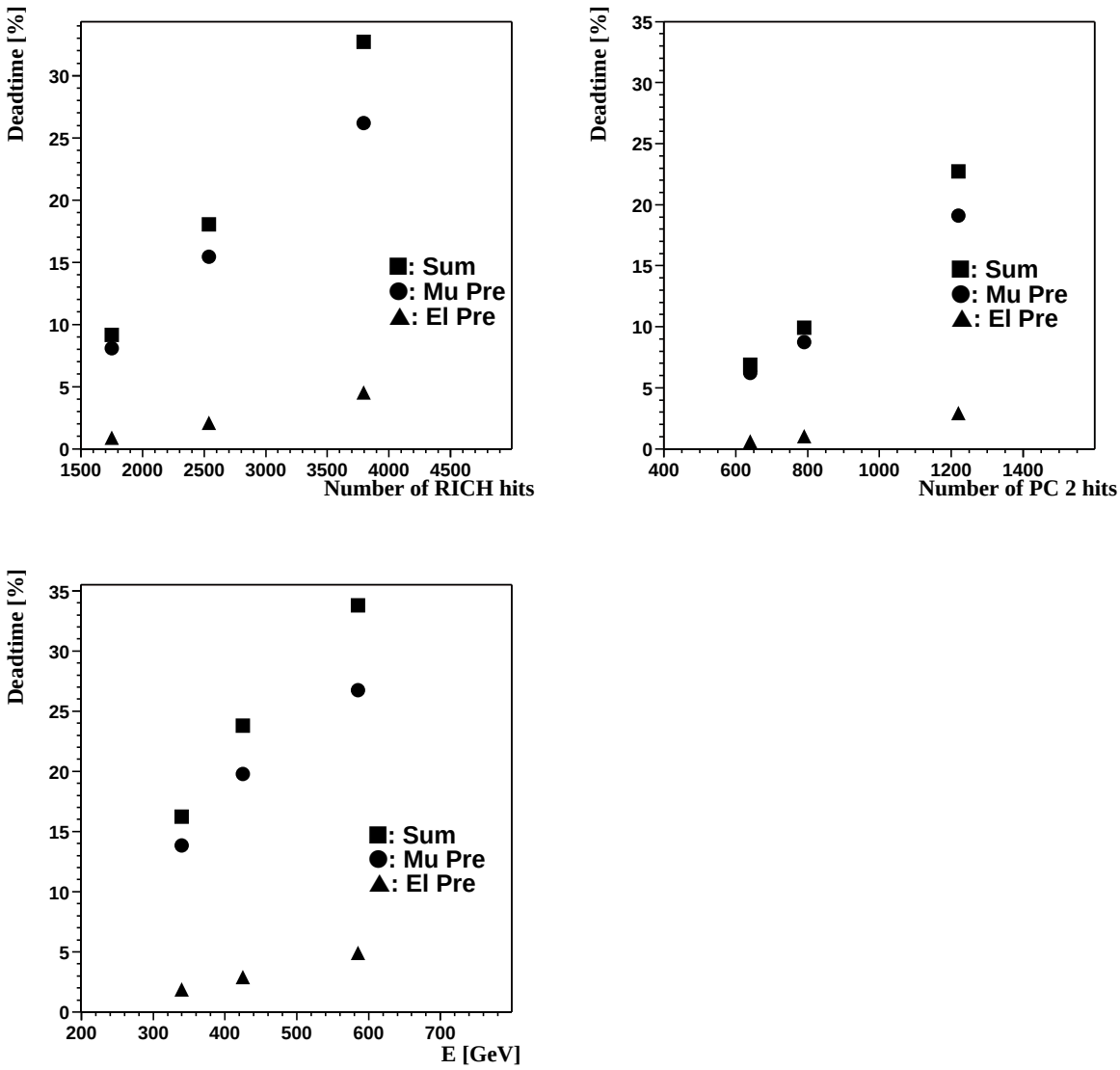

Figure 5.16: *Deadtime at 20 MHz target rate with respect to a multiplicity veto separated by the pretrigger source. Top left: The deadtime as a function of the cut on hits in the RICH. Top right: The deadtime as a function of the cut on hits in PC 2. Bottom: The deadtime as a function of the cut on the energy deposition in the inner calorimeter.*

spread in deadtime because they show exactly that range in maximally occupied bunches compared to the average bunch occupancy which Figure 5.18 confirms. A deeper analysis of the target rate behaviour shows that at highly occupied bunches the actual target rate was up to a factor 1.5 times higher than the nominal target rate of 20 MHz [Sym01]. The spectra of the averaged occupancy of each single run look different, too. For the run

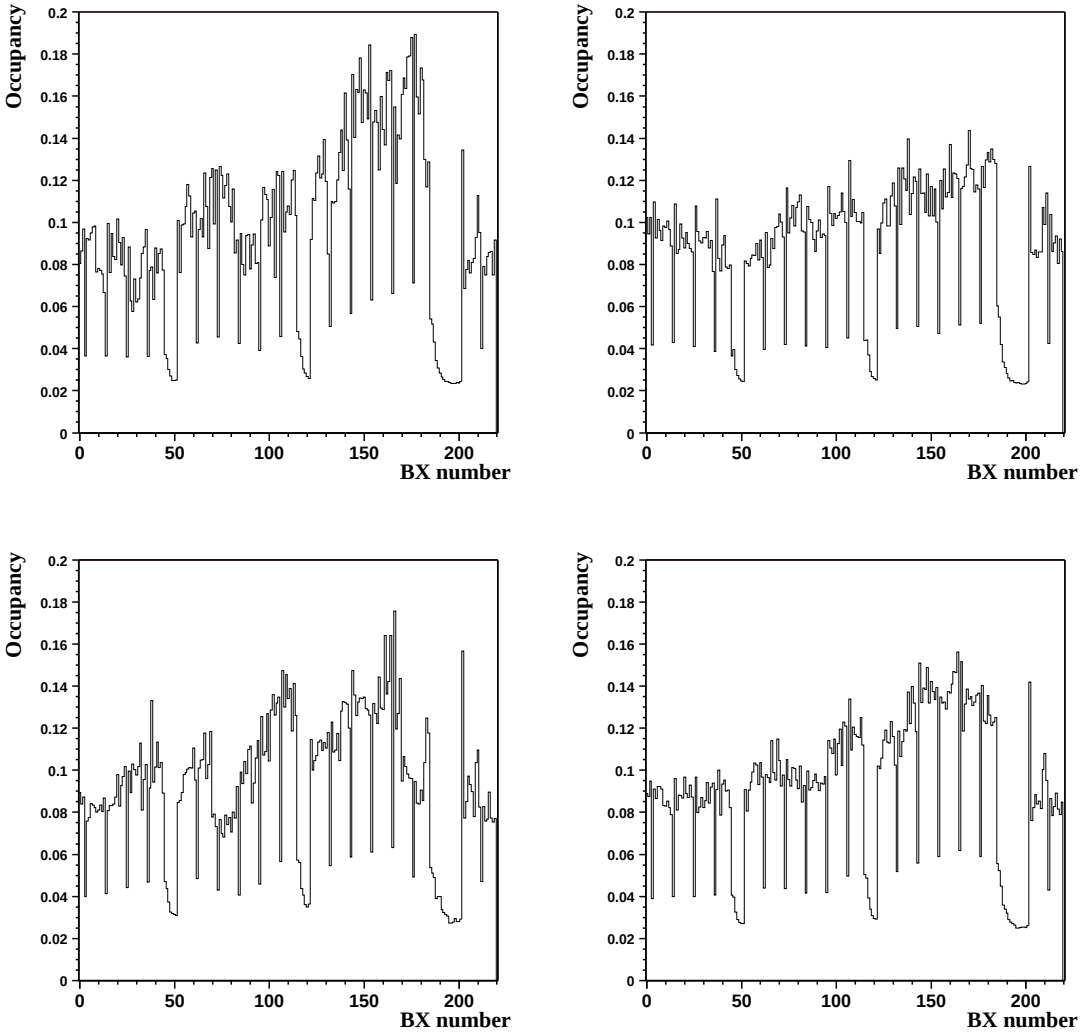

Figure 5.17: *The beam structure for the different analysed runs at 20 MHz target rate. Different wire material was used for each run. Top left: Beam structure for run 14569 taken with the Carbon wire. Top right: Beam structure for run 14546 taken with the Titanium wire. Bottom left: Beam structure of run 14594 taken with the Aluminum wire. Bottom right: Overall beam structure of all analysed runs.*

with the lowest deadtime the maximal occupancy is slightly above 30 %. For the other two runs, the values are at around 40 %. Run 14594 shows single events with occupancies well above 40 % that do not appear in the other runs. In Figure 5.17, the physical BX weighted by the averaged occupancy is shown for the individual runs and for the full data set. The beam structure is most visible compared to the other data samples. This is a clear effect as the mean value of the averaged occupancy is more than twice that of the 5 MHz run.
We also analyse the FLT track rate (i.e. tracks that arrive at the TDU) as a function of the occupancy and fit a power law

$$a \cdot x^b$$

to the data points. Since the trigger combines hits in the trigger layers to form its recon-

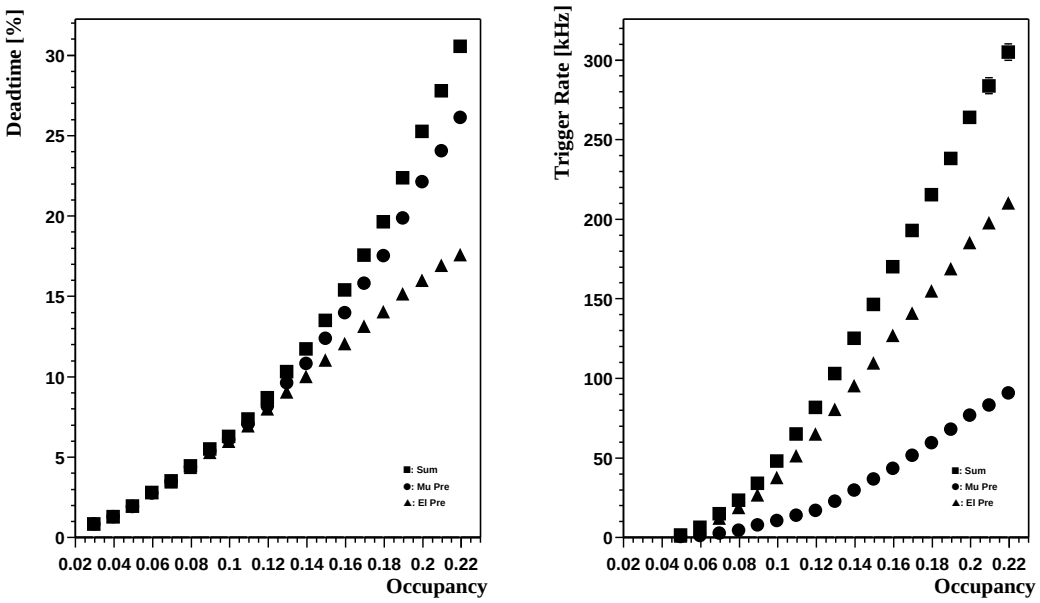

Figure 5.18: *Left: Deadtime as a function of the occupancy for the 20 MHz interaction rate separated by the pretrigger. The deadtime increases with increasing occupancy which is a clear effect due to highly occupied bunches. Right: single-track trigger rate for 20 MHz interaction rate as a function of occupancy.*

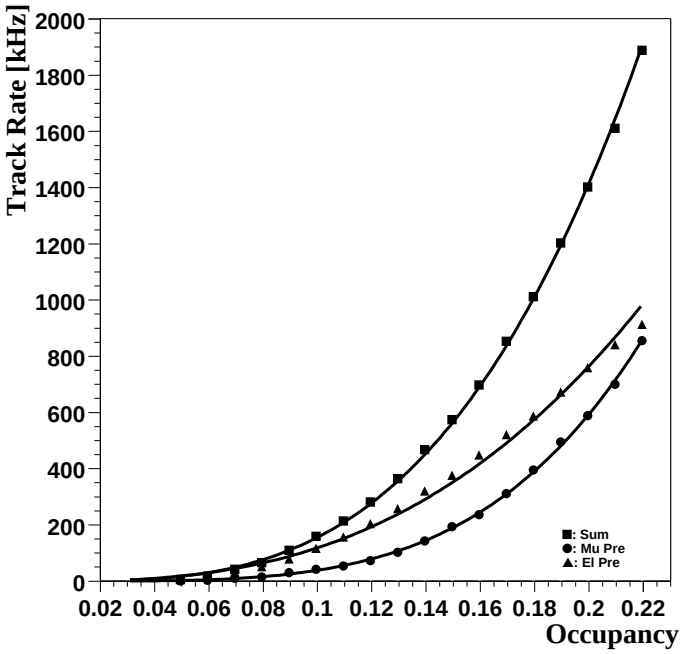

Figure 5.19: *Track rate as a function of the outer tracker occupancy fit by a power law. The exponents are 2.69 for electrons and 3.94 for muons, respectively.*

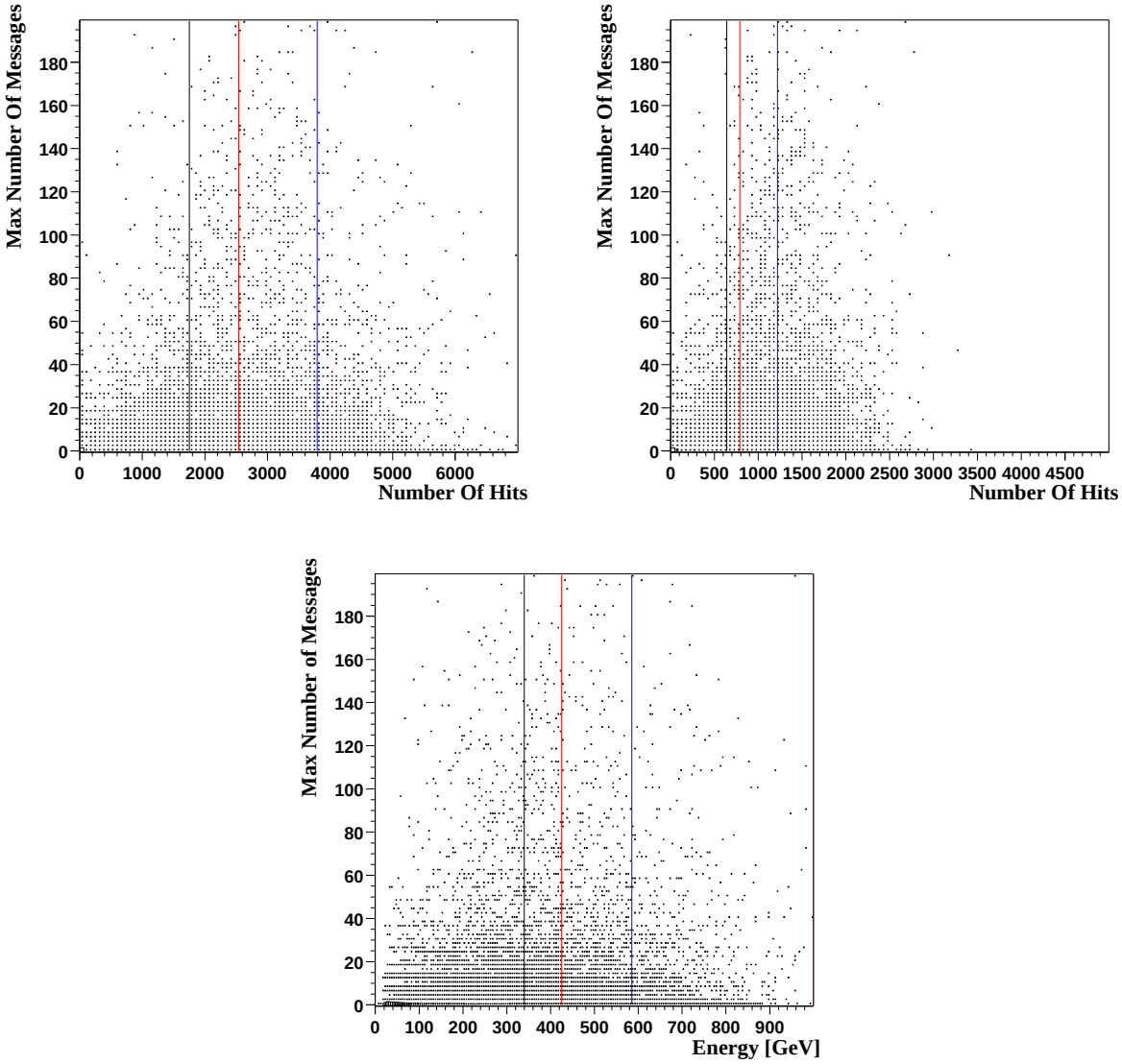

Figure 5.20: *The maximal number of messages of one TFU of the network as a function of the hits in the RICH (top left) or of the hits in PC 2 (top right) or of the energy deposition in the inner calorimeter (bottom) for 20 MHz target rate. The vertical lines indicate the veto cuts at different levels of J/ψ loss.*

structed tracks (messages) the rate of found tracks depends on the amount of present hits. The track rate should roughly scale with the number of hits to the power of b –with b being the average number of combined hits. The measured exponents are 2.69 ± 0.01 (*stat.*) for the outer tracker (i.e. electrons only) and 3.94 ± 0.02 (*stat.*) for the muon channel. On average, the trigger combines 2.7 hits in the electron channel and 4 for in the muon channel. Assuming that the number of used hits scales with the number of used superlayers both results can be made plausible by a simple calculation: For the electron channel we combine the information of twelve layers of the outer tracker plus one for the pretrigger. For the muon channel, we use twelve outer tracker layers and five muon layers. The pretrigger

adds two layers. Multiplying the tracks for the electron channel by the number of layers for the muon channel (in total: 19) and divide it by number of layers used for the electron channel (in total: 13) it results in 3.93 which is in agreement with the result (3.94) from the fit.
The fact that the masking is derived from more recent runs than the analysed data has to be taken into account. The number of messages in the network increases by roughly 45 % with masking compared to without masking. The number of hits and the deposited energy tend towards the higher end of the spectra. Like in the analysis of the other interaction rates, no clear correlation of message load in the network and hits or energy deposition is evident (Figure 5.20). A multiplicity veto will improve the situation with respect to message load in the system. A major fraction of the events with high network load will be discarded depending on the applied veto cut. Some of the events with high load are not rejected by the veto. The average message load per superlayer looks like Figure 5.10 scaled by almost a factor four.

5.2.1 Estimated Single-Track Trigger Rate

The estimated trigger rates for muon and electron pretrigger at minimal and nominal momentum p_T-cut are

$$394.0 \pm 5.7\ (stat.)\ kHz \ \text{ and } \ 216.6 \pm 4.3\ (stat.)\ kHz,$$

respectively. With applied masking we estimate the rate at minimal momentum cut to be

$$464.1 \pm 6.3\ (stat.)\ kHz \ \text{ and } \ 244.0 \pm 4.6\ (stat.)\ kHz$$

at nominal momentum cut. Both rates are by far too high to be handled by the SLT. The trigger design gives a maximal for the acceptable rate of 50 kHz [Schu95]. Running the FLT at much higher rates is impossible. The trigger concept never took into account to run the FLT as a single-track trigger. Table 5.6 shows that even with a veto at 10 % J/ψ

20 MHz Target Rate	No Veto	Maximal Hits in RICH			Maximal Hits in PC 2			Max. Energy In. ECAL [GeV]		
		1750	2540	3795	640	790	1220	340	425	585
Deadtime [%]	42.1	9.5	18.8	34.5	7.1	10.3	23.7	17.0	24.8	35.5
Deadtime (mask)[%]	47.5	10.9	21.8	39.2	7.9	12.0	27.6	19.5	28.5	40.2
μ Rate (nom) [kHz]	88.8	11.1	33.2	69.4	6.4	12.5	42.5	29.2	47.9	76.5
e Rate (nom) [kHz]	136	25.6	53.4	103	16.9	27.5	69.0	45.3	68.3	115
μ Rate [kHz]	129	22.1	56.4	106	13.9	24.4	71.0	49.4	76.0	115
e Rate [kHz]	283	71.1	138	231	46.7	76.4	169	115	164	249

Table 5.6: *Overview of deadtime and single-track trigger rate without masking at 20 MHz and at various cuts with respect to hits in RICH and PC 2 and energy deposition in inner calorimeter, respectively. The single rates (nom) are evaluated at nominal p_T-cut of 1.0 GeV/c for muons and 1.4 GeV/c for electrons, respectively. The lower two rows show the single rate with a minimal p_T-cut of 0.5 GeV/c for electrons and muons, respectively.*

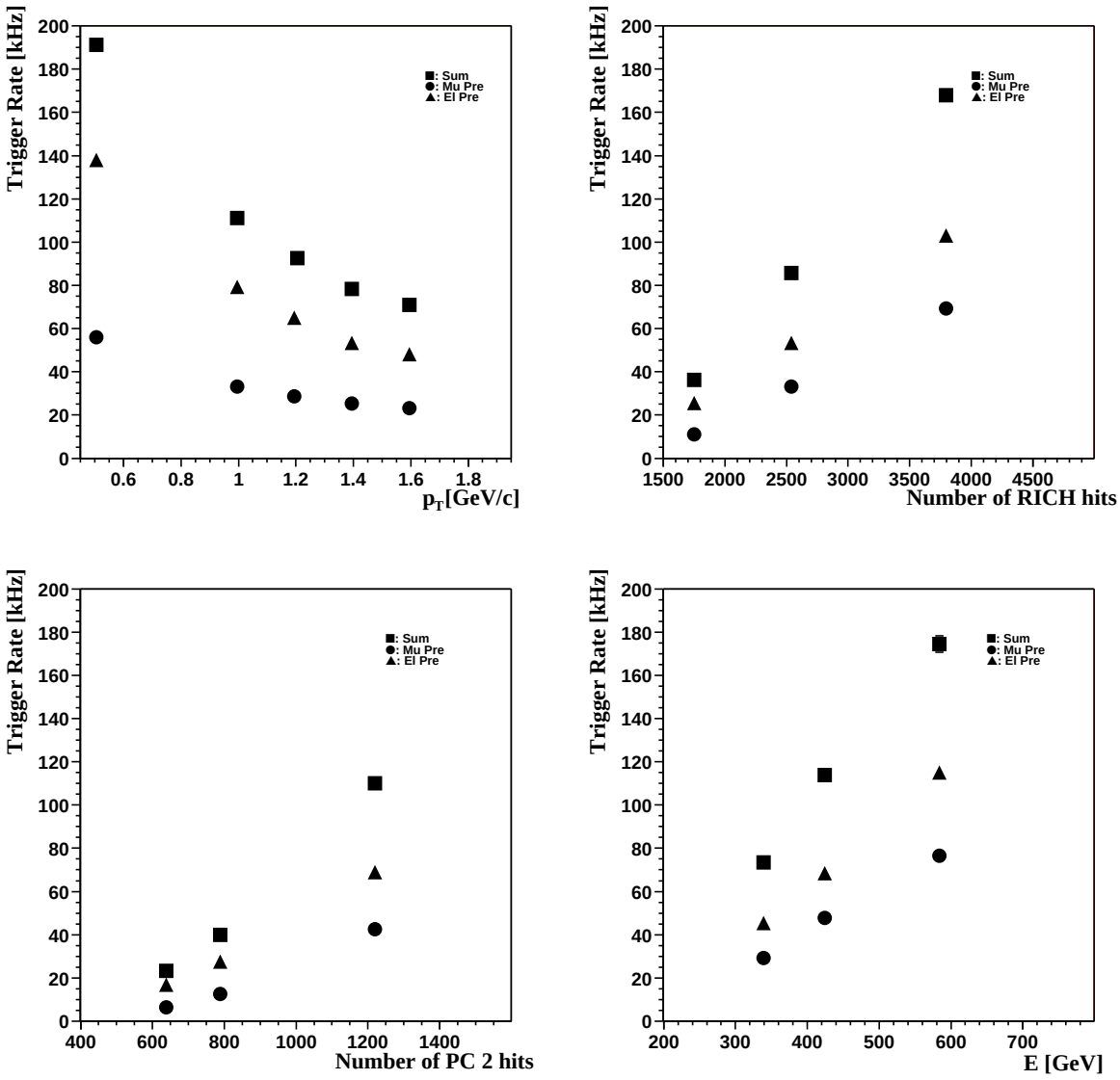

Figure 5.21: *The trigger rate for 20 MHz target rate for the various cuts. The trigger rate with respect to p_T-cut is evaluated at a 5% J/ψ loss. The rates with respect to a veto on RICH or PC 2 or ECAL are evaluated at nominal p_T-cut of 1.0 GeV/c for muons and 1.4 GeV/c for electrons, respectively.*

loss in most cases only one of the two pretrigger systems can be used.
The sum of the single rates for muon and electron pretriggers differs from the values stated above because the number of events for which both pretrigger generate a decision increases.

5.2.2 Rate Estimation for the Pair Trigger

Without clone removal, the pair trigger rate for both pretriggers enabled is

$$15.5 \pm 1.5\ (stat.)\ kHz.$$

The rate for di-muon and di-electron are 6.0 kHz and 7.2 kHz, respectively. With clone removal enabled and without masking we estimate the pair trigger rate to be

$$17.1 \pm 1.3\ (stat.)\ kHz \text{ and } 19.3 \pm 1.3\ (stat.)\ kHz$$

with masking, respectively. The di-muon or di-electron rate is without masking 8.1 kHz and 11.1 kHz and with masking 8.5 kHz or 13.9 kHz, respectively. Table 5.7 summarises the different pair trigger rates with respect to veto cuts. The difference in the sum of the single rates with respect to the overall rate is due to the reason stated in section 5.1.4.

20 MHz Target Rate	Maximal Hits in RICH			Maximal Hits in PC 2			Max. Energy Inner ECAL [GeV]		
	1750	2540	3795	640	790	1220	340	425	585
μ Rate (cr) [kHz]	0.17	1.98	4.39	0.09	0.17	2.67	1.21	2.84	4.48
e Rate (cr) [kHz]	0.26	1.64	4.74	0.09	0.17	1.89	1.12	2.07	4.31
μ Rate [kHz]	0.15	1.96	4.37	0.08	0.15	2.71	1.06	2.79	4.37
e Rate [kHz]	0.30	1.66	4.30	0.08	0.23	1.81	1.06	1.96	3.84

Table 5.7: *Overview pair trigger rate without masking at 20 MHz and at various cuts with respect to hits in RICH and PC 2 and energy deposition in inner calorimeter, respectively. The rates (cr) are evaluated with clone removal. In both cases, the p_T-cut is set to 0.5 GeV/c for electrons and muons, respectively.*

5.3 Estimation of the Systematic Error

The presented results include some uncertainties which are summarised as the systematic error. We present some sources of the systematic error.

Effects related with Beam Structure

The analysis of the data taken at different interaction (or target) rates showed a non-uniform bunch structure. Some of the bunches are higher occupied than other bunches. We studied the effect of those bunches on the occupancy, the deadtime and the trigger rate for the different target rates. We excluded about 10 to 15 of the higher occupied bunches and determined the relative increase or decrease of the deadtime, occupancy and the trigger rate. The systematic error for the occupancy is about 10 % for 5 MHz target rate and about 4 % for 10 and 20 MHz target rate. The deadtime varies in a range between 12 % and 14 % for the different interaction rates. For the 20 MHz run we stated a difference in deadtime of the order of 50 %. The spread could also be verified by the above method if we exclude more than 10 to 15 bunches. The error on the trigger rate is for all interaction rates of the order of 4 %. The effect of the non-uniform bunch structure on the deadtime and the trigger rate was shown in section 5.2.
Rate fluctuations with respect to the nominal target rate contribute also to the systematic error. In addition to the effect of the non-uniform bunch structure, we saw that the highly occupied bunches are due to rate fluctuations between the nominal target rate and the

instantaneous rate. The average rate fluctuations for the target are of the order of ±10 % as shown in [Kni00].

Uncertainties of the Simulations

The efficiency of the muon pretrigger simulation which was used for the entire analysis lies in a range between 93 % for the worst case and 98 % for the best one. The numbers are in agreement with the ones stated in [Ada01a].
The simulation of the FLT describes the hardware in almost perfect agreement as shown in [Mic02]. Small discrepancies between the hardware and the simulation are found in the ordering of tracks for the removal of identical tracks (clone removal) at the TPU and for the calculation of the invariant mass at the TDU. The impact on the trigger rate is negligible since this effect only appears for events with large track multiplicities which lead to a trigger in most of the cases.

Effects due to Masking

In some cases, a masking was used in the analysis to reflect the behaviour of imperfections of the detector or the data transmission. We have to distinguish two different maskings: The detector masking as used by the realistic MC which describes the performance of the detector of the year 2000 and a channel masking which was evaluated and applied by the FLT.
The detector masking was evaluated for one or more runs but not for all of the runs of the year 2000. Small changes in the performance are not reproduced in a precise way.
The channel masking for the FLT for various runs showed fluctuations up to 17 % of the affected channels [Riu01] which results in an uncertainty for the trigger rate of the order of 4 %. The estimate of the systematic error for the occupancy and for the deadtime due to the uncertainty which channels need to be masked is in a range between 4 % and 10 %.
Tests of the FLT hardware in the year 2000 revealed that some of the optical data links did not work. The number of links that needed to be masked ranged between 30 and 50 out of approximately 1100 for the outer tracker and muon system (tubes and pads). The uncertainty of the number of links to be masked results in a systematic error of 20 % for the occupancy as seen by the TFU wire memory. The systematic error for the trigger rate is 10 %.
The largest effect of the systematic error arises from the fact that it is not possible to recreate perfectly the content of the wire memory in the simulation as compared to the reality in the hardware. Problems of the data path between the FED and the TFU wire memory are submit to fluctuations which cannot be quantified in a unique number.

The systematic error of the results due to the various effects discussed above is large compared to the statistical error. The large systematic error allows only for rough estimates with respect to occupancy, deadtime and trigger rate for upcoming runs at the discussed target rates.

5.4 Summary and Conclusion

The motivation for this study is to give an estimate on the FLT performance with respect to trigger rate in the single-track trigger mode and for a pair trigger. The critical issue of deadtime is examined. It is also investigated if there is a correlation between message load in the system and hits in detector components not used in the FLT, and with energy deposition in the calorimeter.
The deadtime of the system is moderate for 5 and 10 MHz interaction rate whereas at 20 MHz the deadtime is too high for reasonable physics studies. For 20 MHz interaction rate, we admit that the model to calculate the deadtime results in too high values which means that the assumption that one TFU blocks the complete network is not applicable.
For all three interaction rates, clear correlations of message load and hits in the RICH and PC 2 and energy deposition in the inner calorimeter are difficult to see.
The estimated single-track trigger rates for 5 MHz target rate at a nominal p_T-cut of 1.0 GeV/c for muons and 1.4 GeV/c for electrons is 20 kHz for the use of muon and electron pretrigger. This rate can be handled by the SLT without any implication. The rate can be reduced when a veto in the RICH and/or the ECAL is applied. A veto in PC 2 can also be taken into account.
The estimated trigger rate for a target rate of 10 MHz at nominal p_T-cut is in the order of 50 kHz for both pretriggers together. This rate can only be reduced with a veto at 10 % J/ψ loss to an acceptable rate that can be handled by the SLT. Rate fluctuations, however, might still generate complications for the SLT.
An interaction rate of 20 MHz is only reasonable for single lepton triggering with the muon pretrigger only at nominal p_T-cut and with a veto at 10 % J/ψ loss. Even at that limited setup rate fluctuations harm the performance of the system.
We also show in this analysis that for higher interaction rates (10 or 20 MHz) the pair trigger is in favour of the single track trigger. For 20 MHz interaction rate we have an occupancy of about 9 % and we expect a pair trigger rate of 19 kHz which is below the limit of the input rate to the SLT.
Table 5.8 summarises the results of the rate and latency measurement. The single-track trigger rates are taken at veto cut for the RICH corresponding to a 5 % J/ψ loss and nominal p_T-cut. The pair rate are determined with clone removal enabled and a combined usage of electron and muon pretrigger.

Interaction Rate [MHz]	Occupancy [%]	Deadtime [%]	μ trigger rate [kHz]	e trigger rate [kHz]	Pair trigger rate [kHz]
5	3.9	4.4	5.1	12.1	0.45
10	5.7	10.1	8.3	28.3	2.0
20	9.2	42.1	31.2	51.7	17.1

Table 5.8: *The results of rate and latency measurement. The single-track trigger rates are taken at veto cut for the RICH corresponding to a 5 % J/ψ loss and nominal p_T-cut. The pair rates are given for a combined setup of muon and electron pretrigger. The clone removal is enabled.*

Chapter 6

Acceptance and Efficiency Studies

During the year 2000 running period the First Level Trigger (FLT) was in the commissioning phase and was only partially used. We use a bit-level simulation to understand the behaviour of the FLT and especially that of the Track Finding Unit (TFU), which performs the fast online-tracking. Based on the simulation we try to estimate the single-track and J/ψ efficiency. We also examine the geometrical acceptance, the behaviour as a function of the transverse momentum p_T of the track, of x_F and with respect to the transverse momentum p_T of the J/ψ.
We use both SLT-triggered data and Monte Carlo samples to determine the efficiencies. Main emphasis of this analysis is given to the muon channel $J/\psi \to \mu^+\mu^-$.
First, we give an overview of the used event samples and present the method to determine the efficiency. In the following sections, we study the acceptance and efficiency for single tracks originating from $J/\psi \to \mu^+\mu^-$ events and also for the events themselves.
Two sections concentrate on the acceptance and efficiency as a function of the transverse momentum $p_T^{J/\psi}$ of the J/ψ and as a function of the kinematic variable x_F.
Finally, we present an alternative method to determine the J/ψ efficiency and give a summary and a conclusion.

6.1 Data and Monte Carlo Samples

In this section, we present the data and Monte Carlo samples used for efficiency determination and the method how we derive the single-track efficiency.
During the data taking in the year 2000, data were triggered by the SLT. Out of this data sample the SLT group provided a "hard selection" of $J/\psi \to \mu^+\mu^-$ candidate events. At the time this selection was created it was the best available reference track sample for efficiency determination.

6.1.1 "Hard Selected" J/ψ

In total, the sample consists of 11761 $J/\psi \to \mu^+\mu^-$ events that are triggered by the SLT only which means that there is no FLT online bias. The criteria of the "hard selection" are as follows [Schme00]:

- The momentum of the muon track candidate does not exceed 200 GeV/c,

- the transverse momentum p_T of the track is larger than 0.8 GeV/c and the sum of $|p_T|$ of the two tracks is above 2.5 GeV/c,
- the invariant mass of a track pair of an event to select is larger than 2.0 GeV/c^2,
- for each SLT track a corresponding VDS segment exists.

6.1.2 Monte Carlo Samples

In addition to the real data sample, the SLT group provided a set of Monte Carlo (MC) events for the channel $J/\psi \to \mu^+\mu^-$. Besides the "true information" as generated by the Monte Carlo ("MCtruth") these samples comprise the simulated SLT information with its trigger decision. Both pieces of information (MCtruth and SLT information) are available for a perfect working detector as well as for a masking that reflects the average detector performance for the running period 2000.

6.2 Method

The FLT simulation is run inside the ARTE framework to process the samples described above. For each event we simulate the muon pretrigger based on hit coincidences in the pads of MU 3 and MU 4 which is a mandatory input for the FLT simulation.
The pretrigger transmits its track candidates coded in an 80 bit message which is received by the TFUs of the MU 4 superlayer. The message is updated if a hit is found and sent to the following superlayers through the entire FLT. Found and updated (i.e. "valid") messages are converted to tracks at the specific superlayer.
We select reference tracks for all superlayers used by the FLT (see section 6.2.1) and try to match them with a simulated FLT track candidate. The ratio of simulated FLT tracks matching to a reference track and of the total sample of reference track determines the efficiency (see section 6.2.2).
The simulation allows us to describe imperfections of the used superlayers or of the FLT itself as recorded during the year 2000 run by applying a masking of single channels or links, respectively.
The FLT simulation assigns to each track candidate a time stamp at generation and at the processing in each superlayer. By means of this time stamp the FLT simulation discards track candidates that arrive later than 103 bunch crossings after generation at the Trigger Decision Unit (TDU).

6.2.1 Selection of Reference Tracks

Reference tracks are defined as follows:

- The reference track has to be inside the FLT acceptance which means that at least one TFU has to be crossed in each superlayer. During the year 2000 data taking the inner tracker and the pixel system were not equipped with TFUs (i.e. could not be used by the FLT) which limits the FLT acceptance to the outer tracker and muon tube and pad chambers (outer region).

In each of the stereo layers of the outer tracker and the muon system a hit is required. Since there are no stereo views for the pad layers MU 3 and MU 4 at least one hit is required here.

- The reference tracks of one event must have opposite charge. For real data the charge is assigned according to the sign of the track slope in PC 1 since the slope is measured as precisely as possible in this superlayer and thus provides the best knowledge. For MC the charge is assigned according to the charge of the generated particle.
- We require a minimal momentum of 5 GeV/c because muons with lower momentum do not pass the absorber layers of the muon system. In addition, we require a transverse momentum of at least 0.5 GeV/c.

The track parameters of each track that fulfils the criteria above are stored for each superlayer.

6.2.2 Matching Procedure

In the following, we describe the strategy to find out if a reference track is found by the FLT.
For each event the FLT simulation generates messages (or tracks, which is equivalent) according to found hits in the pad layers or according to found triple hit coincidences for the outer tracker layers or the MU 1 layer. In a first step, we determine the residuals for x and y position in each superlayer between simulated FLT tracks and –depending on the input– real SLT tracks or MC tracks, respectively.
In Figure 6.1 we present the residuals for the best matches between the hard selected reference tracks and the simulated FLT tracks. The discrete residual plot in y for the muon pad chamber reflects the pad size and the binning applied by the FLT. The residual plot for the pad chamber in x direction looks different since the FLT takes the wire information of the tube chambers and uses a finer binning. For MC samples we find a continous residual distribution since we have the continous impact point information.
We fit signal and background with the sum of a gaussian and a quadratic function

$$f(x) \;=\; p_0 \cdot \exp\left(-\frac{1}{2}\cdot\left(\frac{x-p_1}{p_2}\right)^2\right) + p_3 + p_4 \cdot x^2 \tag{6.1}$$

and determine the widths σ_x and σ_y (parameter p_2). We calculate a quadratic function s^2 of the track parameters which is defined as

$$s_i^2 \;=\; \frac{(x^{ref} \;-\; x_i^{sim})^2}{\sigma_x^2} \tag{6.2}$$

for two parameters x- and y-position. The variables x^{ref} represent the track parameters of the reference track and x_i^{sim} those of the simulated track. The σ_x^2 is taken from the residual fit as shown in Figure 6.1. The index i reflects the fact that the simulation generates additional messages that can be matched with the reference track. The simulated FLT track with minimal s^2 is considered closest to the reference track. In the case that the errors σ_x^2 are known and understood the function s^2 becomes a χ^2 distribution. In

this analysis, we calculate the s^2 only for the x-position and require that FLT track and reference track do not differ by more than 20 cm in y-direction which is approximately two times the pad size. We select this criterion because the y information is not known by the SLT in MU 1. To be able to directly compare SLT triggered data with MC data we apply this criterion for MC tracks, too.
For a match of a reference track with a simulated FLT track we only take tracks into account for which an update exists in all previous superlayers. Additionally, we require that the simulated FLT track of the superlayer of interest matches with the same reference track as in the previous layers. The reason for this requirement is that we want to assure that the FLT tracking follows one reference track. All the results are stored for each superlayer and used to determine the single-track efficiency of the specific superlayer (see section 6.3.4). In the approximation that we have gaussian like errors we determine the probability of s^2. Figure 6.2 (left) shows a s^2 probability distribution of a superlayer for all combinations of reference tracks and simulated tracks. The applied cut on s^2 is 18. The same distribution

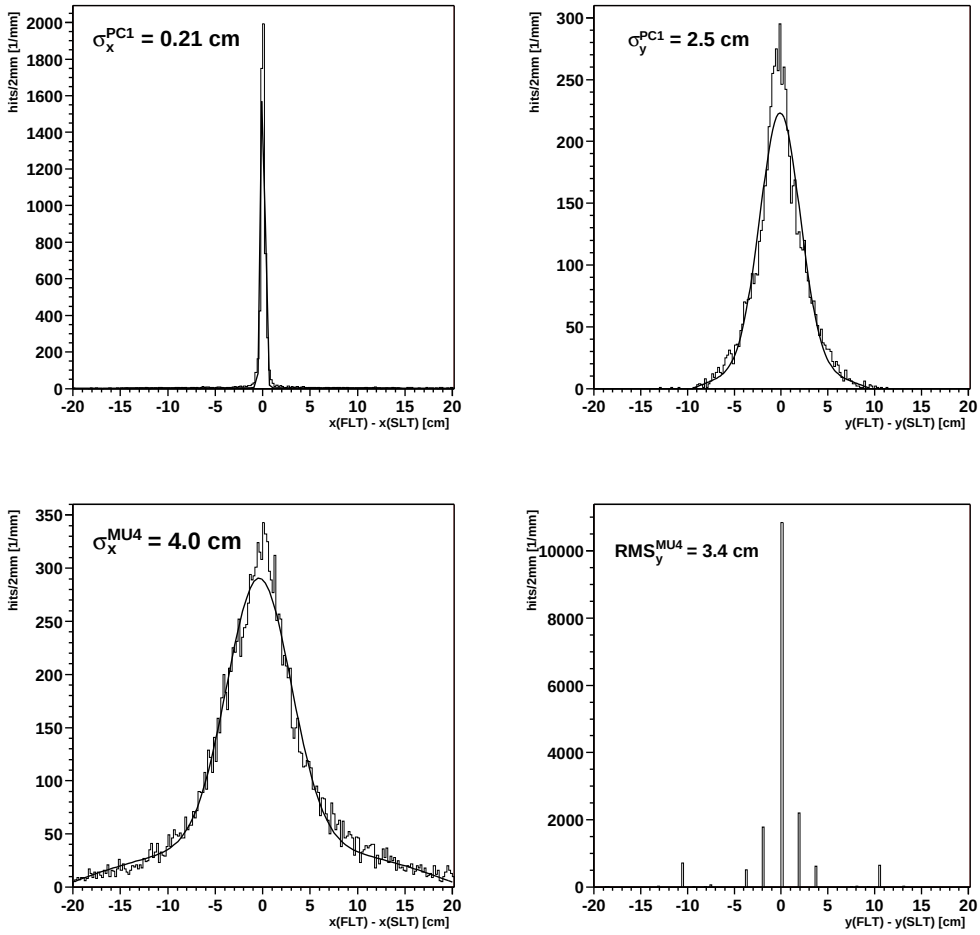

Figure 6.1: *Residuals of simulated FLT tracks and triggered SLT tracks for the best matches at PC 1 and MU 4. The discrete residuals of MU 4 reflects the pad size and the binning of the FLT.*

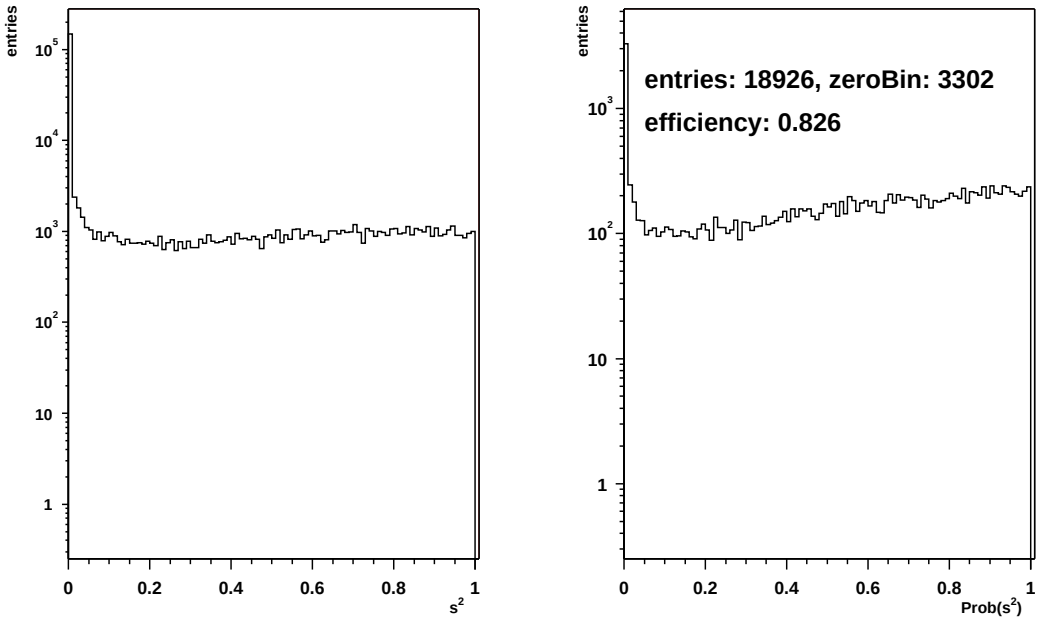

Figure 6.2: *Left: s^2 probability distribution of all combinations of hard selected reference tracks and simulated FLT tracks. The applied cut for the s^2 test is 18. Right: The probability distribution of s^2 for the reference track found closest to a simulated track.*

is evaluated for the best match. We expect the s^2 probability distribution to be flat if the measured quantities obey a gaussian distribution and all combinatorical possibilities are recorded.
Figure 6.2 (right) shows the probability of the s^2 distribution which we use to determine the efficiency. The analytical expression to calculate the s^2 probability for n degrees of freedom is given by:

$$P(s^2, n) \;=\; \int_{s^2}^{\infty} \frac{z^{n/2-1}\; e^{-z/2}}{2^{n/2}\;\Gamma(n/2)}\; dz \tag{6.3}$$

The s^2 probability distribution for the best match slightly increases towards higher probability because we bias it by requiring a subset (i.e. the best match) out of all combinatorical possibilities. Entries in the zero bin represent reference tracks with a probability between zero and the limit determined by the bin size to be found by a simulated FLT track, i.e. reference tracks that cannot be retrieved by a simulated FLT track[1].
Entries at zero probability are a measure of inefficiency. We derive the single-track efficiency according to:

$$\epsilon_{track} \;=\; 1 \;-\; \frac{entries(prob(0))}{total\ entries}. \tag{6.4}$$

Total entries represents the number of reference tracks and *entries(prob(0))* indicates the number of tracks that cannot be retrieved by a simulated FLT track. The method to

[1]Entries at probability one would indicate that those reference tracks are found all the time. A peak at probability one would indicate that the criteria to match an FLT track to the reference track is not strict enough and consequently the allowed distance between the tracks to match should be made more narrow.

determine the efficiency presented in this section is only a good approximation. A more sophisticated method requires a separate study of the background in order to improve the understanding of the errors that enter the quadratic function s^2.

6.3 Results for Single-Track Acceptance and Efficiency

In this section, we first calculate the geometrical and kinematical acceptance for muon tracks originating from simulated $J/\psi \to \mu^+\mu^-$ events.
We then build a subsample of tracks for perfect MC to determine the hit efficiency of superlayers used by the FLT for triggering as this is a mandatory quantity for the track efficiency.
Besides the reference tracks taken from the MC samples, we use the hard selection as reference to determine the single-track efficiency. Since the real data are biased by the SLT trigger decision we investigate this bias in the MC sample.
At the end of this section we present the track and event efficiency as a function of the p_T cut since increasing this cut is a useful handle to reduce the trigger rate as long as the J/ψ efficiency is basically preserved.
We present the single-track efficiency of the FLT with respect to the requirement that the reference tracks are in the "outer region". In addition, we present the results for the single-track efficiency with respect to the p_T of the track, to p_T and the x_F of the J/ψ.

6.3.1 Track Acceptance

For $J/\psi \to \mu^+\mu^-$ MC events we categorise to what part of the HERA–B detector the tracks belong to, i.e. outer region (outer tracker and muon tube and pad system), inner region covered by inner tracker and pixel system or not in the acceptance of HERA–B at all (e.g. beam pipe). For this study we do not require a minimal transverse momentum but we still demand a momentum of at least 5 GeV/c. A track of the J/ψ is considered to be in the outer region if it fulfils the first criterion stated in section 6.2.1. A track which has no impact point in a superlayer that is connected to a TFU is considered to be not in the outer region.
A track whose ratio of p_T/p_z is in a range between 0.01 and 0.1 (the approximate angular coverage of the inner tracker and the muon pixel system) and is not in the outer region is assigned to be in the inner region. We include tracks in this category that cross from the inner to the outer tracker.
Tracks that do not satisfy neither criteria above are flagged as 'not in the HERA–B acceptance'. Tracks with impact points in the region of the electron beampipe are also accumulated in this category.
Figure 6.3 shows the resulting geometrical acceptance for the categories mentioned above. The sum of the points in the histogram is one. We distinguish tracks that are not in the HERA–B acceptance: they are either in the beampipe or they are outside of the active detector volume, i.e. the tracks have impact points only up to a certain superlayer. The circles and the upside down triangles at p_T of 0.2 and 0.4 GeV/c happen to fall on top of each other.

The geometrical acceptance becomes rather flat above a p_T threshold of 0.7 GeV/c.

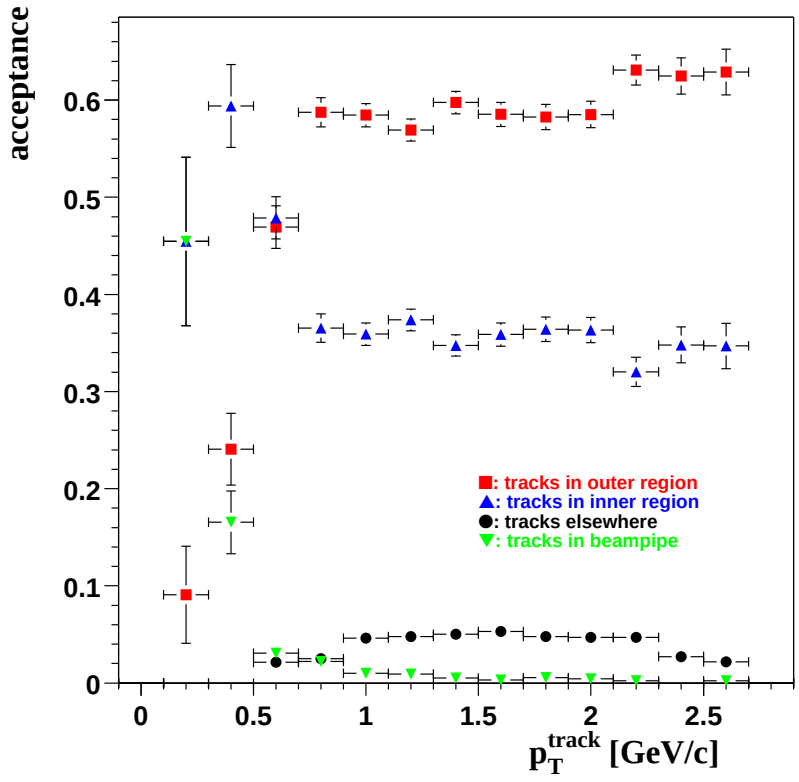

Figure 6.3: *Geometrical and kinematical acceptance of muon tracks from $J/\psi \to \mu^+\mu^-$ MC events. At lower p_T, the tracks are either in the inner part or not in the HERA–B acceptance. With increasing values of p_T the tracks populate the outer region more. The sum of the data points is one. The circles and the upside down triangles at p_T of 0.2 and 0.4 GeV/c happen to fall on top of each other.*

At lower values of p_T, most of the tracks are in the inner region of the detector or completely in the beampipe. With increasing p_T the number of tracks that are in the acceptance of the outer region increases.
The acceptance of the outer region covers a range between 10 % at p_T less than 0.2 GeV/c and 64 % at 2.6 GeV/c. Figure 6.4 shows the p_T^{track}-spectrum of the muons originating from $J/\psi \to \mu^+\mu^-$events. The average transverse momentum is 1.3 GeV/c.

6.3.2 Hit Efficiency

The track efficiency depends strongly on the hit efficiency of the detector. A bad track efficiency can be due to a bad performance of the detector layer itself.
We evaluate the hit efficiencies of the superlayers used for triggering by the FLT with MC techniques. We use the MC impact point information to reconstruct tracks. For all tracks we check if a hit can be found in all stereo views of the wire memory of the corresponding TFU within the width of one cell. Each track that has at least one hit within the width of one cell contributes to the hit efficiency. Consequently, the numbers presented in Table 6.1 are the product of the efficiencies to have at least one hit within one cell close to the

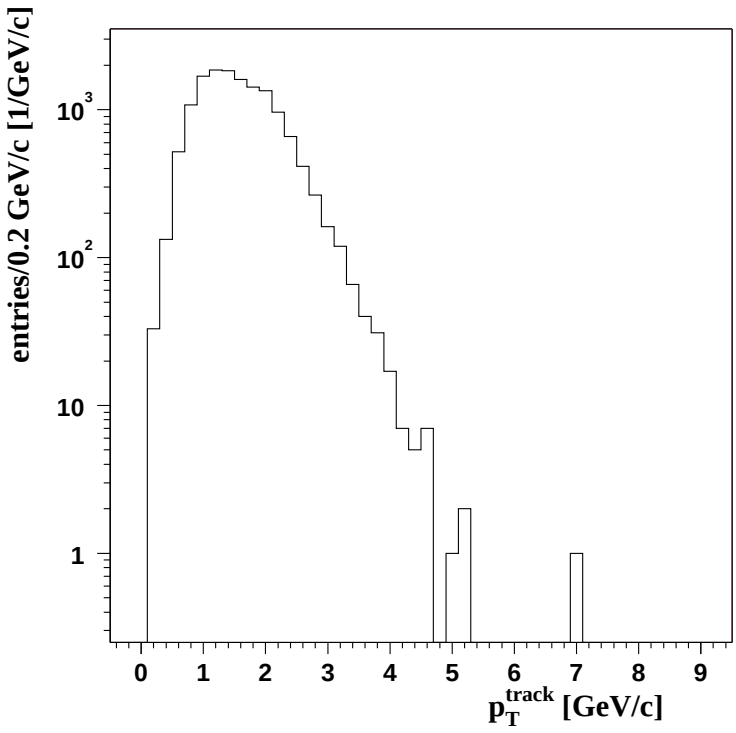

Figure 6.4: *p_T spectrum of muon reference tracks from $J/\psi \to \mu^+\mu^-$. A minimal track momentum of 5 GeV/c for the muon is required.*

reference track in each view. The numbers in Table 6.1 are normalised to all reference tracks.

We emphasise that the results for the hit efficiency can be different from the results found for the detector only [Hul01] since we include in the hit efficiency possible inefficiencies of the transmission (e.g. failure in the optical data transmission, mapping errors) of the data from the FED to the TFU on a statistical basis.

The hit efficiencies for MC events without any masking ("perfect MC") are found to be above 90 % for all superlayers as shown in Table 6.1. The statistical error is of the order of 0.5 %. The hit efficiency for each single cell was set to unity.

For MC events that simulate the actual performance of the detector ("realistic MC") as in the year 2000 run the hit efficiencies are in the range between 70 and 95 %. The statistical error is between 0.7 and 0.5 % (Table 6.1).

Table 6.1 summarises the hit efficiencies of the superlayers for perfect and realistic MC as seen by the wire memory of the TFU. We expect hit efficiencies of the order of 0.99 for perfect events. The hit efficiencies for perfect MC events are significantly lower. One known reason is a problem in the mapping between detector channels and the wire memory. As a consequence, a hit wire is related to a point which is not inside the accepted range of the wire memory, or it is not close to the expected impact point position. Details on this problem can be found in [Noe01]. A detailed study of the hit efficiency of 98.5 % for MU 4 revealed that the problems are located in one module below and above the notch of the electron beampipe. The hit efficiency of 97.6 % for MU 1 is related with problems of the mapping. In addition, we chose a strict requirement for a hit to be within one cell around

	MU 4	MU 3	MU 1	TC 2	TC 1	PC 4	PC 1
Perfect MC [%]	98.5	99.9	97.6	90.6	96.6	97.1	94.1
Realistic MC [%]	93.8	95.0	70.7	77.6	82.0	88.4	84.4

Table 6.1: *Efficiency for finding all hits in a given superlayer as seen by the wire memory of the TFU without SLT bias. The low hit efficiencies of the outer tracker layers are discussed in [Noe01].*

the expected position. Details are described in chapter 7.
The low hit efficiency for the layers MU 3 and MU 4 for realistic MC reflects the problems (readout, etc.) of those layers during the year 2000 [Nam00]. Since the muon pretrigger forms pad coincidences to generate a trigger we expect to have hits in the specific tube layers. During the year 2000 run the performance of the pad layers decreased with time [Her00]. Compared to perfect MC, the drop in hit efficiency from MU 3 to MU 1 is larger because the performance of MU 1 was significantly below expectation.

6.3.3 Bias due to SLT Trigger Decision

At the end of the year 2000 run the hard selected data set triggered by the SLT was the best available reference track sample. The SLT trigger decision however imposes a bias. We determine the size of the bias by comparing the FLT efficiencies for the events that are triggered by the SLT with the efficiencies for events without the trigger decision of the SLT.
The tracking in the muon system is highly biased by the SLT trigger decision. The SLT uses the vertical wire information which is used by the FLT, too. The FLT was not used for triggering during the data taking in the year 2000. The SLT performed its trigger algorithms directly on the pretrigger input. To reduce the high input rate from the pretrigger the SLT requires a hit in each of the single-layers. Each view consists of two single-layers that are shifted by half a cell with respect to each other to give redundant information for triggering. The SLT performs in the outer tracker a similar tracking algorithm like the FLT which may bias the FLT efficiency. It is important to understand the biasing effects and their respective magnitudes to get reliable results for the FLT efficiency.
The SLT group provides different MC sets to unravel the bias. In total, we have four different data sets:
With and without the trigger decision of the SLT and each with masking and without, respectively.
We process each data set individually with the FLT simulation and determine the track efficiency. We calculate the ratio of efficiencies for data sets with SLT trigger decision and without for each superlayer. We apply the same procedure for the data sets with masking and without. The track efficiency for the TPU is evaluated by correcting the track efficiency of PC 1 by a factor of 0.96 which reflects the efficiency of the TPU [Res01]. This factor comprises problems in the binning of momentum values and has implications on the applied p_T-cut. For the J/ψ efficiency we take the squared TPU efficiency (0.96^2) [Res00]. The obtained results for the track as well as for the J/ψ efficiency are multiplied by the TDU efficiency which is 0.92 and takes into account the tracks that arrive too late, i.e. later

than 103 bunch crossings after the interaction took place, at the TDU [Res01].
Table 6.2 summarises the bias imposed by the SLT trigger decision for each superlayer (TPU and TDU are considered as a superlayer). The biases evaluated for realistic MC are used to correct the hard selected data to compare them and to determine at what level the realistic MC describes the reality of the year 2000 run (see Figure 6.5). The bias due

	MU 4	MU 3	MU 1	TC 2	TC 1	PC 4	PC 1	TPU	TDU
Perfect MC									
Track [%]	98.3	98.8	95.8	92.5	92.6	91.5	90.3	90.3	90.4
J/ψ [%]	97.6	97.5	94.4	90.3	89.8	87.2	84.1	83.9	84.0
Realistic MC									
Track [%]	95.0	96.1	80.3	75.3	71.4	70.1	66.9	67.0	66.6
J/ψ [%]	94.1	95.8	72.8	61.8	52.3	52.2	49.3	49.3	48.4

Table 6.2: *Ratio of efficiencies for track and J/ψ due to the bias from the SLT trigger decision evaluated individually for perfect and realistic MC for each superlayer used by the FLT.*

to the SLT is stable for perfect MC in the outer tracker and is slightly higher (correction factor changes for every superlayer) in the muon system. A stable bias for the outer tracker means that the tracking of the FLT does not depend on the tracking of the SLT. The ROIs (Regions Of Interest) of the SLT are larger than those of the FLT.
The bias due to the SLT for realistic MC is stable up to TC 1. The relative steps between TC 1 and TC 2 and between MU 1 and MU 3 are higher than for perfect MC which is an effect of the masking.
The total correlation between FLT and SLT including the pretrigger for perfect MC is about 10 % and for realistic MC it is of the order of 33 %. The FLT finds 90 % of the reference tracks for perfect MC that SLT has also triggered. In the case of realistic MC the FLT finds only 67 % of the SLT triggered reference tracks.

6.3.4 Single-Track Efficiency

For the track efficiency we require that both reference tracks be in the geometrical acceptance of the FLT. We only accept track pairs that have unlike charge, a minimal momentum of 5 GeV/c and a minimal transverse momentum of 0.5 GeV/c.
The results shown in Figure 6.5 are for MC with a perfect detector, for MC that assumes a realistic detector performance and for the hard selected J/ψ data. All the results are pure FLT efficiencies, i.e. they are corrected with respect to the bias due to the SLT and to the pretrigger efficiency.
The track efficiency for the TPU and the TDU are determined as described in the previous section. The single-track efficiency is for perfect MC, for realistic MC and for real data:

$$(59.2 \pm 0.5)\ \%, \quad (16.6 \pm 0.4)\ \% \ \textit{and} \ (18.8 \pm 0.2)\ \%.$$

As can be seen from Figure 6.5 the realistic MC and the SLT triggered data (hard selected) agree well for each superlayer. The large decrease of efficiency at MU 1 observed

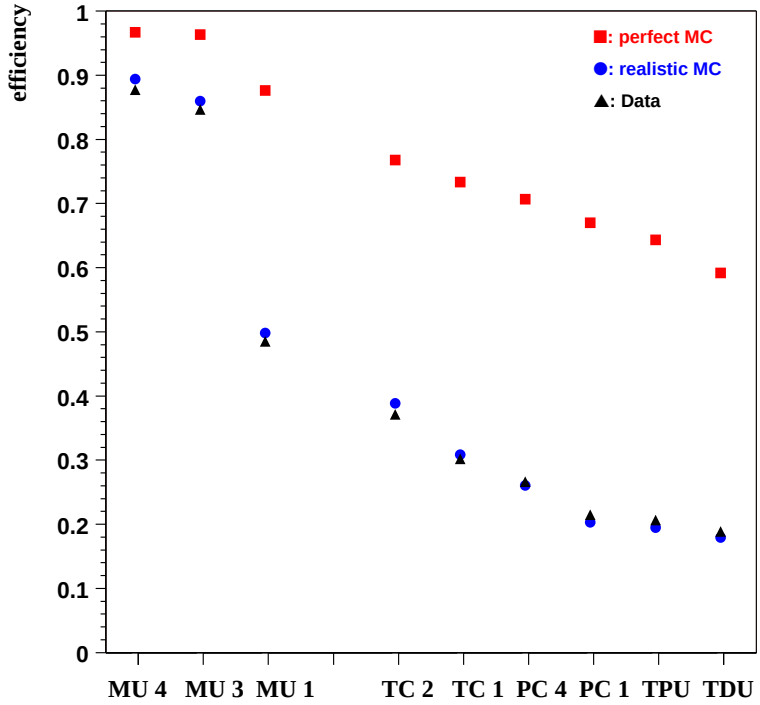

Figure 6.5: *Single-track efficiency for MC events and real data. It is required that the reference tracks be inside the geometrical acceptance of the outer region, that they have unlike charge, a minimal momentum of 5 GeV/c and minimal p_T of 0.5 GeV/c.*

in realistic MC and data is a dramatic deterioration of performance and is subject of a separate analysis (see chapter 7). The tracking algorithm of the FLT needs to be checked if improvements can be done to reduce the loss of efficiency from superlayer to superlayer (e.g. loss from MU 1 to TC 2). The efficiency for data is also in agreement with the result obtained during the year 2000 run [Fla00b].
If we do not require a minimal momentum and a minimal p_T the performance of the tracking algorithm gets worse since tracks that do not fulfil these requirements are hardly reconstructable by the FLT. These results are approximately 5 % lower.
In addition to this selection criteria for the reference tracks, it turned out that the track efficiency of the FLT also depends on the coding of track parameters that is used by the muon pretrigger. The pretrigger can either code the parameters according to an average momentum distribution of the J/ψ or according to a minimal momentum coding which requires a minimal momentum for a track to reach a certain position in the detector [Ada01a]. The effect of the pretrigger coding is of the order of a few percent. The minimal coding enlarges the Region of Interest (ROI) which consequently improves the track efficiency because the probability becomes larger to find coincidences in a larger ROI.
Besides the information of the MC impact point which is used for the track parameters, we also investigate the track efficiency based on the SLT information: Instead of using the MC impact point, we use the points that the SLT simulation found for this track and that finally lead to a trigger for the event. It is the same kind of information for MC that is

	Muon + OTR		OTR only	
	ideal	aligned	ideal	aligned
Ideal [%]	81.3	61.1	96.5	90.9
Wrongly Mapped [%]	76.9	57.7	90.5	84.8
Hard Coded [%]	81.5	61.2	96.4	91.8
Hot, Dead, Noisy [%]	63.0	48.3	74.8	70.9

Table 6.3: *Effect of detector inefficiencies on track efficiency for ideal and aligned geometry separated for tracking including muon and outer tracker and outer tracker only. The statistical error is of the order of 1 %.*

provided with the hard selected data. The results for these perfect and realistic MC are in agreement with the results based on MC impact point information including the bias due to the SLT trigger decision. The shape of the efficiency curve looks similar to the one presented in Figure 6.5.
Within the statistical error there is no difference between positive or negative charged muons.
The track efficiency at the TPU for the perfect MC sample is slightly above the expected 60 % that is derived from a different simulation ("toy simulator"). One of the differences between MC and the toy simulator is the way how the hits are set in the wire memory. The discrepancy of both approaches to evaluate the track efficiency for a perfect detector performance is studied in [Noe01].

Toy Simulator

The toy simulator generates tracks as straight lines originating from the target. The effect of the multiple scattering is neglected. The tracks cover a momentum range between 5 GeV/c and 200 GeV/c according to a 1/p distribution. The tracks have a minimal transverse momentum of 0.5 GeV/c. The toy simulator generates only tracks that are in the sensitive region that is connected with TFUs with one exception: the notch for electron beampipe is not treated correctly. Hits in the notch are generated in the wire memory that are not set in reality. The efficiencies determined by the toy simulator are higher than the efficiencies obtained from MC. The toy simulator allows to study the impact of detector ineffiencies by applying a masking which reflects the imperfection. The study of these effects is more comfortable and faster as in case of MC. The effects of the detector imperfection as presented in Table 6.3 are determined with the toy simulator. The definition of the detector inefficiencies was presented in section 5.1.1.
In Table 6.3 we summarise the effect of detector inefficiencies on the single-track efficiency. We separate the results for ideal and aligned geometry. In the ideal case we assume an equidistant spacing of the wires throughout the region that is connected to the TFU. In the aligned case we use the real spacing of the wires which takes into account the support structures and the separation of the superlayers into two halves. In addition, we separate the results for tracking in the outer tracker only and for tracking in the outer tracker and the muon system. The results are derived by using the toy simulator. The effects of the different inefficiencies shown in Table 6.3 need to be compared to the ideal case. The

largest effect is caused by the hot, dead and noisy channels because they affect directly the required triple coincidence that is necessary for an update of the track. Those channels decrease the efficiency by 21 %. The hard coded channels compared to the ideal case have no effect within the statistical error on the track efficiency. The wrongly mapped channels decrease the track efficiency by 5.6 % because hits in the detector are connected to a place somewhere in the TFU wire memory.
For tracking including the muon system the efficiency is 61 % which we have to compare to 59 % efficiency derived by MC techniques. Differences are an idealised description of the muon system in the toy simulator which treats the multiple scattering differently than in the MC data.

6.3.5 Single-Track Efficiency as a Function of p_T^{track}

In section 6.3.1, we presented the geometrical and kinematical acceptance for tracks originating from $J/\psi \to \mu^+\mu^-$ events with respect to p_T of the track. Since adjusting the p_T-cut in the TPU is a powerful handle to control the output rate of the FLT we investigate the effect of increasing the p_T-cut on the single-track efficiency. We also present the total acceptance times efficiency which is the fraction of tracks that are matched in each superlayer and arrive in time at the TDU out of all reference tracks.
For this analysis, we select events that have both tracks in the geometrical acceptance of the outer region (outer tracker and muon tube and pad system) or one track in the outer region and one in the inner region (inner tracker and muon pixel system). For tracks to be in the outer region they are required to have at least one hit in each stereo view of a region covered by one TFU.

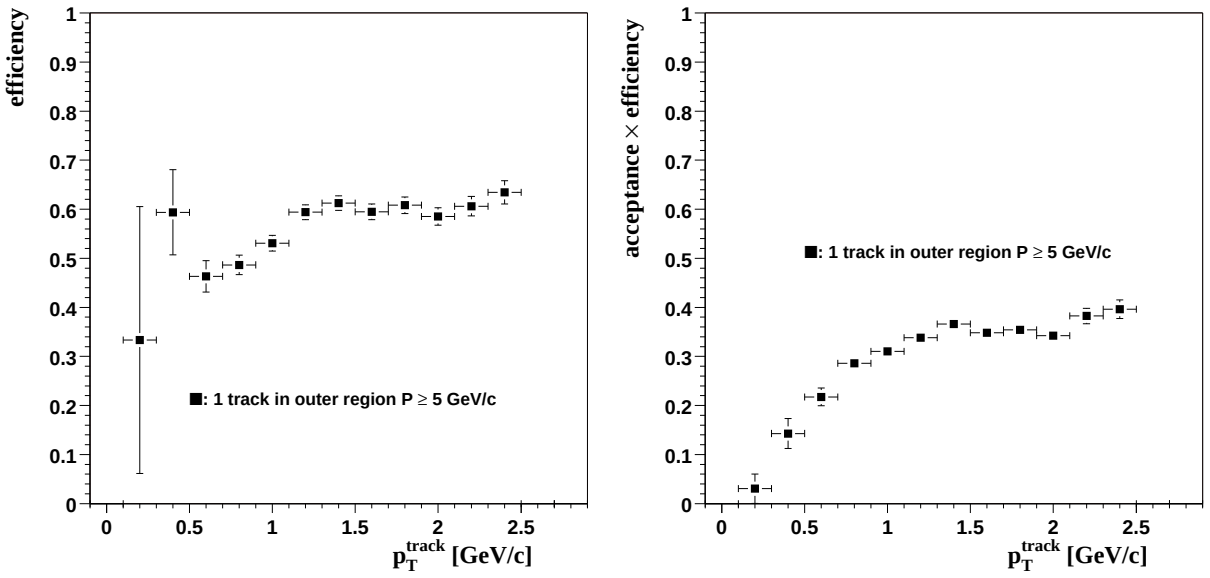

Figure 6.6: *Left: Single-track efficiency of the FLT for the outer region with respect to p_T bins. It is required that the reference tracks are inside the geometrical acceptance of the outer region, that they have a minimal momentum of 5 GeV/c. Right: Total acceptance times efficiency for the same reference tracks with respect to p_T-bins.*

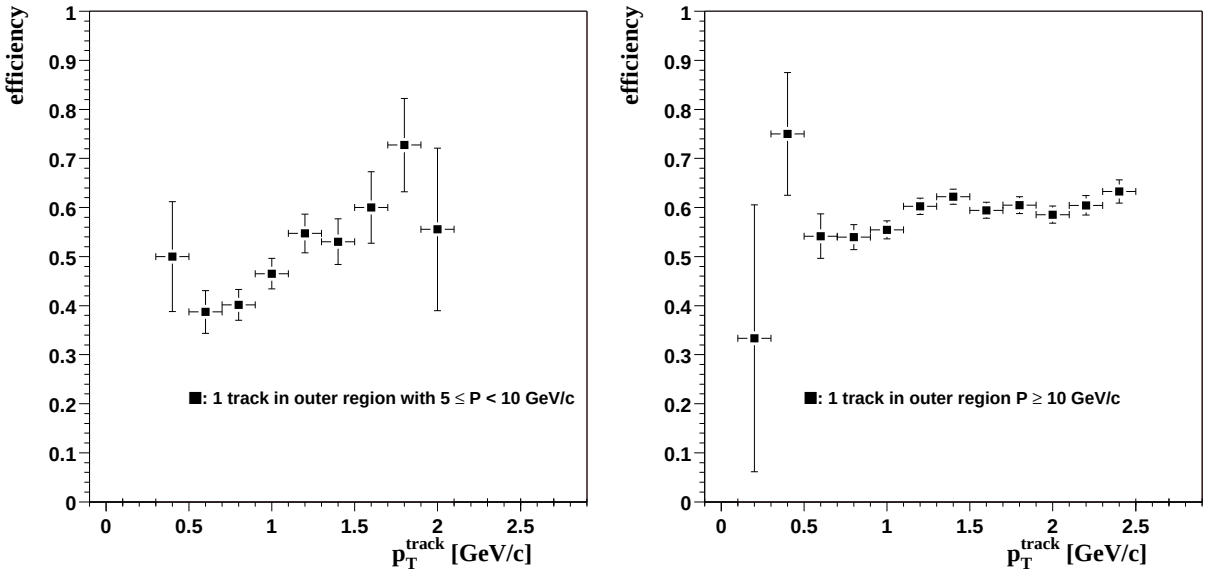

Figure 6.7: *Effect of the multiple scattering on the track efficiency. Left: Efficiency for track with a momentum between 5 and 10 GeV/c. The decrease of efficiency towards lower values of p_T is clearly evident. Right: The track efficiency for tracks whose momentum is larger than 10 GeV/c which results in flat efficiency distribution with respect to p_T.*

Figure 6.6 shows the single-track efficiency with respect to p_T. The efficiency is flat at 62 % for values of p_T above 1.2 GeV/c. The average efficiency for transverse momenta above 0.5 GeV/c yields

$$(59.1 \pm 0.5)\ \%$$

which we can compare with the track efficiency at the TPU level of ≈ 64 % as shown in Figure 6.5. The efficiency presented in Figure 6.5 assumes a pretrigger efficiency of unity. For the study above we only see a pretrigger efficiency of 0.94 which was determined by a different measurement. The numbers presented above need to be corrected by a factor of 1.06 to arrive at the same level of pretrigger efficiency and to be able to compare the results. Taking this into account we find the results to be compatible.
In Figure 6.6, we see a decrease of efficiency which can be explained as follows: The efficiency drop for values of p_T smaller than 1.4 GeV/c is due to the multiple scattering for the central region. The absorber in the inner muon system is made of iron around the central region (dx $\times$ dy: 1.6 $\times$ 1.2 m^2) whereas the absorber for the outer region consists of concrete. Figure 6.7 demonstrates this effect of the multiple scattering: On the left, we show the track efficiency for tracks with a momentum between 5 and 10 GeV/c. The decrease with respect to efficiency is clearly visible. On the right, we present the track efficiency for tracks with a momentum larger than 10 GeV/c which results in a flat efficiency with respect to the transverse momentum.

6.4 Results on J/ψ Event Basis

We briefly discuss some aspects on the general decay kinematics of the J/ψ. We then determine the event acceptance which means to have at least one track or both tracks originating from the J/ψ within a specified geometrical acceptance. We concentrate on the event acceptance for possible trigger scenarios. Finally, we calculate the event efficiency and the total acceptance times efficiency. We separate between the cases with at least one track or both tracks found by the FLT.

6.4.1 General Decay Kinematics

In Figure 6.8 we present the spectrum of the transverse momentum of accepted $J/\psi \rightarrow \mu^+\mu^-$ events for perfect MC. We use the MC momentum information of the leptons and reconstruct the momentum components of the J/ψ out of which we calculate the p_T of the J/ψ:

$$\vec{\mathbf{p}}_T^{J/\psi} = \vec{\mathbf{p}}_T^{\mu 1} + \vec{\mathbf{p}}_T^{\mu 2}. \tag{6.5}$$

The average transverse momentum of the J/ψ is 1.5 GeV/c. The spectrum ranges up to a transverse momentum of approximately 5 GeV/c. The fact that the J/ψ is generated with a transverse momentum has an impact on the leptons coming from the J/ψ. In Figure 6.9 we present the transverse momentum of one lepton versus the p_T of the other lepton of $J/\psi \rightarrow \mu^+\mu^-$ events requiring a minimal momentum of each lepton of 5 GeV/c. The transverse momenta of the leptons show an anti-correlation which we expect since the J/ψ

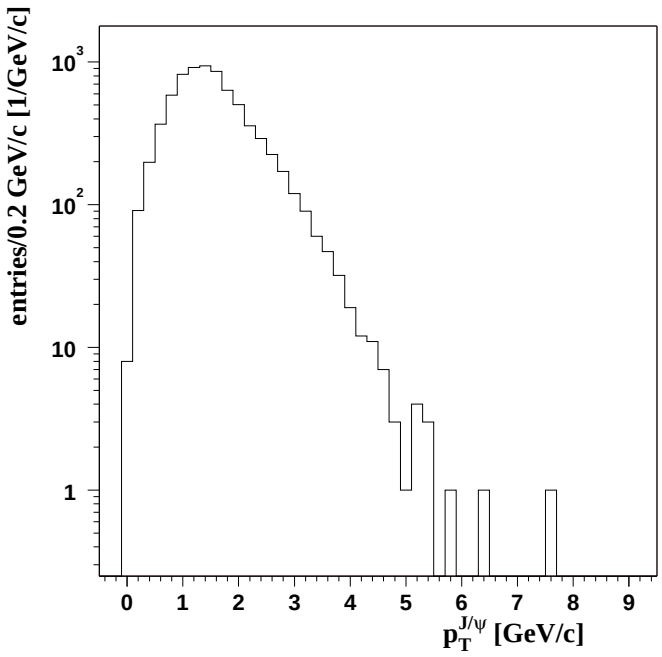

Figure 6.8: *Reconstructed transverse momentum of the J/ψ based on momentum components of the leptons for MC data. A minimal momentum of 5 GeV/c for the leptons is required.*

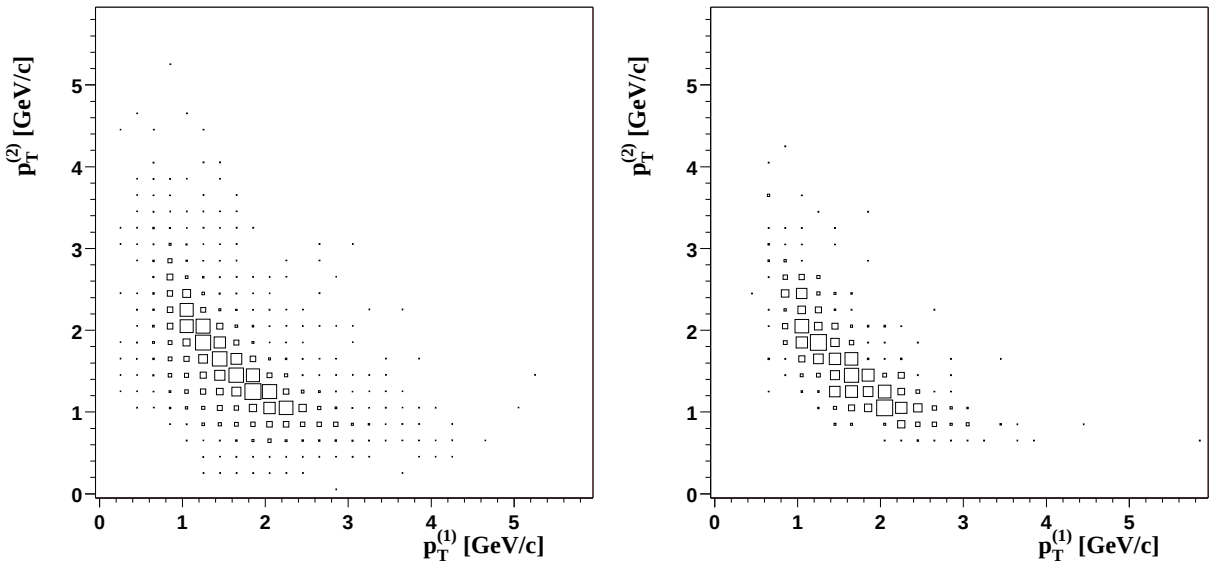

Figure 6.9: *Left: The transverse momentum of one lepton vs the transverse momentum of the other lepton of $J/\psi \to \mu^+\mu^-$ events (lin. scale for z-axis). We require a minimal momentum of 5 GeV/c for the leptons. Right: The reconstructed transverse momenta as calculated by the TPU.*

is generated with an intrinsic transverse momentum (see Figure 6.8). In the rest frame of the J/ψ both leptons decay back to back. If the J/ψ had no transverse momentum the transverse momenta of both leptons would be equal but with opposite direction. In case that p_z of the J/ψ is zero in the CMS both leptons are maximally transverse. An intrinsic transverse momentum leads to an anti-correlation of the transverse momenta of the leptons since one lepton gets additional p_T whereas the other lepton gets reduced p_T. The intrinsic p_T of the J/ψ is conserved. The absolute value of one particle is larger than that of the second. In Figure 6.9 on the right we present the distribution of the transverse momenta of both leptons that are reconstructed by the FLT on the TPU level. Both distributions of transverse momenta are important to understand the event acceptance as a function of p_T of the track for the various cases stated below.

6.4.2 Event Acceptance

We investigate the event acceptance for the FLT with respect to p_T^{track} for various combinations of two tracks from various detector regions. These are possible options which are discussed for the data taking of 2002. In order to illuminate the single-track or pair trigger option, we consider the following possibilities by selecting

- events with at least one track in the outer tracker and the outer muon tube and pad system (outer region). It is a single–lepton trigger requiring that one of the tracks exceeds a given p_T threshold,

- events with two tracks in the outer region that both exceed a given p_T threshold (pair trigger in outer region),
- events with at least one track in the outer region or at least one track in the inner region,
- events with either two tracks in the outer region or two tracks in the inner region or one track in the outer and one track in the inner region. Here we require that both tracks exceed a common p_T threshold (pair trigger for entire HERA–B acceptance),
- events with two tracks in the outer region or one track in the outer and one track in the inner region. We require only one track to exceed a p_T threshold.

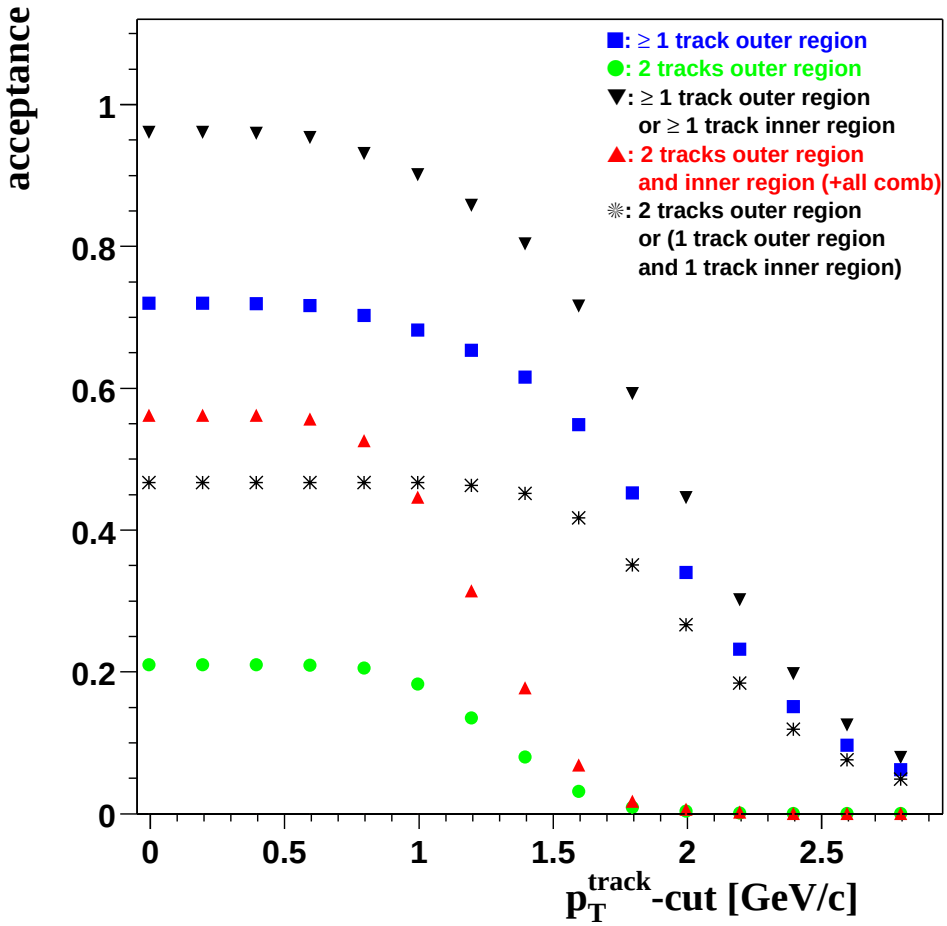

Figure 6.10: *MC* $J/\psi \to \mu^+\mu^-$ *event acceptance as a function of the cut on* p_T^{track} *for various event selections.*

The resulting acceptances are shown in Figure 6.10. If the inner region were covered by the FLT a pair trigger (upward pointing triangles in Figure 6.10) would be the preferred trigger scenario. Without FLT-coverage of the inner region a pair trigger scenario decreases the event acceptance by more than 50 % (circles in Figure 6.10).

A good compromise between those pair trigger scenarios is the solution that the FLT provides a single-track trigger. The SLT performs its search on the candidate from the FLT and looks for a second track in the inner region.
The acceptance decreases for a p_T-cut larger than 1.0 GeV/c which can be explained in the following way:
The J/ψ mass is 3.1 GeV/c^2. When a J/ψ decays the leptons can have a transverse momentum up to 1.55 GeV/c which is half of the available mass of the J/ψ converted to p_T. Consequently, up to a p_T-cut of 1.5 GeV/c we expect at least one track to contribute to the acceptance which should show no decrease up to that p_T-cut. Indeed the acceptance starts to drop before, which is due to the fact that there are tracks that do not have a transverse momentum or only a very small one and consequently do not contribute to acceptance. Above a p_T-cut of 1.6 GeV/c the acceptance decreases rapidly.
If we require that both tracks are above a p_T threshold the acceptance drops even faster and is almost zero above 1.6 GeV/c because of the mass of the J/ψ that can be shared by the two leptons. If the J/ψ has some transverse momentum due to its generation the transverse momentum that can be shared by the two leptons is higher.
The acceptance for two tracks in the outer region is of the order of 20 %. We have to take into account that the likelihood to have two tracks above a p_T threshold in the outer tracker becomes smaller with increasing values of p_T. For small transverse momenta the tracks are more likely in the inner part. The acceptance quoted here is subject to stricter combinatorics. For single-tracks we require one out of two possibilities to have at least one track in the acceptance whereas we demand two out of two for both tracks to be in the acceptance for an event.
The inner tracker most probably cannot provide input to the FLT. A pair trigger for the inner and outer region is not possible. The event acceptance for a pair trigger in the outer region only is rather low. A preferable solution with respect to event acceptance is a single-track trigger in the outer region performed by the FLT and to trigger the second track by the SLT in either the outer region or the inner region.

6.4.3 A Cross Check: 'Single-Track' versus 'Event' Acceptance

Besides the acceptance with respect to the selected trigger scenario we are able to investigate if the naive assumption is valid that the single-track acceptance squared results in the J/ψ acceptance.
Out of the acceptance to have at least one track in the inner or outer region (upside-down triangles in Figure 6.10) we calculate the acceptance to have one track.
Let A_{tr} be the probability to have one track in the acceptance. Consequently, the probability not to have a track is 1 - A_{tr}. The probability to have at least one of the tracks in the acceptance is given by "1 - the probability to lose both tracks":

$$A_{all} \;=\; 2 \cdot A_{tr} \;-\; A_{tr}^2, \tag{6.6}$$

under the assumption that the tracks are not correlated. We apply equation 6.6 to the value A_{all} = 95 % given for the acceptance to have at least one track in the outer or inner region at p_T-cut zero. We get A_{tr} = 77 % and square this. The result (60 %) is close, but slightly higher than the curve described by the black triangles at p_T-cut = 0 and indicates that there are correlations between the tracks. The squared single-track acceptance is

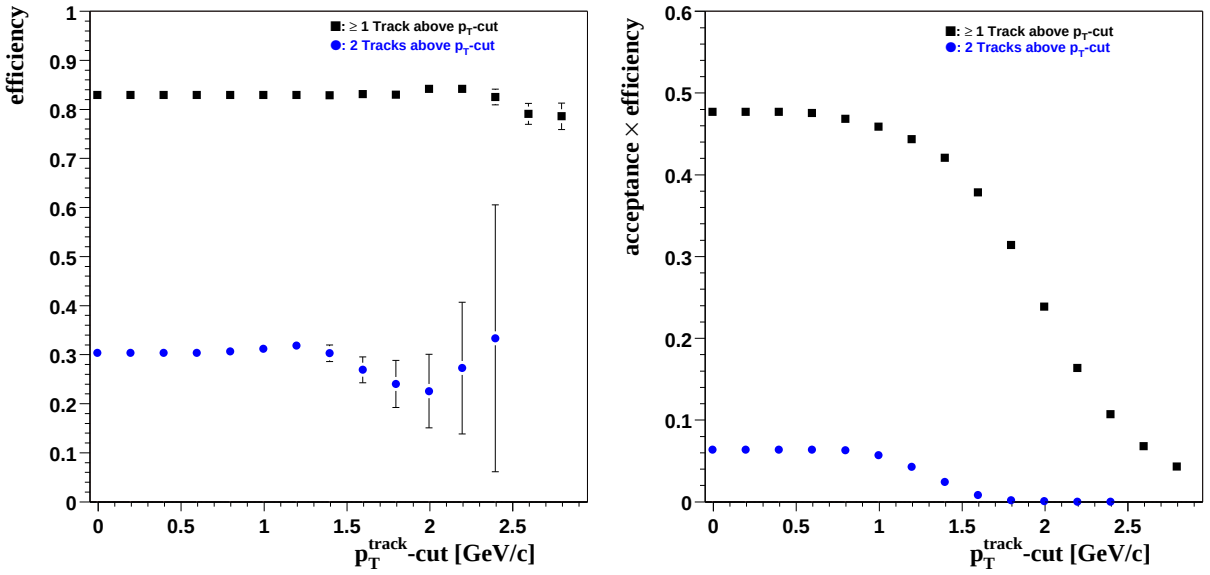

Figure 6.11: *Left: Single-track and double-track efficiency as a function of p_T-cut for events with two tracks in the outer region or one track in the outer and one track in the inner region normalised to all MC $J/\psi \to \mu^+\mu^-$ events. Right: Total acceptance times single-track and double-track efficiency as a function of p_T-cut for the same selection.*

higher because we require for the events described by the black triangles that both tracks exceed the p_T-cut which results in a lower acceptance.
We find that the assumption that the squared single-track acceptance results in the J/ψ acceptance is approximately valid.

6.4.4 Event Efficiency

In this section, we determine the FLT efficiency for the outer region to have a single-track or to have both tracks originating from a J/ψ. We also perform the check as in the previous section.
We select events with two tracks in the outer region or one track in the outer and one track in the inner region. We require that the reference tracks have at least a momentum of 5 GeV/c. In Figure 6.11 (left) we present the efficiencies for the FLT to find at least one track in the outer region and to have two tracks that exceed a common p_T-threshold. The single-track efficiency is about

$$(82.0 \pm 0.8)\ \%.$$

The efficiency to have two tracks above a common p_T-threshold up to 1.2 GeV/c is about

$$(30 \pm 1)\ \%$$

and flat within the statistical error.
We perform the same consistency check for the single-track and double-track efficiency as in the section above. The single-track efficiency to have at least one track in the outer region

gives $A_{all} = 82$ %. We apply equation 6.6 and get the single-track efficiency $A_{tr} = 57$ % which is compatible within the pretrigger efficiency with the track efficiency of 59 % as stated in section 6.3.4. We square A_{tr} and get 33 % for the double-track efficiency which is close, but slightly higher than the curve described by the circles for the same reason as above. This calculation is not applicable to the total acceptance times efficiency since we have to take geometrical implications for the single-track acceptance into account: We require at least one track to be in the outer region whereas the second track can be as well in the outer region or in the inner region. For an adequate consistency check we need to weight the efficiencies by the geometrical acceptances to have a track in the outer or inner region, respectively.

6.4.5 Total Acceptance times Efficiency

The total acceptance times efficiency comprises the acceptance and the efficiency as discussed in the previous sections.
In Figure 6.11 (right), we summarise the effects of geometrical acceptance, kinematics and FLT efficiency for events with two tracks in the outer region or one track in the outer and one track in the inner region:

$$A_{tot} \;=\; A_{geo} \cdot \epsilon_{FLT,alg} \cdot \epsilon_{TPU} \tag{6.7}$$

The total acceptance times efficiency to have at least one track up to a p_T-cut of 0.5 GeV/c per track is

$$(48.2 \pm 0.7)\ \%.$$

For larger p_T-cuts the efficiency starts to decrease. For two tracks above a certain p_T-cut the total acceptance times efficiency is about

$$(6.5 \pm 0.6)\ \%$$

up to a cut of 0.5 GeV/c and decreases more rapidly than in case of one track. The efficiency ϵ_{TPU} for the TPU is 0.96 as stated in section 6.3.4. The TDU efficiency is not taken into account here because the transverse momenta are calculated at the TPU. For the pretrigger we use unity efficiency. Increasing the p_T-cut from 0.5 GeV/c to 0.8 GeV/c reduces the total J/ψ acceptance times efficiency by 3.4 % (rel.) for the single-track case and by 5.7 % (rel.) for the two track case.

6.5 Acceptance and Efficiency as a Function of the Transverse Momentum $p_T^{J/\psi}$ of the J/ψ

In the section above, we studied the performance of the FLT as a function of p_T of the tracks. Now we examine the behaviour of the FLT as a function of the p_T of the J/ψ using $J/\psi \to \mu^+\mu^-$ events from MC.
We select events with either two tracks in the outer region, or one track in the outer region and one in the inner region and determine the acceptance of the outer region. In Figure 6.12 we show the geometrical and kinematical acceptance as a function of $p_T^{J/\psi}$. The larger the p_T of the J/ψ the higher is the acceptance of the FLT because with higher p_T

most of the leptons are in the outer tracker area. The acceptance ranges between 54 % and approximately 70 % at the largest p_T of the J/ψ. The choice of events for this analysis guarantees that we have at least one track detectable by the FLT. The acceptance as described by the circles in Figure 6.12 decreases for values of $p_T^{J/\psi}$ between 0.2 GeV/c and 1.0 GeV/c which is due to the event selection. The acceptance for a track to be in the outer region at lower values of p_T^{track} is reduced (see Figure 6.3). Since it can happen that a track which is in the inner region contributes to the acceptance the acceptance as a function of $p_T^{J/\psi}$ can decrease. In the case that we require both tracks to be in the outer region this decrease disappears.
Next, we evaluate the FLT efficiency as a function of $p_T^{J/\psi}$. We use the same event selection as above and look for reference tracks that are in the geometrical acceptance and that are matched by the FLT. Figure 6.13 (left) shows the efficiencies of the FLT to find at least one of the reference tracks or both of the reference tracks, respectively. For the single-track efficiency we require a minimal p_T of the track of 1.0 GeV/c and for two tracks we demand that both tracks exceed a p_T threshold of 0.5 GeV/c. The efficiency to find at least one track above the p_T threshold is of the order of 80 %. The efficiency to find two tracks which both have a transverse momentum above 0.5 GeV/c is of the order of 30 %. The efficiency for two tracks decreases slightly with increasing $p_T^{J/\psi}$.

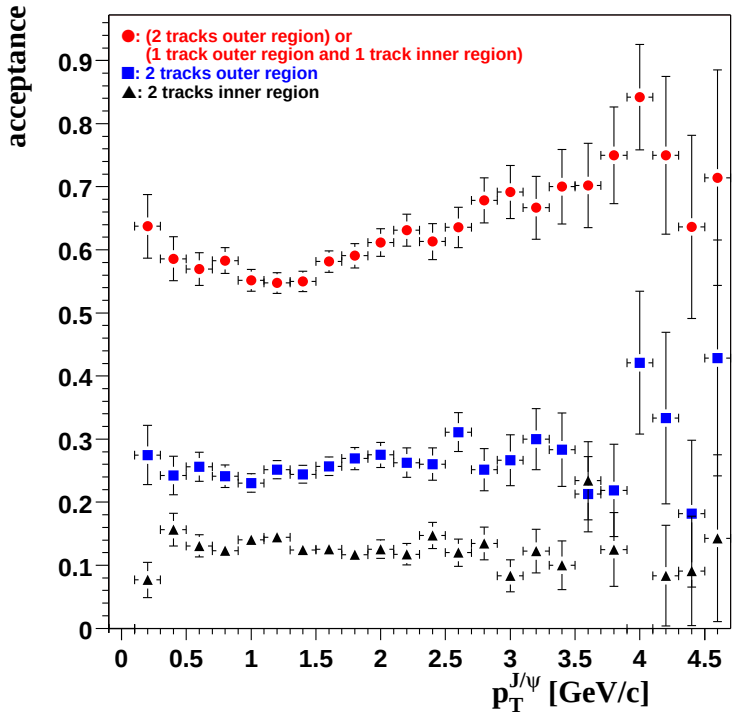

Figure 6.12: *Geometrical and kinematical acceptance of the FLT as a function of the transverse momentum of the J/ψ based on MC events. The events are selected such that at least one track from the J/ψ decay is in the sensitive FLT area (circles). No p_T^{track}-cut is applied. The acceptance to have two tracks in the outer region is of the order of 30 % (squares). The acceptance to have two tracks in the inner region results in 15 % (triangles).*

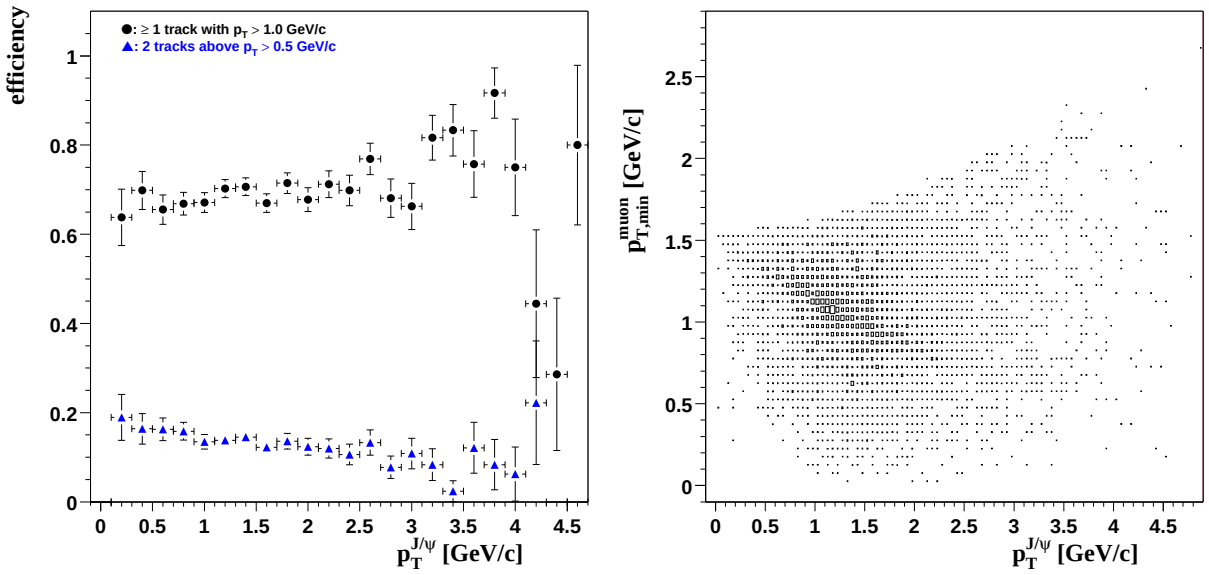

Figure 6.13: *Left: Efficiency of the FLT as a function of $p_T^{J/\psi}$. We require for the single-track efficiency that a track exceeds a p_T threshold of 1.0 GeV/c. For events with both tracks in the FLT acceptance we require that both tracks have a transverse momentum above 0.5 GeV/c. Right: The minimal p_T^{track} of the leptons vs $p_T^{J/\psi}$. The higher the transverse momentum of the J/ψ, the lower the minimal p_T of the lepton.*

The transverse momentum of the track p_T^{track} decreases with increasing values of $p_T^{J/\psi}$ because one of the leptons gets a larger p_T^{track} whereas the other lepton gets a reduced transverse momentum (see Figure 6.13 right) which is due to the kinematics of the decay. The general kinematics were discussed in section 6.4.1. The single-track efficiency is reduced at values below 0.7 GeV/c as shown in Figure 6.5.
Finally, we present the total acceptance times efficiency for a J/ψ as a function of $p_T^{J/\psi}$ in Figure 6.14. The overall efficiency to find two tracks with a transverse momentum above 0.5 GeV/c is basically flat with respect to p_T of J/ψ and gives a result of

$$8\ \%.$$

The overall efficiency to find at least one track ranges between

$$40\ \%\ \textit{and}\ 60\ \%$$

depending on the value of the transverse momentum $p_T^{J/\psi}$ of the J/ψ.

6.6 Acceptance and Efficiency with respect to x_F

In the previous sections, we determined the acceptance and efficiencies as a function of the transverse momentum which is an invariant variable. For the longitudinal component the dimensionless variable x_F (Feynman-x) is used. The variable x_F is the fraction of the momentum of the J/ψ in forward direction with respect to the maximal forward momentum.

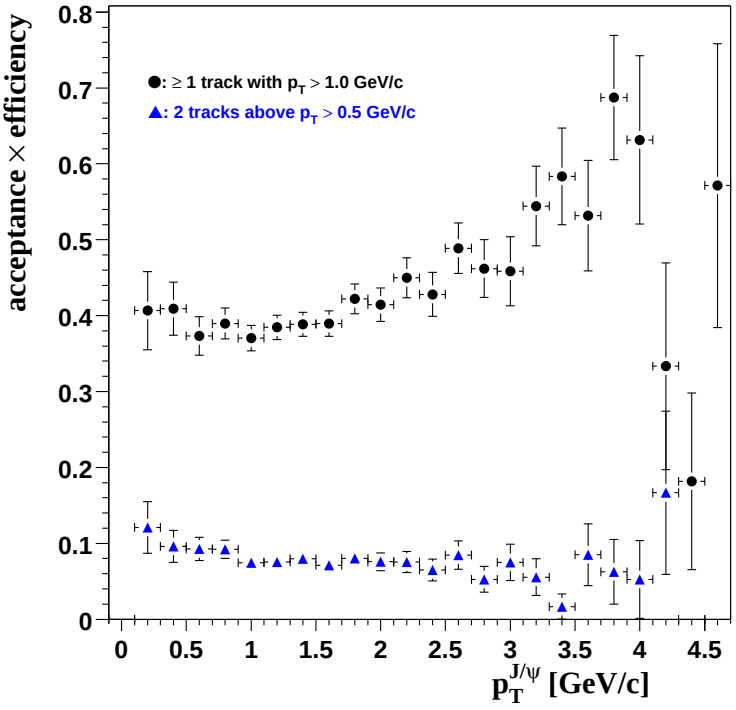

Figure 6.14: *Total acceptance times efficiency of the FLT as a function of* $p_T^{J/\psi}$ *for* $J/\psi \to \mu^+\mu^-$ *events. We require for the single-track efficiency that the* p_T *of the track exceeds a threshold of 1.0 GeV/c. For events with both tracks in the FLT acceptance we require that both tracks have a transverse momentum above 0.5 GeV/c.*

In this section, we determine the performance of the FLT with respect to x_F.
We take the definition of x_F as given in section 1.4.1. Assuming that the transverse momentum is much smaller than the longitudinal we get

$$x_F \approx \frac{2 \cdot p_{z,CMS}^{J/\psi}}{E_{CMS}}. \tag{6.8}$$

The approximation of x_F in equation 6.8 represents the fraction of the momentum in forward direction from the total available energy in the center-of-mass system (CMS). The momentum component $p_{z,CMS}^{J/\psi}$ refers to the J/ψ. The momenta of the two leptons are used to reconstruct the momentum of the J/ψ. They are measured in the laboratory frame and have to be transformed to the center-of-mass system. We use the following transformation (boost) according to [PDG98]:

$$\begin{pmatrix} E_{CMS}^{J/\psi} \\ \mathbf{p}_{CMS}^{J/\psi} \end{pmatrix} = \begin{pmatrix} \gamma & -\gamma\beta \\ -\gamma\beta & \gamma \end{pmatrix} \begin{pmatrix} E^{J/\psi} \\ \mathbf{p}^{J/\psi} \end{pmatrix} \tag{6.9}$$

with

$$\beta = \frac{\mathbf{p}_{lab}^{J/\psi}}{E_{lab}^{J/\psi} + m} \quad \text{and} \quad \gamma = \frac{E_{lab}^{J/\psi} + m}{E_{CMS}^{J/\psi}}. \tag{6.10}$$

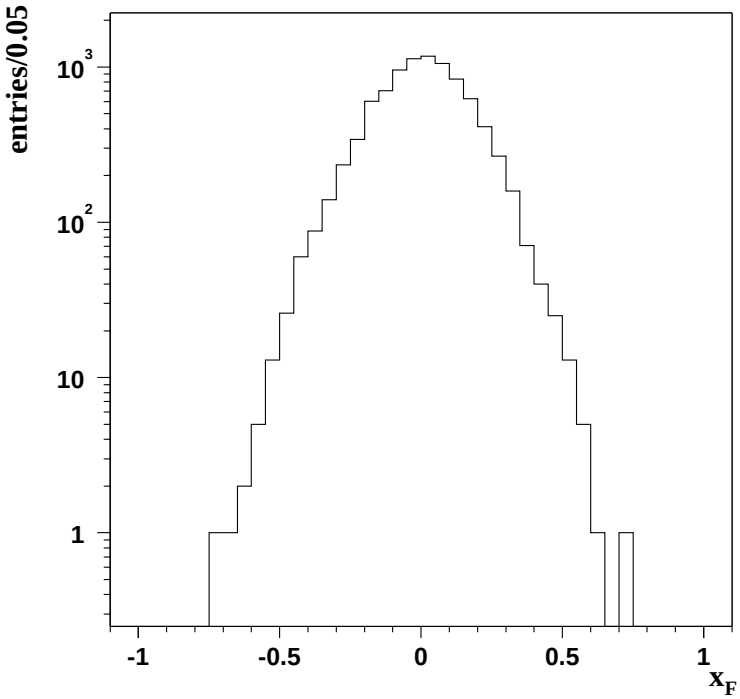

Figure 6.15: x_F *distribution of* $J/\psi \to \mu^+\mu^-$ *events from MC.*

x_F expressed in variables of the laboratory system (E^2_{CMS} is a constant):

$$x_F \;=\; \frac{2}{E^2_{CMS}} \left(p_{z,J/\psi} \cdot (E_{lab} \;+\; m) \;-\; p_{z,lab} \cdot E_{J/\psi} \right). \tag{6.11}$$

The center-of-mass energy E_{CMS} is 41.6 GeV, the measured momentum and the energy of the laboratory system is 920 GeV and m represents the proton mass because we assume the J/ψ to be produced in proton-proton interactions.

In Figure 6.15 we present the x_F distribution for MC $J/\psi \to \mu^+\mu^-$ events. We require that both leptons of the event have at least a momentum of 5 GeV/c. The distribution is symmetric around the origin. HERA–B covers an x_F range between ± 0.5.

Positive values of x_F mean that the J/ψ is produced in the center-of-mass system with a p_z in forward direction and consequently the major fraction of the tracks is in the inner region (inner tracker and muon pixel system). Negative values of x_F mean that the tracks are in the outer region (outer tracker and muon tube and pad system).

The following two sections treat the acceptance and the efficiency to have a single track or both tracks for the FLT as a function of x_F. We also show the geometrical acceptance for the inner region.

6.6.1 Single-Track and Event Acceptance vs x_F

We calculate the geometrical and kinematical acceptance as a function of x_F. In Figure 6.16 we present the event acceptance for events with at least one track or two tracks in the inner region. Both distributions reach their maximum in the positive x_F region.

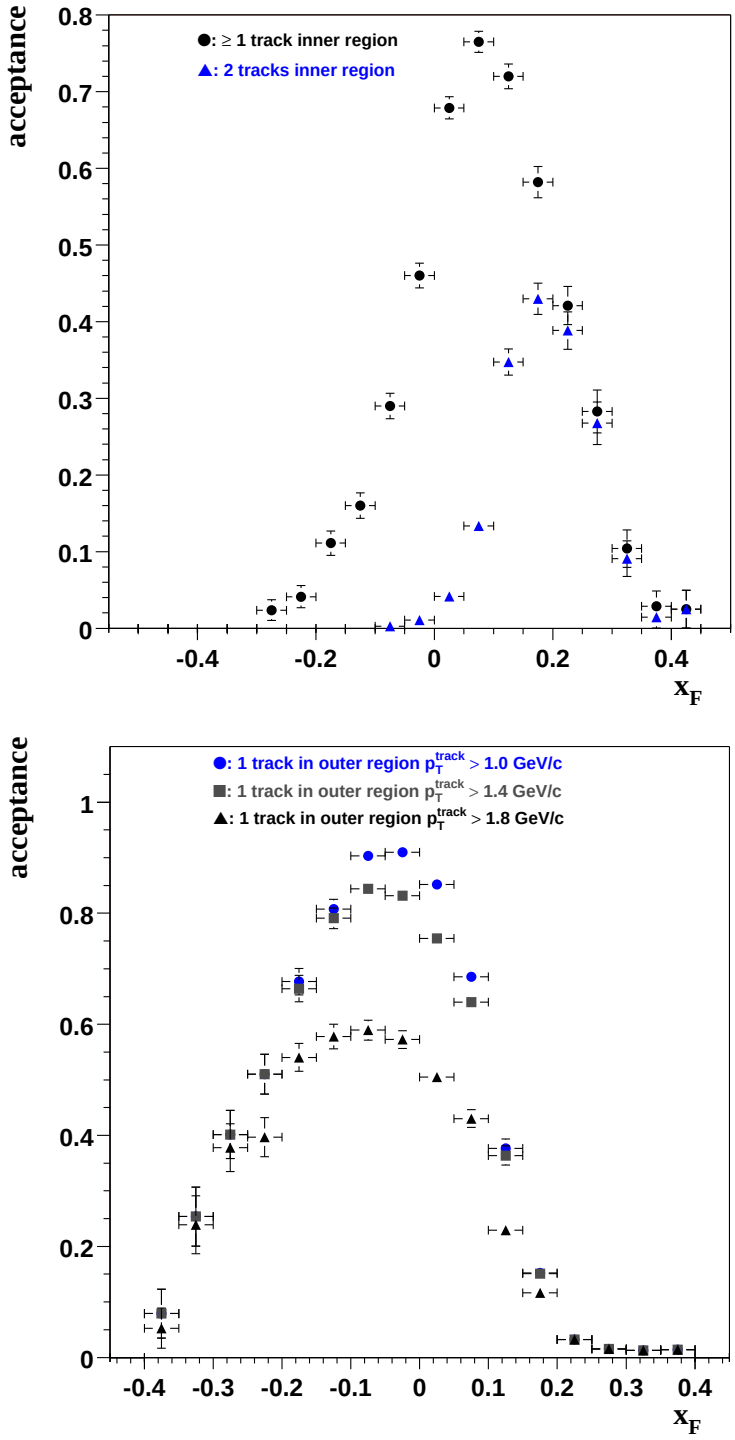

Figure 6.16: *Top: Geometrical and kinematical acceptance with respect to x_F for $J/\psi \to \mu^+\mu^-$ MC events with at least one track (circles) or both tracks (triangles) in the inner region. No p_T^{track}-cut is applied. Bottom: Geometrical and kinematical acceptance with respect to x_F for $J/\psi \to \mu^+\mu^-$ MC events with one track above a certain tranverse momentum in the outer region.*

We evaluate the geometrical and kinematical acceptance for the outer region as a function of x_F for events with two tracks in the outer acceptance or one track in the outer part and the other one in the inner part. In Figure 6.16 (bottom) we present the acceptance as a function of x_F for three different p_T-cuts for the single-track. The distributions tend towards negative values of x_F. The acceptance decreases from 78 % for a p_T-cut of 1.0 GeV/c to 48 % for a p_T-cut of 1.8 GeV/c. The entries for positive values of x_F come from the fact that we select also events with one track in the outer and one in the inner region. Both tracks contribute to the value of x_F. At positive values of x_F we can have a track in the outer region but the main contribution to x_F comes from the track in the inner region. The reversed argument is valid for the acceptance for the inner region shown in Figure 6.16 (top).

6.6.2 Single-Track and Event Efficiency vs x_F

The FLT single-track as well as the event efficiency as a function of x_F for two different event selections are shown in Figure 6.17. We select events with one track in the outer region and the other track either also in the outer region or in the inner region (Figure 6.17 left). The right plot of Figure 6.17 shows the efficiencies for events with both tracks in the outer region. We require that at least one track has a p_T above a threshold of 1.0 GeV/c for the single-track efficiency or that both tracks exceed the minimal p_T threshold of 0.5 GeV/c.

For values of x_F in a range between -0.4 and -0.1 we evaluate a single-track efficiency

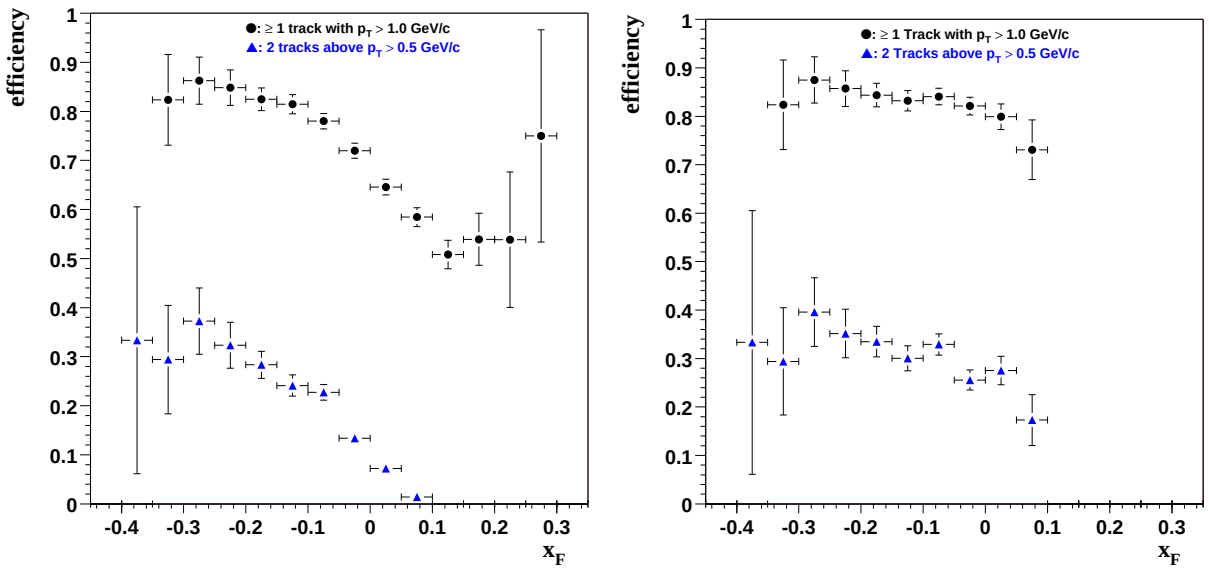

Figure 6.17: *Left: FLT efficiency for $J/\psi \to \mu^+\mu^-$ MC events with "two tracks in the outer area"* **or** *"one track in the outer and one in the inner area". We show the efficiencies to either find a single-track with a transverse momentum above 1.0 GeV/c or to find two tracks that exceed a p_T threshold of 0.5 GeV/c. Right: Single-track and double-track efficiency of the FLT for $J/\psi \to \mu^+\mu^-$ MC normalised to events with two tracks in the outer area with the same p_T^{track}-cuts as for the plot on the left.*

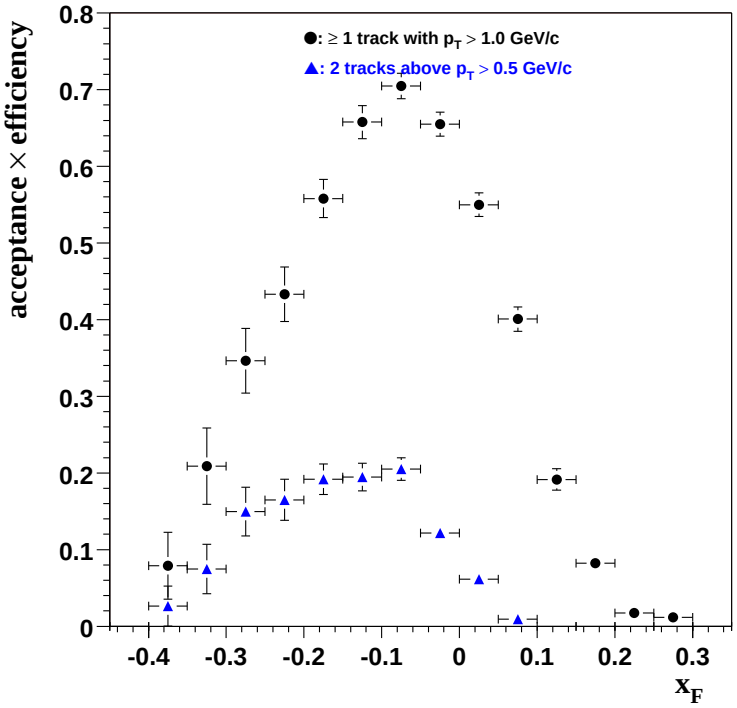

Figure 6.18: *Total FLT acceptance times efficiency for $J/\psi \rightarrow \mu^+\mu^-$ events with two tracks in the outer area or one track in the outer and one in the inner area. We show the efficiencies to either find a single-track with a transverse momentum above 1.0 GeV/c or to find two tracks that exceed a p_T threshold of 0.5 GeV/c.*

around 80 %. The efficiency decreases for values of x_F larger than zero and reaches a plateau of 55 % for positive x_F up to 0.3. The extent to positive x_F and the decrease of efficiency is a clear effect of the logical "OR" of the selection of events (see Figure 6.17 left). If we select events with both tracks in the outer region the single-track efficiency results in 80 % and is flat for x_F being in a range between -0.4 and 0 (Figure 6.17 right). For events with one track in the outer and one in the inner area the efficiency is on the order of 60 % for values of x_F between -0.3 and 0.3. The efficiency decreases slightly for x_F larger than 0.05.
The peak efficiency in case of two tracks is 35 %. The efficiency decreases rapidly for x_F larger than -0.1 since tracks begin to cross into the inner part.
In Figure 6.18 we present the total J/ψ acceptance times efficiency consisting of geometrical and kinematical acceptance and FLT efficiency with respect to x_F. The peak efficiency for a single-track is around 70 % near x_F = -0.05. For two tracks we get about 22 %.
The geometrical acceptance of the outer region covers the range of negative values of x_F between -0.5 and about zero. The geometrical acceptance of the inner region enlarges the range of x_F significantly to positive values up to 0.3. Depending on the event selection the efficiency of the FLT can be extended also to positive values of x_F but the efficiency decreases significantly. We expect based on the geometrical acceptance of the inner region with respect to x_F a significant increase of the total acceptance times efficiency by including the inner tracker into the FLT.

6.7 Measurement of the J/ψ Efficiency from Event-Counting in Data

In this section we describe a second method to determine the J/ψ efficiency for the FLT and present results for triggered data and MC samples. We calculate the J/ψ efficiency based on counting the number of events within a certain mass range. We use the method described here to determine the J/ψ efficiency for the hard selected data to take into account all the combinatorical possibilities of the reference tracks. The method is also applied to the MC samples to compare the results with the hard selected results.
In case of the hard selected events, it can happen that there are two reference tracks that match with the simulated tracks but do not originate from a J/ψ. In case of MC, we know that we have only two reference tracks that originate from the J/ψ. The trigger decision is made if the reconstructed mass exceeds a given threshold independent if it is indeed a J/ψ.

6.7.1 Method

For triggered (hard selected) data we use the track parameters determined by the SLT and propagate the tracks through the magnet to the vertex detector. By incorporating hits measured by the vertex detector in front of the magnet the information on the momentum of the reference tracks can be refined. With this information we are able to calculate the invariant mass of an event. It happens that there are more than two reference tracks available for a specific event. An investigation of the track parameters of those additional tracks showed that they are clone tracks, i.e. tracks with almost identical track parameters. To remove the clone tracks from the sample we choose the pair with the highest invariant mass.
For MC the situation is simpler since we only have two reference tracks per event and the track parameters are available from the generation.
Figure 6.19 shows the invariant mass for all reference tracks of the SLT triggered sample (left) and the invariant mass of reference tracks that are found by the FLT for PC 1 (right). The sharp turn-on at a mass of 2.5 GeV/c^2 in the hard selection is due to the cut on the sum of the transverse momenta of tracks at 2.5 GeV/c.
We fit signal and background to a gaussian sitting on top of an exponential function:

$$f(m) \;=\; N \cdot \exp\left(-\frac{1}{2}\cdot\left(\frac{m - M_{J/\psi}}{\sigma_{J/\psi}}\right)^2\right) + \exp(p_3 + p_4 \cdot m) \tag{6.12}$$

with N (i.e. the number of J/ψ) defined as:

$$N \;=\; \frac{h \cdot bin\ width}{\sigma_{J/\psi}\cdot\sqrt{2\cdot\pi}} \tag{6.13}$$

with h being the height of the gaussian function. The J/ψ efficiency is the ratio of the number of found J/ψ in a certain superlayer and the total number of J/ψ that can be found. If only one track is found by the FLT the event does not contribute to the J/ψ efficiency. The number of J/ψ's is a parameter of the fit function.
For MC we get the number of J/ψ's directly from the histogram since the mass distribution looks like a delta function.

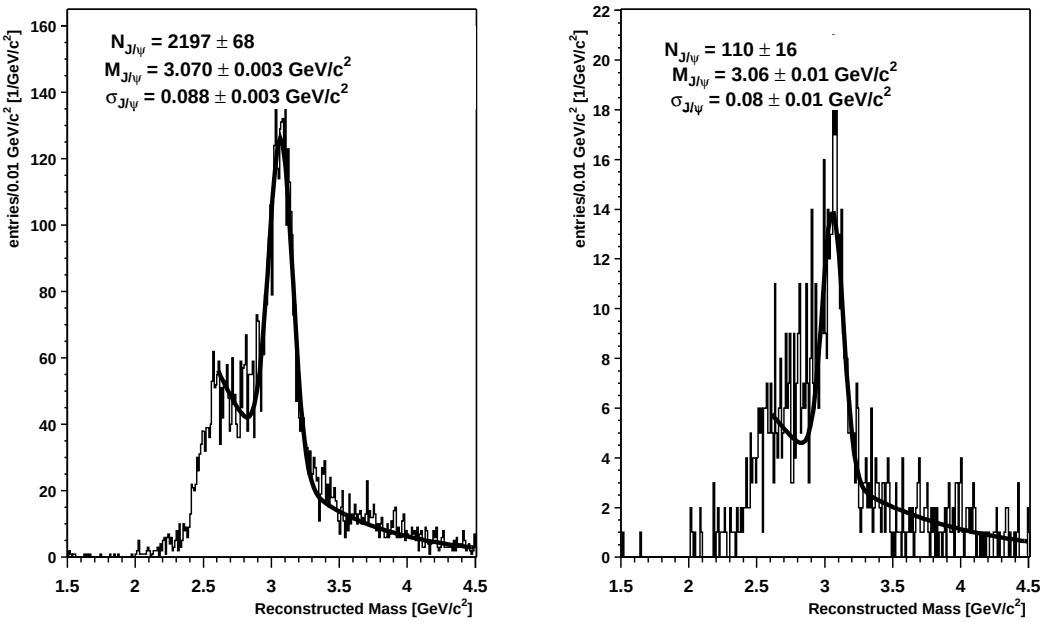

Figure 6.19: *Maximal invariant mass for the hard selected data sample. Left: The total available number of J/ψ of the data sample. Right: Maximal invariant mass calculated out of reference tracks found at PC 1.*

6.7.2 Results

Figure 6.20 summarises the J/ψ efficiency per superlayer for the available data sets. Comparing Figure 6.5 with Figure 6.20 we see that the single-track efficiency squared gives approximately the J/ψ efficiency. The decrease in efficiency between the layers MU 3 and MU 1 is larger than in the case of the track efficiency as shown in Figure 6.5. The relative decrease in efficiency is about the square of the relative decrease as in the case of the single-track efficiency. The large decrease in efficiency at MU 1 for realistic MC and data is also larger as in the case of the track efficiency.
The final efficiency of the FLT (TDU) is calculated by applying the squared TPU efficiency (0.96^2) to the J/ψ efficiency for PC 1 [Res00]. The efficiency for the TDU again taken as 0.92 [Res01].
The final J/ψ efficiency for hard selected data and realistic MC results in

$$(3.9 \pm 0.6\ (stat.))\ \%.$$

For perfect MC the efficiency is

$$(36.2 \pm 0.2\ (stat.))\ \%.$$

We cannot compare directly the results obtained by the method here and the results presented in section 6.4.4 since we select different sets of reference tracks: In this analysis we restrict the reference tracks to be in the outer region whereas in section 6.4.4 we require at least one track in the outer region. In addition, we assume a unity pretrigger efficiency in this section and have a lower pretrigger efficiency in section 6.4.4 since we allow tracks

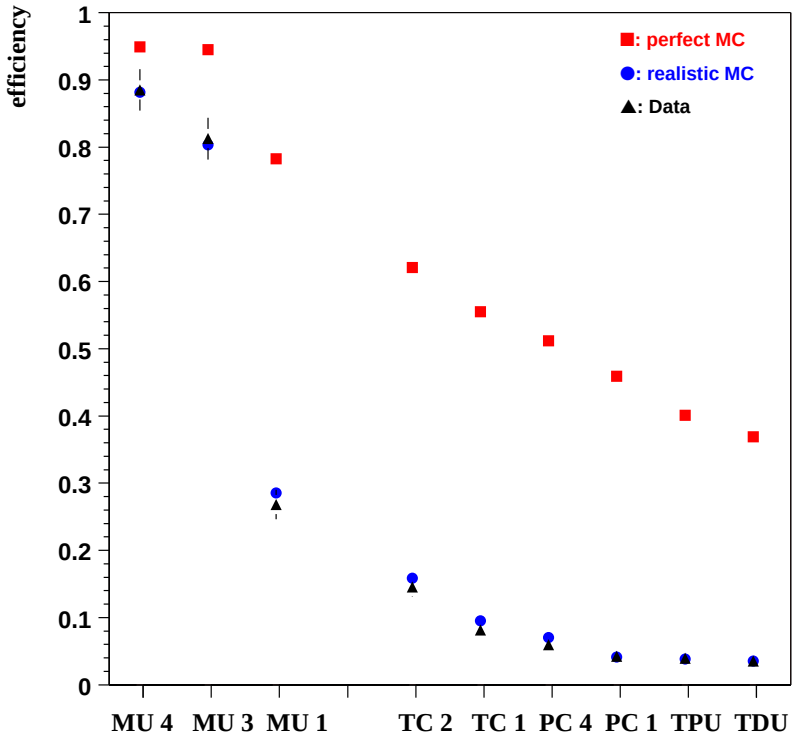

Figure 6.20: *Efficiency per superlayer for $J/\psi \to \mu^+\mu^-$ events for available data sets.*

in the pixel region which is not covered by the pretrigger simulation.
The error bars for the points that describe the SLT triggered data are calculated from the errors of the fit by means of error propagation. The error of the fit dominates the total uncertainty which is due to the method chosen here to determine the J/ψ efficiency. For MC such a fit procedure is not needed since the mass distribution looks like a delta function at a mass of 3.09 GeV/c^2.

6.8 Estimation of the Systematic Error

The presented results include in addition to the statistical error some systematic uncertainties. In this section, we describe some uncertainties which are summarised as the systematic error.

Uncertainties of the Simulations

The efficiency of the muon pretrigger simulation which was used for the entire analysis ranges between 93 % for the worst case and 98 % for the best one [Ada01a].
The FLT simulation describes the hardware in almost perfect agreement with small discrepancies as stated in section 5.3.

Method of Efficiency Calculation

The track efficiencies are calculated from a quadratic function s^2 which is described by a χ^2 function in case of gaussian distributed variables. We expect that the distribution is flat. The efficiency is determined from the entries in the bin that covers the probability between zero and a value which is given by the bin size. It can happen that the distribution is slightly higher at bin with lower probability before becoming flat for other values of probability. This occurs if variables used for determination of s^2 are not gaussian distributed. The efficiency may be different if we take additional bins for probabilities larger than that given by the first bin into account.
We studied the effect of the s^2 probability cut on the efficiency. We included the bins up to a probability of 0.2 in steps of the bin size. We determined the efficiency and calculated the ratio between the efficiency derived from bin zero only and the efficiency derived with the added bins. Figure 6.21 shows the relative efficiency as a function of the probability cut for PC 1. The solid line represents the expectation. The difference between the expected relative efficiency (0.8) at a probability cut of 0.2 and the actual probability gives the size of the systematic error. The systematic error ranges between 3 % and 7 %.

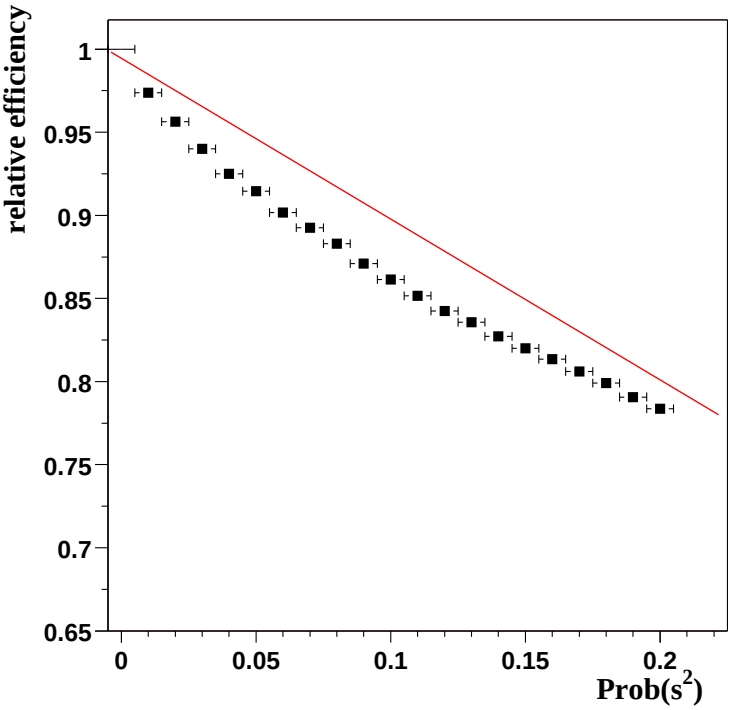

Figure 6.21: *Relative efficiency for PC 1 as a function of the probability cut. We expect at a cut of 0.2 a relative efficiency of 0.8. The difference between the expectation and the actual relative efficiency is used for the systematic error. The solid line represents the expectation.*

Effects of Masking

A masking that reflects the detector performance of the year 2000 is used for the realistic MC sample. The efficiency determined with the realistic MC agrees well with the hard selected data which was accumulated over several different runs. An estimate of the systematic error is not possible since a precise reproduction of the real detector performance at the time when the data was taken was not recorded.
The effect of the channel masking applied by the FLT is estimated by comparing the efficiencies for realistic MC with channel masking and without. The results differ by 4 % which we assume to be the systematic error.

6.9 Summary and Conclusion

We present in this analysis methods to determine the track and J/ψ acceptance and efficiencies for the FLT.

- The geometrical and kinematical acceptance for tracks originating from J/ψ is presented as a function of p_T^{track}. For values of p_T^{track} below 0.5 GeV/c a major fraction of the tracks are in the inner part or in the beampipe. For values of p_T^{track} above 0.7 GeV/c the geometrical track acceptance is 60 % for tracks in the outer part (including the muon tube and pad system) and is 35 % for the inner region.

- The pure FLT single-track efficiency for perfect MC data is 59 %. The results for realistic MC and the SLT triggered data are 16 % and 18 %, respectively. A large decrease of efficiency is observed in MU 1 for MC and data. It is subject of a separate analysis (see chapter 7).

- The FLT efficiency for single-tracks as a function of p_T^{track} shows a slight turn-on at low values of p_T^{track} and is flat above values of 1.2 GeV/c. Tracks with low transverse momentum pass the region close to the inner tracker where multiple scattering dominates.

- The acceptance of the FLT as a function of $p_T^{J/\psi}$ is 45 % at 0.2 GeV/c and increases up to 68 % at a transverse momentum of 3.8 GeV/c.
  The efficiency for a single-track with a transverse momentum of at least 1.0 GeV/c is about 70 % and increases up to 80 % for values of the transverse momentum of the J/ψ above 3.2 GeV/c. The efficiency for two tracks that both exceed a p_T^{track} threshold of 0.5 GeV/c is around 16 % and increases only slightly towards the end of the p_T-spectrum of the J/ψ.

- We have studied the behaviour of the FLT with respect to the scale-independent kinematic variable x_F. For the geometrical and kinematical acceptance of $J/\psi \to \mu^+\mu^-$ events with the additional requirement that a single-track exceed a certain p_T threshold of 1.0 GeV/c we obtain a maximal acceptance of 77 % at a value of x_F of zero. With a p_T requirement of 1.4 GeV/c the maximal acceptance is 68 % and for a transverse momentum of at least 1.8 GeV/c the peak acceptance reaches 47 %.
  The FLT efficiency for one track with a transverse momentum of at least 1.0 GeV/c

results in 75 % for negative x_F and starts to decrease for larger values of x_F. The maximal FLT efficiency for two tracks in outer region above a p_T threshold of 0.5 GeV/c is 30 % at x_F of -0.1. The total acceptance times efficiency decreases rapidly and is almost zero for x_F of 0.1.

- Finally we used a method to determine the J/ψ efficiency from data and applied this method also to the MC samples. The J/ψ efficiency of the FLT measured by simple event counting is 36 % for perfect MC and 4 % for realistic MC and triggered SLT data. The naive assumption that the squared single-track efficiency results in the J/ψ efficiency is only approximately valid.

We learn from the results of the single-track efficiency that the tracking algorithm does not reach the design values. In the design phase a J/ψ efficiency of the order of 48 % was expected [Her94]. The obtained results of this analysis show a lower J/ψ efficiency. The single-track efficiency for perfect MC is about 60 %. The J/ψ efficiency is 36 % which is 25 % below expectation. The tracking algorithm should be improved, if possible, such that the losses from superlayer to superlayer do not exceed 1 %.
The data show clearly that the single-track as well as the J/ψ efficiency depend strongly on the detector performance. The muon pad efficiency for the year 2000 data taking was 75 % for MU 3 and 68 % for MU 4, respectively. The tube chamber efficiency for MU 1 turned out to be about 96 % instead of close to 99 % [Her00]. The bad pad efficiencies directly affect the performance of the muon pretrigger. Due to this performance we assume a unity pretrigger efficiency in this analysis. The low tube efficiency enters the track efficiency to the third power since the FLT requires a triple coincidence.
We have to take into account that the data were taken without the inner tracker. Based on the MC studies in this analysis we see that the acceptance of the inner region is about 40 %. For the start-up of the upcoming run it is mandatory to have the information of the inner region –both the inner tracker and the pixel system– available for trigger purposes. In case that the FLT is restricted to the information of the outer region because of technical problems, a scenario with a single-track trigger of the FLT and a track search in the inner region by the SLT is a preferred solution (see Figure 6.10).

Chapter 7

Efficiency Loss in Muon Layer MU 1

The analysis of the efficiencies presented in the previous chapter shows a drastic loss of the order of 36 % for the single-track efficiency for the SLT-triggered (hard-selected) data and for the realistic MC events. Note that the decrease of efficiency between the layers MU 3 and MU 1 as shown in Figure 7.1 is larger than 36 % since the efficiency is corrected due to the bias of the SLT trigger decision. The decrease in efficiency for perfect MC events is about 9 % which is much lower than for the data.

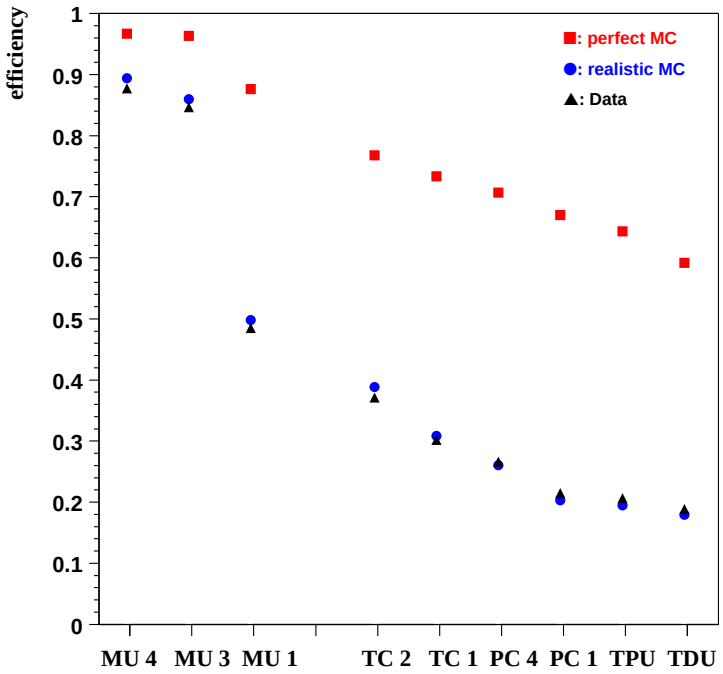

Figure 7.1: *The single-track efficiency for tracks originating from $J/\psi \to \mu^+\mu^-$ events for the hard-selected data and for perfect as well as realistic MC. The realistic MC sample uses a masking that describes the performance of the detector of the year 2000 data taking. Note that the decease of efficiency is larger than 36 % due to the correction of the bias from the SLT trigger decision.*

In this chapter, we figure out the reasons that are responsible for the efficiency loss in this specific superlayer. We use both SLT-triggered data and Monte Carlo (MC) samples to study the inefficiencies. We investigate two main categories of losses:

1. Tracks that are inside a calculated ROI but are not updated and

2. tracks that are outside the ROI in at least one stereo view.

We describe in these sections the method to find the inefficiencies in the layer MU 1 and provide the definition of the different track categories.

7.1 Method

We process perfect MC events or the SLT-triggered data for the channel $J/\psi \to \mu^+\mu^-$ with the muon pretrigger and the FLT simulation inside the ARTE framework. We use the event samples described in section 6.1. We use reference tracks as defined in section 6.2.1 with one exception: we omit the requirement for unlike charge. We accept all tracks that are inside the outer region (outer tracker and muon tube and pad system).
The track candidates are represented by an 80 bit message. The message is updated if a hit is found and sent to the following superlayers through the entire FLT. Found and updated (i.e. "valid") messages are converted to tracks at the specific superlayer.
We select all messages generated by the simulation of a specific TFU at MU 1. We require for all messages that their "parent" (i.e. the message of the previous superlayer) message matches with the same reference track in the previous superlayer. First, we look for valid messages that match with the reference track. In case that there is no valid message that matches to the reference track we look for the invalid message that describes the track in the best way.
We use the following approach to determine the "best invalid" message:
Each message determines an ROI. We calculate the middle of the ROI for each view and determine the arithmetic mean of these three points. We apply the same procedure for the reference track: We determine the impact point of the track in each view and derive its arithmetic mean. The message with the smallest distance between those two points is considered to be the best invalid message.
The FLT simulation allows to access all messages (i.e. valid and invalid) of a specific superlayer. The "invalid" messages are of special interest since the track finding stops and they contribute to the inefficiency. In addition, the simulation provides insight into the calculation of the track parameters as performed by the hardware.
The simulation grants also access to the bit pattern describing the hits in the Wire Memory. The action of the Coincidence Matrix which looks for triple hit coincidences in these patterns can be studied as well. It is the most crucial part since it determines if a track is found or lost.
We investigate the performance of single TFUs that are crossed by the reference tracks. We study critical parameters and determine residuals of parameters of the reference track and the simulated track (represented by a message). We compare the results of found and matched tracks with cases of invalid messages and study why the message became invalid.

7.2 Track Categories

In order to get a measure of the inefficiency we categorize the messages (that represent the tracks). In total, we have three categories:

- We look for messages at a specific TFU that are valid and match to the reference track in MU 1. We also require that the appropriate message in MU 3 has matched to this reference track. The messages of this category determine the efficiency of the algorithm since they correlate with the reference track and are updated (i.e. a triple coincidence is found) as expected.

- Another category consists of messages that are invalid (no update at the specific superlayer) but the reference track is inside the ROIs of all three stereo views.
  Main emphasis is put on this category since there is a message that describes the reference track well but the update fails due to some reason.

- There are invalid messages that describe the reference track but the track is outside of the ROI in at least one stereo view.

7.3 Algorithmic Inefficiency

The use of perfect MC events to examine the algorithmic inefficiency provides some advantages compared to the use of the hard selected data. There is no detector inefficiency included in the perfect MC events. The selection of reference tracks is simpler since we can select directly the tracks that originate from a J/ψ. The information of the position of the track is more precise than in the hard-selected data.
In addition to the selection criteria for reference tracks stated in section 6.2.1, we require that MC reference tracks have at least one entry per stereo view in the hit table and that each belongs to only one TFU. This selection excludes the inefficiency due to the electron beam pipe. Tracks with a y-position slightly larger than y = 0 can also cause hits in the lower y-half which belong to a different TFU and vice versa. A comparison of FED and channel (see section 7.4.3) then will give misleading results.
The inefficiency estimated by the use of perfect MC is

$$(9.2 \pm 0.6)\ \%.$$

The category of tracks that result in an invalid message contribute with 6.0 % and the tracks that are out of the ROI and result in an invalid message with 3.2 %.

7.4 Tracks *inside* the ROI resulting in invalid messages

In this section, we start to investigate reasons for track losses which should lead to an update since the track is inside the determined ROI. We use the hard-selected data as well as perfect MC events.
We check certain aspects of the algorithm that could contribute to the inefficiency. The

large stereo angle of MU 1 ($\pm 20°$) and the absorbers that cause multiple scattering require special attention. In addition, we look for possible problems in the calculation of the start of the ROI and check if geometrical effects influence the efficiency. Finally, we estimate an approximate size of the decrease in efficiency that is related with a decreased detector performance.

7.4.1 Effect of the "shift flag"

The implementation of the "shift flag" can be one reason for algorithmic inefficiency. The "shift flag" is needed to steer the Coincidence Matrix. The functionality of the Coincidence Matrix is presented in section 4.2.3.
The stereo angle of the first muon layer is 20°. Each module of this layer that is read out consists of 32 wires. Several modules are connected to one TFU. We determine the middle of the distance between two wires that belong the opposite stereo views (i.e. the crossing of two wires with opposite stereo angle as shown in Figure 7.2). We calculate the distance d of this middle and the vertical wire. We find that the distance d increases wire by wire due to the large stereo angle and reaches approximately two cells at the end of a module (see Figure 7.2 for details). There are steps in this distance d after 16 wires or

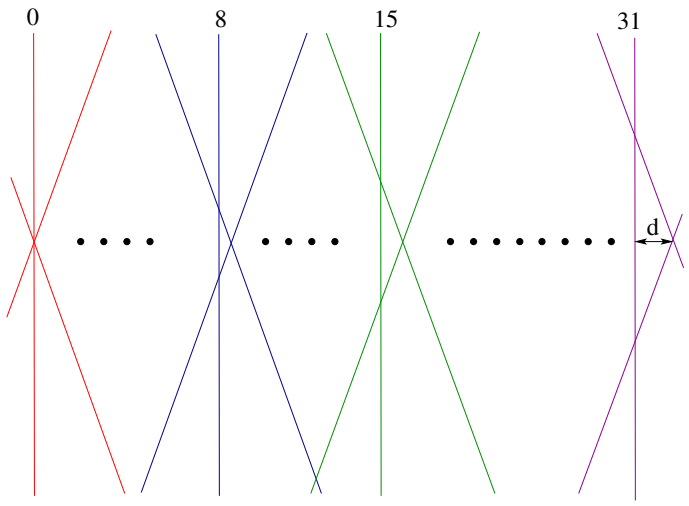

Figure 7.2: *The distance d between the middle of the two stereo wires and the vertical wire over the ROI range of 32 wires contained by a module of the muon detector in an idealized picture. At the end of the module, the distance reaches almost the distance of two wires. The "shift flag" takes this distance into account to find a coincidence.*

after 8 and 24 wires. These steps have to be taken into account for the implementation of the Coincidence Matrix. The "shift flag" has to compensate these steps for the search for triple hit coincidences. The "shift flag" depends on the distance d at the start of the ROI. In the current version of the tracking algorithm the shift flag is fixed to a specific value and not adjusted dynamically as foreseen in the design of the board [TFU99].
A fraction of the reference tracks should result in a coincidence as stated in the previous section but get lost. An investigation of the wire memory pattern that were produced by

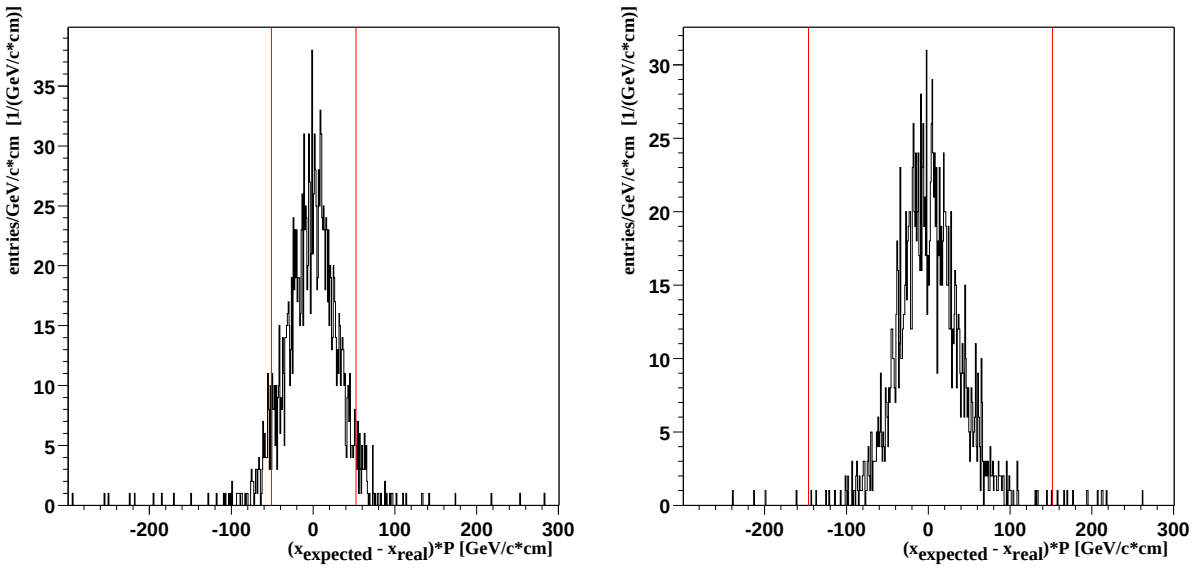

Figure 7.3: *The deviation in x times the momentum of the track of the expected position of the track and the actual position at a given superlayer. The vertical lines show the three sigma limit applied by the track-finding algorithm. Left: The deviation of the expected track position and the actual track position for the extrapolation from MU 3 to MU 1. Right: The same plot for the extrapolation from MU 1 to TC 2 which is also affected by the multiple scattering.*

those reference tracks showed that a coincidence is found with the other value of the "shift flag". In total,

1.4 %

of the reference tracks (hard-selected as well as perfect MC) are lost due to the static assignment of the value for the "shift flag" by the algorithm.

7.4.2 Effect of Multiple Scattering

We examine the treatment of the multiple scattering by the algorithm and if it causes any inefficiency.
In front of each of the first three layers of the muon system a large absorber made of steel and concrete is installed. The absorbers cause multiple scattering –depending on the momentum of the particle– of the reference tracks which needs to be taken into account by the track-finding algorithm.
The size of the ROI is adjusted according to the momentum information provided by the pretrigger. It is smaller for tracks with larger momentum. The extrapolation to the successive layer is affected by the multiple scattering. In order to study this effect we use MC reference tracks and calculate the distance between the projected (estimated) position at the successive superlayer and the actual position which we derive from the MC impact point information. We fit a gaussian function to the distribution and compare the obtained width σ of the fit with the values that are used in the tracking algorithm. The distance between the expected track position and the actual position at a given superlayer times the

momentum of the track is shown in Figure 7.3. The vertical lines in the plots represent a three sigma cut calculated from the values applied by in the track-finding algorithm. The multiple scattering also affects the extrapolation from MU 1 to TC 2. The widths obtained by the fit are below the values that are applied by the algorithm with the exception for the extrapolation from MU 3 to MU 1. The value used by the algorithm is only half of the width determined as described from MC. Increasing the value in the algorithm does not improve the efficiency. We conclude that the multiple scattering is not a source of inefficiency.

7.4.3 Mapping Problems

The relation of the detector wires via the Linkboard to the wire memory of the TFU is described by the mapping. The Front-End-Driver (FED) and channel number is related to "one wire" in the wire memory.
The mapping can be an important source of inefficiency if detector wires are not mapped to the expected position in the wire memory but somewhere else in the range of the wire memory. A wrongly mapped channel does not lead to the required triple hit coincidence in case of stereo layers like in the outer tracker or the first muon layer[1].
We use $J/\psi \rightarrow \mu^+\mu^-$ events from perfect MC to check the mapping in MU 1. On one hand, we select the impact points of the two leptons and look for entries in the hit table. From the entries in the hit table we access the muon database and derive the corresponding FED and channel number.
On the other hand, we scan the wire memory of each view within the calculated ROI and determine the corresponding FED and channel number for each hit wire as predicted by the mapping. The comparison for valid messages results in an agreement for the whole layer (a logical "and" of the three stereo views) of

$$(97.2 \pm 0.3)\ \%$$

for valid messages and increases up to

$$(99.0 \pm 0.1)\ \%$$

if we extend the size of the ROI by eight wires at the beginning and at the end. The increase gives an indication that a problem in the calculation of the ROI exists.
For tracks that are inside the ROI but result in invalid messages we find an agreement of

$$(94.4 \pm 1)\ \%$$

and for the extended ROI an agreement of

$$(96.8 \pm 1)\ \%.$$

The agreement per stereo view ranges between 97.9 % and 98.3 % and for the extended ROI of the order of 99 %.

[1] The second muon layer MU 2 consists also of stereo layers but is not used by the FLT.

	total	+20°	0°	-20°
valid tracks				
ROI [%]	97.2	98.9	98.9	99.3
extended ROI [%]	99.0	99.7	99.6	99.7
invalid tracks in ROI				
ROI [%]	94.4	97.9	98.0	98.3
extended ROI [%]	96.8	98.9	99.0	98.9

Table 7.1: *Results of the FED and channel comparison for valid tracks and tracks that are invalid but in the ROI. The extended ROI is enlarged by 8 wires at the beginning and at the end.*

The overall effect of the mapping failure for tracks inside the ROI that result in invalid messages (0.06 · (1-0.944)) is of the order of maximal

$$0.3\ \%.$$

The failure of the mapping is negligible for the losses of tracks that are inside the ROI but lead to invalid messages. We cannot conclude from the FED and channel comparison if the mapping is a reason for the losses of tracks that are outside the ROI since we do not know the position of the ROI with respect to the reference hit table entry. Further investigations on this category follow in section 7.5. Table 7.1 summarises the results of the FED and channel comparison for the entire muon layer MU 1 and for each stereo view. We separate the results for the ROI and the extended ROI enlarged by eight wires at the beginning and the end.

7.4.4 Calculation of the First Wire of the ROI

The calculation of the number of the first wire (referred to as "n calculation") of the ROI is another crucial item of the tracking algorithm.
The first wire of the ROI is determined individually for each stereo view from the track parameters such as position in x and y, the deviation of the track from a track with infinite momentum (i.e. a straight line pointing from the target to the given position) and of the size of the ROI in the previous superlayer. Shifts in the calculation of the first wire of one view with respect to another view can lead to the loss of a triple hit coincidence. We examine the effect of the n calculation with perfect MC. Again, we determine for each simulated hit the corresponding FED and channel and predict the associated wire in the wire memory. From the FLT simulation we take the calculated n (i.e. the first wire of the ROI) for each view and determine its wire number. Then we calculate the distance between the wire number that is hit by the MC track and the first wire of the ROI for each view:

$$d^v = i_{wire}^{hit\ table} - i_{first\ wire}. \tag{7.1}$$

The distance d^v (v denotes the stereo view) is calculated individually for each stereo view with the associated wire numbers (denoted by i). Figure 7.4 shows the difference d^0. We see the difference between the wire that is hit and the first wire of the ROI in number of

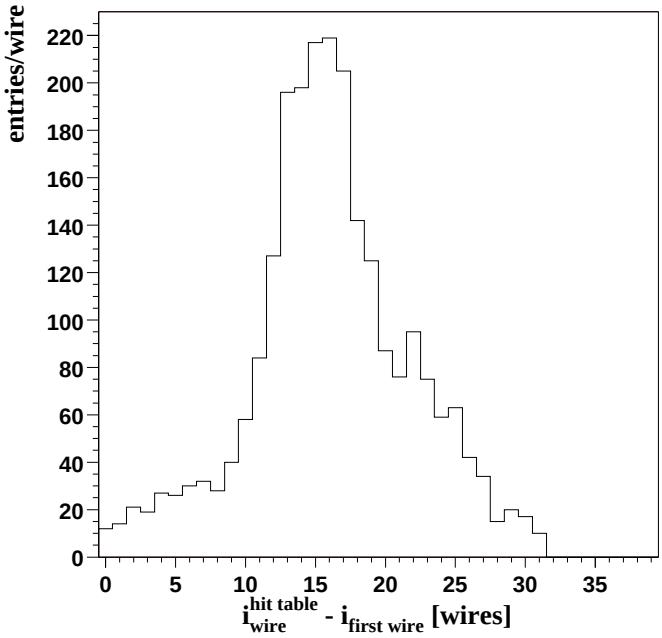

Figure 7.4: *Difference d^0 between the hit wire and the first wire of the ROI in number of wires. In most of the cases, the hit wire is in the middle of the ROI.*

wires. In most of the cases, the hit wire is in the center of the ROI. The maximal size of the ROI is 32 wires which is not exceeded. We determine the difference

$$\Delta^{r,s} = d^r - d^s, \; r \neq s \tag{7.2}$$

with r and s being two different stereo views. We expect that $\Delta^{r,s}$ peaks around zero for valid and updated tracks since this is a mandatory condition for the Coincidence Matrix to find a triple hit coincidence (see section 4.2.3).

In Figure 7.5, we present the distribution of $\Delta^{r,s}$ for valid messages (left) and for tracks inside the ROI that result in invalid messages (right). The Coincidence Matrix is designed to find up to four coincidences in the y-direction. The stereo wires together with the vertical wire form a triple coincidence. The limit of the four coincidences restricts the maximal allowed difference between the two stereo wires to four wires. The maximal difference between the vertical wire and one of the stereo wires under the same limit of four coincidences must not exceed two wires. Otherwise the coincidence is outside the acceptable range covered by the Coincidence Matrix (see also section 4.2.3). Finally, we get: The maximally allowed value for $\Delta^{+,-}$ is ± 4 and for $\Delta^{r,0}$ is ± 2.

We see in Figure 7.5 that this limit is significantly exceeded even in the case of valid messages. We investigate those events and create the wire memory pattern that enters the Coincidence Matrix using only the hit information of the muons from the J/ψ. In this case, 13 % of the valid messages did not show any coincidence due to hits of the muons. Consequently, the found coincidence must be due to additional hits generated by other tracks of this event.

We analyse the events with tracks that are inside the ROI but result in invalid messages. Tracks with a value of $\Delta^{r,s}$ within the limit stated above should result in coincidences

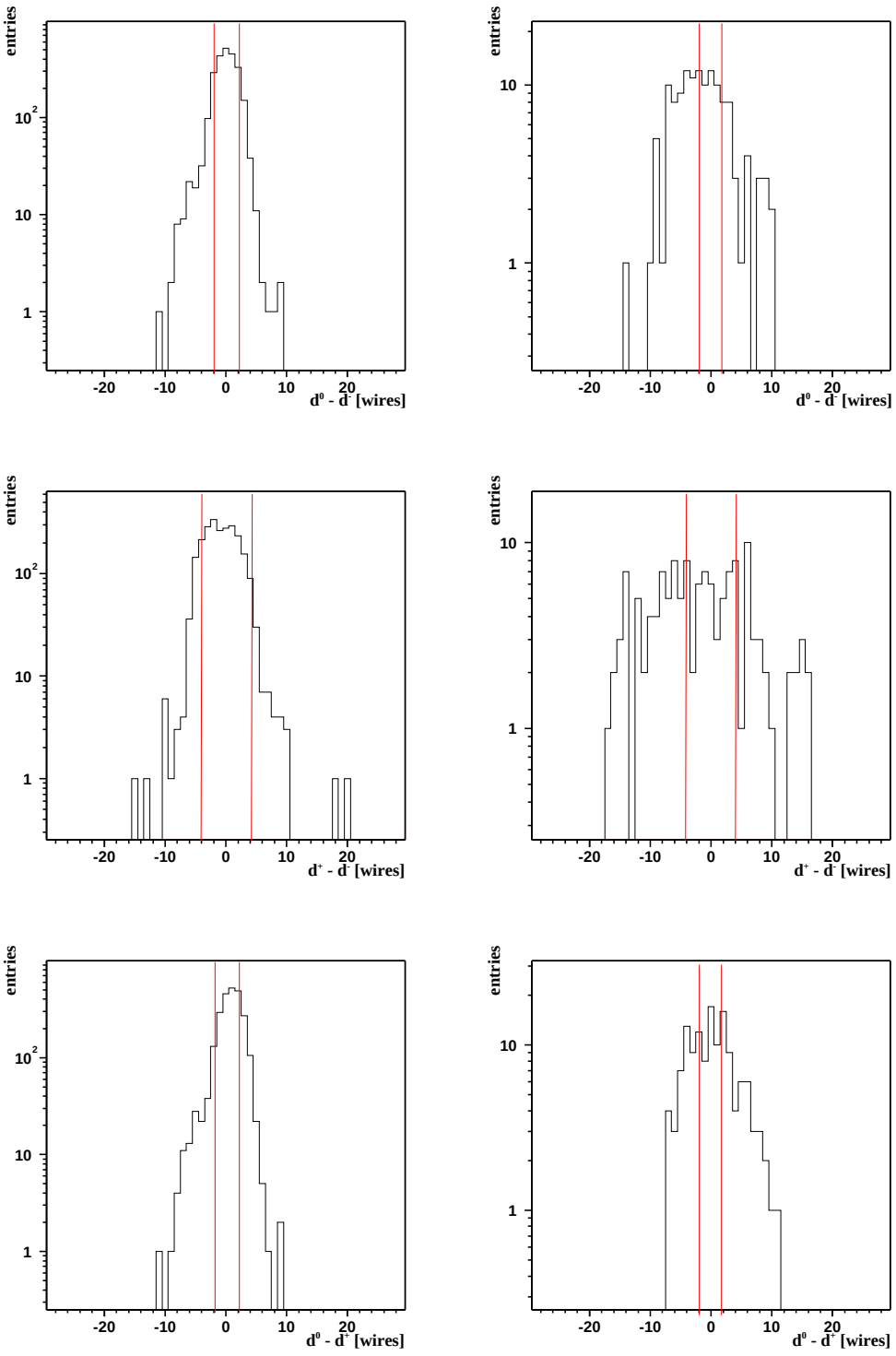

Figure 7.5: *Left: Difference* $\Delta^{r,s}$ *calculated by the information provided from MC for valid simulated tracks. Tracks exceeding the given limits are valid due to random coincidences which happens for 13 % of the tracks. Right: Difference* $\Delta^{r,s}$ *for tracks that are inside the ROI but result in invalid messages.*

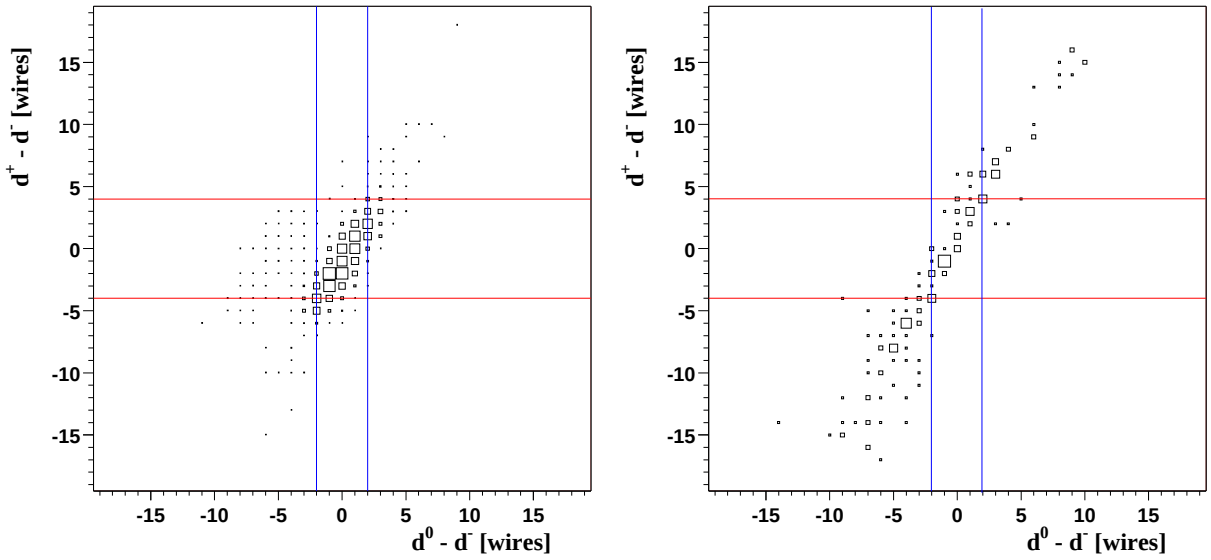

Figure 7.6: *The difference $\Delta^{0,-}$ versus $\Delta^{+,-}$ for valid tracks (left) and tracks inside the ROI that result in invalid messages (right). Invalid tracks inside the limit are found by a different setting of the "shift flag" or lost due to a $\Delta^{r,s}$ exceeding the limit in one of the other views. The lines represent the limits as specified in the text.*

and lead to valid messages. The analysis of such events shows that all tracks actually can be found with a different value of the "shift flag" (see section 7.4.1). Tracks with values $\Delta^{r,s}$ outside the limit are lost because any other value of $\Delta^{r,s}$ is exceeding the limit (see Figure 7.6 right). The Coincidence Matrix cannot form a coincidence for those tracks.
We conclude a problem in the n calculation. The problem is partially covered by random coincidences that keep the message "valid" and thus the reference track is not lost. The remaining inefficiency of

4.6 %

is caused by a problem of the calculation of the first wire of the ROI and by shifts of the determined ROIs with respect to each other. The problem can be solved by minimising the relative shifts of the ROIs in the algorithm.

7.4.5 Inefficiencies related to Geometrical Effects

The real geometry of the detectors is different from the geometry used in the wire memory. The wire memory assumes an equidistant spacing of the wires throughout its range because the region that is connected to a TFU is defined by its starting point, the corresponding ranges and the number of wires.
In reality, there are shifts between the wires due to necessary support structures, borders of modules and the distance between the two halves of superlayers serving the positive and negative x-region in the experimental area.
Shifts with respect to the expected wire position in the wire memory and the real x position could lead to a wrong assumption as to what wires are hit resulting in failure to form a

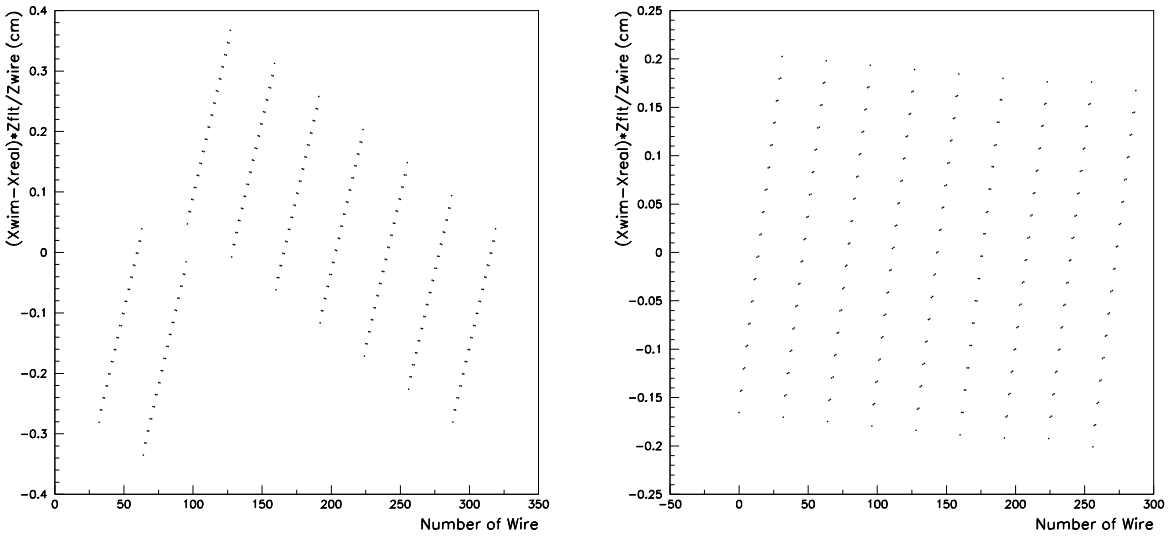

Figure 7.7: *The difference between the wire position as recorded in the detector table in ARTE and the wire position of the wire memory for a TFU of the muon system. Left: The step at the beginning of the wire memory is due to the fact that this TFU covers a region on both x-halves of the detector. Right: The distance shows no step for a TFU that covers a consecutive region [Riu01a].*

triple hit coincidence. We calculate the difference between the x-position of the wire as recorded in the detector table of ARTE and the wire in the wire memory. Figure 7.7 shows this difference for two TFUs for the wires of the negative stereo angle. The maximal deviation of the predicted wire position in the wire memory and position of the wire in the detector table is smaller than 0.4 cm for all stereo views which is approximately a shift of half a cell. Such a small shift imposes no additional inefficiency since the Coincidence Matrix is still able to find triple hit coincidences. The step in Figure 7.7 (left) is due to the gap between the two halves serving the different x-regions in the experimental area.

7.4.6 Estimation of the Detector Inefficiency

Since the decrease in efficiency for perfect MC events is well below 36 % we assume that a major fraction of the FLT tracking inefficiency is related to a degraded detector performance.

Figure 7.8 shows occupancy plots for the different stereo layers of MU 1. Broken high voltage groups or problems with the readout electronics degrade the performance of MU 1 which affects the tracking performance of the FLT.

The hard-selected events were triggered by the SLT which uses a different algorithm compared to that of the FLT. The SLT uses only the hit information of the vertical (0°) wires whereas the FLT requires in addition hits in the stereo views (±20°). In a first step, we need to decide which reference tracks have hits in the stereo views and consequently should be found by the FLT.

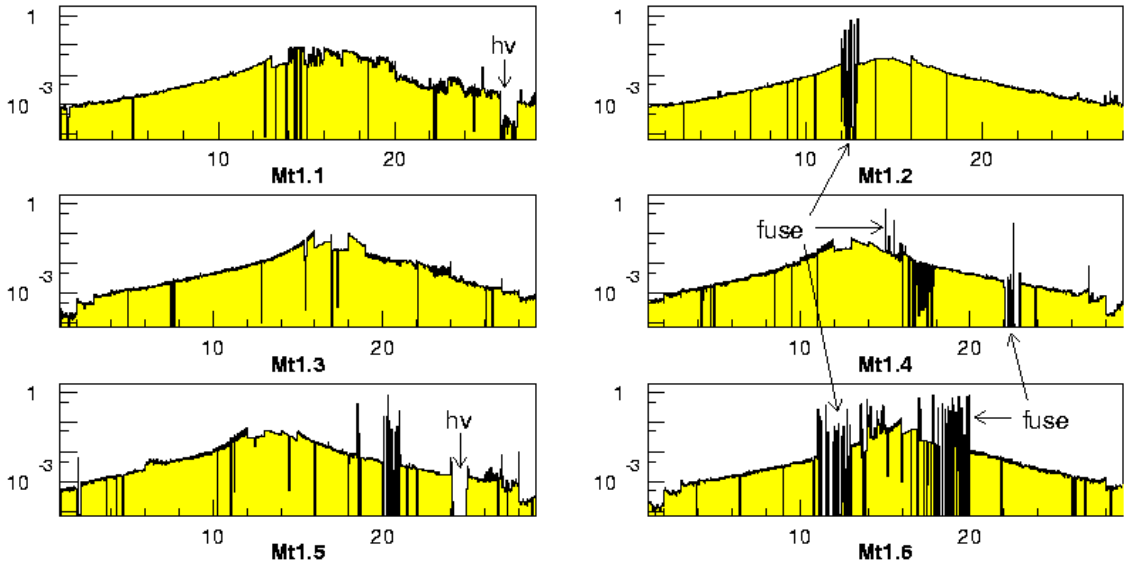

Figure 7.8: *Muon tube chamber occupancies for run 17246. High voltage failures or malfunctioning readout electronics degrade the detector efficiency which affects also the FLT efficiency. "Mt1.x" indicates the different stereo views of the tube chambers of MU 1. [Her00]*

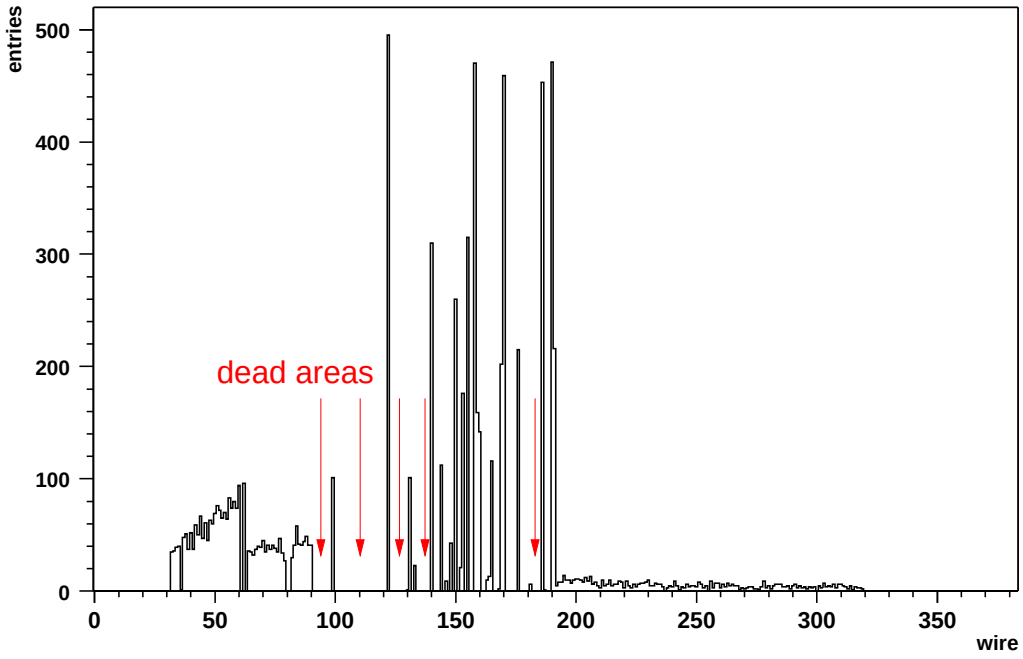

Figure 7.9: *Occupancy as seen by the wire memory of TFU 74 for the hard-selected data. The arrows indicate dead regions.*

Figure 7.9 shows the occupancy for the hard selected data as seen by the wire memory of the negative stereo view of TFU 74. Large areas with no occupancy indicate dead regions of the detector. We determine the distance between the impact point of the reference track and the closest hit for the vertical wires. The RMS of the distribution is 1.2 cm which is mainly due to multiple scattering. Without multiple scattering we would expect an RMS of about half a cell size (0.4 cm). The y-information of the reference track is also dominated by multiple scattering. The position is known to within ±5 cm. The value of the RMS and the estimated accuracy of the y-position are squared and added. We consider this result ($\approx$ 2.5 cm) to be a one sigma cut. We require that the distance between the closest hit and the expected impact point in the stereo layers is smaller than a two sigma range ($\approx$ 5 cm). We count the number of tracks that are outside the specified range since those tracks cannot result in a triple coincidence. We calculate the ratio of those tracks and the number of all reference tracks which results in an estimation of the detector inefficiency of about

$$(25 - 28)\ \%.$$

This number is in agreement with the number stated in [Her00]. The remaining decrease of efficiency of about 10 % is in agreement with the algorithmic inefficiencies as stated above.

7.5 Tracks *outside* the ROI resulting in invalid messages

We analyse single events of perfect MC with reference tracks that are outside of the ROI in at least one view to find out why this is the case.
The extrapolation from the layer MU 3 to the layer MU 1 (Figure 7.10) is performed such that the upper edge of the current ROI in MU 3 is projected according to the positive deviation from the straight line (i.e. $d\xi$) which gives the upper end of the predicted ROI in MU 1. From this upper point in MU 1 the width of the predicted ROI is subtracted to get the first wire of the ROI.
Scanning single events shows that there are coincidences, but outside of the lower border

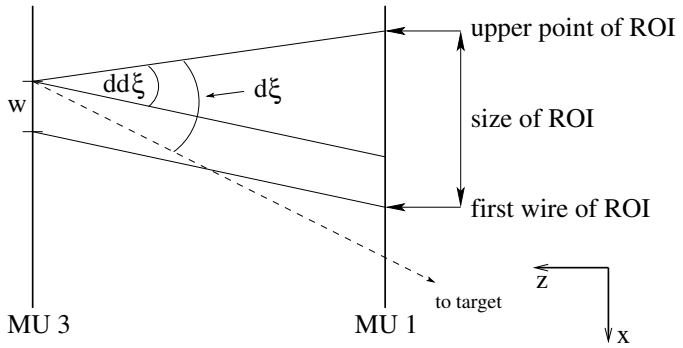

Figure 7.10: *Extrapolation from MU 3 to MU 1. The deviation from projectivity ($d\xi$) points to the upper end of the ROI. The first wire of the ROI is calculated by subtracting the width of the ROI from the upper point.*

of the ROI. The maximum width of the ROI is 31 wires for one message. To enlarge the ROI in MU 1 it is necessary to send two messages from MU 3: The first message covers the range of wires calculated by the corresponding Look-Up Table (LUT) and the second one is fixed to 31 wires. An investigation of the bit values of the input parameters for the $d\xi$ calculation showed no misbehaviour.
In some events, hits are inside the ROI in one or two stereo views but not in the mandatory other stereo views.
The remaining inefficiency of

$$3.2\ \%$$

for the tracks that are outside the ROI and result in invalid messages is due to ROI sizes that are too small and an incorrect determination of $d\xi$.

7.6 Summary and Conclusion

We investigated the large decrease of track efficiency by 36 % as seen with the hard-selected reference tracks.

- The static value of the "shift flag" causes an inefficiency of 1.4 % for the hard-selected reference tracks as well as for perfect MC tracks.
- The major fraction of the efficiency loss for tracks that are inside the ROI but result in invalid messages is due to a faulty calculation of the first wire of the ROI (n calculation) producing a shift of the stereo views with respect to each other. This shift destroys possible triple hit coincidences and sums up to an inefficiency of 4.6 %.
- A major fraction, about 26 %, is lost because of detector inefficiency. The hard-selected data are triggered by the SLT which uses only the vertical wires of MU 1. The FLT requires also hits in the stereo views to form a triple hit coincidence. The loss is due to missing hits in the stereo views close to the reference tracks.
- The reason for losses of tracks that are outside of the ROI for at least one stereo view is due to a wrong calculation of the "deviation ($d\xi$) from projectivity". Coincidences are outside the lower border (first wire) of the ROI. An enlargement of a single ROI (represented by a message) is not possible since the size of the ROI is already at the limit of 32 wires. An enlargement of the ROI size is only possible at the cost of additional message transfer between MU 3 and MU 1.

Table 7.2 summarizes the sources of inefficiency and their size for the hard-selected data and the MC sample. Some of the losses could only be studied by the MC sample. We learn from this analysis that tracking performed by the FLT strongly depends on the detector performance. Since the FLT algorithm looks for triple hit coincidences it is a crucial task for the detector to provide a high common chamber efficiency for all stereo views.
The implementation of a dynamical assignment of the "shift flag" according to the expected position in the detector is desirable.
The problem of the n calculation requires to minimise the relative shift of the stereo views with respect to each other.
The TFU geometry is in principle defined as a start coordinate and a number of wires that

	Data	MC
Total loss [%]	36	9.2
Detector inefficiency [%]	≈ 26	
Algorithmic inefficiency [%]	10.4	9.2
Static shift flag [%]	1.4	1.4
First wire of ROI [%]		4.6
Deviation ($d\xi$) [%]		3.2

Table 7.2: *Sources of efficiency loss of FLT tracking in MU 1 separated for hard-selected data and perfect MC.*

are assumed to have equidistant spacing. The TFU geometry that takes into account the position of the modules as realised in the detector itself improve the performance of the tracking algorithm.
The inefficiency which is related that tracks are outside the ROI is solved by changing the calculation of the deviation from projectivity ($d\xi$) which needs to be shifted to lower values to include coincidences that are at the border of the ROI. Another possibility to solve this inefficiency is to enlarge the ROI. The enlargement of the ROI requires some care with respect to the average message load between MU 3 and MU 1 and its impact on the latency.

Summary and Conclusion

The trigger system of the experiment HERA–B was designed to extract events that contain the decay $J/\psi \to l^+l^-$. The task of the First Level Trigger (FLT) is to perform a fast online tracking at an input rate of 10.4 MHz. The desired reduction is a factor of 200. For the purpose of fast online tracking a custom-designed electronics board, the Track Finding Unit (TFU) was designed. The network of outer tracker and muon system consists of 55 boards.

In this thesis, we studied the performance of the network with respect to the occupancy (as seen by the TFU wire memory), the deadtime and trigger rate for interaction rates of 5, 10 and 20 MHz.
The occupancy is 3.9 % for an interaction rate of 5 MHz, 5.7 % for 10 MHz and 9.2 % for 20 MHz. For the deadtime we assumed that a single TFU that has to process more than 5 tracks (or messages which is equivalent) in an event blocks the entire network. We estimate a deadtime of 4.4 % for an interaction rate of 5 MHz, 10.1 % for 10 MHz and 42.1 % for 20 MHz. The deadtime is moderate for 5 and 10 MHz. The assumption results in an upper limit of the deadtime. Note that we await the data taking to verify the results of the deadtime.
We estimated the output rate of the FLT for the single-track and for the pair trigger mode. With the nominal p_T-cut of 1.4 GeV/c for electrons and 1.0 GeV/c for muons we estimate a single-track trigger rate of 20.7 kHz for an interaction rate of 5 MHz, 52.9 kHz for 10 MHz and 216 kHz for 20 MHz. The output rate of the FLT for 10 and 20 MHz exceeds the acceptable input rate of the SLT which is of the order of 30 kHz. Note that it was not foreseen to run the FLT in a single-track trigger mode.
The estimated pair trigger rate is much lower. We expect a pair trigger rate of 0.27 kHz for 5 MHz, 2 kHz for 10 MHz and 17.1 kHz for 20 MHz target rate. All the pair trigger rates are well below the limit for the maximal input rate of the SLT. A pair trigger setup allows for higher interaction rates.
The deadtime as well as the trigger rate are studied with respect to the p_T^{track}-cut and to a multiplicity veto at different levels of J/ψ loss. At a J/ψ loss of 5 % the single-track trigger rate of the FLT is even for an interaction rate of 10 MHz below the limit of the maximal input rate of the SLT.

The geometrical acceptance and the efficiency for a single track as well as for a full J/ψ is essential to understand the performance of the FLT. The geometrical acceptance is studied with $J/\psi \to \mu^+\mu^-$ events from MC. The efficiencies are determined from triggered data taken in the year 2000 and also estimated by MC samples. In addition, we studied the acceptance and the efficiencies as a function of the p_T^{track}-cut, as a function of the transverse

Efficiency	perfect MC [%]	realistic MC [%]	Data [%]
Single-Track	59.2	16.6	18.8
J/ψ	36.2	3.9	3.9

Table 8.1: *The efficiency of the FLT to detect a single-track or a J/ψ event for the MC samples and the triggered data.*

momentum of the J/ψ, $p_T^{J/\psi}$, and as function of the Feynman variable x_F.
The geometrical acceptance with respect to p_T^{track} is 60 % for tracks in the outer region (outer tracker including muon tube and pad system) with a p_T^{track} above 0.7 GeV/c. Below a p_T^{track} of 0.5 GeV/c the major number of tracks lies in the inner region (inner tracker and muon pixel) or in the beam pipe.
We also studied the geometrical acceptance for J/ψ events. A pair trigger is best suited with respect to the output rate of the FLT. The acceptance for tracks with a minimal p_T^{track} of 0.5 GeV/c is 20 % for the outer region. For two tracks in the outer and inner region the acceptance is 55 %. Since the inner region could not be used by the FLT during the data taking in 2000 a trigger scheme with one track in the outer region for the FLT and the second track either also in the outer or in the inner region triggered by the SLT leads to an acceptance of 46 %. All acceptances decrease significantly for p_T^{track}-cuts above 1.0 GeV/c due to the kinematics of the J/ψ.
The single-track efficiency for perfect MC is 59 %. For a realistic MC that includes the estimated detector performance of the year 2000 the single-track efficiency is 16 %. For hard selected $J/\psi \to \mu^+\mu^-$ events triggered by the SLT the efficiency is 18 %. The realistic MC as well as the data show a significant efficiency loss at the first muon layer MU 1.
The J/ψ efficiency from event counting results in 36 % for perfect MC and in 4 % for realistic MC as well as for the hard selected data. The efficienies determined with perfect MC are below the expectations of 71 % and 48 %, respectively. Table 8.1 summarises the results.
For the acceptance and efficiency to have at least one track in the outer region we require a p_T^{track} larger than 1.0 GeV/c. In the case that we require two tracks in the outer region we require that each track has p_T^{track} larger than 0.5 GeV/c. The geometrical acceptance of the FLT as a function of $p_T^{J/\psi}$ is larger than 45 % for values of $p_T^{J/\psi} \geq 0.2$ GeV/c. The efficiency to find at least one track exceeds 70 %. The efficiency for two tracks is around 16 %.
The geometrical acceptance of the FLT with respect to the scale-independent variable x_F is higher than 60 %. The geometrical acceptance of the FLT ranges in x_F between -0.3 and 0.1. The single-track efficiency is 75 %. The efficiency for two tracks is 30 %. Table 8.2 summarises the results.
HERA–B can contribute to a deeper understanding of processes of heavy quark production and QCD physics in the negative x_F range. The trigger scenario for the upcoming run allows to extend the range in x_F to the positive regime. The entire range in x_F covers values between -0.3 and 0.4 which has not yet been covered by one single experiment.

Efficiency	Acceptance $p_T^{J/\psi}$ [%]	Efficiency $p_T^{J/\psi}$ [%]	Acceptance x_F [%]	Efficiency x_F [%]
single-track	> 45	> 70	≥ 60	≥ 80
J/ψ	≈ 25	≈ 16	≈ 25	≥ 20

Table 8.2: *The efficiency of the FLT to detect a single-track or a J/ψ event as a function of the transverse momentum of the J/ψ and as function of the variable x_F. The numbers are determined with perfect MC events.*

The single-track efficiency for the hard selected data showed an efficiency loss of the order of 36 % at the muon tracking layer MU 1. The investigation of this drastic loss revealed that a major fraction, (25-28) % (abs.), of the inefficiency is due to a bad detector performance for the stereo views. The SLT already triggered the event which means that at least the vertical wire is hit. The inefficiency due to the tracking algorithm is about 10 % (abs.).
The pure algorithmic inefficiency of the FLT tracking algorithm is studied with perfect MC. Due to the improved knowledge on track and hit position for MC the algorithmic inefficiency is slightly lower and results in 9.2 % (abs.). A large fraction (4.6 % (abs.)) of the inefficiency is caused by the calculation of the first wire of an ROI and by relative shifts between the different views. Due to a wrong calculation of the track slope it happens that the track is not contained inside the ROI of at least one view. This effect causes 3.2 % (abs.) of the inefficiency. The stereo angle of $\pm 20°$ for MU 1 makes a correction necessary for the coincidence finding which is done by the Coincidence Matrix. The LUT to steer this correction was not implemented during the data taking of the year 2000. The inefficiency due to the missing correction is 1.4 % (abs.). The tracking algorithm and its implementation in hardware have proven to find tracks. The low efficiency determined from the hard selected data showed that the FLT performance strongly depends on the detector performance. Missing hits in one of the stereo views leads to the loss of the track candidate.
The analysis showed also that the tracking algorithm can be improved for the first muon layer MU 1. The large stereo angle of MU 1 requires a correction of the relative distance between the stereo views in order to find triple hit coincidences. The correction is foreseen to happen dynamically which is desirable for the upcoming data taking. The relative shift of the calculated ROIs with respect to each other needs to be minimised.

The analysis showed that the general concept of the FLT works and that the FLT is able to find tracks at an acceptable efficiency for events from perfect MC. We emphasise that a deviation from perfect conditions especially from a perfect detector performance reduces the efficiency of the FLT drastically. As a consequence, we see that the general concept of the FLT is very intolerant to changes with respect to efficiency of the involved subsystems such as the trigger layers. We also have to emphasise that we have no alternative concept at hand to cope with the requirements of the FLT at a higher efficiency.
The data taking of the year 2002 will increase our understanding of the FLT and open possibilities to improve the system further.

Appendix A

Glossary

ARTE	Analysis and Reconstruction Tool and Environment of HERA–B.
ASIC	Application Specific Integrated Circuit. Chip designed for custom purposes.
BX	Bunch crossing.
CM	Coincidence Matrix.
CPU	Central Processing Unit. Main processing unit of a microprocessor.
DPRAM	Dual-Ported-RAM. Memory chip with two connected bus systems allowing two memory accesses within one clock cycle.
DSP	Digital Signal Processor.
ECAL	Electromagnetic Calorimeter.
EVC	Event Controller. Steering unit made of DSPs included in the data acquisition system of HERA–B.
FCS	Fast Control System. Control system to synchronise the detector readout of HERA–B.
FED	Front End Driver. Readout electronics at the detector.
FIFO	First In First Out. Order scheme for sequential data access. Data written first is also read out first.
FLT	First Level Trigger.
4LT	Fourth Level Trigger.
GEM	Gas Electron Multiplier.
HERA	Hadron Electron Ring Accelerator.
ITR	Inner Tracker.
LUT	Look Up Table. Table realised by memory chips.
MC	Monte Carlo. Simulation technique to simulate physical interaction by a computer.
MUON	Muon detector system.
MSGC	Micro Strip Gas Chamber.
OTR	Outer Tracker.
RAM	Random Access Memory. Readable and writeable memory chip allowing unconditioned access.
RICH	Ring Imaging Čherenkov Counter.
ROI	Region Of Interest. Search region in the detector checked by trigger algorithms for tracks.

SHARC Super Havard Architecture Computer. Name of a Digital-Signal-Processors of Analog Devices.

SLB Second Level Buffer. System realised with SHARCs for intermediate storage of the event data while the execution of the trigger algorithm of the SLT.

SLICER First part of the SLT trigger algorithm which looks for coincidences in the tracking layers within the ROIs specified by the FLT.

SLT Second Level Trigger.

TDU Trigger Decision Unit. Takes the final trigger decision of the FLT.

TFU Track Finding Unit. Custom-designed electronics processor to perform tracking on the FLT.

TLT Third Level Trigger.

TPU Track Parameter Unit. Custom-designed electronics board to reconstruct the track parameters.

TRD Transition Radiation Detector.

VDS Vertex Detector System.

VME Versa Module Eurocard. Standardised 64 bit interface.

WM Wire Memory. Memory to store the hit information of the detector.

X-Refit Second part of the SLT trigger algorithm which reconstructs the track candidates of the FLT in an xz projection. X-Refit uses only the vertical wires (strips in case of the VDS).

Y-Refit Third part of the SLT trigger algorithm which performs a 3-dimensional track reconstruction.

Appendix B

Parameter definitions

Most of the parameters are coded such that the binning is constant in terms of measurement uncertainty. Consider the measured variable $\tilde{x}$, it is coded using a function $f(\tilde{x})$. If the initial assumption is valid:

$$const. := k = \Delta f = \frac{df}{d\tilde{x}} \cdot \Delta\tilde{x}(\tilde{x})$$

$$\Rightarrow \frac{df}{k} = \frac{d\tilde{x}}{\Delta\tilde{x}(\tilde{x})} \Rightarrow f = k \cdot \int \frac{1}{\Delta\tilde{x}(\tilde{x})} d\tilde{x}$$

This formula can, for example, be used for the ECAL and a constant error binning is achieved. For the ECAL the uncertainty in energy is $\Delta\tilde{E} \sim \sqrt{\tilde{E}}$, therefore $f(\tilde{E}) \sim \sqrt{\tilde{E}}$ or for the momentum it is $\Delta\tilde{P} \sim \tilde{P}^2$ $f(\tilde{P}) \sim -1/\tilde{P}$.

A commonly used coding for constant fractional errors is:

$$\Delta\tilde{x} = b \cdot \tilde{x} \Rightarrow$$

$$\Rightarrow f(\tilde{x}) = \int_{\tilde{x}_{\min}}^{\tilde{x}} \frac{du}{b \cdot u} = \frac{1}{b} \ln\left(\frac{\tilde{x}}{\tilde{x}_{\min}}\right) \Rightarrow \tilde{x} = \tilde{x}_{\min} e^{f(\tilde{x})b} \tag{B.1}$$

$\boxed{P \text{ (7 bits)}}$ is the nominal momentum of the track derived from the measured energy $\tilde{E}$ in the ECAL or the estimated momentum of the muon system or the high-p_T pretrigger. The Energy resolution of the ECAL is $\Delta E/\tilde{E} \approx 10\%/\sqrt{\tilde{E}}$, and the range is $5...200 GeV$. A convenient binning is hence

$$P = \text{int}\left(10 \cdot \left(\sqrt{\tilde{E}/GeV} - \sqrt{5}\right)\right) \qquad \tilde{E} = \left(0.1 \cdot P + \sqrt{5}\right)^2 GeV \tag{B.2}$$

which defines $P[0...119;7]$.

$\boxed{\eta \text{ (1+8 bits)}}$ is the $\tilde{y}/\tilde{z}$ coordinate of a track candidate at TC2. Between TC2 and MU4 the coordinates of the last detected point are used. The most significant bit is used as sign bit. The remaining 8 bits allow for up to 256 bins. The binning is based on the granularity of the ECAL, which provides the initial measurement of $\tilde{y}$ for electrons and

positrons. The position of the electron/positron showers are determined by the center-of-gravity method. For the FLT the ECAL position resolution is assumed to be a quarter of the ECAL module size. An ECAL module has a quadratic surface of $(11.15\,cm)^2$ and the ECAL is 42 ($\pm$ 21) modules high in y direction. Depending on its distance from the proton beam pipe an ECAL module consists of 1, 4, or 25 ECAL cells. The η-encoding is different for different detector regions.
With p the precision, g the granularity, and $l_{\mathrm{mod}} = 11.15cm$ the size of an ECAL module we measure $\tilde{y}$ in units of l_{mod}:

$$\tilde{y\prime} = \frac{\tilde{y}}{\tilde{z}} / \frac{l_{\mathrm{mod.}}}{z_{\mathrm{ECAL}}}$$

and encode it as follows:

$$\tilde{y\prime} \leq 6 \;\rightarrow\; \eta = \mathrm{int}(\tilde{y\prime} \cdot g_1/p) \qquad (p = 1/4;\, g_1 = 5) \tag{B.3}$$

$$\tilde{y\prime} > 6 \;\rightarrow\; \eta = \mathrm{int}[(\tilde{y\prime} - 6) \cdot g_2/p] + 128 \quad (p = 1/4;\, g_2 = 2) \tag{B.4}$$

$$\Rightarrow \Sigma_{binning} = 120 + 120 = 240\,\mathrm{bins}$$

In order to enable the granularity detection by use of the upper 2 bits only the granularity boundaries are aligned to multiples of 64. Accordingly, $2 \cdot 192$ bins are needed and hence 9 bits are sufficient.

$\boxed{\xi\ (1{+}9\ \mathrm{bits})}$ is the $\tilde{x}$ coordinate at TC2. The most significant bit is used as sign bit. The bin sizes are determined by the detector granularities and the number of bits available. In the inner part, i.e. MSGC region and at least some of the 5 mm OTR region, there will be a one-to-one matching of detector cells to bins. Various schemes which represent the detector cells by a smaller number of ξ bins are under study. The granularity discontinuities are fixed to multiples of 32 to enable the recognition of the granularity by using bits 5...9 only.

$$\xi = \mathrm{int}\,(|\tilde{x}|/1.2mm) \quad \forall \quad |\tilde{x}|/mm \in [\,0, 230.4\,] \tag{B.5}$$

$$\xi = 192 + \mathrm{int}\,((|\tilde{x}|/mm - 230.4)/4.33) \quad \forall \quad |\tilde{x}|/mm \in [\,230.4, 784.64\,] \tag{B.6}$$

$$\xi = 320 + \mathrm{int}\,((|\tilde{x}|/mm - 784.64)/8.66) \quad \forall \quad |\tilde{x}|/mm \in [\,784.64, 1893.12\,] \tag{B.7}$$

$$\xi = 448 + \mathrm{int}\,((|\tilde{x}|/mm - 1893.12)/17.32) \quad \forall \quad |\tilde{x}|/mm \in [\,1893.12, 3001.6\,] \tag{B.8}$$

$$\Rightarrow \Sigma_{binning} = 192 + 128 + 128 + 64 = 512\,\mathrm{bins}$$

In total there are 512 bins needed which is 9 bits information. In the outer region of the tracking the momenta are small and hence a slightly lower resolution is tolerable.

If there would be no need of determining the granularity from the first 4 bits there could be a more optimized binning.

$\boxed{w\ (2\ \mathrm{bits})}$ number of adjacent cells in TC2. No more than 4 adjacent cells are combined into one cluster by a TFU, hence 2 bits are sufficient[1].

$\boxed{d\xi\ (1{+}7\ \mathrm{bits})}$ Minimal track slope. The most significant bit is used as sign bit. This variable is set initially by the pretrigger (determined by the momentum threshold and

[1] The double-U, w, stands for 'width', but because it is written in italics, 'w' instead of 'w', it was sometimes interpreted as omega, ω.

measured momentum for this message) and updated after each tracking step. The track slope should be able to distinguish between two neighbouring cells (spacing $1.2mm$ in the MSGC area or $4.33mm$ in medium tracking) in the first super layer (PC1) looking from TC2 (distance $\approx 5.6m$). The minimal slope, measured in $\tan(\mathrm{d}\tilde{\xi})$, to resolve is hence 1.2 mm/5.6 m = 0.0002 or 4.33 mm/5.6 m = 0.0008. The minimal momentum in the medium and outer tracking is 5GeV which defines the slope deviation from projectivity to be $\tan(d\tilde{\xi}) \leq 0.049$. In the MSGC area (where the fine binning is needed) the minimal track momentum is 13GeV and the slope less than 0.019.

$$|\tan(d\tilde{\xi})| \leq 0.019 \quad \rightarrow \quad \mathrm{int}\left(|\tan(d\tilde{\xi})|/0.0002\right) \tag{B.9}$$

$$|\tan(d\tilde{\xi})| > 0.019 \quad \rightarrow \quad 95 + \mathrm{int}\left((|\tan(d\tilde{\xi})| - 0.019)/0.0009\right) \tag{B.10}$$

$$\Rightarrow \Sigma_{binning} = 95 + 33 = 128\,\mathrm{bins}$$

Therefore 128 bins or 7 bits are needed plus 1 bit for the sign which is the charge of the track. It is the angle between a straight line from ξ to the target and the lower boundary of the search area (after the cross-over point).

$\boxed{dd\xi \text{ (8 bits)}}$ defines the size of the track "window" in x: $d\xi_{max} - d\xi$. Its granularity is given by the maximal window size and the detector resolution. The maximal size is $32 \cdot 0.866cm$ and the highest resolution is $1.2mm$: 231 bins or 8 bits are necessary. $dd\xi$ is the angle between the two boundary lines of the search region at the cross-over point. This variable is set initially by the pretrigger (determined from the measured energy $\tilde{E}$ and the energy threshold E_0 for this message) and updated after each tracking step. After the last tracking step its size shrinks to 2 bits since only the actual number of adjacent cells has to be recorded for the second level trigger. These bits are written right aligned into the data field by the TFU.

$\boxed{BX \text{ (8 bits)}}$ is the Bunch-Crossing number. The FLT pipeline length is 128(7 bits). To enable wrap-around detection an additional bit is used.

$\boxed{ID \text{ (2 bits)}}$ is the pretrigger type or track ID.

$\boxed{FLAG \text{ (1 bit)}}$ flag bit to indicate that this message has to be passed to the next TFU independent of the outcome of a hit search.

$\boxed{DEST(8 \text{ bits})}$ destination(s) for message: each TFU which has to receive the message gets its bit set.

$\boxed{n\xi \text{ (1 bit)}}$ is the number of ROIs to search in the next TFU minus one to implement larger ξ dimensioned ROIs. $n\xi = 1$: search two ROIs else search one.

$\boxed{All \text{ (1 bit)}}$ is a Flag indicating that all TFUs have found a hit for this message. This is useful in combination with $FLAG$ to check the FLT using the data. It also provides a method of "photon" identification during tracking.

Appendix C

Overview of TFU Look Up Tables

LUT 0: Calculation of $n1$

$$n1 = MIN \left\{ \begin{array}{rl} (x(\xi, d\xi, z_-) - x0^-) & \cdot \frac{nx^-}{sx^-} \\ (x(\xi, d\xi, z_0) - x0^0) & \cdot \frac{nx^0}{sx^0} \\ (x(\xi, d\xi, z_+) - (x0^+ + sy \tan \alpha^+)) & \cdot \frac{nx^+}{sx^+} \end{array} \right\}$$

$$x(\xi, d\xi, z_v) = \xi \frac{z_v}{z_{Ref}} + d\xi \, (z_{Ref} - z_v)$$

LUT 1: Calculation of sf

Only needed for TFUs of MU 1.

LUT 2: Calculation of $dn1+$

$$\begin{array}{c} dn1+ \;=\; (y0 + sy - y_{mid}) \tan(\alpha^+) \cdot \frac{2}{cellSx^+} \\ \eta_{max} = \eta + d\eta/2,\; y_{mid} = 1/2 \cdot (\eta_{max} + \eta_{min}) \end{array}$$

LUT 3: Calculation of $dn1$

$$dn1 = 0$$

LUT 4: Calculation of $dn1-$

$$\begin{array}{c} dn1- \;=\; (y0 - y_{mid}) \tan(\alpha^-) \cdot \frac{2}{cellSx^-} \\ \eta_{min} = \eta - d\eta/2,\; y_{mid} = 1/2 \cdot (\eta_{max} + \eta_{min}) \end{array}$$

LUT 5,6,7: Calculation of $dn2+, dn2, dn2-$

$$\begin{aligned} dn2+ &= \Big(x(\xi, d\xi, z_+) - \Big(x0^+ - sy \cdot \tan(\alpha^+) + cellSx \cdot n1(\xi, d\xi, z)\Big)\Big) \cdot \frac{2}{cellSx^+} \\ dn2 &= \Big(x(\xi, d\xi, z_0) - \Big(x0^0 + cellSx \cdot n1(\xi, d\xi, z)\Big)\Big) \cdot \frac{2}{cellSx^0} \\ dn2- &= \Big(x(\xi, d\xi, z_-) - \Big(x0^- + cellSx \cdot n1(\xi, d\xi, z)\Big)\Big) \cdot \frac{2}{cellSx^-} \end{aligned}$$

LUT 8,9: Calculation of $dl+, dl, dl-$

$$dl = \Big(w \cdot \tfrac{z}{z_{Ref} \cdot cellSx}\Big) + swap$$

$$swap = \left\{ \begin{array}{llll} 1 \Rightarrow & MU, & TC2, & TC1 \\ 0 \Rightarrow & other & layers & \end{array} \right\}$$

ADD: $n2$

$$n2 = n1 + \tfrac{dn1+dn2}{2}$$

LUT 10: Calculation of h

$$\begin{aligned} h_{cross} &= cellSx / \tan(\alpha_{stereo}) \\ n_{bottom} &= (\eta - 1/2 \cdot d\eta - y_{cross}) / h_{cross} \\ n_{top} &= (\eta + 1/2 \cdot d\eta - y_{cross}) / h_{cross} \end{aligned}$$

n_{bottom}	n_{top}	h
< 1	< 1	0
< 2	< 1	1
< 1	< 2	2
> 2	> 2	3

LUT 10: Calculation of w_l

$$w_l = \tfrac{w \cdot z_v}{z_{Ref} \cdot cellSx^v} + 1$$

LUT 11: Calculation of $l1$

$$l1 = \Big[\Big(\tfrac{dd\xi}{cellSx^v} \cdot \tfrac{z_{Ref} - z_{v,min}}{z_{Ref} - z_{SL}} + 1\Big) + 1\Big] >> 1$$

LUT 12/13: Calculation of ξ_l

$$\xi_l = \xi^{max} - \left(\frac{\xi \cdot z_{SL}}{z_{Ref}} - x0\right) \cdot cellSx - locOff$$

ξ^{max} is the maximal possible value for ξ_l which is 2047. $locOff$ is a offset to avoid negative values later on in the process tree and is set to $locOff = \frac{\xi^{max}-384}{2} = 832$.

LUT 14,15,16: Calculation of $l2+, l2, l2-$

$$l2\pm = \begin{array}{ll} sw & \left\{\begin{array}{lll} lb<32,\, n\xi \equiv 0 \Rightarrow & lb \cdot \left(2 - \frac{1}{\cos\alpha}\right) - 0.5 \\ lb<32,\, n\xi \equiv 1 \Rightarrow & 0 \\ lb>32,\, n\xi \equiv 1 \Rightarrow & lb - 32 \end{array}\right\} \quad lb = \; 2 \cdot l1 + dl + h/2 \\ !sw & \left\{\begin{array}{lll} lb<32,\, n\xi \equiv 0 \Rightarrow & lb \\ lb<32,\, n\xi \equiv 1 \Rightarrow & 0 \\ lb>32,\, n\xi \equiv 1 \Rightarrow & lb - 32 \end{array}\right\} \quad lb = \; 2 \cdot l1 - dl + h/2 \end{array}$$

$$l2 = \begin{array}{ll} sw & \left\{\begin{array}{lll} lb<32,\, n\xi \equiv 0 \Rightarrow & lb - 0.5 \\ lb<32,\, n\xi \equiv 1 \Rightarrow & 0 \\ lb>32,\, n\xi \equiv 1 \Rightarrow & lb - 32 \end{array}\right\} \quad lb = \; 2 \cdot l1 + dl + \frac{h}{2} \\ !sw & \left\{\begin{array}{lll} lb<32,\, n\xi \equiv 0 \Rightarrow & lb \\ lb<32,\, n\xi \equiv 1 \Rightarrow & 0 \\ n\xi \equiv 1 \Rightarrow & lb - 32 \end{array}\right\} \quad lb = \; 2 \cdot l1 - dl \end{array}$$

$$sw = \left\{\begin{array}{llll} 1 \Rightarrow & MU, & TC2, & TC1 \\ 0 \Rightarrow & other & layers & \end{array}\right\}$$

Logic: n

$$n = n\xi \; ? \; l2 \; + \; n2 \; : \; n2$$

Logic: l

$$l = n\xi \; ? \; 32 \; : \; l2$$

ADD: ξ_M

$$\xi_M = \xi_l - n_0$$

LUT 17/18: Calculation of $\xi_{min,M}$

$$\xi_{min,M} = \xi^{max} - \xi_M - w_l$$

LUT 22: All'

$$mux = \left\{ \begin{array}{lll} layer < TC2 \Rightarrow & 1 & no-update \\ layer \geq TC2 \Rightarrow & 0 & update \end{array} \right\}$$

f_0	All	All'
0	0	1
0	1	1
1	0	0
1	1	1

LUT 23: Calculation of $d\xi_{max,1}$

$$d\xi_{max,1} = (i_{kM} + 1 + locOff - \xi_{min,M}) \frac{cellSx}{z_{Ref} - z_{SL}} \cdot shift$$

LUT 24: Calculation of E_0

$$\begin{aligned} d\xi_{geo} &= \frac{|\xi| + r_{Mag}}{z_{SL} - z_{Mag}} \\ d\xi_{kin} &= \frac{A}{p \cdot z_{SL}} \quad A = 302.4GeV \cdot cm \\ E_0 &= MIN\,(d\xi_{kin}, d\xi_{geo}) \end{aligned}$$

LUT 25: Calculation of $d\xi_1$

$$d\xi_1 = (i_M + locOff - \xi^{max} + \xi_M) \frac{cellSx}{z_{Ref} - z_{SL}} \cdot shift$$

$$\left\{ \begin{array}{ll} layer \geq TC2 \Rightarrow & shift = \frac{z_{Ref}}{z_{SL}} \\ layer < TC2 \Rightarrow & shift = 1 \end{array} \right\}$$

ADD: ik_M

$$ik_M = k_M + i_M$$

ADD: i_l

$$i_l = n_0 + i_M$$

ADD: ik_l

$$ik_l = i_M + k_M + n_0$$

LUT 26/27: Calculation of η'

η is only updated in MU 1. In MU 3 and MU 4 η is only forwarded. The remaining layers code η with respect to the reference layer of the following layer.

LUT 27: Calculation of $\eta 1$

Code destination in y-direction into a bit pattern.

LUT 29: Calculation of $d\xi_{max}^{new}$

$$d\xi_{max}^{new} = \left\{ \begin{array}{ll} layer \geq TC2 \Rightarrow & MIN\left(E_0, d\xi_{max,1}\right) \\ layer < TC2 \Rightarrow & d\xi_{max,1} \end{array} \right\}$$

LUT 30: Calculation of $d\xi^{new}$

$$d\xi^{new} = \left\{ \begin{array}{ll} layer \geq TC2 \Rightarrow & MAX\left(-E_0, d\xi_1\right) \\ layer < TC2 \Rightarrow & d\xi_1 \end{array} \right\}$$

LUT 31/32: Calculation of ξ_n

$$\xi' = (x0 + cellSx \cdot (i_{kl} + 1)) \cdot \frac{z_{ref,next}}{z_0}$$

LUT 33: Calculation of $d\xi_{max}$

$$d\xi_{max} = \left\{ \begin{array}{ll} layer < TC2 \Rightarrow & d\xi_{max}^{new} \\ layer \geq TC2 \Rightarrow & d\xi^{new} \end{array} \right\}$$

LUT 35: Calculation of $d\xi'$

$$d\xi' = \left\{ \begin{array}{ll} layer < TC2 \Rightarrow & d\xi^{new} \\ layer \geq TC2 \Rightarrow & d\xi_{max}^{new} \end{array} \right\}$$

LUT 37: Calculation of ξ_{max}^{next}

$$\xi_{max}^{next} \;=\; ((i_{kl} + 1) \cdot cellSx) \cdot \frac{z_{next}}{z_{curr}} + d\xi' \cdot (z_{curr} - z_{next})$$

LUT 38: Calculation of ξ_{min}^{next}

$$\xi_{min}^{next} \;=\; (i_l \cdot cellSx) \cdot \frac{z_{next}}{z_{curr}} + d\xi_{max} \cdot (z_{curr} - z_{next})$$

LUT 39/40: Calculation of $dd\xi', n\xi'$

$$dd\xi' = (d\xi_{max} - d\xi') \cdot (z_{Ref} - z_{Next})$$

LUT 41/42: Calculation of $DEST1/DEST2$

Loop over destinationTFUs

$$DEST1 \mid= \; 1 << TDI(TFU) \quad DEST2 \mid= \; 1 << TDI(TFU)$$

Logic

OR: $DEST'$ =$DEST1$ OR $DEST2$

Bibliography

[Abe01] K. Abe et al.,
Observation of Large CP Violation in the Neutral B Meson System,
Phys. Rev. Lett. 87, 091802 (2001)

[Ada01] M. Adams,
Studies on Hit Multiplicities,
Hera–B Note 00-059, April 2001

[Ada01a] M. Adams,
PhD Thesis in preparation,
University of Dortmund

[Aff99] A. Affolder et al. (KTeV collaboration),
Fermilab Preprint (1999) presented at Heavy Quark '98 Workshop, Fermilab, Oct. 1998

[Alt88] G. Altarelli, M. Diemoz, G. Martinelli and P. Nason,
Total Cross-Sections For Heavy Flavor Production In Hadronic Collisions And QCD,
Nucl. Phys. B **308**, 724 (1988)

[Ang98] A. Angelopoulos et al. (CPLEAR collaboration),
First direct observation of time-reversal non-invariance in the neutral kaon system,
Phys. Lett. **B 444** (1998) 43

[Arg87] ARGUS Collaboration,
B MESON RESULTS FROM ARGUS,
Uppsala 1987 Proceedings, High energy physics, Vol.1 (1987) 360-362

[Art96] HERA–B Software Group,
ARTE The Event Reconstruction and Software Tool for HERA–B,
Hera–B Note, 1996

[Aub01] B. Aubert et al.,
Observation of CP Violation in the B^0 Meson System,
Phys. Rev. Lett. 87, 091801 (2001)

[Bab98] The BaBar Physics Book,
Physics at an Asymmetric B Factory,
SLAC-R-504 October 1998

[Bee91] W. Beenakker et al.,
QCD corrections to Heavy Quark Production in Hadron-Hadron Collisions,
Nucl. Phys. **B351** 507 (1991)

[Boc90] R. K. Bock et al.,
Data Analysis Techniques for High-Energy Physics,
Cambridge Univ. Press (1990) and references therein

[Bod95] G. Bodwin, E. Braaten, G. Lepage,
Rigorous QCD Analysis of Inclusive Annihilation and Production of Heavy Quarkonium,
Phys. Rev. **D 51**, 1125 (1995)

[Bra96] E. Braaten, S. Fleming, T.C. Yuan,
Production of heavy quarkonium in high energy colliders,
Ann. Rev. Nucl. Part. Sci. **46**, 197 (1996)

[Bra92] S. Brandt,
Datenanalyse,
BI-Wissenschaftsverlag Mannheim, 1992

[Cab63] N.Cabbibo,
Unitary Symmetry and Leptonic Decays,
Phys. Rev. Lett. **10** (1963) 531

[Car90] R. Carosi et al.,
A Measurement Of The Phases Of The CP Violating Amplitudes In $K^0 \to 2\,\pi$ *Decays And A Test Of CPT Invariance*,
Phys. Lett. **B 237** (1990) 303

[Cas98] C. Caso et al., Particle Data Group,
Europ. Phys. Jou. **C 3** (1998)

[Chr64] J. H. Christenson, J. W. Cronin, V. L. Fitch and R. Turlay,
Evidence For The $2\,\pi$ *Decay Of The* K_2^0 *Meson*,
Phys. Rev. lett. **13** (1964) 138

[Dre98] H.-B. Dreis et al.,
Operation of a large GEM-MSGC detector in a high intensity hadronic test beam using fully pipelined readout electronics,
Hera–B Note 98-149 (1998)

[Duj01] D. Dujmic,
Open Charm Production at HERA–B,
PhD thesis, University of Texas at Austin, 2001

[Eck96] R. Eckmann,
The HERA–B Magnets,
Hera–B Note 96-087, 1996

[Fla00a] J. Flammer,
Track Parameter Unit Documentation,
Hera–B Note 00-055, April 2001

[Fla00b] J. Flammer,
The HERA–B FLT Status Report,
Hera–B Note 00-161, October 2000

[Fla01] J. Flammer,
Entwicklung der Simulation des ECAL Pretrigger Systems für das Experiment HERA–B und Analyse der Effizienzen des Zerfalls $J/\psi \to e^+e^-$,
PhD Thesis University Hamburg, 2001

[Fom97] B. Fominykh, S. Nowak,
HERA–B Muon Detector in HBGEAN Versions 04-04 and 05-01,
Hera–B Note 97-075, April 1997

[Fri57] J. I. Friedman, V. L. Telegdi,
Nuclear Emulsion Evidence For Parity Nonconservation In The Decay Chain $\pi^+ \to \mu^+ \to e^+$,
Phys. Rev. **105** (1957) 1681

[Fri97] S. Frixione et al.,
Heavy Quark Production,
hep-ph/9702287

[Fuk98] Y. Fukuda et al.,
Evidence for oscillation of atmospheric neutrinos,
Phys. Rev. Lett. **81** (1998) 1562

[Ful99] T. Fuljahn,
Aufbau und Charakterisierung des schnellen Kontrollsystems für das Experiment HERA–B,
PhD Thesis University of Hamburg, 1999

[Gar57] R. L. Garwin, L. M. Lederman, M. Weinrich,
Observation Of The Failure Of Conservation Of Parity And Charge Conjugation In Meson Decays: The Magnetic Moment Of The Free Muon,
Phys. Rev. **105** (1957) 1415

[Gas87] R. Gastmans, W. Troost,
Production of heavy quarkonia from gluons,
Nucl. Phys. **B 291**, 231 (1987)

[Gav95] R. Gavai et. al,
Quarkonium production in hadronic collisions,
Int. J. Mod. Phys. A **10** (1995) 3043

[Gel98] A. Gellrich and M. Medinnis,
Higher Level Triggering Software,
NIM A 408(1998) 173

[Gel00] A. Gellrich,
A Large Linux-PC Farm for Online Event Reconstruction at HERA–B,
ACAT October 2000, Fermilab, Batavia, Illinois, USA and references herein

[Ger00] E. Gerndt,
HERA–B Pretrigger and FLT Latency,
Hera–B Trigger Note 00-001

[Gla61] S. Glashow,
Partial Symmetries Of Weak Interactions,
Nucl. Phys. **22** (1961) 579

[Gri87] D. Griffiths,
Introduction to Elementary Particles,
p. 135; John Wiley & Sons (1987)

[Hal84] F. Halzen, A. Martin,
Quarks and Leptons;
John Wiley & Sons (1984)

[Her94] HERA–B–Kollaboration,
Hera–B Proposal,
DESY-PRC 94/02

[Her95] HERA–B–Kollaboration,
Hera–B Design Report,
DESY-PRC 95/01

[Her00] HERA–B–Kollaboration,
Hera–B Status Report,
DESY-PRC 00/04

[Hul01] W. Hulsbergen,
Hit efficiency of the outer tracker,
Hera–B Note 01-077, October 2001

[Hum87] B. Humpert,
Narrow heavy resonance prouction by gluons,
Phys. Lett. **B 184**, 105 (1987)

[Jar85] C. Jarlskog,
Commutator Of The Quark Mass Matrices In The Standard Electroweak Model And A Measure Of Maximal CP Violation,
Phys. Rev. Lett. **55** (1985) 1039

[Kaw02] D. Kawall et al.,
A Test of CPT and Lorentz Invariance from Muonium Spectroscopy,
hep-ex/0201010

[Kla01] M. Klasen, B. A. Kniehl, L. N. Mihaila and M. Steinhauser,
Evidence for colour-octet mechanism from CERN LEP2 $\gamma\gamma \to J/psi + X$ data,
hep-ph/0112259

[Kni00] C. Knierim,
Messung und Analyse von Ratenfluktuationen am HERA–B Target,
Diplom Thesis, University of Dortmund, 2000

[Kob73] M.Kobayashi and T.Maskawa,
CP Violation In The Renormalizable Theory Of Weak Interaction,
Prog. Theo. Phys. **49** (1973) 652

[Lae92] E. Laenen, J. Smith and W. L. van Neerven,
All order resummation of soft gluon contributions to heavy quark production in hadron-hadron collisions,
Nucl. Phys. B **369**, 543 (1992)

[Lee56] T. D. Lee and C. N. Yang,
Question Of Parity Conservation In Weak Interactions,
Phys. Rev. **104** (1956) 254

[Lei00] M. Leitch et.al.,
Measurement of Differences between J/ψ and $\psi\prime$ Suppression in p–A Collisions,
Phys. Rev. Lett. **84** 3256 (2000)

[Lue54] G. Lüders,
Kgl. Danske Vidensk. Selsk. Mat.-Fys. Medd **28** (1954) No. 5

[Mak62] Z.Maki, M.Nakagawa and S.Sakata,
Remarks On The Unified Model Of Elementary Particles,
Prog. Theo. Phys. **28** (1962) 870

[Men90] R. Meng, G. A. Schuler, J. Smith and W. L. van Neerven,
Simple Formulae For The Order α_s^3 QCD Corrections To The Reaction P Anti-$P \to Q$ Anti-Q X,
Nucl. Phys. B **339**, 325 (1990)

[Mic02] A. Michetti, D. Ressing, I. Riu,
Hera–B First Level Trigger Test Vector Test,
FLT internal document, January 2002

[Nam00] S. Nam et.al.,
Muon Group Meeting,
Hera–B Note 00-173, October 2000

[Nas88] P. Nason, S. Dawson, R. K. Ellis,
The Total Cross-Section For The Production Of Heavy Quarks In Hadronic Collisions,
Nucl. Phys. **B303**, (1988) 607
The One Particle Inclusive Differential Cross-Section For Heavy Quark Production In Hadronic Collisions,
Nucl. Phys. B **327** (1989) 49, [Erratum-ibid. B **335** (1989) 260]

[Neg00] I. Negri,
Mapping of the OTR and the muon detectors for the First Level Trigger,
FLT internal document, April 2000

[Nir99] Y. Nir,
CP Violation In and Beyond the Standard Model,
script of SLAC summer institute, July 1999

[Noe16] E. Noether,
Der Endlichkeitssatz der Invarianten endlicher Gruppen,
Mathe. Ann. **77** (1916) 89-92

[Noe99] M. Nörenberg,
Objektorientierte Simulation der Trigger Decision Unit des HERA–B First Level Triggers,
Diplom Thesis University of Hamburg, 1999

[Noe01] M. Nörenberg,
Tracking efficiency of the FLT in the single lepton runs,
Hera–B Note in preparation

[Pau55] W. Pauli, in:
Niels Bohr and the Development of Physics,
Pergamon Press, London 1955, p. 30

[PDG98] Particle Data Group,
Review of Particle Properties,
European Physics Journal **C 3, 1-4** (1998)

[Res96] D. Ressing,
First level trigger for HERA–B,
NIM A 384 (1996) 131

[Res00] D. Ressing,
Private Communication

[Res01] D. Ressing,
Status of the FLT and Trigger Rates,
Hera–B Note 01-063, April 2001

[Riu01] I. Riu,
FLT Channel Masking,
Hera–B Note 01-024, February 2001

[Riu01a] I. Riu,
Private Communication

[Scha98] S. Schaller,
Untersuchung der Beiträge einzelner Protonenbündel zur Wechselwirkungsrate des Hera–B Experimentes,
Diplom Thesis, MPI Heidelberg, 1998

[Schme00] M. Schmelling et.al.,
Physics Commissioning Meeting,
Hera–B Note 00-133, August 16, 2000

[Schu94] G.A. Schuler,
Quarkonium production and decays,
hep-ph/9403387

[Schu95] H.D. Schulz,
Trigger Concept of the HERA–B Experiment,
Nucl. Physics B **44** (1995) 441-447

[Schw00] U. Schwanke,
Trigger and Reconstruction Farms in the HERA–B Experiment and Algorithms for a third level trigger,
PhD Thesis Humboldt University of Berlin, 2000

[Schw51] J. Schwinger,
The Theory Of Quantized Fields. I,
Phys. Rev. **82** (1951) 914;
The Theory Of Quantized Fields. II,
Phys. Rev. **91** (1951) 713

[Spr00] S. Spratte,
Bestimmung der Wechselwirkungsrate des HERA–B Targets und Untersuchung des Coasting Beams am HERA Protonenring,
PhD Thesis University of Dortmund, 2000

[Sym00] M. Symalla,
Vorbereitende Untersuchungen zur Bestimmung der Wechselwirkungsraten und deren Zeitstruktur an einem Drahttarget mit Hilfe der Energieinformation des HERA–B elektromagnetischen Kalorimeters
Diplom Thesis University of Dortmund, 1999

[Sym01] M. Symalla,
Private communication

[TFU99] *Technical Specification FLT Track Finding Unit V4.2*,
University of Mannheim, Lehrstuhl für Informatik V
http://www-li5.ti.uni-mannheim.de/mass_par/doc/tfudocu.ps

[TFU00] *HERA–B FLT Message Transfer Module LVDS*,
University of Mannheim, Lehrstuhl für Informatik V
http://www-li5.ti.uni-mannheim.de/mass_par/doc/messlvds.ps

[Vog99] R. Vogt,
J/ψ production and suppression,
Phys. Rept. **310**, 197 (1999)

[Wag 99] W. Wagner,
Auswertung der Daten des HERA–B Vertexdetektors im Hinblick auf die physikalischen Eigenschaften der verwendeten Siliziumstreifenzähler,
PhD Thesis, Ludwig-Maximilian-University Munich, 1999

[Wag00] G. Wagner,
Aufbau und Test der mit Digitalen-Signal-Prozessoren realisierten Komponenten des Datennahmesystems von HERA–B ,
PhD Thesis University of Hamburg, 2000

[Wei67] S. Weinberg,
A Model Of Leptons,
Phys. Rev. Lett. **19** (1967) 1264

[CWu57] C.S. Wu et al.,
Experimental Test Of Parity Conservation In Beta Decay,
Phys. Rev. **105** (1957) 1413

Acknowledgement

At the end of PhD thesis there is not much left what needs to be done but only to express the gratitude to all that helped in any possible way to bring the thesis to an end.
First of all, I would like to thank my wife Ulrike for her love and patience, for her support and for her motivation in the past years. The next thanks are to my parents for their support since my first day on this planet. I could not have made it here without their guidance.
Thanks to my supervisor Dr. A. Schwarz for various discussions and his companionship during the work on this thesis. Thanks to Prof. Dr. W. Schmidt-Parzefall for any discussion and the other experts opinion.
Many, many thanks to Dr. M. Hohlmann who gave advice during the last year and his never ending patience in correcting my "lumberjack" English.
Without the help of the members of the FLT group this thesis would not have been possible. I am grateful to Dr. E. Gerndt for any advice, to Dr. A. Michetti for his italian spirit he spread in our group, to Dr. I. Négri for her sense of humour which enlighted the sometimes frustrating work, to Dr. F. Ratnikow who introduced me to the "mysterious" algorithm of the TFU, to Dr. D. Reßing for answering all my questions concerning the TFU algorithm and many more items, to Dr. I. Riu for her manyfold help, to Dr. B. Schwingenheuer for his many good ideas and any advice that finally lead to the desired results and to Dr. A. Somov for various discussions.
Many thanks to my office mates, Dr. J. Flammer, M. Nörenberg, C. Rothe and L. Sözüer for the nice atmosphere and all their help. In addition, thanks to Dr. J. Flammer and M. Nörenberg for their help in the daily struggle with ARTE, Root, C++, and...to be continued.
Thank you to all the people who helped: M. Adams, Dr. H. Albrecht, Dr. M. Bräuer, M. Bruinsma, Dr. A. Gellrich, Dr. P. Kreuzer, Dr. D. Krücker, Dr. B. Lewendel, Dr. M. Medinnis, R. Pernack, Dr. D. Samtleben, Dr. J. Spengler.
Another round of thanks to our colleagues in Mannheim, Dr. J. Gläß and A. Wurz, for their help and answers concerning our hardware.
Thanks to the "Eisprinzessinnen" M. Bahte, Dr. T. Fuljahn, D. Kahnert, M. Symalla and Dr. R. Zimmermann for many happenings on the funny side of life.
Last but not least, thanks to all that contributed but might not have been mentioned here.